Fast X-ray diffraction crystal size distribution analysis

Dissertation

zur Erlangung des Doktorgrades

“Doctor rerum naturalium”

der Georg-August-Universität Göttingen

im Promotionsprogramm Geowissenschaften / Geographie

der Georg-August-University School of Science (GAUSS)

vorgelegt von

Sigmund Heinrich Neher

aus Göttingen

Göttingen 2018

Betreuungsausschuss:

Herr Prof. Dr. W. F. Kuhs, Abteilung Kristallographie, Geowissenschaftliches Zentrum Göttingen, Georg-August-Universität Göttingen

Herr PD. Dr. H. Klein, Abteilung Kristallographie, Geowissenschaftliches Zentrum Göttingen, Georg-August-Universität Göttingen

Mitglieder der Prüfungskommission:

Referent: Herr Prof. Dr. W. F. Kuhs, Abteilung Kristallographie, Geowissenschaftliches Zentrum Göttingen, Georg-August-Universität Göttingen

Korreferent: Herr PD. Dr. H. Klein, Abteilung Kristallographie, Geowissenschaftliches Zentrum Göttingen, Georg-August-Universität Göttingen

Weiter Mitglieder der Prüfungskommission:

Frau Prof. Dr. S. Webb, Abteilung Mineralogie, Geowissenschaftliches Zentrum Göttingen, Georg-August-Universität Göttingen

Frau PD. Dr. H. Sowa, Abteilung Kristallographie, Geowissenschaftliches Zentrum Göttingen, Georg-August-Universität Göttingen

Herr Dr. B. Schmidt, Abteilung Mineralogie, Geowissenschaftliches Zentrum Göttingen, Georg-August-Universität Göttingen

Herr Dr. V. Karius, Abteilung Sedimentologie, Geowissenschaftliches Zentrum Göttingen, Georg-August-Universität Göttingen

Tag der mündlichen Prüfung: **3. Juli 2018**

Preface

This PhD thesis was prepared at the Geoscience Center Göttingen (dept. Crystallography) of the Georg-August-University Göttingen. The thesis work has been carried out from June 2013 until Mai 2018 and was partially (two years) funded by a grant of the German Research Foundation (DFG KU920/20-1). I personally invoked to propose for this grant and was involved in the preparation and application procedure. My position funding was followed-up by the German Research Foundation grand DFG KU920/18 and by the SUGAR-III project of the Federal Ministry of Education and Research (BMBF 03G0856B). During the thesis work period it was under my responsibility to advance a novel fast X-ray diffraction-based method for the determination of crystallite size distributions, called FXD-CSD. This included the complete software development of the software package *fxd-csd,* written in Python and comprising about 5000 lines of code. Furthermore, testing routines had to be plan and perform. Accompanying to the development the method was used to answer fundamental research questions. In that period related data was collected at the 'Deutsches Elektronen-Synchrotron' (DESY), the European Synchrotron Radiation Facility (ESRF) and with inhouse X-ray diffraction lab equipment.

The thesis comprises three peer-reviewed research papers, all having FXD-CSD as applied core method. The first manuscript (Chapter 2) describes the method and its functionality as well as its application range and limitations. Chapter 3 is demonstrating the application of the method, having technical ceramics as samples under investigations. In Chapter 4, FXD-CSD is used to answer fundament research questions, concerning crystal coarsening in gas hydrates. Chapter 1 provides an introduction to all necessary topics needed to understand the procedure of FXD-CSD and gives an overview over the previous work carried out in our group. The thesis closes with a general conclusion and an outlook regarding future applications and further improvements

Acknowledgments

Above all, I thank my supervisors Prof. Dr. Werner F. Kuhs and PD. Dr. Helmut Klein for supporting me during my time as PhD student and want to thank them for the fruitful scientific discussions during that time. Furthermore, I want to emphasize that Prof. Dr. Werner F. Kuhs constantly cared about, that I always was contracted during that time. I am aware that this is not necessarily common and want to express my appreciation to him.

I thank Ulf Kahmann for always being there in case something technical went wrong in the lab and for always giving a helping hand if needed. I also want to thank Karin Offerle for preparing my numerous contracts and doing all the administrative paperwork. Nils Hoffmann and Jan Martin Möller I like to thank for their technical assistance and the always welcome distraction whenever I needed a brake.

I thank my PhD fellows, Dr. Sofiane Saouane, Dr. Rubén Ganero García and their Supervisor Prof. Dr. Francesca Fabbiani for their help, concerning single crystal growing and performing single crystal diffraction measurements.

My thanks go to PD. Dr. Heidrun Sowa for the interesting and always informative discussion on crystal symmetry.

My special thanks go to Dr. Marwen Chaouachi, a further PhD fellow and my office mate, and Dr. Andrzej Falenty for the fruitful scientific discussions and the good times spend together at numerous beam times.

I thank my brother Prof. Dr. Richard Neher and my father Prof. Dr. Erwin Neher for their help on implementing the beam profile deconvolution.

I thank Dr. Nina Albrecht for proof reading this thesis and for being a welcome lunch fellow for years.

I thank my family and friends for supporting me before and during my time as PhD student.

Finally, I am grateful to my beloved girlfriend Natalie for being around and supporting me the last two years. It was her, who gave me the strength and the stamina to finish this thesis.

Table of contents

Chapter 1 Introduction

Fast **X**-ray **D**iffraction **C**rystal **S**ize **D**istribution analysis (FXD-CSD) constitutes a novel method to determine volume-based crystal size distributions (CSD) of crystalline powders or polycrystalline materials in the lower µm range. The method uses the diffracted integrated intensity of thousands individual crystals to determine the crystal volumes of the sample *via* a reference-based scaling procedure. The scaling is possible through a reference sample X-ray measurement with known CSD. In this context it is important not to confuse CSD with grain size distribution or particle size distribution, in which a grain or particle can consist of multiple crystals or particles not necessarily crystalline.

For the sample and the reference sample measurement, a two-dimensional detector and a goniometer with at least one rotation axis is mandatory. The integrated intensities are obtained *via* step-wise rotation measurements. This way several hundred frames are collected for each sample. The collected data is analyzed by a specially developed software package, written in Python.

With FXD-CSD it is possible to measure volume-based CSDs with unprecedented sampling statistics in a short amount of time and with almost no sample preparation needed. Because of the penetrative nature of X-rays and its short measurement duration the method can be considered as destruction free and facilitates *in situ* measurements also under non-ambient conditions.

The following sections introduces the reader in to all topics necessary to understand the following publications (Chapter 2, Chapter 3 and Chapter 4) and provides an overview of the preceded work on CSD determination *via* X-ray diffraction at the Abteilung Kristallographie, Geowissenschaftliches Zentrum Göttingen (GZG) of the Georg-August-Universität Göttingen. The last section of the present chapter gives a short introduction to the following publications.

1.1 Crystal structure

Crystalline material consists of atoms, molecules, or ions, arranged in a highly ordered fashion, in a three-dimensional **lattice**. Due to this ordered nature the lattice can be described by a small part of it. This smallest possible section, an imaginary box spanned by three axis, is called **unit cell** and contains all information to depict the crystal structure by geometric translations (see Figure 1.1). The length of the three axis and angles between them are called **lattice constants.** The angles between the axis and their generalized proportions define the seven lattice systems i.e. triclinic, monoclinic, orthorhombic, tetragonal, trigonal, hexagonal, and cubic. With symmetry operations (rotation, reflection, inversion and improper rotation) lattice systems can be transformed to 230 distinct **space groups** which describe all possible crystal structures. Detailed information on crystals symmetry, being one fundamental topic of crystallography, can be found in any crystallography text book (e.g.: Borchardt-Ott, 1997) and shall not be further elaborated here.

The **Miller index** notation is used to describe vectors and planes within the crystal lattice. Planes are described by three signed integers, *h, k,* and *l* and directions by u, v, and w. Written in brackets *(hkl)* they denote the plane orthogonal to the given axis intercepts; for example, is *(011*) intersecting axis b and c at 1, shown in Figure 1.1. Different types of brackets are used to clarify the notation: square brackets *[uvw]* are used for directions, round brackets *(hkl)* for planes and curly brackets *{hkl}* are used to include all symmetry equivalent planes e.g. the six cube faces {100}. To denote a set of equivalent directions, *<uvw>* is used. When using no brackets either a lattice point is meant, or one is writing about *hkl*-planes in general. Negative directions are written with a bar, as in $\bar{h}$ for $-h$.

Further aspects of crystalline matter, which are of special importance to the main topic of this thesis are the **d-value**, being the distance between two planes with the same hkl and the **multiplicity** of crystal planes. The multiplicity describes the number of symmetry equivalent *hkl*-planes that belong to one *hkl*-family, thus all have the exact same d-value. Best example are the six faces of a cubic crystal: (100), (010), (001), $(\bar{1}00)$, $(0\bar{1}0)$ and $(00\bar{1})$ of the {100} family with a multiplicity of 6.

In theory crystals are perfectly arranged and are, indeed closer to perfection than any other state of matter in nature, but several factors can hinder this perfection. These are for example impurities and lattice defects. They introduce tension into the lattice and result in bond length deviations from their ideal value. This can lead to a breakup of the bulk volume structure into many, slightly distorted sub crystal units. The measure, in which extend this breakup is present, is called **mosaicity**.

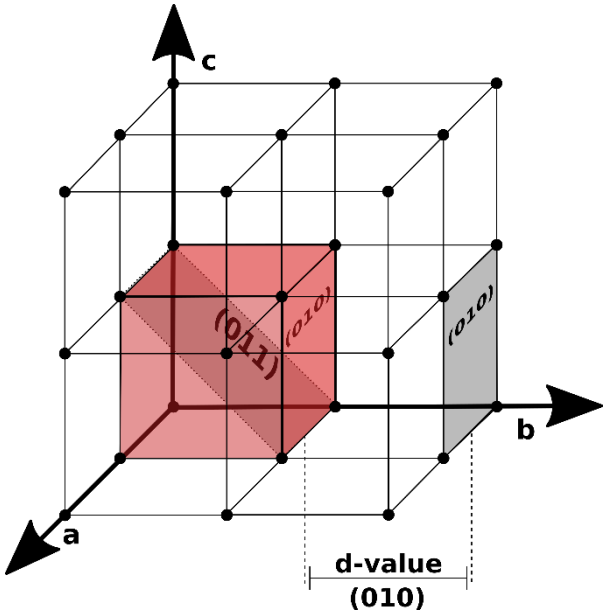

Figure 1.1: Cubic crystal lattice. The unit cell is highlighted in red. Two *hkl*-planes ((011), (010)) are shown.

Macroscopically, crystals can build crystal structure characteristic facets which perfectly follow the *hkl*-planes; to do this they need to grow slowly in equilibrium with their ambient conditions. In polycrystalline materials the outer shape of the crystals is mostly xenomorph or even externally altered, e.g.: by mechanic deformation.

1.2 Microstructure of polycrystalline materials

Looking at structural materials such as metals or ceramics, utilized in every day live, most people are not aware that many of them are of crystalline nature, in fact they are composed out of many small crystalline units. These units, called grains or **crystallites** – hereafter the latter shall be preferred – are the building blocks of **polycrystalline materials** and specify most physical properties of the material (Nye, 1957). They can have more influence on the material properties than their atomic composition or even their crystallographic structure. Polycrystalline materials are to be distinguished from non-crystalline materials like glass, plastic or composite materials, and of course from powders of single crystals.

Concerning the **microstructur**e of polycrystalline materials, the most important parameters are the internal structure of the crystallites (dislocations and secondary phases), the crystallite size, the

crystallite size distribution (CSD) and the crystal orientation in respect to the workpiece and towards each other. The latter is called **texture** or preferred orientation and can strongly influence the material properties because it describes the alignment of anisotropic crystallite properties (Hosford, 1993). Texture can be described by an orientation distribution function (Bunge, 1993) which e.g. can be used to link single crystal properties with the properties of the workpiece. In theory, a random texture – no preferred orientation – can for example result in the elimination of anisotropic crystal properties while a strong pronounced texture can almost mimic the properties of an anisotropic single crystal (Hosford, 1993). The **crystallites** itself virtually always incorporate lattice defects such as vacant atom positions, extra atoms between the lattices or impurity atoms. Depending on their concentration and degree of order, lattice defects have great impact on the physical properties of materials. Dislocations, i.e. two-dimensional ordered lattice defects, for example influence the plastic deformation behavior of metals through dislocation movement.

The **crystallite size** and its distribution, the **CSD** has crucial impact on the properties of polycrystalline materials and has always been of interest to research and manufacturing. The importance of the CSD is due to the fact that the strength of a polycrystalline material can widely be described as invers proportional to its average grain size. The average is of course depending on the shape of the CSD but has not been taken in to account routinely in the past. Commonly the relationship between crystal size and material strength is described by the empirical Hall-Petch equation (Hall, 1951; Petch, 1953) and is known as grain-boundary strengthening or Hall-Petch strengthening . Especially in ductile materials (metals) dislocation movement is the main deformation mechanism but dislocations can only move until they hit the next grain boundary. Thus, smaller crystallite sizes result in more grain boundaries and hinder dislocation movement and conversely, bigger crystallites result in less grain boundaries and dislocations can move further. Simplifying the microstructure to an average crystal size can therefore only be sufficient if the CSD is more or less symmetric and the smaller and stronger crystallites balance the larger ones. The fact that the shape of the CSD can be crucial and is influencing the slope of the Hall-Petch relation is first described by Kordylewski (1990; 1993), but seldomly accounted for because reliable CSD data is in most cases not available. Grain boundary sliding (GBS) constitutes another important deformation process, relevant for fine grained microstructures. GBS takes place preferably at elevated temperatures (Gottstein, 2014) and is also reported to be CSD dependent(Dey *et al.*, 1997; Yu & Shi, 2010).

Mean crystal sizes deduced from two-dimensional surfaces taken with imaging techniques (e.g. light or electron microscopy) and analyzed *via* line sectioning (number of intersection points or cord length)(Underwood, 1970) hardly reflect the real mean of the present CSD because the crystal section plane is not necessarily representative for its volume (German, 2010). A good estimate can only be achieved with superior counting statistics which is hard to establish, especially when the CSD is broad. The importance of the fact that the mean crystal size is likely to be insufficiently recorded or that cord length or even area based size distributions insufficiently reflect the crystal size volume proportions was recently accounted for by Raeisinia et al. (2008) and Lehto et al. (2014). These two authors introduced a volume weight to the size distribution. While the work of Raeisinia et al. (2008) is based on simulations and the work Lehto et al. (2014) is based on crystal size distributions obtained *via* linear intercept length measurements and the volume weight applied is measured *via* a point-sampled intercept length method. The details of how the described findings are made shall not be of primary importance here, important to note is that great efforts are made to deduce information about the

volume based CSD because only with that it is possible to apply the Hall-Petch relation to materials with skewed CSDs (Lehto *et al.*, 2014).

In brittle materials like ceramics the Hall-Petch relationship is also applied. Here the critical material strength is dominated by crack propagation hindered by grain boundaries and pores (Orowan, 1949). Compared to ductile materials, crack propagation ultimately results in material failure instead of plastic deformation. For ceramics it is reported that from intermediate grainsizes on (~15 µm) the Hall-Petch relation is not necessarily valid anymore because crack propagation can be lowered by inhomogeneous crystal size distributions, meaning that extraordinary big crystals, compared to their direct surrounding stop cracks (Chantikul *et al.*, 1990; Carniglia, 1972). The mechanism behind that is called grain bridging (Swanson *et al.*, 1987).

1.3 Microstructure genesis

The genesis of microstructure can be highly complex and is by far not fully understood at present (Asta *et al.*, 2009). Additionally, it has to be considered differently for different types of materials and how they are manufactured. One scenario is the nucleation and crystal growth from melts, as for cast metals. A second scenario takes place when plastically deformed material is thermally treated. As a result, the heat energy activates recovery, recrystallisation and grain growth which transform the deformation structure. Sintering constitutes a third scenario where powders, not necessarily crystalline, are compacted and heat-treated to induce controlled microstructure changes. Multi-phase scenarios with eutectic behaviors are a further possibility.

The possible scenarios are numerous and all demand special considerations. In the following sections the focus will be on the fundamental theory of nucleation and growth (Section 1.3.1), the heat treatment of cold worked metal (Section 1.3.2), and on sintering ceramics (Section 1.3.3). Besides the brief introduction regarding the fundamental theory, the two other sections describe situations which are of big importance for research and industry and constitute examples which are bracketing a wide range of validity.

1.3.1 Nucleation and growth

A melt, being in liquid state of matter, shows no long-range order but near the melting point can contain a temperature dependent number of subcritical clusters. Their size and duration of existence is mainly a function of temperature and increases with decreasing temperature. When overheating a crystal or undercooling a melt the driving force $\Delta g_u = g_m - g_c$, with the specific free enthalpy of the melt g_m and the specific free enthalpy of the crystal g_c is acting. Δg_u becomes negative at the melting temperature T_m, but nuclei that form at or right below T_m are not necessarily stable, because until a certain nucleus radius r_0 is reached, the required energy for forming the nucleus surface exceeds the energy gained by forming the crystalline nucleus volume. Hence, the melt must be supercooled to form stable crystals. The Gibbs energy G_k (Eq. 1.1) then becomes negative and is given by

$$\Delta G_k = -\frac{4}{3}\pi r^3 \Delta g_u + 4\pi r^2 \gamma \qquad \text{Eq. 1.1}$$

with γ being the specific surface energy.

The rate at which nuclei are formed depends on the driving force and thermal fluctuations of the atomic arrangement in the melt. Hence with further undercooling of the melt ($T < T_m$) the nucleation

rate increases because of the increasing driving force and peaks at some point until it is decaying again because the mobility of the constituents is decreasing. In practice, the nucleation rate is usually much higher than expected by theory because impurities act as nuclei and e.g. the crucible walls lower the nuclei surface area. This knowledge is applied to control the number of nuclei formed during casting of metals; for example, by adding impurities to support the development of a finer microstructure. As stated above, a finer microstructure generally leads to a stronger material. As soon as the nuclei have exceeded their critical size and T is still $< T_m$ they start growing. The resulting crystal shapes depend on numerous factors, such as: the degree of supercooling, the possible solute transport mechanism and its rate, as well as the heat conductivity of solid and liquid or the number of solid phases that are produced. Possible parameter constellations are: great cooling rates and fast transport mechanisms, allowing the most efficient heat dissipation, favoring dendritic crystal growth and low heat conductivity with small cooling rates, which favors the development of coarse microstructure because the released crystallization heat compromises the development of new nuclei.

The specifically evolving CSD depends on the interplay of nucleation rate and growth rate and their development over time. The interplay of nucleation rate and growth rate can be cast in the Johnson-Mehl-Avrami-Kolmogorow (JMAK) equation. Under the assumption of spherical nuclei, radial growth, a random nuclei distribution and a crystal size independent growth rate, the JMAK equation describes the volume transformation of a melt A to the crystalline volume B, as a function of time. The function has an “s”-like shape, showing at first a slow but rapidly changing transformation rate and ending with a fast but rapidly decreasing transformation rate. In between there is a region of rapid transformation (e.g. see Figure 1.2, 2nd column 2). The beginning is dominated by nucleation where not much transformation is happening. The end is dominated by a decreasing growth rate because the supply of A is becoming a shortage and impedes the growth. This behavior was first described by A. N. Kolmogorow and further studied by A. F. Mehl, W. A. Johnson and M. Avrami (Kolmogorow, 1937; Johnson & Mehl, 1939; Avrami, 1939, 1940, 1941).

In his book “Kinetic Theory in earth science”, Lasaga (1998) applied the above described theory to an example taken from geoscience. The author is modeling the possible rock microstructural CSDs, which are to be found in igneous rocks if different nucleation and growth scenarios take place. By assuming Gaussian shaped temporal evolution of the nucleation rate I(t) and the growth rate G(t), tailored to take place in a time period of 100 years, Lasaga (1998) illustrates the effect of moving the relative positions of the two distribution maxima in time (see Figure 1.2). Lasaga (1998) states, that even though the assumptions are highly simplified, the simulations demonstrate that only when the growth rate maxima take place before the nucleation maxima, anything alike the CSDs observed in natural samples are produced. Furthermore, it shows that quantifying the CSD of any crystalline material can provide crucial information to understand its formation process.

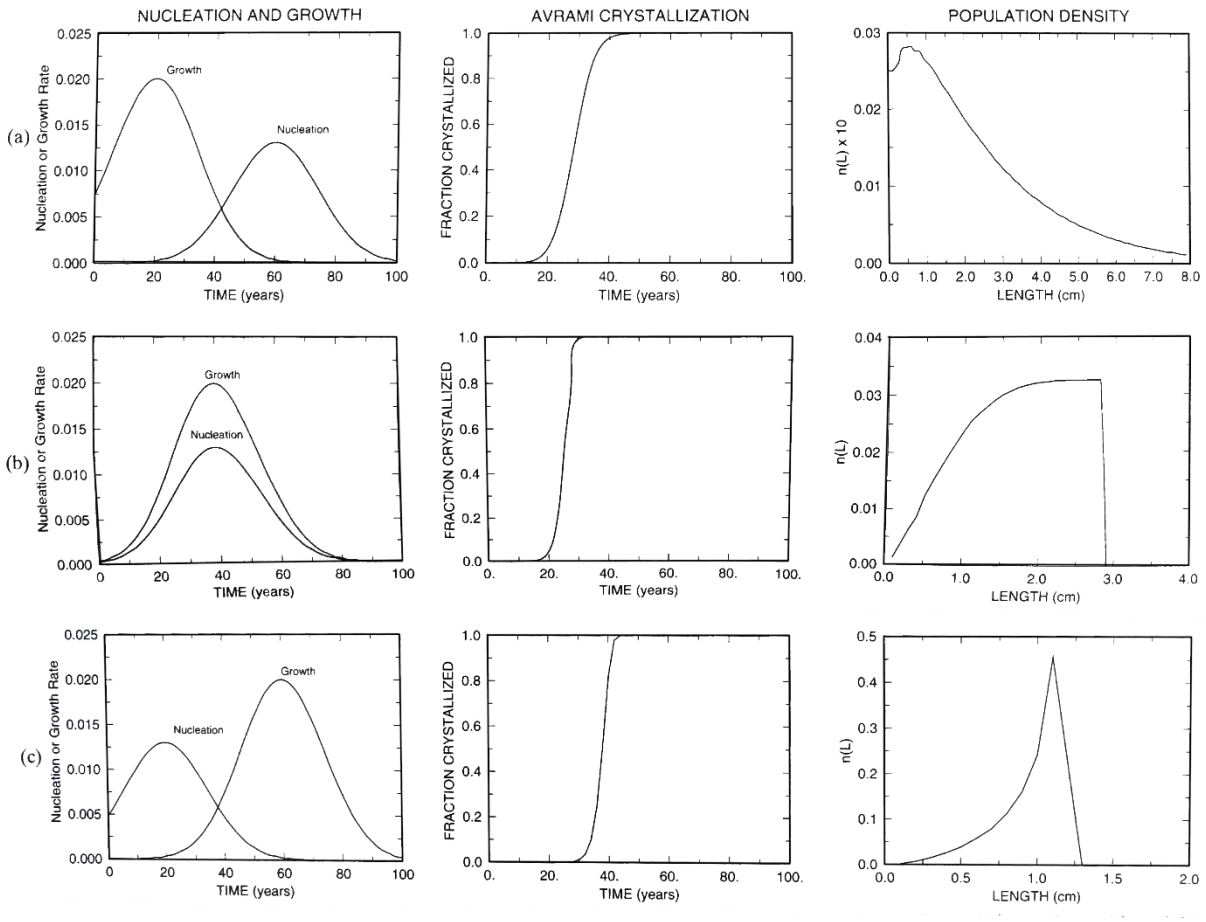

Figure 1.2: Theoretical rock microstructure calculation for three different model scenarios (a), (b), and (c). It is shown how the relative positions in time, of the nucleation rate evolution, and growth rate evolution (1st column) is impacting the function graph of the JMAK equation (2nd column; here solely called "Avrami") and what CSD shapes (3rd column; shown as population density distribution) could be produced. (Lasaga, 1998).

1.3.2 Microstructure development in deformed metals

In this section a short introduction to annealing phenomena of cold worked metals and the associated thermology is given. Note that in this section the term grain is used synonym to crystallite; this is following the relevant literature.

The microstructure of cold worked metals is fine grained, highly textured and the crystallites inherently contain many dislocations. The deformation-microstructure stores, induced through plastic deformation, parts of the deformation energy. The stored energy constitutes the driving force for all microstructural changes and occurs readily, when activated by heat treatment. The process is commonly subdivided in recovery, recrystallisation, and grain growth. The delimitation of these definitions can be fluent.

Recovery describes the re-arrangement, or extinction, of dislocations by atom diffusion. Only small-angled grain boundaries are developed and move through the grain. Small-angle grain boundaries are areas of high dislocation density between slightly (<10°) misoriented sub-grains (Humphreys & Hatherly, 1995).

Recrystallisation is defined as the development and movement of high-angle grain boundaries (grain misorientation >15°) under the consumption of the deformation texture. During recrystallisation the

sub-grains start growing, consuming their surroundings, and their distortion to other grains increases until large-angle grain boundaries are present (Humphreys & Hatherly, 1995).

Once the deformation texture is consumed completely and the crystals keep on growing, further coarsening is called **grain growth**. Still driven by the aim to reduce the total energy of the system, the surface area is reduced when bigger grains grow on the expense of smaller grains. The process of grain growth can be subdivided into **normal grain growth** (continuous grain growth), and **abnormal grain growth** (discontinuous grain growth). This distinction concerns the development of the present CSD. During normal grain growth the shape of the CSD stays unchanged, staying self-similar; all growing crystals grow with a rate proportional to their volume. The shape of the resulting CSD is depending on the underlying growth mechanism which has to occur in a uniform manner to not influence the shape of the distribution over time. One mechanism is for example the random motion of grain boundaries which results in a Rayleight distribution (Louat, 1974). In case the grain boundary movement is curvature driven a Hillert distribution is observed (Hillert, 1965). If surface tension is controlling grain growth a log-normal distribution is evident (Feltham, 1969). During abnormal grain growth certain energetical favorable grains grow faster and the shape of the CSD is changing. This ultimately can lead to a bimodal distribution.

1.3.3 Sintering

Sintering comprises the manufacturing prosses of consolidating compressed powders (ceramic or metallic) through heat treatment. The starting material, the powder, is brought to its desired shape and heated to high temperatures, right below the melting point. By doing so, the shape of the workpiece is preserved but the microstructure changes. One commonly divides between solid phase sintering and liquid phase sintering. During liquid phase sintering the temperature exceeds the solidus of at least one present phase. The most abundant and common sintering products in every day live are pottery and structural ceramics like bricks and roof tiles.

During sintering the microstructure evolves from a compacted but still porous powder towards a polycrystalline material. Many findings of fundamental research on sintering have been carried out with metal oxides like alumina. In principle, the mechanisms and especially the driving forces behind the structural change are similar to that introduced in the previous section. Apart from the presence of pores, the difference is rather a matter of terminology, which is introduced in the 2nd publication (Chapter 3).

An interesting example for an industrial application concerning the evolution of crystal size and its distribution is the manufacturing of optical corundum ceramics. Transparent corundum ceramics are used for highly scratch resistant windows (e.g. watch or smartphone covers) or for halogen light bulbs Halogen light bulbs constitutes a high temperature environment where corundum is superior to silica glass because corundum has a higher melting point. To reach good light transmissivity, optical ceramics need to have a low number of pores and a small amount of grain boundaries. Both, grain boundaries and pores, are sources for light scattering which have to be avoided to reach the desired transmissivity. To accomplish this, optical ceramics are sintered in a two-step procedure. 1) the material is sintered at a low temperature to achieve slow grain boundary movement, preventing pores being trapped within crystals. 2) subsequently the ceramic can be heat treated with higher temperatures to support fast grain boundary movement to coarsen the microstructure. Here abnormal grain growth is desirable because it can speed up the coarsening. (Krell *et al.*, 2003; Apetz & Bruggen, 2003)

1.4 X-ray diffraction

X-ray diffraction represents the core method used for FXD-CSD. For this reason, it shall be introduced here as the essential prerequisite to follow the explanations in the ensuing chapters. A special focus shall be given to single crystal intensity measurements and the associated intensity corrections, since it has a large thematic overlap with the measurement strategy used for FXD-CSD.

1.4.1 Bragg's Law

X-rays constitute a part of the electromagnetic wave spectrum with wavelengths between 10 nm and 1 pm. These lengths are typically expressed in Angstrom, since 1 A (100 pm) overlaps with typical crystallographic quantities, such as bond length and atom or molecule size. Commonly used wavelengths for diffraction experiments vary from around 0.1 Å at synchrotron facilities to about 2 Å, using e.g. chrome or manganese X-ray tubes. In many cases, including the here presented articles, monochromatic radiation is used, and the wavelength can be used as known variable.

If X-rays hit matter they interact with the electrons surrounding the atoms and scattered radiation of the same wavelength is emitted. This effect is known as elastic scattering or Thompson-scattering (He, 2009). When X-rays interact with electrons orbiting around ordered atoms (as it is the case in crystals), the emitted X-ray wavelets interfere with each other. Constructive interference occurs when the scattered radiation is in phase, which depend on the relative path length of the X-rays traveling through the crystal (thus on the atomic positions and the directions of incoming and outgoing beam). The loci of constructive interference are characteristic for the three-dimensional lattice for any particular crystal type. The geometric relationship between the incident beam and the direction of constructive interference θ depends on the d-values, the distances d between the lattice planes, and the wavelength λ of the incident radiation. The relation is described by Bragg's law:

$$n\lambda = 2d\ sin\theta \qquad \text{Eq. 1.2}$$

Figure 1.3 shows one direction of constructive interference. At the angle θ, also known as Bragg angle or glancing angle, the depicted rays have different pathlengths. The difference in pathlength match exactly a multiple of the used wavelength and the diffracted radiation leave the crystal in phase.

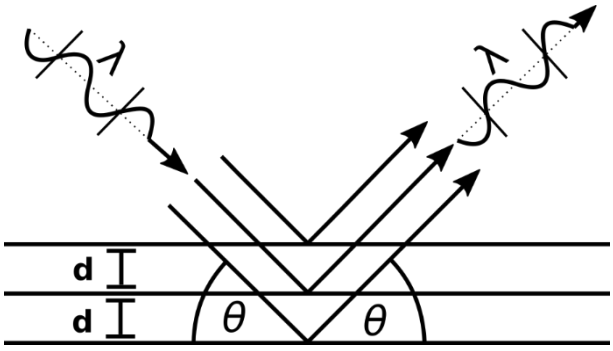

Figure 1.3: Bragg reflection at a crystal lattice with the distance d and at the Bragg angle θ. The pathlength difference of the three beam paths shown equals a multiple of the wavelength.

1.4.2 Ewald's sphere

A different approach to discuss X-ray diffraction is the so-called **Ewald sphere**, named after Paul Peter Ewald, a pioneer in early X-ray diffraction crystallography. Analogue to the Bragg law, the Ewald sphere construction describes diffraction conditions, but does this in reciprocal space. The incident and

diffracted X-ray radiation are described as vectors and the real crystal lattice as a reciprocal lattice. Figure 1.4 illustrates the Ewald's circle construction, the two-dimensional complement to the Ewald's sphere, with the radius $r_{\lambda^*} = \frac{1}{\lambda}$ located in the rotation centre $\mathrm{O}_{\mathrm{real}}$, and the reciprocal lattice with its centre at $\mathrm{O}_{\mathrm{reci}}$. Each reciprocal lattice point (RLP) represents the multitude of all parallel *hkl*-planes. The RLPs are plotted from $\mathrm{O}_{\mathrm{reci}}$ in direction of their *hkl*-plane normal, with the length of the inverse of their d-value (for details on the construction e.g. see Borchard-Ott (1997). Using the reciprocal lattice eases the explanation of diffraction occurring because the complete lattice can be shown.

Rotating the crystal corresponds to rotating the reciprocal lattice around $\mathrm{O}_{\mathrm{reci}}$. Diffraction occurs whenever an RLP intersects the Ewald's sphere. The diffracted radiation is propagating towards the direction of the intersection point. One important aspect of this approach, concerning integrated rotation intensity measurements as carried out for FXD-CSD, is the ability to depict the smeared-out nature of real diffraction conditions. The Ewald's circle, as well as the reciprocal lattice points, are drawn blurry to show that the d-value of the lattice and the wavelength of the used X-ray radiation has some variation. Consequently, real diffraction conditions are not super sharp, and the diffraction conditions have finite dimensions.

The diffracted intensity is a function of the rotation angle and, when recorded continuously, depicts a curve. This curve is called **rocking curve** and, if the reciprocal lattice point passed the Ewald's sphere entirely, represents the full integrated intensity. Furthermore, the Ewald's sphere allows to discuss diffraction in oblique-angled orientations. This is very important for FXD-CSD because the usage of two-dimensional detectors facilitates the measurement of oblique-angled orientations (see Section 1.5). Oblique-angled orientations require additional intensity corrections, namely the Lorentz factor and the polarization factor. Although the theoretic aspects of these corrections are basically described in Chapter 2, the Lorentz factor shall be described separately and more detailed in the following section.

1.4.3 Lorentz Factor

The shape of the rocking curve results from diffraction geometry dependent and geometry independent factors. The latter are the instrument conditions, i.e. incident beam divergence and beam spectrum distribution, and the crystal properties, i.e. the imperfection of the crystal lattice and the crystal size. These are the reasons for the already mentioned blurring. Their contribution to the shape of the rocking curve equals the convolution of instrument conditions and crystal properties.

Geometry-dependent factors are the lattice parameters and their orientation in respect to the rotation axis, together they are called the angular velocity factor (Lipson *et al.*, 2006) or Lorentz factor, first observed by Hendrik A. Lorentz. Using the Ewald's circle in Figure 1.4, the contribution of the lattice parameters can be observed. When rotating the crystal, all RLPs rotate around $\mathrm{O}_{\mathrm{reci}}$ with the same angular velocity, but since they vary in their distance to the centre, they have different orbital velocities. Hence, the time they intersect with the Ewald's circle, is a function of the length of their reciprocal lattice vector. This simple relation is obviously only valid for *hkl*-planes orientated parallel to the rotation axis, as illustrated in Figure 1.4.

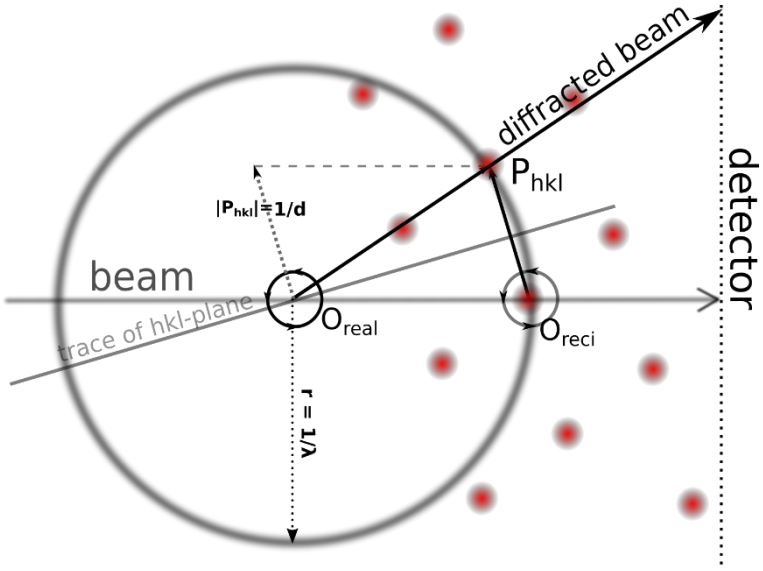

Figure 1.4: Two-dimensional Ewald's circle construction. The sample rotation axis O_{real} and the reciprocal space axis O_{reci} are orthogonal to the paper plane. The crystal lattice is orientated that P_{hkl} is situated in diffraction condition.

All other *hkl*-planes or *hkl*-planes of different orientated crystals and respectively their RLPs are oblique and intersect the Ewald's sphere on orbits not in the paper plane of Figure 1.4. To depict these oblique orientations, Figure 1.5 presents the sketch shown in Figure 1.4 from a different perspective and the RLP P_{hkl} in two different orientations. It is shown, that the orientation of the lattice point is strongly influencing the size of its orbit when rotating the sample. The mathematic expression and the effect on diffraction patterns collected *via* a rotation measurement is shown in Section 2.3.5 and in the Figure App. B-3 and Figure App. B-4.

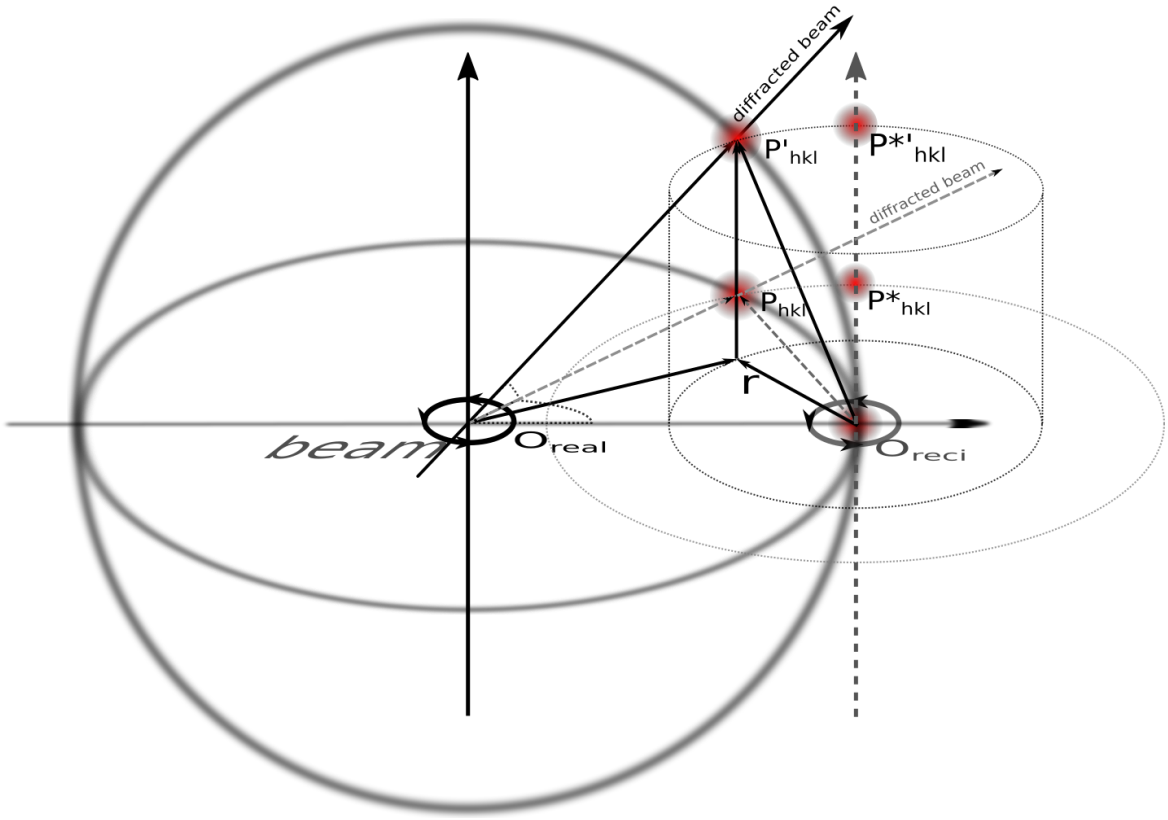

Figure 1.5: Ewald's sphere construction showing the Ewald's circle of Figure 1.4 from a different perspective. The sample rotation axis O_{real} and the reciprocal space axisO_{reci} are depict as arrows. The RLP P_{hkl} is shown in orthogonal orientation like it is shown in Figure 1.4 and is shown in an oblique orientation P'_{hkl}. When rotated around O_{reci}, P'_{hkl} describes a much smaller orbit r, thus intersects the Ewald's sphere much slower and a wider rocking curve is recorded.

1.5 Two-dimensional X-ray diffraction

In the previous section the theory of diffraction is introduced. Here, a more descriptive approach to X-ray diffraction and the resultant patterns shall be given. This is done with regard to FXD-CSD and the used diffractometer setup.

FXD-CSD demands the use of a diffractometer, equipped with a two-dimensional detector with fast readout for spatial resolved intensity measurements and a goniometer with one rotations axis. Figure 1.6 shows a scheme from the diffractometer setup used for most of the measurements presented in the following chapters; it depicts a three-circle Eulerian goniometer, with the diffractometer axis θ, ω, and φ.

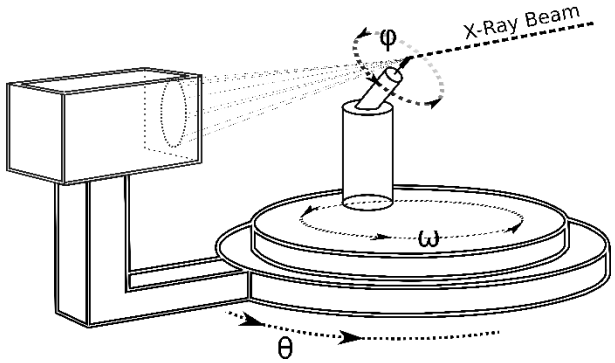

Figure 1.6: Three-circle Eulerian goniometer scheme with the axis θ, ω, and φ and a two-dimensional detector.

X-ray diffraction including its user community can be divided into two camps and scopes of applications. These are powder diffraction and single crystal diffraction, both having quite different demands on the equipment and type of data collected. Single crystal X-ray diffraction is usually concerned with structure determination. For this a single crystal is rotated around at least one goniometer axis to collect the integrated intensity of as many *hkl*-reflections as possible. The crystal orientations at glancing angles and the relative intensity of the collected reflections are used to solve the underlying crystal structure; for further reading on this topic see for example Bennet (2010). The rotation measurements show a distinct number of reflection spots on the detector (see left part of Figure 1.7). The number of peaks on each *hkl*-ring embodies the number of symmetry equivalent planes, the multiplicity, introduced in Section 1.1. In the shown frame, twice the number of expected reflections are visible because the crystal is rotated around one axis about 360°, thus each *hkl*-plane is measured in two orientations, which is a rather special case.

For powder diffraction measurements, as the name suggests, the sample consist of a crystalline powder. These crystals are usually only a few µm in size, of large number ($> 5 * 10^5$), and should be randomly orientated in the sample. Using a diffractometer like it is shown in Figure 1.6, produces the characteristic homogenous diffraction rings without rotating the sample (Figure 1.7 right); at any sample orientation there are enough crystals orientated in diffraction condition to produce this pattern. Powder diffraction data is for example used for quantitative phase analyses or crystal size determinations (line broadening) in the nm scale. For quantitative phase analyses the characteristic 2θ values of the present diffraction rings are assigned to d-values of known structures. If multiple phases are present, the integrated diffracted intensities are related to the phase fractions in the sample (Rietveld-Method); here the multiplicity, in this context called multiplicity factor, is used to purge the effect of multiplicity from the integrated intensity.

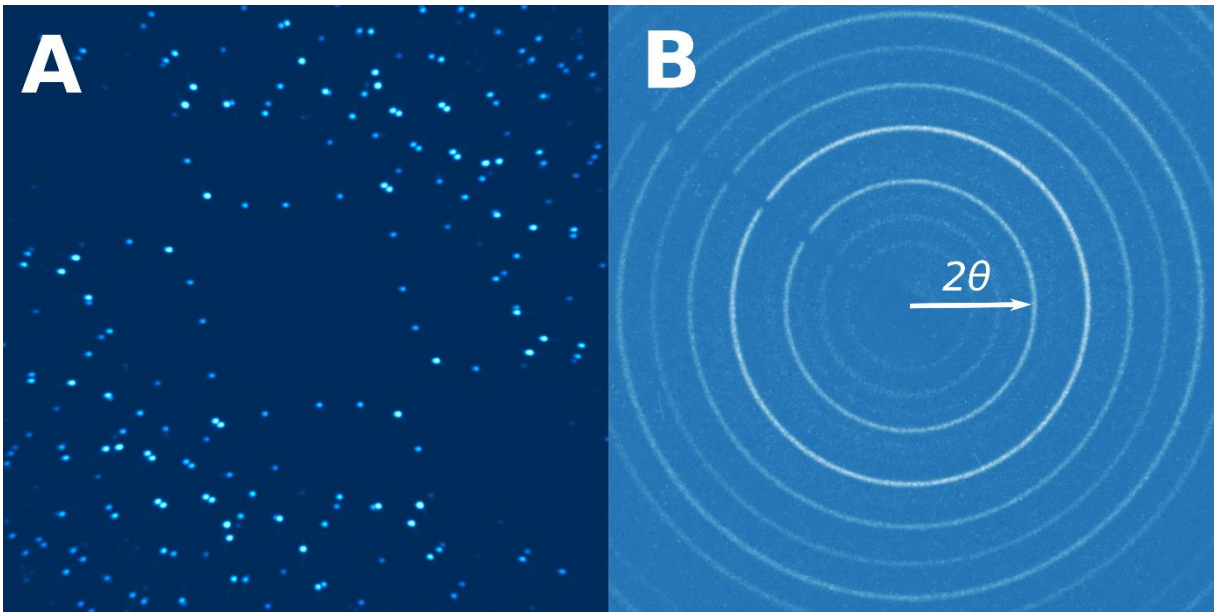

Figure 1.7: Left: Single crystal rotation measurement about one axis. The crystal is in arbitrary crystal orientation. Right: Powder measurement. It becomes clear that a single crystal measurement bears all information about the crystal structure, while a powder measurement provides better information to derive sample d-values *via* the θ angles.

Data collected for FXD-CSD is not in accordance with one of the two introduced methods above. FXD-CSD and the frames collected are rather located in between. For FXD-CSD thousands of single crystals

are measured and analyzed at once and the produced diffraction patterns consist of spotty diffraction rings (Figure 1.8).

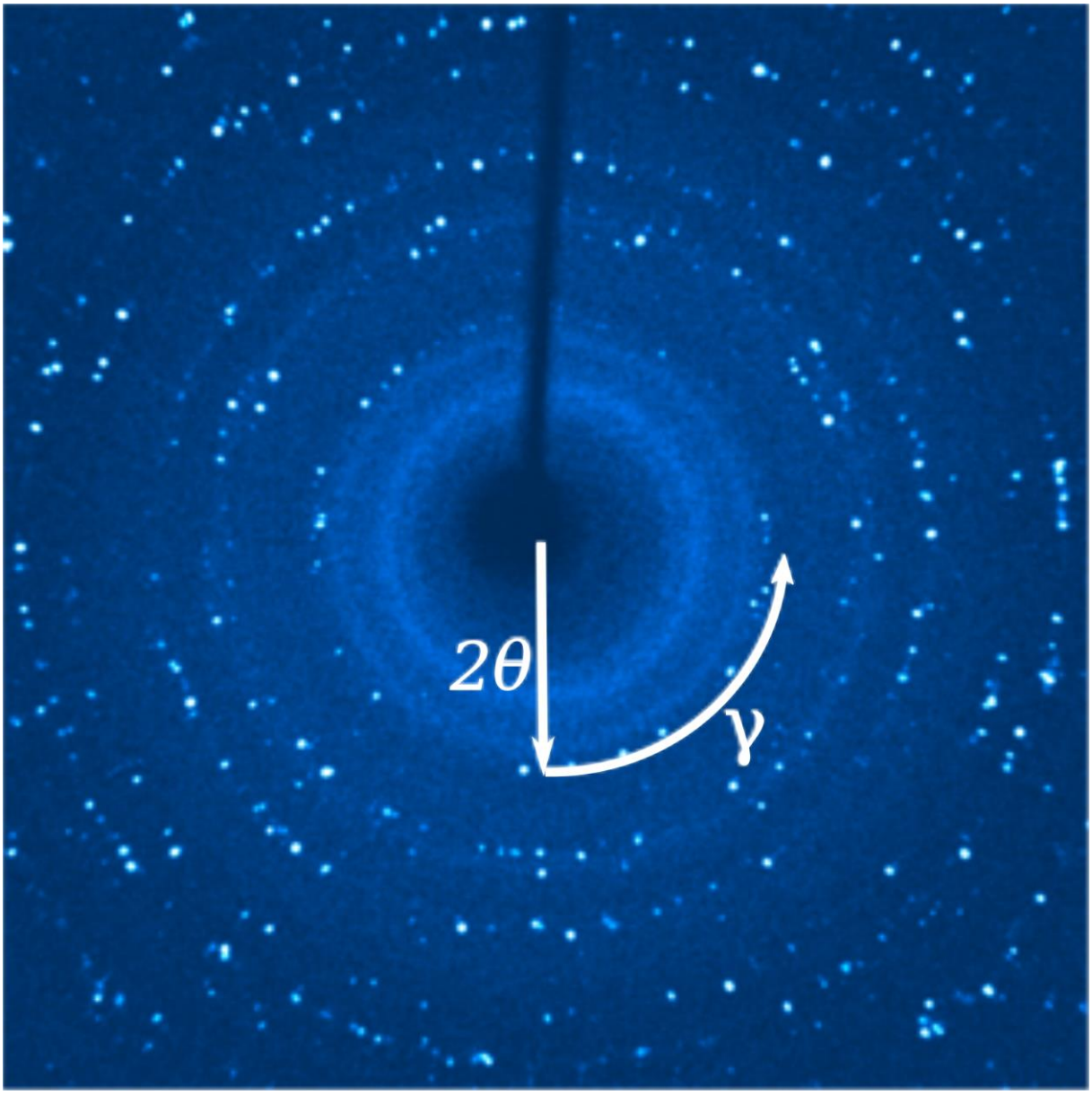

Figure 1.8: Spotty diffraction pattern as typical for FXD-CSD measurements. The number of crystals in diffraction condition is big enough to see numerous individual sports on each concentric *hkl*-ring. Each spot bears the size information of one crystal in the sample.

1.5.1 Integrated diffracted intensity and crystal size

FXD-CSD uses the integrated intensity of individual diffraction spots to deduce the crystal volume they stem from. To be able to do this, the scattering potential of the investigated material needs to be a known quantity. The integrated X-ray intensity of diffraction spots can be predicted when the crystal structure and the types of atoms along the *hkl*-planes are considered. As stated above the underlying process of diffraction is the elastic scattering of X-rays when interacting with electrons. The type of atom and their arrangement, the crystal structure (lattice + basis), is expressed by the structure factor F_{hkl}, which is the Fourier transform of the electron density within the unit cell for a certain *hkl*-plane. Thus, the amplitude of the diffracted intensity of the unit cell is proportional to $|F_{hkl}|$ and the

integrated intensity I_{hkl} is proportional to $|F_{hkl}|^2$ (Hammond, 2009). For details on the derivation of F_{hkl} see for example (He, 2009; Spieß *et al.*, 2009). Obeying the kinematic theory of diffraction, valid for finite and imperfect crystals (mosaic crystals, see Section 1.1), this relation can be extended in a way that the diffracted intensity of a crystal I_{cryst} is proportional the total of *n* unit cells in the crystal volume (Hammond, 2009; Als-Nielsen & McMorrow, 2011).

$$I_{cryst} \propto n^2 |F_{hkl}|^2 \qquad \text{Eq. 1.3}$$

For FXD-CSD this relationship is expressed for individual *hkl*-reflections:

$$I_{hkl} \propto \frac{|F_{hkl}|^2}{V_c} \qquad \text{Eq. 1.4}$$

and is used to relate the measured integrated intensities to the crystal volume V_{cryst}.

1.6 Previous studies

The work presented in this thesis is based on previous studies carried out at the *Abteilung Kristallographie* of the *GZG (Geowissenschaftliches Zentrum Göttingen)* of the Georg-August-University Göttingen. The initial idea to use X-ray diffraction for crystal size determination is closely linked to gas hydrate studies carried out in our group. Gas hydrates have a stability field at low temperatures and/or high pressure and are therefore quite delicate in terms of handling and preparation. Being not stable at ambient conditions makes it hard to apply most other methods commonly used (e.g. scanning electron microscopy) for a crystal size determination on gas hydrates.

The first attempts to deduce gas hydrate crystal size with X-ray diffraction where carried out with the so called Moving Area Detector Method (Bunge *et al.*, 2003) using synchrotron radiation (Klapp *et al.*, 2007). The Moving Area Detector Method was developed for texture measurement with high angular resolution, which till then were usually carried out in a rather coarse step-scan manner (usually 5°) and for microstructure measurements. The key for improving the resolution is translating the detector while recording the intensity. Simply lowering the rotation step size and collecting more frames instead, would have inevitably lead to much longer measurements times because area detectors (image plate detectors with long dead times) back then had low frame rates (> 60 s). To carry out such measurements, special slits had to be used to avoid different *hkl*-rings from overlapping (see Figure 1.9).

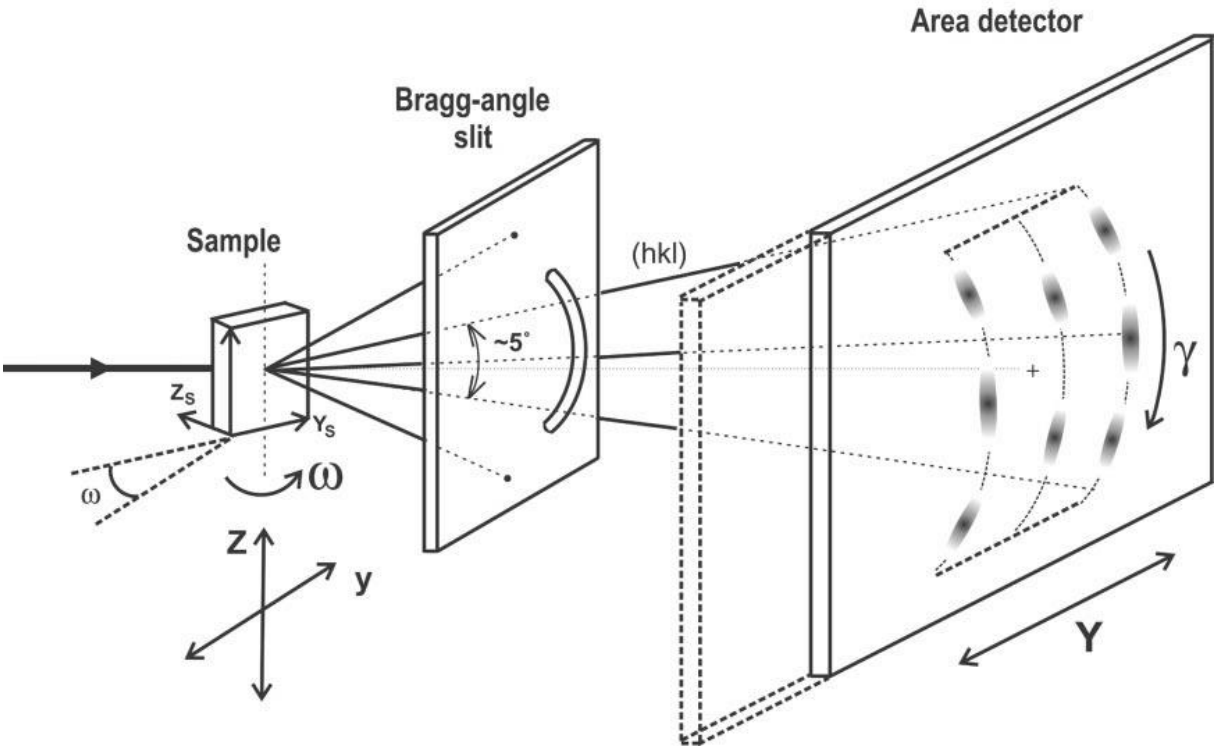

Figure 1.9: Scheme of Moving Area Detector Method setup. The method allows two measurements strategies: 1) the sample is rotated continuously while the detector is translated (shown in the scheme) or 2) the sample and the Bragg-angle slit is translated parallel to the detector, meaning that the incident beam is scanning the sample. The Brag-angle slit is letting through only a part of one *hkl*-ring and the diffracted intensity is recorded continuously. To measure crystal sizes, strategy 2) is used. If sufficiently coarse microstructures are measured the resulting diffraction patterns show individual elongated diffraction spots (strives) because of the coupled detector and sample translation. The length of the elongated diffraction spots is proportional do the crystal diameters in translation direction. From (Bunge *et al.*, 2003).

Stephan Klapp and colleagues (2007) used this method (with sample translation) to precisely measure CSDs of natural and synthetic gas hydrates for the first time. The numbers of observation are reported to be several hundred (max. 600), measuring each sample twice for 90 minutes. The lower limit of application, concerning the crystal size is estimated to be at 30 µm. Further studies on natural gas hydrate CSDs, using the Moving Area Detector Method were published a few years later (Klapp *et al.*, 2009, 2010).

During that time detector techniques improved significantly, and slow image plates were gradually replaced by much faster CCD detectors. Additionally, CCD detectors became cheaper and available for lab diffractometers. This development paved the way for new approaches to deduce crystal size from X-ray diffraction patterns. Most important here and applied by former members of our department is a γ-profile analysis by Rodriguez-Navarro *et al.* (2006). Rodriguez-Navarro *et al.* are using two-dimensional spotty diffraction patterns (similar to the one shown in Figure 1.8) to obtain *hkl*-specific, γ-intensity profiles by integrating the individual *hkl*-rings in θ direction (see Figure 1.10). The frames used, are taken while rotating the sample for usually 1-2 degrees about the φ-axis, integrating the diffracted intensities during rotation and assuring that most of the appearing diffraction spots went completely through reflection state. From the γ-intensity profiles the maximum intensities are extracted[1] and the average intensity is calculated for each measured *hkl*-ring. To deduce the crystal

[1] The program "XRD2DScan" is reading the detector frames and outputs a text file with all detected peaks on one *hkl*-ring or more specifically in a user defined 2θ range (Rodriguez-Navarro, 2006).

size from the measured intensities, several reference samples of the same material with known and different crystal sizes are measured. With the deduced mean intensity values a standard curve is established and an intensity scaling factor is derived.

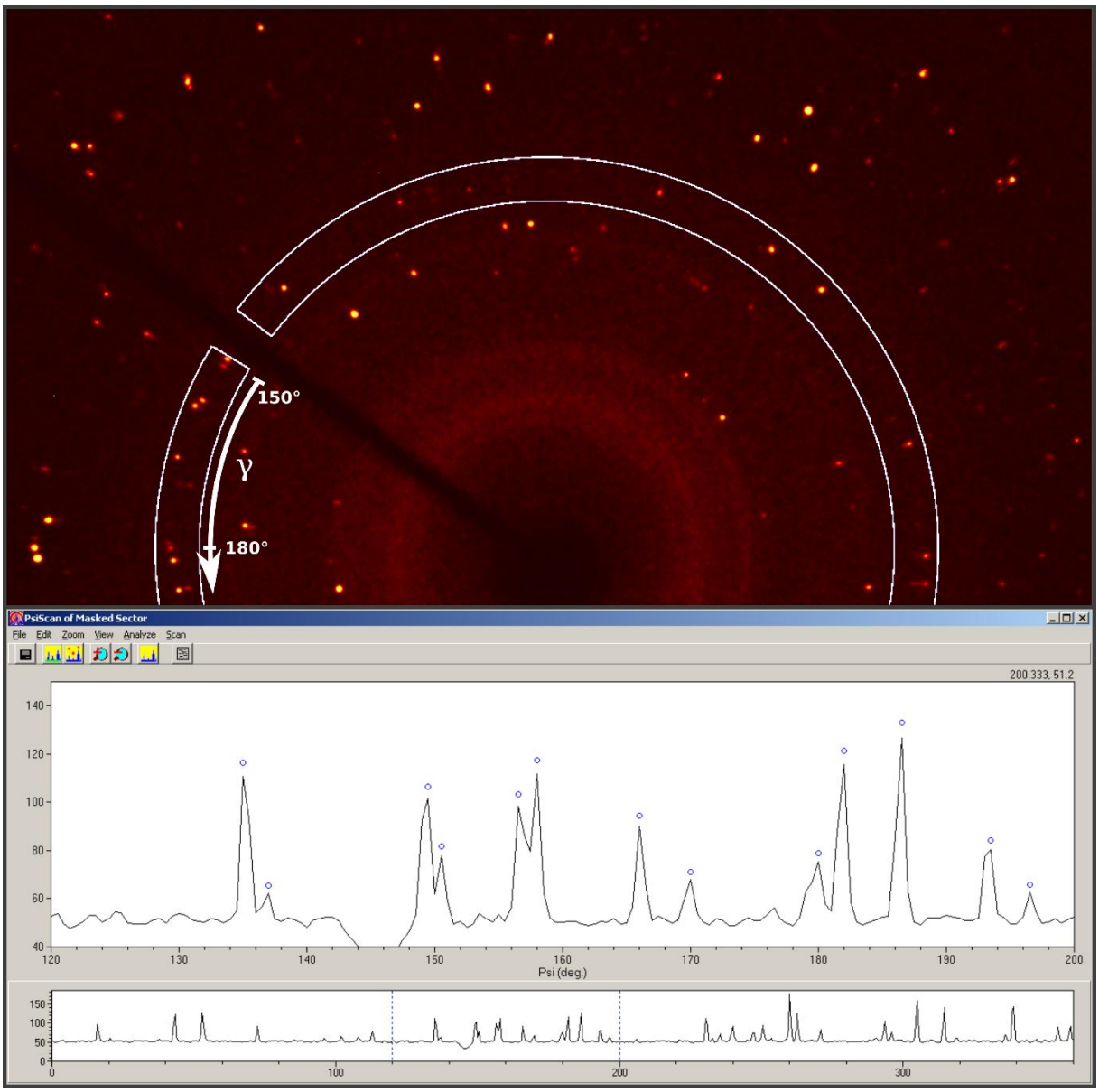

Figure 1.10 Exemplary γ-profile analysis with the "XRD2DScan" software. The upper part shows a spotty diffraction pattern with the area of interest (AOI) highlighted in white (screenshot). The AOI is integrated in θ-direction to obtain the γ-profile shown in the lower part of the figure. The lower part of the figure shows a screenshot taken from the produced γ-profile. The blue markers show the found maxima which are exported as text file. The shown γ-profile also shows the frequently occurring overlapping peaks which cannot be separated by a simple threshold operation. Additional it is evident how the integration in θ-direction is smearing well resolvable peaks. Good examples are visible between 145° γ and 160° γ.

Susanne Hemes, a former member of our department, and colleagues adopted the method by Rodriguez-Navarro *et al.* (2006) to investigate gas hydrate microstructure with our inhouse lab diffractometer (Bruker AXS SMART Apex II CCD with D8 base) and she presented her findings in a diploma thesis (Hemes, 2009). The two most important and fundamental improvements to Rodriguez-Navarro's work are: 1) The used reference samples to establish a standard curve does no longer need to have the same structure as the sample. The established intensity scaling factor is corrected with

respect to the structure factor ratio of sample and reference. The structure factor dependent scaling procedure is in principle similar to the one described in Chapter 2, Section 2.3.1. Each sample intensity is kept as individual data point to compose real CSD histograms. 3) The φ-rotation step-width is decreased to 0.1°. Measuring with smaller rotation step width, decreases the number of diffraction spots on each single frame and lowers the chance of accidental peak overlap. One consequence of measuring with such small rotation steps is that the diffraction spots can occur on more than one frame. To find the individual diffraction spot maxima the software "Max-Intens"[2] is used. The program is reading the output files of XRD2DScan and gives out the maximum intensities of each reflection. Unfortunately, none of the tested materials (Ice spheres, quartz powder or corundum powder) delivered fully satisfying results. The used materials were building agglomerates or did have a too broad size distribution.(Hemes, 2009)

Stefanie Stracke and Mathias Jansen, two bachelor students at our group, were initially working with "XRD2DScan" and planned to study the CSDs of ice I_h and gas hydrates as their bachelor thesis. Besides that, they tested alternative calibration materials and carried out considerations about the possible impact of extinction. The first approach was using an Ylid single crystal, an organic and spherical shaped single crystal for intensity calibration purposes (delivered with the Bruker diffractometer). To use the Ylid crystal the crystal volume was precisely measured to relate its volume with the diffracted intensities. Difficulties during the diffraction measurements of the Ylid crystal made the CSD measurements impracticable but yielded important findings about our inhouse diffractometer. It turned out that a defective monochromator is causing so called satellite peaks which complicated exact intensity measurements (see also Appendix B 5). The measured integrated intensities of diffraction spots stemming from symmetry equivalent *hkl*-planes did not show the same intensities. As a consequence, the single crystal approach was not followed up, but in principle constitutes a possible way. (Jansen, 2010; Stracke, 2010)

Besides the efforts made to find better calibration materials it was decided to use the integrated intensity of the individual peaks in the γ-profiles instead of only using the maximum. When working with integrated intensities the counting statistics are much better which is improving the precision of the method. The first approach to do this was carried out by Marwen Chaouachi, a former member of our group and at that time PhD student. Marwen tried to use the γ-profiles, exported as text files by "XRD2DScan", to extract the integrated peak intensities. The approach included modulating a background function to separate the peaks from the background *via* a threshold operation. The major problem with this first approach is the frequently occurring overlapping peaks, which cannot be separated by a single threshold operation (see Figure 1.10).

At this point, at first informally, I joint the project by suggesting that a two-dimensional intensity extraction approach could work much better. Integrating the AOI (see Figure 1.10) in θ direction inevitably smears the peaks and is wasting most advantages of a two-dimensional detector. At that time, I was sharing an office with Marwen Chaouachi and was writing up my diploma thesis. In the following time I developed the first version of the *fxd-csd* software which at that time was called "00Peak.py" and "OmegaStep.py". This first version was only intended to extract the intensity curves out of the collected frames and was outputting the rocking curves with their detector position as a spread sheet file. All intensity corrections had to be done manually. The way how the absorption

[2] Written by PD. Dr. Helmut Klein.

correction (see Appendix B 3.1) has to be applied, was for example elaborated by Kathrin Nützmann and is part of her M. Sc. Thesis (Nützmann, 2013) in which she used the mentioned early version of the *fxd-csd* program. A further innovation implemented during that time was the S1 scaling procedure as described in Chapter 2, which replaces the formerly needed standard curve (Chaouachi, 2015; Nützmann, 2013; Stracke, 2013).

1.7 Method implementation and software development

As indicated in the last section, my contribution to the project is the software implementation of the method. Most important here is the new three-dimensional approach. Instead of turning two-dimensional data into one-dimensional data by integrating it and using only the maxima intensities, the three-dimensional approach is using the integrated intensities extracted from the consecutive frame series. This way each individual diffraction spot intensity is available with its rocking curve, which is drastically improving the counting statistics. Furthermore, the three-dimensional measurement and analysis technique did improve sampling statistics and increased the range of applicability concerning the number of resolvable spots on the detector. In combination with the automated data reduction and analysis the theory was turned into a widely applicable and user-friendly method. To accomplish this, the following tasks had to be fulfilled:

By far the biggest task was to develop the software to handle the vast amounts of collected data. For this purpose, the program *fxd_csd* was written in Python and now comprises over 5000 lines of codes. *fxd_csd* reads the collected detector frames, extracts the integrated intensity information, performs the needed intensity corrections, applies the appropriate intensity scaling and puts out the sought sample CSD.

The implementation of the intensity corrections (i.e. the angular velocity and polarization factor) turned out to be far from trivial. Despite being well-known for decades, most textbooks describe them in very simplistic forms, only valid for simple diffraction geometries, and are usually expressed using angles and trigonometry. Trigonometric functions and angles are intuitive but are inconvenient when implemented in software and are slower in computation. For *fxd_csd,* using area detectors, allowing all sorts of diffraction geometries, more general expressions, ideally using linear algebra were needed. These expressions had to be implemented without templates and needed to be tested extensively. To test the angular velocity factor for example, single crystal rotation measurements were carried out (bathing the crystals in the beam). These test measurements are performed in the same step-wise manner as the FXD-CSD data is acquired. Subsequently the software is used to extract the intensities and the correction is applied. Measuring a single crystal enables one to identify the measured diffraction spots and evaluate whether the corrected intensities are correct. The evaluation is possible because the relative intensities are known. Three types of crystals were used. The Ylid crystal, a commercially obtained intensity calibration crystal, corundum crystals and grown thiourea crystals. The latter two have been prepared for synchrotron measurements because the Yild crystal was considered to be too delicate and precious to travel.

Another task was to find or produce suitable reference and test materials besides the already mentioned ones used in previous studies. Possible materials need to be single crystalline powders with a narrow and precisely known CSD. Additionally, the crystal shapes should ideally be spherical or highly symmetric to enable an accurate volume determination *via* two-dimensional electron microscopy imaging. This task has - to this day - not been fulfilled in a completely satisfactory manner. The

produced reference material is suitable but bears room for improvement. In the end other tasks, and issues did hinder further efforts on this topic.

1.8 Introduction to the included publications

The following chapters present three peer reviewed publications having FXD-CSD as main topic or FXD-CSD is used as core method to derive the CSD of the samples under investigation. At present, the manuscript underlying Chapter 2 is in print. It was submitted at 5th of May 2018, reviewed positive at 25th of May 2018 and was accepted at the 23rd of July 2018.

Chapter 2: "*A fast X-ray diffraction-based method for a determination of crystal size distributions (FXD-CSD)",* accepted for publication in the Journal of Applied Crystallography, constitutes the main part of this thesis and provides a comprehensive description of the method. Starting with an overview of other methods used to derive CSDs or mean crystal sizes, including non-X-ray diffraction-based approaches, all theoretical aspects and applied intensity corrections are presented. The fundamental functionality and the application range of FXD-CSD is shown by presenting the analysis and results of five samples. The measurements are carried out with the diffractometer setup described in Section 1.5 using a molybdenum X-ray tube. Most valuable here are the results of four corundum crystal size fractions. These samples have been specifically prepared (Chapter 2, Section 2.4) for this purpose and their CSD was determined in advance. This allowed their utilization both as a reference material and as a sample to crosscheck the obtained results.

For this publication the *fxd-csd* software, written by me, was used. This is including the data reduction, data evaluation and the CSD determination. The samples were produced, prepared and measured by me. My contribution to the manuscript preparation comprises drafting, figure preparation and partially the literature search. The final preparation and proofreading were carried out with the aid of Prof. Dr. W.F. Kuhs and PD Dr. Helmut Klein.

Chapter 3: "*Determination of crystal size distributions in alumina ceramics by a novel X-ray diffraction procedure*", published in 2017 the *Journal of the American Ceramic Society*, presents an application example, investigating the microstructure of a polycrystalline material. Again, the diffractometer setup described in Section 1.5 with a molybdenum X-ray tube was used. Here we were able to analyze the microstructural evolution of four alumina substrates with different time spans of sintering. The CSD of all samples was determined and good evidence for abnormal grain growth was found.

My contributions to this publication are the sample preparation, the diffraction measurements, the data analysis (using the *fxd-csd* software), the figure preparation and the drafting of the manuscript. The samples were provided by PD. Dr. Helmut Klein. Finalizing the manuscript was done with the input and correction of my supervisors Prof. Dr. W.F. Kuhs and PD. Dr. Helmut Klein.

Chapter 4: The publication, "*Time Resolved Coarsening of Clathrate Crystals: The Case of Gas Hydrates*", published 2016 in the Journal *Crystal Growth & Design,* constitutes a fundamental research paper. FXD-CSD is the core method used to determine the CSD evolution of gas hydrates. The analyzed data was collected at the European Synchrotron Research Facility (ESRF) in Grenoble, France. The obtained results show the coarsening and the CSD evolution over time and it is shown that they are in accordance with X-ray tomography data of comparable samples.

The presented data was analyzed with a preliminary version of *fxd-csd,* which was used by Marwen Chaouachi for the data reduction and to calculate the diffraction geometry dependent intensity corrections. The data evaluation and intensity scaling were done manually by Marwen. I was attending the beam times and as part of the crew assisting Marwen carrying out the measurements. I was involved in writing the manuscript by drafting the data reduction section.

1.9 References

Als-Nielsen, J. & McMorrow, D. (2011). Elements of Modern X-ray Physics Hoboken, NJ, USA: John Wiley & Sons, Inc.

Apetz, R. & Bruggen, M. P. B. (2003). *J. Am. Ceram. Soc.* **86**, 480–486.

Asta, M., Beckermann, C., Karma, A., Kurz, W., Napolitano, R., Plapp, M., Purdy, G., Rappaz, M. & Trivedi, R. (2009). *Acta Mater.* **57**, 941–971.

Avrami, M. (1939). *J. Chem. Phys.* **7**, 1103–1939.

Avrami, M. (1940). *J. Chem. Phys.* **8**, 212–224.

Avrami, M. (1941). *J. Chem. Phys.* **9**, 177–184.

Bennett, D. W. (2010). Understanding single-crystal X-ray crystallography Weilheim: Wiley-VCH.

Borchardt-Ott, W. (1997). Kristallographie Berlin, Heidelberg: Springer-Verlag.

Bunge, H.-J. (1993). Texture analysis in materials science. Mathematical Methods London: Butterwoth & Co.

Bunge, H. J., Wcislak, L., Klein, H., Garbe, U. & Schneider, J. R. (2003). *J. Appl. Crystallogr.* **36**, 1240–1255.

Carniglia, S. C. (1972). *J. Am. Ceram. Soc.* **55**, 243–249.

Chantikul, P., Bennison, S. J. & Lawn, B. R. (1990). *J. Am. Ceram. Soc.* **73**, 2419–2427.

Chaouachi, M. (2015). Microstructure of Gas Hydrates in Sedimentary Matrices. PhD. Thesis. Georg-August-Universität of Göttingen.

Dey, N., Hsia, K. J. & Socie, D. F. (1997). *Acta Mater.* **54**, 4117–4129.

Feltham, P. (1969). *Scr. Metall.* **3**, 853–854.

German, R. M. (2010). *Crit. Rev. Solid State Mater. Sci.* **35**, 263–305.

Gottstein, G. (2014). Materialwissenschaft und Werkstofftechnik Berlin, Heidelberg: Springer Berlin Heidelberg.

Hall, E. O. (1951). *Proc. Phys. Soc. Sect. B*. **64**, 747–753.

Hammond, C. (2009). The Basics of Crystallography and Diffraction New York: Oxford University Press.

He, B. B. (2009). Two-Dimensional X-Ray Diffraction Hoboken: J. Wiley & Sons, Inc.

Hemes, S. (2009). Röntgenographische Untersuchungen der Kristallitgrößen und Kristallitgrößenverteilungen von Gashydraten. Diploma Thesis. Georg-August-Universität Göttingen.

Hillert, M. (1965). *Acta Metall.* **13**, 227–238.

Hosford, W. F. (1993). *Oxford Engineering Science Series*, Vol. *32*, edited by A.L. Cullen, L.C. Woods, J.M. Brady, C. Brennen, W.R. Eatock Taylor, M.Y. Hussaini, T. V Jones & J. Van Bladel, p. 248. New York: Oxford University Press.

Humphreys, F. J. & Hatherly, M. (1995). Recrystallisation and related Annealing Phenomena New York: Pergamon - Elsevier Science Inc.

Jansen, M. (2010). Messung von Kristallitgrößenverteilungen über Einzelreflexe in Debye-Scherrer-Ringen: Gashydrate. B.Sc. Thesis. Georg-August-Universität of Göttingen.

Johnson, W. A. & Mehl, R. F. (1939). *Transactions of the AIME*, Vol. *135*, pp. 416–442. American Intitute of Mining and Metallurgigcal Engineers.
Klapp, S. A., Hemes, S., Klein, H., Bohrmann, G., MacDonald, I. & Kuhs, W. F. (2010). *Mar. Geol.* **274**, 85–94.
Klapp, S. A., Klein, H. & Kuhs, W. F. (2007). *Geophys. Res. Lett.* **34**, L13608.
Klapp, S. A., Klein, H. & Kuhs, W. F. (2009). *Geological Society, London, Special Publications*, Vol. *319*, 161–170.
Kolmogorow, A. (1937). *Izv. Akad. Nauk SSSR Ser. Mat.* **1**, 355–359.
Krell, A., Blank, P., Ma, H., Hutzler, T., Bruggen, M. P. B. van & Apetz, R. (2003). *J. Am. Ceram. Soc.* **86**, 12–18.
Kurzydeowski, K. J. (1990). *Scr. Metall.* **24**, 879–883.
Kurzydeowski, K. J. & Bucki, J. J. (1993). *Mater. Sci.* **41**, 3141–3146.
Lasaga, A. C. (1998). Kinetic Theory in the Earth Sciences Princeton: Princeton University Press.
Lehto, P., Remes, H., Saukkonen, T., Hänninen, H. & Romanoff, J. (2014). *Mater. Sci. Eng. A*. **592**, 28–39.
Lipson, H., Langford, J. I. & Hu, H.-C. (2006). *Int. Tables Crystallogr.* **C**, 596.
Louat, N. P. (1974). *Acta Metall.* **22**, 721–724.
Nützmann, K. (2013). Crystallite Size Distributions of CH 4 -CO 2 Gas Hydrates from Diffraction Data (Including the Effect of Absorption). MSc. Thesis. Georg-August-University of Göttingen.
Nye, F. J. (1957). Physical properties of crystals New York: Oxford University Press.
Orowan, E. (1949). *Reports Prog. Phys.* **12**, 309–232.
Petch, N. J. (1953). *J. Iron Steel Inst.* **174**, 25–28.
Raeisinia, B., Sinclair, C. W., Poole, W. J. & Tomé, C. N. (2008). *Model. Simul. Mater. Sci. Eng.* **16**, 025001.
Rodriguez-Navarro, A. B. (2006). *J. Appl. Crystallogr.* **39**, 905–909.
Rodriguez-Navarro, A. B., Alvarez-Lloret, P., Ortega-Huertas, M. & Rodriguez-Gallego, M. (2006). *J. Am. Ceram. Soc.* **89**, 2233–2238.
Spieß, L., Teichert, G., Schwarzer, R., Behnken, H. & Genzel, C. (2009). Moderne Röntgenbeugung Wiesbaden: Vieweg+Teubner.
Stracke, S. (2010). Messung von Kristallitgrößenverteilungen über Einzelreflexe in Debye-Scherrer-Ringen: Eis Ih. B.Sc. Thesis. Georg-August-Universität of Göttingen.
Stracke, S. (2013). Kristallinität und Zusammensetzung von Methanhydrat bei der Bildung aus Eis Ih. M.Sc. Thesis. Georg-August-Universität of Göttingen.
Swanson, P. L., Fairbanks, C. J., Lawn, B. R., Mai, Y.-W. & Hockey, B. J. (1987). *J. Am. Ceram. Soc.* **70**, 279–289.
Underwood, E. E. (1970). Quantitative stereology Reading: Addison-Wesley Publisching Company, Inc.
Yu, T. & Shi, H. (2010). *J. Phys. D. Appl. Phys.* **43**, 165401.

Chapter 2 Publication - A fast X-ray diffraction-based method for the determination of crystal size distributions (FXD-CSD).

Journal

Journal of Applied of Applied Crystallography (2018, **51** in print)

Authors

Sigmund H. Neher[a], Helmut Klein[a] and Werner F. Kuhs[a]

[a]GZG Crystallography, University of Göttingen, Goldschmidtstr. 1, Göttingen, 37077, Germany

Abstract

We present a procedure for a fast X-ray diffraction-based crystal size distribution analysis, named FXD-CSD. The method enables the user with minimal sample preparation to determine the crystal size distribution (CSD) of crystalline powders or polycrystalline materials, derived *via* an intensity scaling procedure from the diffraction intensities of single Bragg spots measured in spotty diffraction patterns with a two-dimensional detector. The method can be implemented on any single crystal laboratory diffractometer and any synchrotron-based instrument with a fast-readout two-dimensional detector and a precise sample scanning axis. The intensity scaling is achieved *via* the measurement of a *reference* sample with known CSD under identical conditions; the only other prerequisite is that the structure (factors) of both, *sample* and *reference* material, must be known. The data analysis is done with a software package written in Python. A detailed account is given of each step of the procedure, starting with the measurement strategy and the demands on the spottiness of the diffraction rings, the data reduction, and the intensity corrections needed, followed by the data evaluation and the requirements for the reference material. Using commercial laboratory X-ray equipment several corundum crystal size fractions with precisely known CSD were measured and analysed to verify the accuracy and precision of the FXD-CSD method; a comparison of known and deduced CSDs shows good agreement both in mean size and shape of the size distribution. For the used material and diffractometer setup the crystal size application range is 1 to several tens of µm; this range is highly material and X-ray source dependent and can easily be extended on synchrotron sources to cover the range from below 0.5 to over 100 µm. FXD-CSD has the potential to become a generally applicable method for CSD determination in the field of material science and pharmaceutics, including development and quality management as well as in various areas of fundamental research in physics, chemistry, chemical engineering, crystallography, the geological sciences and bio-crystallization. It can be used also under *in situ* conditions for studying crystal coarsening phenomena and delivers precise and accurate CSDs permitting to test experimentally various theories developed to predict their evolution.

2.1 Keywords and abbreviations

CSD: volume-based crystal size distribution cast in to number of occurrence histograms

ID: intensity distribution is probability distribution of all sampled integrated diffraction spot intensities

VD: volume distribution is the probability distribution of the crystallite volumes

IDH: intensity distribution (ID) represented as binned number of occurrence histogram

PDF: probability density function, fitted to the midpoints of the IDH

S1: diffractometer specific intensity scaling factor between the volume-based CSD of the *reference sample* and its X-ray derived intensity distribution

Reference: sample material used as reference to determine the S1 scaling factor

Sample: used to designate any sample under investigation

S2: structure factor (*hkl*) specific scaling factor between the *sample* under consideration and the *reference*

ISV: irradiated sample volume

CSF: crystal size fraction

Internal-scaling: If more than one *hkl*-ring is analyzed to establish the IDHs of *reference* or *sample* the IDs derived from individual *hkl*-rings are placed on a common scale by relating the squared structure factors of a given *hkl* to one arbitrarily chosen reference *hkl*. The structure factors of the chosen *hkl* are subsequently used for the S2 scaling.

$ID_{cut\text{-}off}$: the observation that IDHs resolving from different hkl-rings do not match on the left tail of the distributions after the *internal-scaling*. A CSD that is partly below the detection limit produces this artefact because the detection limit is structure factor dependent.

$ID_{exaggeration}$: the observation, that IDHs resolving from different *hkl*-rings do not have matching right distribution tails after the *internal-scaling*. This occurs when a CSD measurement is significantly impacted by accidental spot overlap which exaggerates the number of large crystallites; this mismatch is multiplicity dependent.

LLOD: the lower limit of detection of the diffractometer setup, regarding the crystal size

ULOA: the upper limit of application, regarding the crystal size

2.2 Introduction

A novel X-ray diffraction procedure is presented suited to establish volume-based crystal size distributions (CSDs) of polycrystalline materials and crystalline powders *via* single Bragg spot intensities; it is named fast X-ray diffraction crystal size distribution analysis (FXD-CSD) as it allows for a fast and statistically exhaustive determination of CSDs even under *in situ* conditions. The CSDs, expressed as histograms are derived from individual Bragg spot intensities *via* an intensity scaling procedure. Scaling the integrated intensities is done by measuring a *reference* sample with known CSD and scattering power CSDs should not be confused with particle size distributions, for which one particle could be an agglomerate of several crystallites. CSDs are often defined in terms of mathematical functions describing the probability distribution of crystal sizes and can be cast into number occurrence histograms of crystal sizes. They are of growing interest in the manufacturing industry and many fields of science and engineering; the demand of a better microstructural characterisation and a deeper understanding of genesis and evolution of crystal sizes. The growing availability of 2D-detectors have led to an increased interest in X-ray based determination of the mean size of crystallites from spotty diffraction patterns (He, 2011; Ida & Licai, 2011; He, 2009) including first attempts to go beyond the simple determination of the mean crystallite size (Ingham, 2014; Yager & Majewski, 2014) by modelling pre-assumed size distribution functions.

Starting from the material genesis in a phase transformation, the microstructure of polycrystalline materials is determined by the interplay of nucleation and growth kinetics of the transformation process which often is cast into an Kolmogorov-Johnson-Mehl-Avrami equation in all its variants resulting in various distinctive shapes of the resulting CSDs (Eberl *et al.*, 1998; Lasaga, 1998). Starting from the crystalline state, recrystallization and grain growth can take place - usually after plastic deformation - and is of great interest when specific material properties have to be met. In all cases the dominant growth mechanism is influencing the evolution of the CSD and its final state. This can be e.g., a Hillert distribution, occurring when grain growth is grain boundary curvature driven (Hillert, 1965*a*), a Rayleigh distribution when grain boundary sections undergo random motion (Louat & Duesbery, 1994) or a log-normal distribution when surface tension is controlling grain growth (Feltham, 1969). This shows that the mathematical description of the CSD carries information about the growth mechanism and can even provide information about the specific thermodynamic conditions during the initial nucleation and growth process. In practice these distributions can be difficult to discern from each other and necessitate an exhaustive unbiased sampling, which is not easily obtained with currently available methods.

Nucleation and growth processes of pharmaceutical products result in varying CSDs which in turn influence processing, formulating and drug delivery performance; this has sparked considerable recent interest in CSD determination in pharmaceutics (Fujiwara *et al.*, 2005; Bakar *et al.*, 2009; Nagy & Braatz, 2012). Great efforts are made to control the CSDs also in batch crystallisation processes of proteins (Shi *et al.*, 2005). In material science, with respect to the mechanical properties of polycrystalline materials, the Hall-Petch relation is traditionally used to relate average grain size with material strength. However, recent findings show that the simplification of using the average grain size is not always sufficient (Kurzydeowski & Bucki, 1993; Berbenni *et al.*, 2007*a*). Grain bridging in ceramics shows that an inhomogeneous microstructure (e.g. bimodal CSD or elongated crystals) can hinder crack propagation (Swanson *et al.*, 1987; Chantikul *et al.*, 1990; Kruzic *et al.*, 2008; Carniglia, 1972). It

is also reported that the dispersion of the CSD is influencing the mechanical behaviour of metals (Raeisinia *et al.*, 2008; Skripnyak *et al.*, 2017).

All these examples illustrate the value of knowing precise and representative CSDs of polycrystalline materials or crystalline powders and call for methods to reliably establish these distributions. In the following we focus our interest on sizes in the range from several 100 nm to 100 µm, a range frequently encountered in both pharmaceutics and material science. Techniques for the analysis of sizes in this range are numerous and can be categorized into optical methods such as laser light scattering and laser diffraction, physical techniques such as sedimentation and sieving and microscopy techniques such as light optical microscopy, scanning electron microscopy and transmission electron microscopy. Electron microscopy, especially in conjunction with electron backscatter diffraction (EBSD) mappings, delivering fabric information, crystal orientation and sizes information of polycrystalline aggregates, has become the standard tool for microstructure investigations in geo- and material science; yet, EBSD as well as the other microscopic methods require a fair amount of sample preparation and often do not provide exhaustive sampling statistics. Light scattering methods and the mentioned physical techniques only provide particle sizes (which may have their own value) but not reliable crystal size information. Furthermore, all methods mentioned so far do not measure the crystal (or particle) volume directly, thus the obtained size information is sensitive to the shape of the crystals (German, 2010; Konert & Vandenberghe, 1997). To obtain the crystal volume, assumptions about (uniform) shape have to be made, which inevitably lead to uncertainties of the deduced sizes (German, 2010). Besides diffraction contrast X-ray tomography, which can be tedious and provides only a small sampling base, X-ray diffraction is so far, the only routine means to obtain size information in terms of the crystallites volumes unbiased by crystal shape and crystal agglomeration albeit with a complete loss of any shape information. In the following we will first present earlier X-ray based efforts made to obtain crystal size information, highlighting their strengths and limitations, before we move to our novel approach.

The first attempt to deduce crystal sizes with X-rays was made by Scherrer (1918), providing the average domain size, not necessarily the averaged crystal size. With lab equipment line broadening is detectable from crystallite (or domain) sizes in the lower nm range but works only up to ~100 nm and yields averaged size and strain information (Balzar *et al.*, 2004). If, and only if, the mathematical form of the size distribution is known it is also possible to tailor this function with the information obtained from line broadening to represent the size distribution of the specimen (Krill & Birringer, 1998; Langford *et al.*, 2000; Ungár *et al.*, 2001); note, that the information is not deduced from individual crystallites (domains) and deviations from the assumed distribution function are likely to be missed. Furthermore, all results obtained from techniques based on line broadening should be considered only as qualitative measure (e.g. within a series of similar specimens), thus should not be over-interpreted (Scardi *et al.*, 2004). Hybrid methods exploiting peak widths and spottiness have been proposed (Yager & Majewski, 2014), yet they have to make assumptions on the shape of the size distribution, a quantity which is a priory unknown for an new material.

Several attempts have been made to deduce the average crystal size *via* the number of spots on a diffraction ring and the total irradiated volume; the irradiated volume divided by the number of spots detected gives the average crystal size (Schdanow, 1935; Stephen & Barnes, 1937; Hirsch & Kellar, 1952; He, 2011; Ida & Licai, 2011; He, 2009). In the early days blackening on film (Schdanow, 1935; Stephen & Barnes, 1937; Hirsch & Kellar, 1952; Hirsch, 1954) was used, more recently replaced by 2D-

detectors. For the latter, the so-called γ-profile analysis (γ being the angle around the Debye-Scherrer cone) provided *via* peak counting (He, 2011) or *via* statistical fluctuation of the intensity along γ (Ida & Licai, 2011) access to the mean crystallite size. All methods share the task of precisely determining the irradiated volume or the estimation of the effective volume, *i.e.* the sample volume contributing to the observed intensities; this is particularly challenging for beams with higher divergence on laboratory sources.

The methods described in the following, all use the diffracted Bragg intensities of individual Bragg spots as size-sensitive parameter and benefit from modern 2D-detectors with their sensitivity, large dynamic range, high spatial resolution and low background noise. Compared to the previously mentioned approaches, the main advantage in this approach is the independence of the irradiated volume and the possibility to extract individual spot intensities; especially the latter point is essential for our goal to derive the CSD from diffraction patterns. A method suitable for common laboratory equipment using a 2D-detector and intended for crystal sizes in the µm-range was proposed by Rodriguez-Navarro *et al.*, (2006), using several reference samples of the same material with different, known averaged crystal sizes to establish a size-intensity correlation; knowing the slope of the standard line it is possible to deduce the average crystallite size from the measured intensities. This limits considerably the applicability as sometimes it is difficult to find appropriate calibration materials.

The most recent work, aiming for a complete microstructural characterisation, the indexing and structure refinement in a multigrain scenario, has been named “Multigrain crystallography” or “3DXRD” and can be executed only at synchrotron facilities; setups with several detectors combine X-ray tomography and diffraction, allow for a rather complete investigation of microstructure and certainly can also be used to deduce CSDs (Sørensen *et al.*, 2012; Poulsen *et al.*, 2004; Sharma *et al.*, 2012*a*,*b*). These methods are capable of measuring a multitude of microstructural parameters but are quite complex to set up and are only available on a few synchrotron beam lines.

Our novel FXD-CSD method, initially designed for the CSD determination of clathrate hydrates under non-ambient conditions (Chaouachi *et al.*, 2017) and based on earlier work (Klapp *et al.*, 2007), is complementing the available methods capable of CSD determination by offering an alternative, fast and easy to set-up means to determine accurate and precise CSDs. It can be adapted to a wide variety of situations and materials and can be considered as the appropriate tool needed to test various nucleation and growth as well as coarsening theories; likewise, it can support microstructural design for monitoring mass crystallisation processes. FXD-CSD enables the user to measure volume-based, intensity derived CSDs within the time-scale of a good-quality powder diffraction measurement, with a minimum of sample preparation. The main requirements are the availability of a 2D-detector and one goniometer ration axis; then FXD-CSD is applicable to both lab sources and at synchrotron facilities. The sampling statistics are unprecedented even in very basic setups and exhaustive statistical precision can easily be achieved by measuring simply more Bragg spots. Moreover, there are usually several (strong) Debye-Scherrer cones displayed on the 2D-detector which all of them carry the same underlying crystal size information; thus, the method delivers redundant CSD information which can be analysed to check consistency or merged to improve the statistical basis. The only condition for a later quantitative analysis is the data collection on one *reference* sample, with known structure and known CSD, for calibration purposes. It was shown recently that the operational size range reaches down to well below 1 µm (Chaouachi *et al.*, 2017; Neher *et al.*, 2018). Certainly, FXD-CSD does not aim for a complete microstructural characterisation; rather, it is solely designed to make the determination

of crystal size distributions as fast and as widely applicable as possible, ignoring the crystallites' shapes and mutual orientations.

We proceed in the following by presenting in Section 2.3 the basics of the method, all intensity corrections as well as precautions to monitor the data quality; we provide insights into the associated software package and show its functionality. In Section 2.4 we then give a worked example of a CSD determination on corundum powders with independently known CSDs and different mean crystal sizes carried out on a common lab X-ray source and a commercial X-ray diffractometer. In Section 2.5 we discuss advantages, prospects, and limitations of the FXD-CSD and conclude with a short outlook.

2.3 FXD-CSD – Fast X-ray Diffraction Crystal Size Distribution analysis

FXD-CSD is a fast X-ray diffraction-based method to measure crystal size distributions (CSDs) of polycrystalline materials and crystalline powders. At the core of the method is an X-ray data collection on a crystalline *reference* material with well-known CSD and known crystal structure, measured under the same conditions on the same diffractometer as the sample of interest. It is then possible to determine the unknown CSD of a sample by scaling the measured integrated Bragg intensities *hkl* of *sample* and *reference* with the corresponding structure factors and unit cell volumes. In a two-step procedure, first the scale factor S1 between the intensity distribution of reflection $hkl_{reference}$ and the corresponding CSD is established, then the scale factor S2 between the structure factors of the *reference* and the samples is calculated from the known crystal structures; finally the intensity distributions, normalized with S2, are transformed into CSDs by means of scale factor S1 (see Figure 2.1). S1 is *reference* and diffractometer setup specific and the calibration measurement must be repeated whenever the setup is changed.

A CSD is defined as the frequency distribution of crystal sizes as manifested in the crystal size number occurrence of the sample, frequently plotted in the form of histograms. In this context the term 'size' always refers to the volume-based size information; here and in the following it always refers to the diameter of the equivalent sphere of the determined crystal volume. Crystal size and CSD shall not be mixed up with particle size or particle size distribution, on which not much can be learned by FXD-CSD studies.

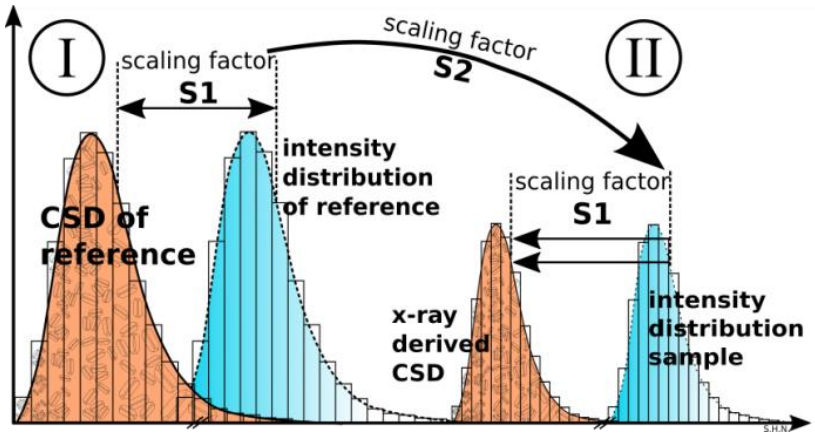

Figure 2.1: Schematic of the intensity scaling (linear space representation). The scaling factor S1 determines the diffractometer-setup specific intensity gain with respect to the independently obtained volume-based CSD for a *reference* material. Possible differences in scattering power (*hkl* specific) between *sample* and *reference* are taken into account by the scaling factor S2.

2.3.1 Theory

FXD-CSD is based on the kinematic theory of diffraction which states that the intensity diffracted by a crystal is proportional to the irradiated crystal volume (Als-Nielsen & McMorrow, 2011) justified by the imperfectness of most crystals and the low coherence of X-ray beams used for our work; concerning the treatment of extinction see Section 2.3.5.2. Consequently, the diffracted intensities of many crystals compose an intensity distribution (ID) which is proportional to the volume distribution (VD) of the irradiated crystals. S1 is established between the intensity mean (I_{hkl}) of the measured *reference* ID and the volume mean V of the *reference* VD:

$$V = S_1 \times I_{hkl} \qquad \text{Eq. 2.1}$$

In practice the mean values are often determined by fitting Gaussian probability density functions (PDF) to the natural logarithmic representation of the ID and the VD. Obviously, the chosen representing mathematical form of ID and VD depends on the actual sample but certainly is expected to be identical for both; other forms can then be adapted for determining S1. To obtain handy values for $\ln(S_1)$ the VD is represented in nm^3. Regarding the logarithm product rule this gives the following presentation of Eq. 2.1:

$$V = e^{ln(S_1) + ln(I_{hkl})} \qquad \text{Eq. 2.2}$$

S2 is established between the *hkl*-specific crystal structure information of reference and sample. The kinematic diffraction theory states that the diffracted intensity is proportional to the structure factor squared F^2 and inversely proportional to the unit cell volume V_c. Hence

$$I_{hkl} \propto \frac{|F^2|_{hkl}}{V_c} \qquad \text{Eq. 2.3}$$

When more than one *hkl*-ring is analysed (as it is usually done and highly recommended in order to use all information available in the data) the intensities of all analysed sample *hkl*-sets are scaled to one chosen reference *hkl* (by scaling with the corresponding structure factors), prior to the S2 determination. This shall be called *internal-scaling.* The scaling factor S2 is then calculated for the chosen reference *hkl*-family as follows:

$$S_2\{hkl\} = \frac{I_{calibrant}}{I_{sample}} = \frac{(|F^2|_{hkl}/V_c)_{calibrant}}{(|F^2|_{hkl}/V_c)_{sample}} \qquad \text{Eq. 2.4}$$

With the scaling factors S1 and S2 one can calculate the sphere-equivalent crystallite diameter D:

$$D = \sqrt[3]{\frac{6 \times I \times S_2 \times S_1}{\pi}} \qquad \text{Eq. 2.5}$$

Performing the scaling in the ln-space the volume CSD (CSD_{Vol}) calculation is done as follows:

$$CSD_{Vol} = e^{\ln(ID_{sample})+\ln(S_2)+\ln(S_1)} \quad \text{Eq. 2.6}$$

The units of CSD_{Vol} depend on the units chosen during the S_1 determination. The CSD_{Vol} can be transformed to a diameter CSD using any crystal habit of choice. In practice it might be necessary to vary the exposure time between reference and sample measurement. This of course needs to be taken in account in addition when scaling the intensities.

2.3.2 Requirements

To establish IDs composed of numerous integrated intensities diffracted by single crystals, a diffractometer with at least one precisely controlled stepping sample rotation axis and a 2D CCD detector is needed (see Figure 2.2). Both, sample and reference material must have a crystal size in the (lower) µm range, being at least one order of magnitude smaller than the primary beam radius to avoid edge effects (see Appendix B 2) and being big enough, to only allow a limited number of crystals in the irradiated sample volume to produce spotty diffraction patterns with a neglectable chance of accidental peak overlap (see Appendix B 2 in the supporting information). Overlapping Bragg spots must be avoided because in case they cannot be separated, the recorded intensity information can not reflect the correct crystal size. If these basic conditions can be met by changing the beam size or the ISV, it is possible to measure spotty diffraction patterns (see Figure 2.2). With step-wise rotation measurements (details in Section 2.3.3) the rocking curves, hence the integrated intensity of each individual reflection is measured. Both, reference and sample must be measured under the same conditions; only the exposure time can be varied as it is trivial to scale for this. Additionally, the crystal structure information must be known for both, reference and sample.

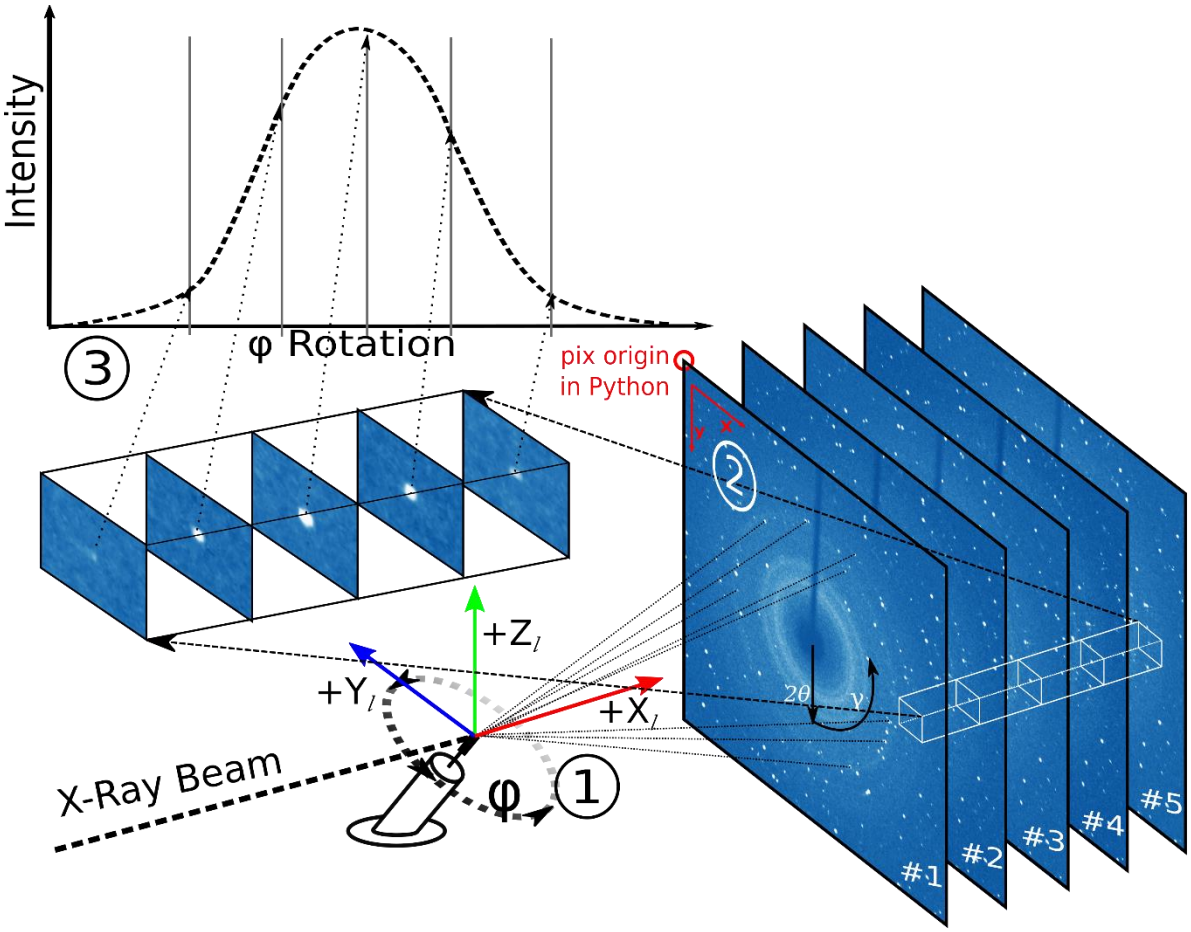

Figure 2.2: ①Diffractometer setup with the φ-axis used for the stepwise rotation; the ω-axis could be used as well and the lab coordinate system (X_l, Y_l, Z_l) - ②Detector frames with spotty pattern. The pixel origin (red circle) is in the upper left corner and transformed to the lab coordinate system – ③ extracted rocking curve

The reference sample should consist of a crystalline powder consisting of single crystals with a narrow and uniform size distribution and good scattering properties. The size distribution must be known and should preferably be volume-based. So far SEM imagery is considered as best and fairly easily accessible way for powder CSD determination. If SEM imagery is the method of choice to obtain the volume-based CSD the crystal shapes should be as isometric as possible, ideally be spherical or should not show size-dependent shape changes; different shapes complicate the volume-estimation from 2D[3] SEM images. The crystal structure type of the reference or sample are not necessarily critical but have to produce at least two, better three diffraction rings within the measured 2Θ range. These rings must be free of ring overlap due to closely neighbouring d-values or systematic overlap. A variation of their multiplicity and differences in their structure factors are uncritical; rather these differences permit to check the results for internal consistency as discussed in the following.

2.3.3 Measurement strategy

The measurements, performed in transmission geometry[4], are carried out in a stepwise or better stepwise sweep rotation manner - a sweep rotation is integrating the intensity between each step

[3] The images carry a limited amount of 3D information when taken in an oblique setting. This depends on the type or setting of the SEM.

[4] Measurements in reflection geometry are possible but have so far not been tested in an exhaustive manner. All software functions and intensity correction, except the absorption correction, are implemented geometry independent.

around one sample rotation axis of the goniometer; in the following we do not discern between both options. In a series of frames, one can distinguish between weak reflections from small crystals and reflections of crystals not oriented in full reflection state; this is not possible in a single frame. The step size should be about 5-10 times smaller than the half width half maximum (HWHM) of the rocking curve to accurately map the intensity course. Step measurements permit the analysis of the rocking curves for edge effects (incomplete rocking curves at the endings of the frame stack) and accidental peak overlap, providing criteria for discarding affected reflections. Compared to a continuous exposure, resulting in one frame, it is then possible to turn the sample by several degrees in total without increased spot overlap and thus improve sampling statistics. If needed, the sample can be turned until the first symmetry-equivalent reflexes appear, which may bias the sampling by measuring the same crystallite twice. For a cubic structure and a low index *hkl* this is ~20°; for lower symmetries the total rotation width can be even larger. Even though it is not of immediate interest in the present CSD work, having hundreds or even thousands of individual rocking curves at hand allows additional insights into crystallite quality.

In a largely texture-free polycrystalline or crystalline powder sample, individual crystals can be considered randomly distributed in reciprocal space, independent from their size; hence the above described way of data collection ensures a statistical unbiased sub-sampling and, given the total number of observations is statistically sufficient, individual defective reflections can be discarded without impacting the resulting CSD. In order to establish good sampling statistics while keeping accidental spot overlap to a minimum, the number of spots on the Debye-Scherrer rings needs to be controlled, considering also the reflections varying multiplicities. This is done *via* changing the irradiated sample volume (ISV). For polycrystalline materials the ISV can be altered by changing the sample size (changing the thickness) and/or the beam size *i.e.* the collimator. The optimal sample thickness is limited in both ways: A sample too thick will increase attenuation effects to a non-negligible level (see Section 2.3.5.2) and a sample too thin will introduce a significant amount of sample edge effects form the surface crystallites. In case of crystalline powders an additional way is changing the crystal concentration in the ISV by dilution with an amorphous material e.g., starch. Considerations about the amount of crystals impacted by sample edge effects include the size of the ISV, the number of crystals in the ISV – and therefore their size, and the surface of the ISV; the decisive parts of the surface differ for polycrystalline materials and powders in a capillary. In a capillary, only the ISV surface parallel to the beam matter. For polycrystalline materials the area impinged by the entering and exiting beam matter as well in case the sample was cut out from a larger piece (see Figure App. B-1). Hence, for both, powders and polycrystalline materials, the primary beam dimensions have to be chosen (e.g. by changing the collimator) with respect to the expected crystal size under investigation. As a rule of thumb, the average crystal size should be at least one order of magnitude smaller than the beam size. Since even a strong occurrence of sample edge effect is not apparent during the analysis and can bias the results significantly we recommend checking the situation with Eq. App. B 1 provided in the supporting information after the analysis. In case the average crystal size is known, this test can of course be done prior to the measurement. If the test reveals a critical amount of sample edge effect, the experiment should be redone with a larger beam-size. Further information on this topic can be found in Section 2.5.2 and in Appendix B 2 in the supporting information.

The described measurement strategy and the subsequent data reduction (see Section 2.3.4) allow to detect peak overlap and to discard the affected data; the amount of peak overlap can be approximated following the considerations in Appendix B 2.3. However, it is possible that peaks overlap exactly and

hence are not discernible. The amount of this accidental full overlap in a non-textured sample of course depends mainly on the number of crystals in the ISV but is negligibly small when the advices above are followed; its amount can be approximated (see Appendix B 2.3).

2.3.4 Data reduction

For each CSD determination two sets of data – detector frames from *reference* and *sample* – are collected and the intensity information is extracted from the spotty diffraction rings visible on the frames. For this purpose and the subsequent data analysis we developed a software package called 'fxd_csd' in Python. The images are loaded with the Python package *fabIO* (Knudsen *et al.*, 2013). Here and in the following sections the relevant program functions are provided in italics. For more detailed information on program handling see the Figure App. B-2.

Concerning the data reduction, the most important program functions, incorporated in the software, are *pickpeaks()* and *omegastep()*. Their functioning is described below (1st, 2nd and 3rd Step). Prior to this step the program once started prompts the user to pick the rings to be analysed and to supply the needed crystallographic structure information.

1st Step: The area of interest, defined by the theoretical ring radius and ring width is set by the user. A fixed background level is set for each ring or an area where the background intensity level is determined is defined for each ring. These areas are bigger or smaller adjacent rings (see Figure 2.3a). Defining a background area where the level is determined instead of a fixed value can be advantageous if the background level is changing during the sample φ-rotation. Using ring shaped areas for determining the thresholds is therefore γ, θ and φ dependent but slows down the data reduction compared to setting a fixed value. The determined background level can be modified by a multiplier, e.g. to avoid the integration of spurious very weak peaks. The background level is used as threshold and applied to the area of interest to separate signal from background. The output is an array showing the cropped intensity data (see Figure 2.3b).

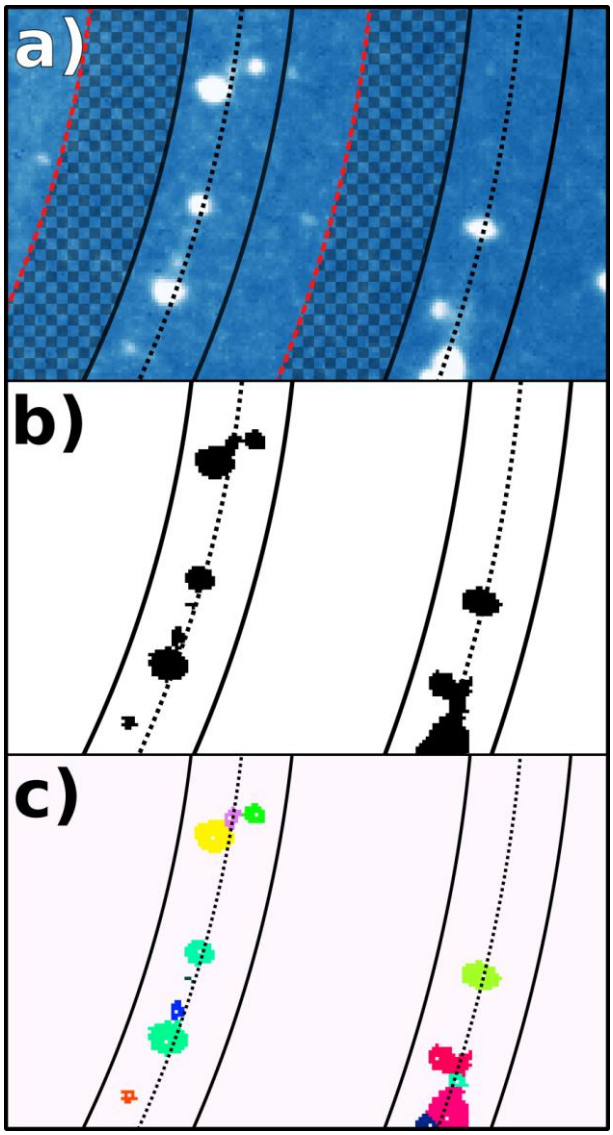

Figure 2.3: Two-dimensional representation of Data reduction. a) Spotty diffraction pattern. Areas of interest are enclosed by solid black lines. Dotted lines mark the centres of the diffraction rings. The areas used for determining the background level are crosshatched and bordered by dashed red lines. b) Detected regions with intensities higher than the used threshold. c) Detected and colour-labelled objects separated by a seeded water-shedding algorithm.

2nd Step: The resulting, cropped data frames are combined into a three-dimensional array, having the frame coordinates as 1st and 2nd dimension and the image number as 3rd dimension. The image number corresponds to the stepwise rotation. Subsequently an object detection algorithm is recording each non-zero voxel volume and assigns a unique label to it (van der Walt *et al.*, 2014); these objects have to be separated from others or the array edges by at least one pixels. This step is allocating the discrete intensity information of the diffraction spots in each consecutive frame they occur. In case of multiple intensity maxima within one object a three-dimensional seeded (maxima) water-shedding is performed (Vincent & Soille, 1991); the minimum distance (controlled by the *minimum_distance* parameter of the *pickpeaks()* function) between the maxima is usually set to five pixels or accordingly five rotation steps. Now the location of all peaks in each frame they appear is known and the intensity can be extracted individually.

Peaks in settings with a high and rapidly varying angular-velocity factor (Lorentz factor) (Lipson *et al.*, 2006) are discarded because they can be stationary – regions near the trace of the rotation axis on the

detector (Figure App. B-3) – and appear in more frames than usual (see Figure App. B-4). This can slow down the data reduction because many images need to be stored to memory. Additionally, the intensity correction in these regions is likely to be faulty because the Lorentz factor calculation there is highly sensitive to angular and positional errors (see Section 2.3.5.1 and Figure App. B-5). As discussed in Section 2.3.3, discarding individual reflections does not introduce any bias into the deduced CSDs. Summing up the intensity of each object in the 1st and 2nd array direction reveals the rocking-curve along the 3rd direction, see Figure 2.2.

3rd Step: Once the data is extracted and corrected, the rocking-curves are evaluated for their quality. Routinely each rocking-curve is tested for the presence of one single maximum between two minima (both located at the beginning and the end of their scan range). Optionally the central moments of the rocking curves can be calculated and used as rejection criteria. These are: Weighted-mean, -variance, -skewness, and -kurtosis describing the mean position, peak spread, the asymmetry of the curve and the flatness or peakedness, respectively; the used equations are given in the Appendix B 6. For each moment the standard deviation σ within the dataset is calculated and observations outside the 2σ interval are rejected automatically if this option is chosen. The rejection criteria can be adjusted depending on the quality of data. Each rocking curve which has past these tests is stored, along with its pixel position (x_{pix}, y_{pix}, z_{image}), ring radius, structure factor, maximum intensity, Lorentz-Polarisation factor, and the integrated intensity, obtained by summing all rocking curve values together.

2.3.5 Intensity correction

The applied intensity corrections resemble a customary single crystal data analysis (Kabsch, 1988; Lipson *et al.*, 2006). In the following only the most important and routinely applied corrections are described in detail, all minor or optional corrections are detailed in the Appendix A 1 and the Appendix B 3. The intensity corrections carried out by the fxd_csd function *condition(),* are applied to the extracted integrated intensity.

2.3.5.1 Angular-velocity factor – Lorentz correction

If rotation measurements are performed diffraction occurs when a reciprocal-lattice point (RLP) transits the surface of the Ewald's sphere. The duration of transition and hence the integrated diffracted intensity depends on the angular velocity of the RLP. The angular velocity of the RLP again depends on its d-value and on the orientation of the lattice plane with respect to the sample rotation axis. The effect on the collected data is shown in Figure App. B-3 and Figure App. B-4 in the Appendix. To correct for this effect a vectorial description of the angular-velocity factor is used (Milch & Minor, 1974):

$$L = \frac{1}{\boldsymbol{\varphi} \times \mathbf{h_r} \cdot \mathbf{h_r} + \mathbf{s}} \qquad \text{Eq. 2.7}$$

Where $\boldsymbol{\varphi} \times \mathbf{h_r}$ expresses the angular velocity perpendicular to the Ewald's sphere, $\boldsymbol{\varphi}$ is a unit vector in the direction of the rotation axis, $\mathbf{h_r}$ is the reciprocal lattice vector in diffraction state and $\mathbf{h_r} + \boldsymbol{s}$ is the vector normal to the sphere and perpendicular to the diffracted beam. The correction factor is applied to the integrated intensity. The function graph is shown in Figure App. B-15.

2.3.5.2 Polarization, absorption, lateral beam profile deconvolution and extinction

Depending on the source and the X-ray optics in use, the polarization of the primary beam coming from the source can affect the performed intensity measurements. The decisive factors are the primary

degree of polarization of the source and the angle between the polarization vector and the diffracted beam, hence the incident radiation is polarized twice, by the monochromator crystal and the sample crystals. Modern synchrotron X-ray sources are almost perfectly circular polarized (not polarized)(Chavanne *et al.*, 1996; Tschentscher & Suortti, 1998; Hiraoka *et al.*, 2005). Tube sources are initially not polarized as well. The degree of polarization therefore depends on the monochromator diffraction angle, hence varies depending on the anode material and the monochromator crystal. Compared to the Lorentz effect this correction has only a minor impact. More detailed information can be found in the Appendix A 1.1.

Further corrections can be applied to address absorption (see Appendix B 3.1) and to correct for lateral incident beam inhomogeneity (see Appendix B 3.2). They have been implemented and tested and are described in detail in the supporting information, however they turned out not to have a significant influence on our FXD-CSD measurements presented here; they certainly could, however, with other diffractometer setups or with strongly absorbing samples.

Extinction is found to be not critical for crystals in the lower µm size range. Nevertheless, if the sample gives reasons (big crystals with low mosaicity) that extinction is critical, one should leave out very strong and low indexed *hkl*; higher indexed *hkl* are less influenced by extinction (Becker & Coppens, 1974a, 1974b, 1975).

2.3.6 Data evaluation

From this point on all further considerations do no longer deal with individual spot intensities. For the further data evaluations, the single spot intensities from each *hkl*-ring are joined together into intensity distribution histograms (IDH). Comparing the IDHs with each other helps the user to decide which *hkl*-rings can be used or should be left out for constructing the final CSDs. For this purpose, the integrated intensities composing the IDHs are scaled according to their own structure factor and a structure factor of one, user chosen, *hkl*-ring (*internal-scaling*, see Section 2.3.1). This necessitates that the binning is done in the same way for all individual IDHs and that the bin size is reasonable in respect to the number of observations; a suitable way is to follow the Freedman-Diaconis rule (Freedman & Diaconis, 1981). Having the internally scaled IDHs established the next evaluation criterion is whether or not the IDHs evolving from different *hkl*-rings match each other. If the underlying CSD is well in the operation range – depending on the X-ray source, the diffractometer, and the crystal structure – and measured properly, at least two, better more IDHs should match perfectly. If the IDHs do not match on the lower end of the histograms it is likely that parts of the CSD are below the detection limit. This is called $ID_{cut\text{-}off}$. Mismatching distributions on the high intensity end are due to massive accidental peak overlap (too many crystallites on the Debye-Scherrer cone). This would lead to the observation that IDH from *hkl*-rings with high multiplicities or a small ring radius extend further to high intensities than others. High multiplicities raise the number of *[hkl]* reflections in each *{hkl}*-family and a small ring radius lowers the angular resolution; this leads to accidental peak overlap and is called $ID_{exaggeration}$. In case these artefacts are observed, the most trustworthy IDs resolve from hkl-rings with the highest structure factors ($ID_{cut\text{-}off}$) and the lowest multiplicity ($ID_{exaggeration}$). Having two or more matching distributions obtained from *hkl*-rings with different structure factors and different multiplicities strongly supports the correctness of the obtained results. This internal consistency test is indeed a unique inherent feature of FXD-CSD.

To help with these considerations the function *condition()* enables the user to choose which of the measured and analysed *hkl*-rings should be further considered. Additionally the user has to define the *hkl*-ring to which the selected intensity histograms shall be scaled; this step, the *internal scaling*, defines also between which *hkl*-rings the later S2 intensity scaling is done (recall Section 2.3.1 and 2.3.1). The *condition()* function automatically produces a graphic with four subplots (see Figure App. B-6), which show the intensity histograms from all chosen *hkl*-rings in different stages of data treatment. These are: the uncorrected data, the impact of the Lorentz and polarization factor and the influence of the internal intensity scaling according to the chosen structure factor. The latter is plotted as number of occurrence histogram and as probability histogram. The probability histograms should match each other completely. Unbiased intensity distributions plotted as number of occurrence histogram are expected to have the same position and width but vary in the number of observations according to their *hkl* multiplicities.

The chosen and scaled intensity distributions are summed up to form one composed histogram which is used for the intensity scaling and CSD determination describe in Section 2.3.1.

2.4 Experimental – Method verification

Our FXD-CSD method has recently been applied to a number of cases in geo- and material science using synchrotron X-rays (Chaouachi *et al.*, 2017) and lab X-ray sources (Neher *et al.*, 2018). To systematically verify the principle, as well as the limits of FXD-CSD when used on a common lab X-ray source, the LaB_6 standard reference material (SRM) 660a[5] from the National Institute of Standards and Technology (NIST) - in the following called LaB_6-Powder - and four corundum **C**rystal **S**ize **F**ractions (CSF I - IV) with different mean crystal sizes are analyzed here. The corundum CSFs are produced *via* sedimentation in water[6]. All samples are characterized by scanning electron microscopy (SEM) imaging to obtain their volume-based crystal size distribution (CSD) as accurately as possible. Thus, the CSDs of all samples are established and they all can be treated as reference material or as unknown sample. Synchrotron measurements of the LaB_6-Powder were already published (Chaouachi *et al.*, 2017) and are available for comparison with the lab X-ray results obtained here.

2.4.1 Sample SEM CSD characterization

For the CSD characterization all samples (see Table 2.1) are dispersed on a specimen holder and investigated *via* SEM imagery (FEI Quanta 200 FEG) (see Figure 2.4 and Figure 2.5 as well as Figure App. B-7 and Figure App. B-9). Details on preparation and the subsequent analysis referred to below, are found in the Appendix A 2 and B 4. To analyze their size distribution a Python script is used to manually draw enclosing rectangular boxes around each crystal. The box dimensions (dx, dy), corresponding to the half-axis of the crystal, are automatically stored as text file for the crystal volume calculations. In case of the LaB6-Powder a spherical crystal shape is assumed for volume calculation; the average of dx and dy is used as sphere diameter. The volume calculation of the corundum CSF is calculated using a cuboid model; the used dimensions are derived from d_x and d_y, including an assumption for the 3rd dimension (see Appendix A 2).

[5] A newer batch of the NIST standard (SRM 660b) turned out to be not suitable because the powder contains large amounts of agglomerated crystals what do not have to be single crystals.

[6] In total 10 corundum CSFs are produced (see Appendix B 4). The CSFs with bigger mean crystal sizes are not analysed because the diffraction data shows satellite peaks, an artefact coming from a defective part of the monochromator (see Appendix B 5).

The resulting CSDs can be presented either as diameter- or volume-based CSD histogram. Figure 2.6 shows the resulting CSDs as diameter histogram with log-normal probability density functions (PDF) fitted to the mid points of the histogram bins; the assumption of a log-normal CSD is supported by the good quality of fit; to avoid duplication this is at first shown in Table 2.4. Table 2.1 shows the SEM-derived CSD mean values calculated from the log-normal fitting parameters. The volume-based presentations of the CSDs are shown in Figure App. B-10.

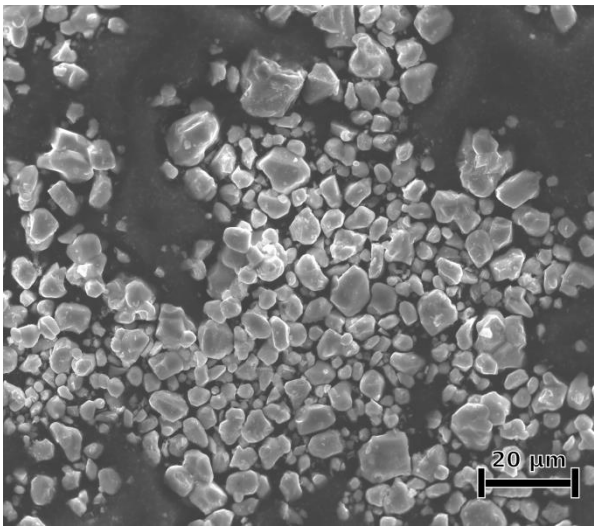

Figure 2.4: Example SEM image of LaB_6-Powder

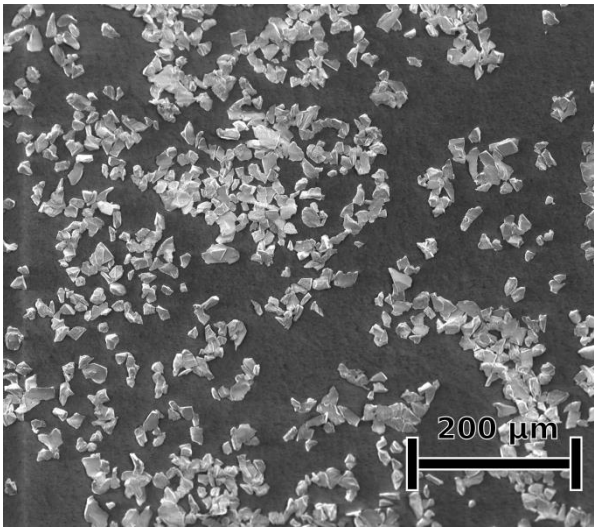

Figure 2.5: Example SEM image of CSF III

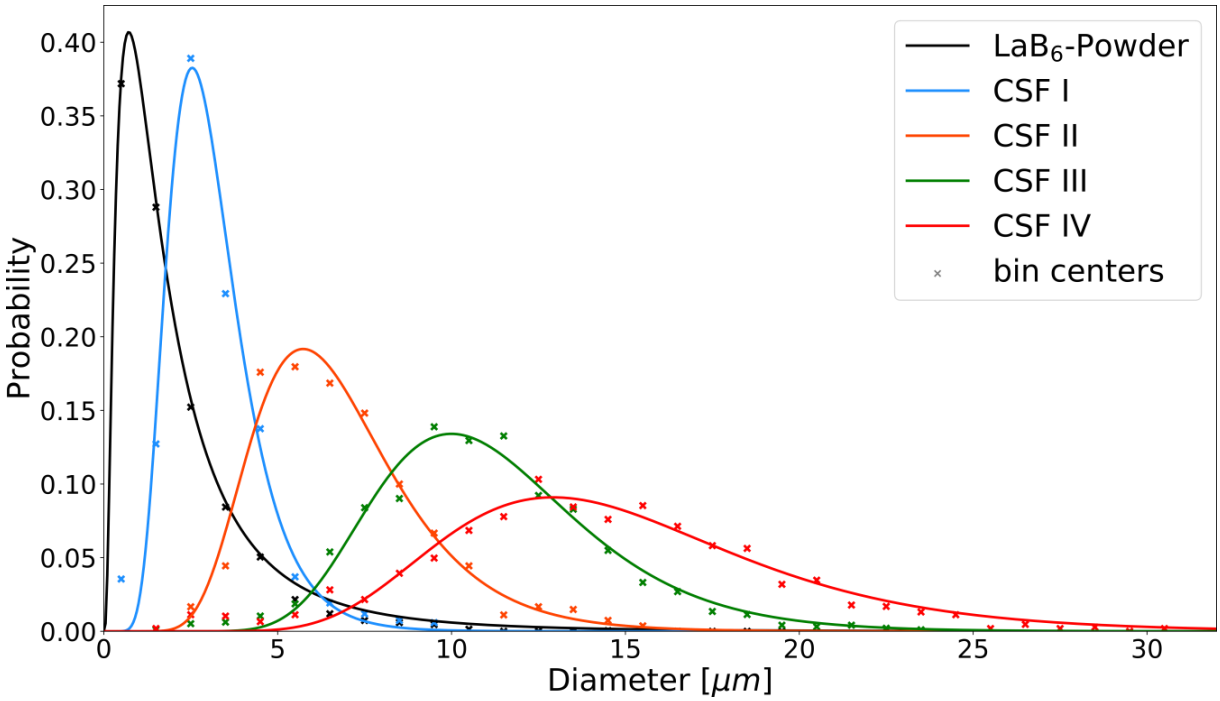

Figure 2.6: SEM derived diameter CSDs of all measured samples and their log-normal PDF fit curves. The data entries show the bin midpoints of the histograms. The bin size is 1 µm. The diameters are calculated from the SEM derived crystal volume, assuming spherical crystal shape (see Appendix A 2).

2.4.2 Sample preparation

For the X-ray measurements the samples are mixed with starch[7] and filled in Kapton® capillaries with a diameter of 0.8 mm. The starch is used to dilute the powder and control the number of crystals in the irradiated sample volume. The Kapton® capillaries are mounted with a brass holder on the goniometer head. This way it is possible to obtain a rotationally symmetric sample with no pronounced preferred crystal orientation. A good starch-to-sample proportion is obtained by starting from a mixture of even weight proportions and gradually adding starch, while repeatedly checking the diffraction pattern on the diffractometer.

2.4.3 FXD-CSD Measurements

All samples are measured with a Bruker AXS Apex II CCD diffractometer (D8 Base) with a fixed χ-angle, equipped with a Molybdenum tube (Mo-K_α, λ= 0.71073 Å) in the sweep-stepwise rotation manner (see Section 2.3.3). Apart from the exposure time all other scan parameters and diffractometer settings are kept the same for all samples measured[8]; the sweep-step size is set to 0.025° in φ, the total φ-rotation is 10° (see Table 2.1). All samples are measured three times at different positions along the capillary axis. The sample to detector distance is set to 60 mm; this corresponds to a 2Θ range of 0 – 26° on the detector. All diffraction rings present in this 2Θ range are listed in Table 2.1. Figure 2.7 shows an example frame of the LaB_6-Powder. Visible are six spotty diffraction rings. Noteworthy is the relatively strong background underneath the 100 and the 111 *hkl*-ring, originating from starch. Figure 2.8 shows example frames from all analysed corundum samples. They show spotty diffraction patterns of six rings with more or less similar spot intensities while having different exposure times (see Table 2.1). Also apparent are significant differences in the number of spots on the diffraction rings and the background level. This is traceable to the differences in the exposure time, the change in the sample-starch proportions and variations in the compaction of the mixture in the capillary.

Visually comparing the LaB_6-Powder frame (Figure 2.7) with the frame of the CSF 1 (Figure 2.8A), both measured with the same exposure time, reveals that the LaB_6 crystals diffract similar amounts of intensity, even though the LaB_6-Powder sample has a smaller mean crystal size (see Table 2.1); this is expected due to the superior scattering power of LaB_6.

[7] Mondamin® "Feine Speisestärke" Unilever, corn starch. Starch from other manufactures turned out to be crystalline.

[8] The LaB_6-Powder and the CSF I sample have been measured at different occasions. To correct for possible intensity differences due to a different diffractometer setup, the CSF III was measured at this occasion again and used as reference to link both datasets.

Table 2.1: Samples and measurement parameters

CSF III is used as *reference*; all others are used as *sample*.

Sample	SEM derived mean[1] crystal size [µm]	exposure time	Total φ-rot. range	Discernible *hkl*-rings[2]
LaB_6-Powder	2.46	120 s	10°	{100}, {110}, {111}, {200}, {210}, {211}
Corundum CSF I	3.16	120 s	10°	{102}, {104}, {110}, {113}, {024}, {116}
Corundum CSF II	6.83	120 s	10°	{102}, {104}, {110}, {113}, {024}, {116}
Corundum CSF III	**11.30**	**60 s**	**10°**	**{102}, {104}, {110}, {113}, {024}, {116}**
Corundum CSF IV	15.10	30 s	10°	{102}, {104}, {110}, {113}, {024}, {116}

[1] Calculated from Log-Normal PDF fit. [2] The corundum 006 and 202 *hkl*-rings are not listed because they are too weak to be seen.

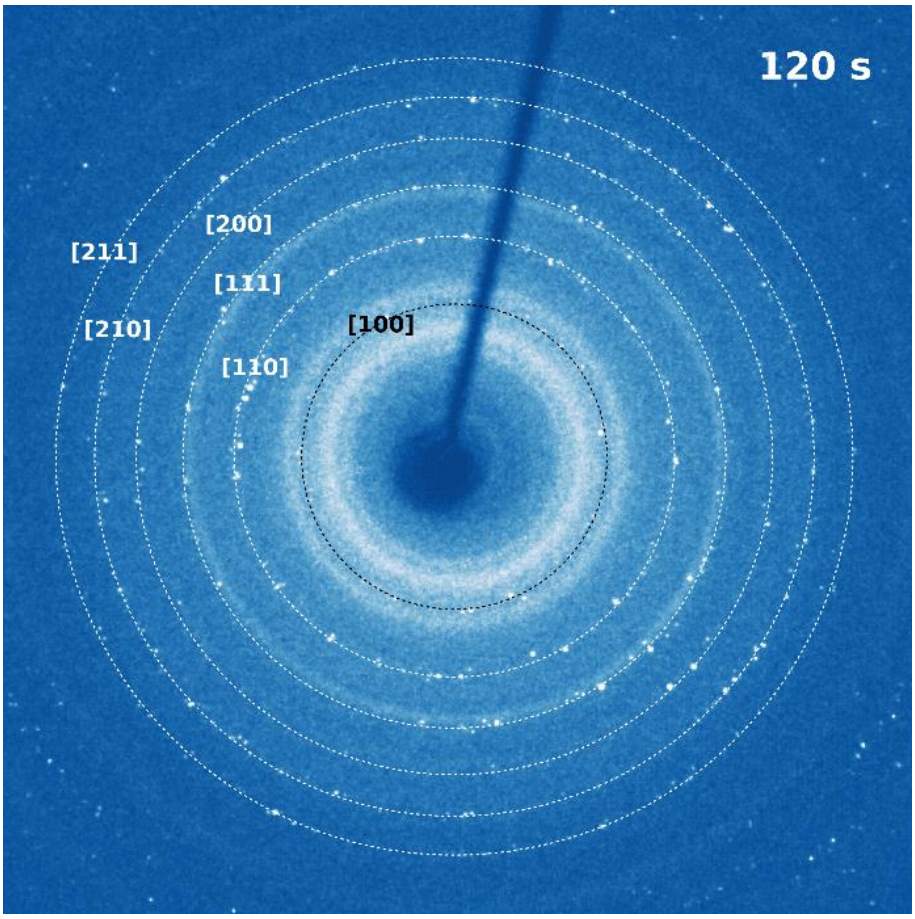

Figure 2.7: Single frame spotty diffraction pattern of LaB6-Powder.

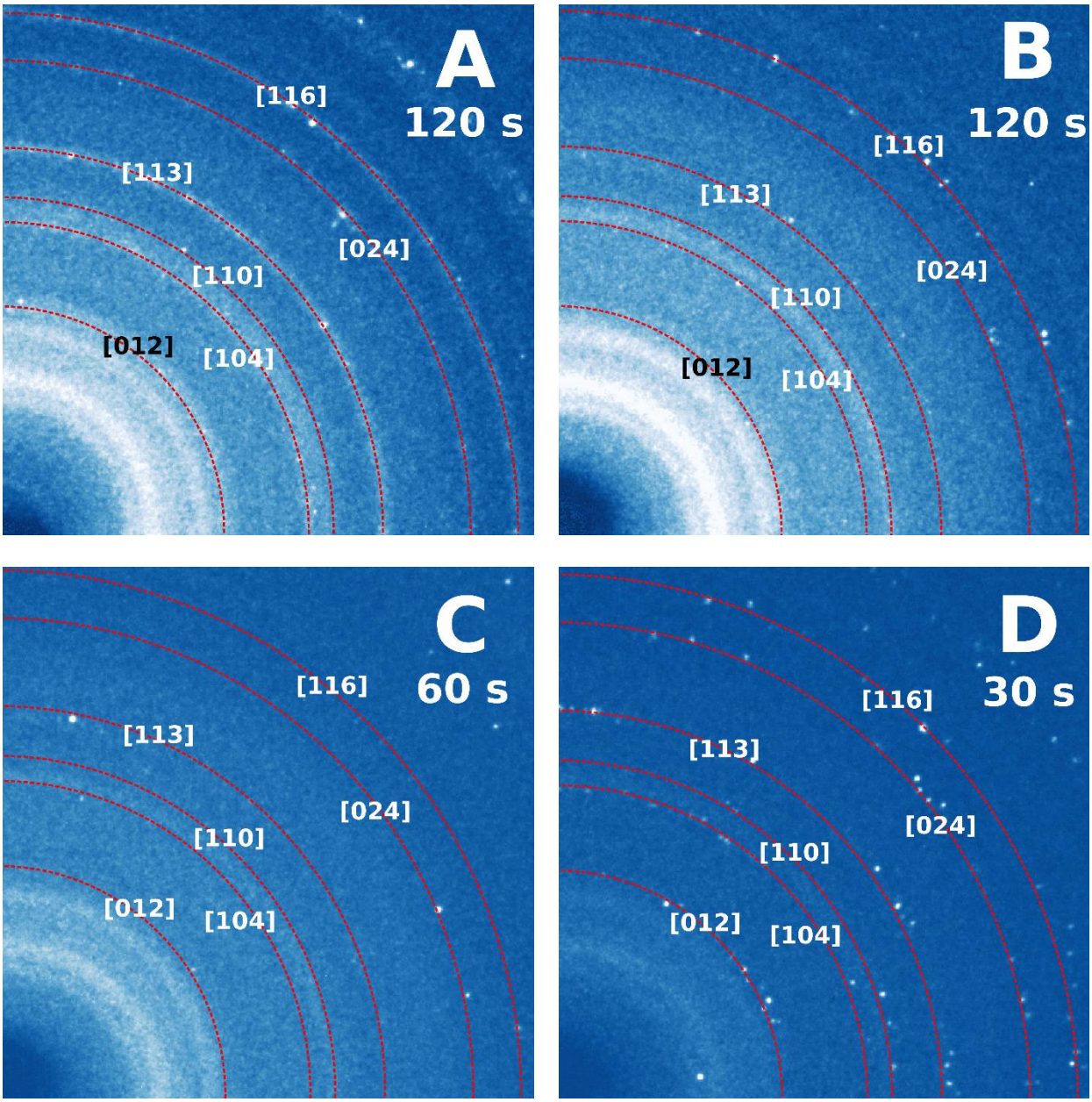

Figure 2.8: Single frame spotty diffraction patterns (A-D) of the CSF I – IV sample. Note the different exposure times.

2.4.4 Data Evaluation and *hkl*-ring selection

For the data evaluation, as described in Section 2.3.6, all intensity distribution histograms (IDH), extracted from the different sample datasets (frame stacks) are plotted. This is done automatically by the program function *condition()*; while all function parameters (recall Section 2.3.6) are kept the same[9]. Figure 2.9 shows the IDH of all analyzed *hkl*-rings derived from the LaB_6-Powder sample frames. Table 2.2 provides the used crystallographic information as well as the total numbers of observations *n*. Looking at the IDHs it is apparent that the histograms of individual *hkl* do not quite match each other on either side. Additionally, the numbers of observations do not faithfully reflect the *hkl*-multiplicities (Table 2.2). This all indicates that all, or at least most of the IDHs do not mirror the complete sample

[9] Because of the already mentioned monochromator issue (see Appendix B 5) the *minimum_distance* parameter of the *pickpeaks()* function are increased to 15 pixel. For a better inter-comparison this is done for all samples. Unfortunately, this lowers the number of observation significantly as it eliminates accidentally close reflections.

CSD; the IDHs are affected by $ID_{cut\text{-}off}$ by a significant amount of accidental peak overlap, i.e. by $ID_{exaggeration}$ (see Figure 2.9 and recall Section 2.3.6). If all IDHs are influenced by $ID_{cut\text{-}off}$, the $ID_{exaggeration}$ is harder to recognize in a probability density histogram: the IDHs are normalized, which means that missing observations at small sizes lead to an overestimation of histogram regions at larger sizes resulting in a shifted distribution narrower than expected; the distribution, however, could be compensated by systematic overlap broadening the distribution at larger values leading back to the expected width. Only a comparative study of different *hkl*-histograms IDH can help to disentangle the situation: In the case of LaB_6-Powder the unsatisfactory internal agreement means, that this material is not suitable to be used as FXD-CSD *reference* on data measured with laboratory X-ray source, at least not with the one used here. Nevertheless, the intensity distributions of the 100 and 200 *hkl*-rings, which have the highest structure factors and low multiplicities and therefore should be least impacted, are used as FXD-CSD *sample* and their CSD is determined using the CSF III sample as *reference*.

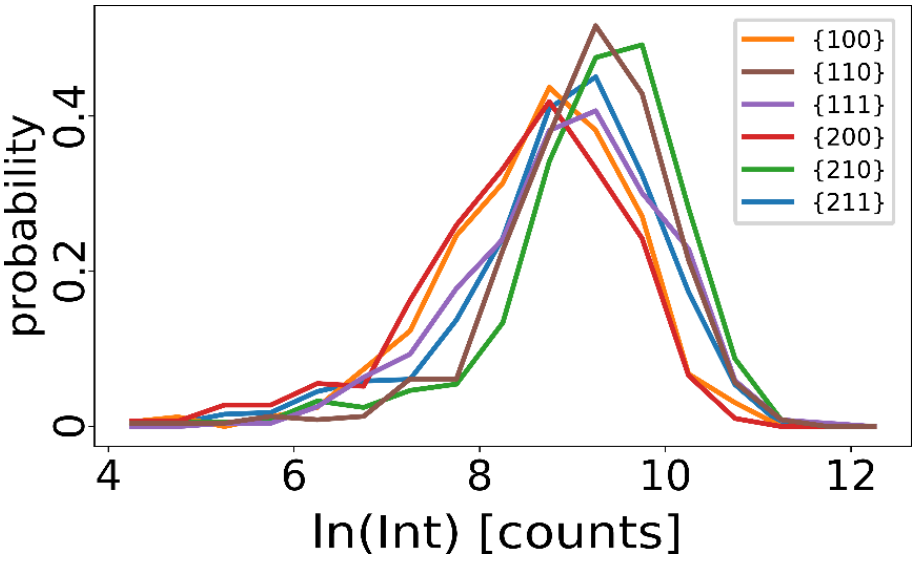

Figure 2.9: Probability representation of the intensity distribution histograms of the LaB6-Powder sample after the intensity correction and internal structure factor normalization. The number of occurrence in each bin is divided by the total number of occurrence of each IDH. Apparent is that neither sides of the histograms match in position, which on the left side is due to IDcut-off and on the right side is due to IDexaggeration.

Table 2.2: LaB_6-Powder sample parameters

Information on the measured *hkl* of LaB_6 (SG: $Pm\bar{3}m$). Bold *hkl*-families are used for analysis.

hkl	Radius [pix]	|F(hkl)|	M	*n*
100	172	39.73	6	325
110	248	48.62	12	457
111	305	48.00	8	472
200	358	46.25	6	578
210	404	40.46	24	732
211	448	34.61	24	888

n: number of observations, M: *hkl* multiplicity

Evaluating the corundum CSF samples is done in the same manner and shows that the CSF I sample measurement shows a somewhat similar picture (see Figure 2.10) as for LaB_6-Powder. The main restriction here is the presence of $ID_{cut\text{-}off}$. $ID_{exaggeration}$ is also well possible, most evident when looking at the IDs derived from the 113 and 116 *hkl*-rings in the number of occurrence histograms; these *hkl*-rings have the highest multiplicities which favour accidental peak overlap (see Table 2.3). The 012 seems to be impacted by $ID_{exaggeration}$ as well, which in this case could be due to the small radius, which in turn results in a smaller angular resolution. For the further analysis the only choice is the ID derived from the 024 *hkl*-ring, because it has a low multiplicity of 6 and a strong structure factor.

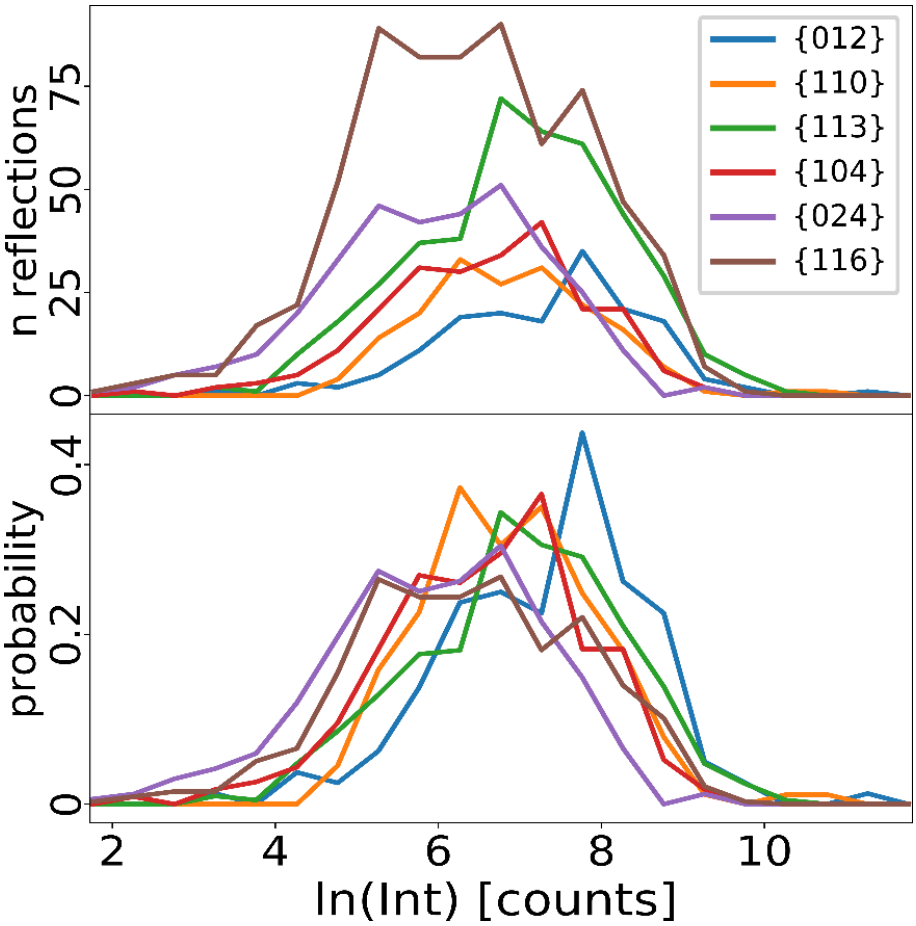

Figure 2.10: Intensity distribution histograms of the CSF I sample after the intensity correction and internal structure factor normalization. The upper plot shows the number of occurrence representation, the lower plot shows the probability density representation. For the latter the number of occurrence in each bin is divided by the total number of occurrence of each IDH. Apparent is that neither side of the histograms match in position, which on the left side is due to $ID_{cut\text{-}off}$ and on the right side is due to $ID_{exaggeration}$.

For the CSFs II - IV samples the IDs match quite satisfactorily. The best internal agreement is obtained for CSF III (see Figure 2.11); consequently, it is used as *reference* in the following CSD determination. Table 2.3 shows the used crystallographic information and lists which *hkl*-rings are used in the final CSD determination. The individual *hkl*-IDs of sample CSF II and IV are shown in Figure App. B-11 and Figure App. B-12; the reasons for the specific *hkl* choices can be found in the figure captions. For all CSF samples the 012 *hkl*-ring is not used for the final analysis because it is impacted by a higher background, originating from the starch in the sample; this is most evident in the diffraction patterns

of the CSF I. Figure 2.12 shows the summed up IDs of all measured corundum CSFs after scaling the intensity with respect to their exposure time. Apparent are the overall increasing spot intensities corresponding to the increasing mean crystal size, in full agreement with expectance from the SEM observations (compare with Table 2.1).

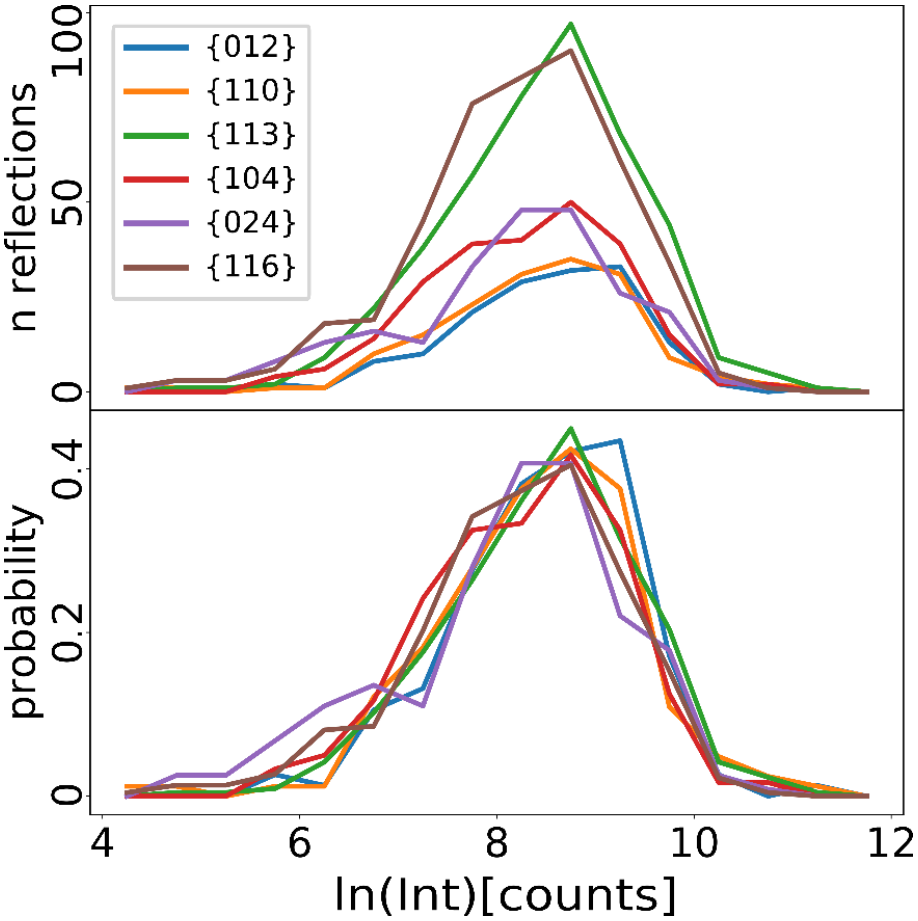

Figure 2.11: Intensity distribution histograms of the CSF III sample after the intensity correction and internal structure factor normalization. Apparent is that both sides of the histograms match in position. The number of occurrence histogram – upper plot – shows the impact of the multiplicity on the number of observations and is in good agreement with the expectation (see also Table 2.3). The lower plot shows the probability representation; here the number of occurrence in each bin is divided by the total number of occurrence of each IDH.

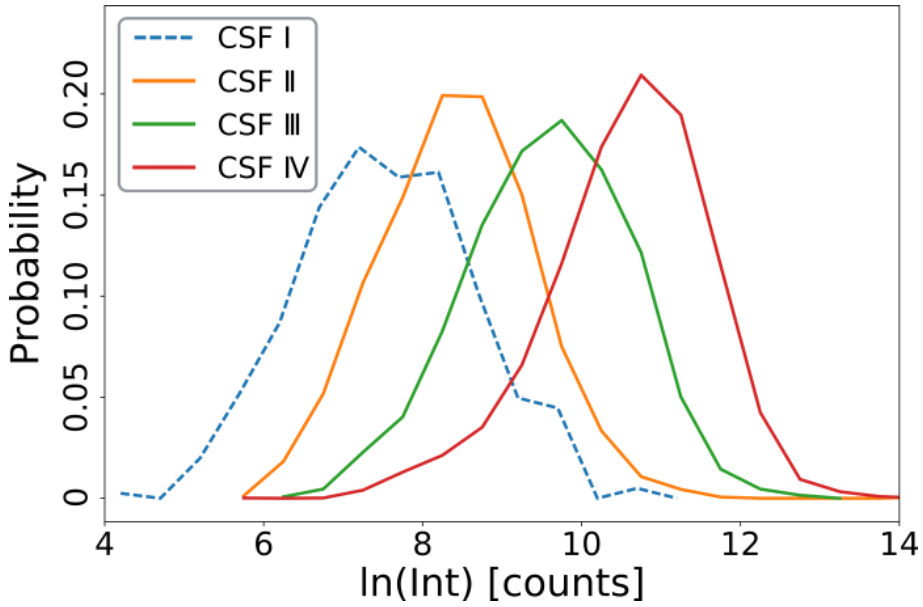

Figure 2.12: Resulting IDHs of all CSF samples. The used hkl-rings are internally scaled to the 024 structure factor and scaled according to their exposure time. This result shows a very satisfactory agreement with the SEM derived mean crystal sizes shown in Table 2.1.

Table 2.3: Corundum CSF Parameters

Information on the measured *hkl* of corundum (SG: R$\bar{3}$c). Bold *hkl*-families are used for the final analysis.

hkl	r [pix]	|F(hkl)|	M	n CSF I	n CSF II	n CSF III	n CSD IV
012	219	46.29	6	160	85	152	908
104	301	82.19	6	177	**95**	**165**	**969**
110	325	60.1	6	419	386	**435**	**1803**
113	373	74.54	12	230	253	**240**	1246
024[1]	458	93.09	6	**334**	**255**	**236**	**1338**
116	504	103.26	12	672	732	**445**	**2179**
				334	**350**	**1521**	**6289**

[1] Used for internal intensity scaling. *n*: number of observations, M: *hkl* multiplicity

2.4.5 S1 Scaling

CSF III is used as *reference* to establish the S1 scaling factor which is applied to all other samples[10]. The *reference* IDH is composed out of the individual IDHs originating from the {104}, {110}, {113}, {024} and {116}- *hkl* families and internally scaled to the structure factor of the 024 *hkl*-reflection. The S1 scaling factor determination – performed by running the function *determ_S1()* – is visualized in Figure 2.13. The determined scaling factor is ln(S1) = 18.812.

[10] CSF I and the LaB_6-Powder sample are measured separately, several months later. The CSF III is measured to again serve as reference. In this case the determined S1 is ln(S1) = 19.22

To determine the CSDs of all corundum CSFs *via* FXD-CSD CSF III, so far only used as the *reference* material, could also be treated as a *sample*, using the CSF II as *reference*; in this case the scaling factor is ln(S1) =17.855.

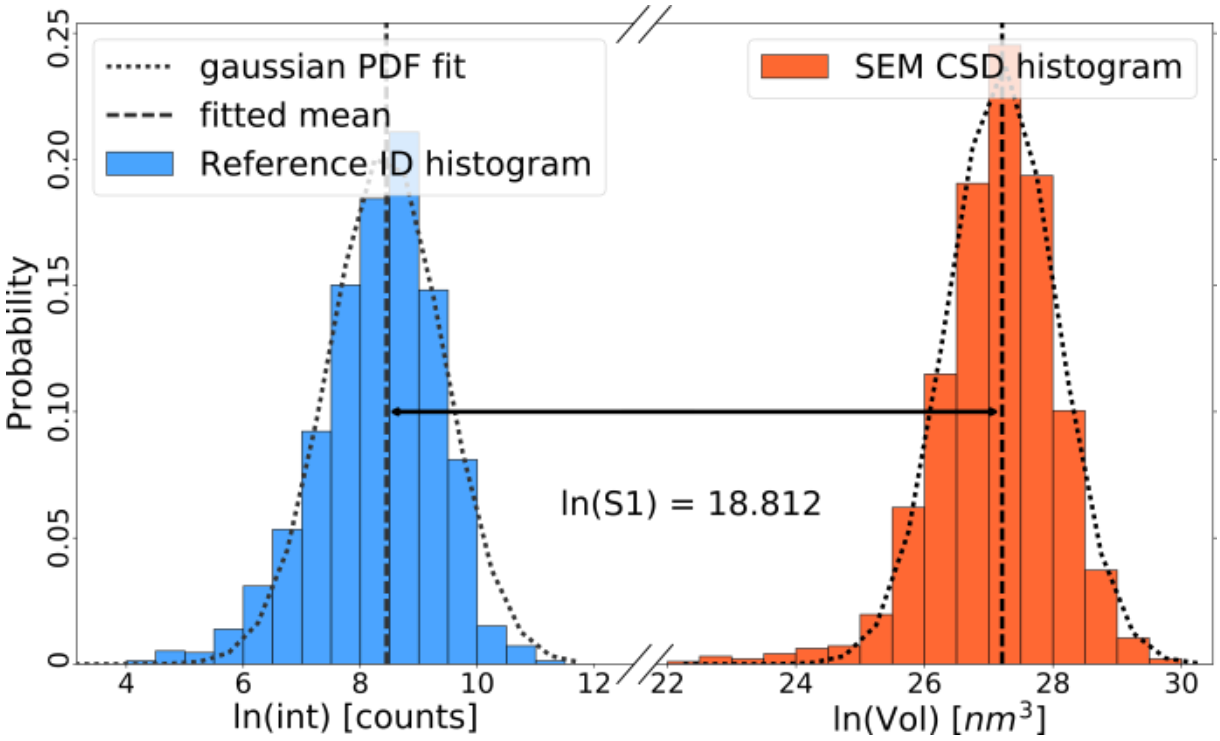

Figure 2.13: Plot of S1 scaling factor determination with the CSF III used as reference as generated by *determ_S1()*. Probability *vs.* ln(int)[counts] in blue from the diffraction measurement and the probability *vs.* the crystal volume in ln([nm³]) from the SEM measurements in orange; the intensity is expressed in counts and plotted on a log-scale. Both, IDH and CSD are shown with fitted Gaussian PDF (a log-normal in linear space). The mean value of the IDH is 8.44 ± 0.08 ln(Int)[counts] and of the CSD 27.21 ± 0.02 ln(Int)[counts]. The IDH has a FWHM of 2.30 ± 0.06 ln(Int)[counts] and the SEM derived CSD 1.97 ± 0.04 ln(Int)[counts].

2.4.6 S2- and exposure time intensity scaling

Concerning the CSD determination within the corundum CSF series, the S2 scaling factor is 1; all IDs are scaled to the structure factor of the 024 *hkl*-plane by *internal-scaling*, i.e. the reference and the sample have the same structure factor. The only factor which has to be considered is a scaling according to the different exposure times; this is simply the ratio between the exposure time of *reference* and *sample* (Table 2.1).

In case of the LaB_6-Powder, S2 is 1.41, calculated between the 024 *hkl*-plane of corundum and the 200 *hkl*-plane of LaB_6 (see Eq. 2.3) and applied to the measured LaB_6-Powder intensities.

2.4.7 Resulting CSDs

The resulting CSDs are presented in two ways: 1) as diameter distributions (Figure 2.14) as this is arguably the most intuitive way and 2) as volume distribution on a log-scale (Figure 2.15) because it is the most direct way, obtained without any crystal shape assumption. For a better quantification probability density functions (PDFs) are fitted to the histograms. We chose a log-normal PDF for the diameter distribution histograms and a Gaussian PDF for the volume histogram distributions. Since the measured CSDs are not expected to have any particular mathematical form one can pick any

reasonably well-fitting functional form. In both figures the corundum CSF samples show increasing crystal sizes in correspondence with their mean crystal size (see Table 2.1) and in the diameter distributions plot (Figure 2.14) an increase of the distribution width with increasing crystal size is apparent. That the increase in distribution width is only apparent here is indeed well explained by the nature of the log-scale used in the crystal volume plot (Figure 2.15). The deduced LaB_6-Powder sample CSD has a mean value of 7.51 µm, which is much bigger than the expected value (compare Figure 2.6 and Table 2.1). This can be explained by the fact that only parts of the CSD are measured and the smaller crystallites remain undetected by diffraction; already evident in the individual IDH evaluation (recall Section 2.4.4). The high-end tail (~12 µm) of the distribution looks correct if one compares it with the biggest crystals seen in the SEM images (Figure 2.4). Table 2.4 and Table 2.5 show the fitting parameters of the diameter CSDs and the volume CSDs, respectively; for comparison the SEM derived CSD information is listed as well.

Overall there is good agreement between the CSD determined with the FXD-CSD method and the one measured *via* SEM imaging. Only the LaB_6-Powder sample and the smallest corundum crystal size fraction CSF I show significant deviations; the mean crystal size of the FXD-CSD derived CSD is too big. This is due to the small size part of the CSD being situated below the detection limit; the evaluation of the individual *hkl* IDHs did already indicate this (recall Section 2.4.4).

Focusing on the three bigger corundum crystal size fraction samples (CSF II, CSF III, CSF IV), it is evident that the mean crystal sizes, as determined *via* FXD-CSD do not deviate more than 1 µm from the SEM derived data (Table 2.4). Moreover, also the full width half maximum (FWHM) of these three samples is in good agreement (Table 2.5).

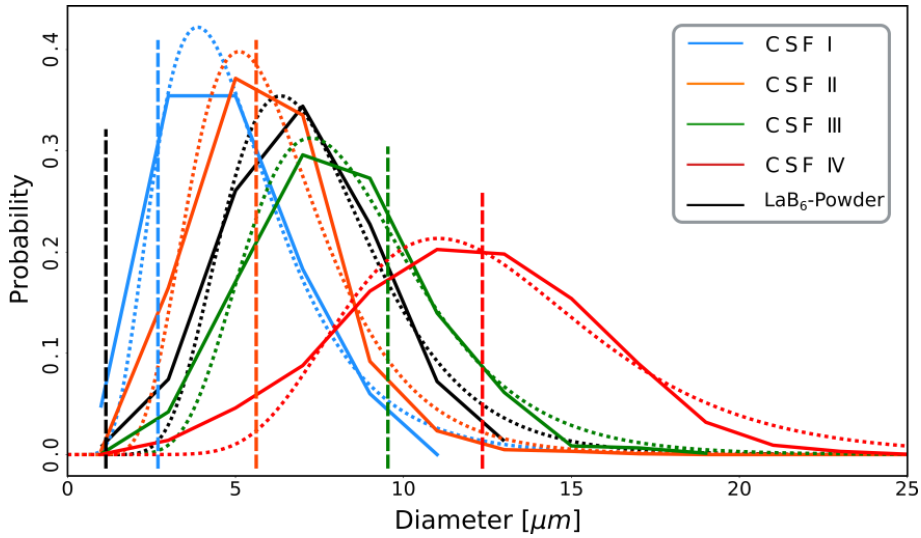

Figure 2.14: Diameter CSDs of all samples with log-normal PDF fits shown as dotted lines. The dashed lines show the SEM derived mean values and illustrate their good agreement with the FXD-CSD derived CSDs for the CSF II – IV samples. The CSF I and the LaB6-Powder are significantly offset.

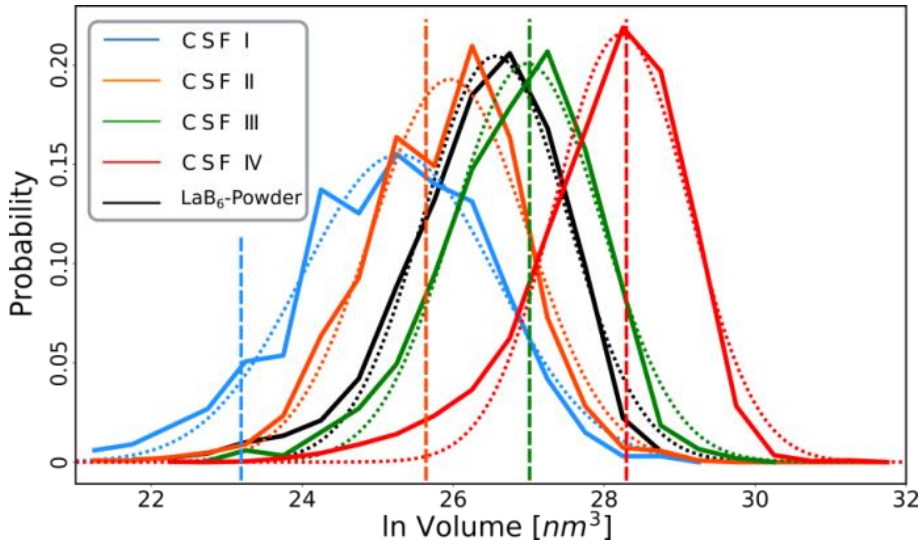

Figure 2.15: Logarithmic volume CSDs of all samples with Gaussian PDF fits shown as dotted lines. The dashed lines show the SEM derived mean values and illustrate their good accordance with the FXD-CSD derived CSDs for the CSF II – IV samples. The CSF I and the LaB6-Powder show a significant offset between the SEM derived mean value and fitted function; the mean value of the LaB6-Powder is not even within the plotted area (ln(Vol)= 20.99).

Table 2.4: Parameters of diameter CSDs

Log-normal PDF[1] fitting parameters of crystal diameter CSDs derived with FXD-CSD in comparison with the SEM derived CSDs and the arithmetic mean values of the histograms.

Sample	CSD origin	μ ln(*d*)[μm]	σ ln(*d*) [μm]	χ^2	Mean[2] crystal *d* ± Δ*d*[4][μm]	Mode[3] *d* ± Δ*d*[4] [μm]
LaB_6	FXD	1.960 ± 0.026	0.336 ± 0.023	0.004	7.51 ± 0.20	6.34 ± 0.19
	SEM	0.307 ± 0.028	0.820 ± 0.020	0.007	4.46 ± 0.04	0.72 ± 0.02
CSF I	FXD	1.549 ± 0.029	0.443 ± 0.032	0.003	5.19 ± 0.17	3.87 ± 0.16
	SEM	0.909 ± 0.012	0.385 ± 0.011	0.003	2.67 ± 0.06	2.14 ± 0.05
CSF II	FXD	1.765 ± 0.018	0.371 ± 0.013	0.006	6.25 ± 0.12	5.11 ± 0.11
	SEM	1.653 ± 0.009	0.338 ± 0.008	0.001	5.52 ± 0.07	4.65 ± 0.06
CSF III	FXD	2.091 ± 0.016	0.333 ± 0.014	0.003	8.56 ± 0.16	7.24 ± 0.15
	SEM	2.166 ± 0.006	0.282 ± 0.005	0.001	9.07 ± 0.08	8.05 ± 0.07
CSF IV	FXD	2.504 ± 0.017	0.322 ± 0.014	0.003	12.89 ± 0.23	11.03 ± 0.22
	SEM	2.435 ± 0.010	0.331 ± 0.008	0.002	12.16 ± 0.16	10.41 ± 0.15

[1] $\frac{1}{x\sigma\sqrt{2\pi}}\, e^{\frac{(\ln x-\mu)^2}{2\sigma^2}}$ [2] $e^{\mu+\frac{\sigma^2}{2}}$ [3] $e^{\mu-\sigma^2}$ [4]Fitting error and error introduced by applying the S1 scaling factor (see Appendix A 3).

Gaussian PDF[1] fitting parameters of crystal volume CSDs derived with FXD-CSD in comparison with the SEM derived CSDs and the arithmetic mean values of the histograms.

Table 2.5: Parameters of Volume CSDs

Gaussian PDF[1] fitting parameters of crystal volume CSDs derived with FXD-CSD in comparison with the SEM derived CSDs and the arithmetic mean values of the histograms.

Sample	CSD origin	Mean Vol., μ ln(*Vol*)[nm³]	σ ln(*Vol*) [nm³]	χ^2	FWHM ln(*Vol*) [nm³]	FWHM PDF fit [μm]	d^2 sphere [μm]	$\sqrt[3]{\overline{Vol}}$ [μm]
LaB_6-Powder	FXD	26.160 ± 0.042	0.942 ± 0.042	0.002	2.247 ± 0.087	4.62	5.37	7.00
	SEM	20.990 ± 0.086	2.635 ± 0.070	0.001	6.206 ± 0.166	2.69	1.36	1.09
CSF I	FXD	25.282 ± 0.066	1.283 ± 0.063	0.002	3.021 ± 0.156	4.13	4.80	4.57
	SEM	23.318 ± 0.063	1.150 ± 0.066	0.001	2.708 ± 0.063	2.22	2.95	2.38
CSF II	FXD	25.955 ± 0.051	1.030 ± 0.051	0.004	2.424 ± 0.120	4.15	4.75	5.72
	SEM	25.653 ± 0.332	1.010 ± 0.027	0.000	2.379 ± 0.064	4.21	6.42	5.17
CSF III	FXD	26.981 ± 0.039	0.980 ± 0.039	0.001	2.307 ± 0.092	5.46	6.35	8.05
	SEM	27.209 ± 0.019	0.838 ± 0.016	0.001	1.973 ± 0.037	5.85	10.78	8.69
CSF IV	FXD	28.232 ± 0.038	0.885 ± 0.038	0.002	2.085 ± 0.090	8.66	15.16	12.22
	SEM	28.039 ± 0.029	0.950 ± 0.023	0.001	2.237 ± 0.055	8.74	14.21	11.46

[1] $\frac{1}{\sqrt{2\pi\sigma^2}}\, e^{\frac{(x-\mu)^2}{2\sigma^2}}$ [2] Volume equivalent sphere diameter

2.5 Discussion and Conclusion

With FXD-CSD we introduced a generally applicable X-ray diffraction-based method to measure CSDs of crystalline powders and polycrystalline materials with unprecedented counting statistics. With the primary goal of only deriving precise and robust CSDs, thus neglecting crystal shape or position within the sample and no need for estimating the irradiated sample volume, FXD-CSD is highly flexible in its application, fast in its implementation and does not demand any particular effort for sample preparation. FXD-CSD constitutes a tool to measure CSDs with such a high statistical significance that mathematical function fitting can be done in a way that allows for secure discrimination between functions that can be quite similar (e.g.: log-normal-, Weibull-, Hillert- or Rayleigh distributions); this eventually can give insights into the underlying formation processes leading to specific distributions.

In the following section we first describe the standard procedure of how an unknown sample is prepared and measured to obtain suitable data for a FXD-CSD analysis. In the subsequent sections we will cover a number of issues that came up while applying FXD-CSD and merit some further discussion.

2.5.1 Practical proceeding

Providing that a good *reference* (see Section 2.3) material is at hand and that the crystallographic (structural) information of *sample* and *reference* are available the following procedure is advisable for FXD-CSD measurements in transmission geometry. All considerations concerning the irradiated sample

volume (ISV) and the subsequent measurement strategy are based on the diffractometer setup used in this manuscript, described in Sections 2.3.2 and 2.3.3, and have to be adapted if needed. The following choices and tests need to be made to successfully apply the method:

1) The first and most important objective is to obtain spotty diffraction patterns from the sample under investigation which should look similar to the frames shown in Figure 2.8. For this, the number of crystals in the ISV has to be in an appropriate range. To tune this number either the ISV itself is changed or the number of crystals has to be adapted, the latter of course is only possible if the sample under investigation is a powder. With a collimator pinhole with d = 0.5 mm and a Kapton® capillary with d = 0.8 mm used here, the ISV is in the order 0.125 mm^3, which has proven to be a good starting point for powders in the lower µm range; this may involve that the sample has to be diluted with starch as filling smaller capillaries with powder can be difficult. In the end the degree of dilution is highly CSD dependant and has to be found by trial and error. In case of polycrystalline materials, it is advantageous to use a sample thickness of ~0.5 mm as starting material and ideally forming a sharp angle wedge by grinding; this way the ISV can be changed by changing the sample position on the diffractometer. With single test frame measurements (no rotation) the spottiness needs to be tested. The exposure time must be chosen regarding the structure factors of the material under investigation; starting with long exposure times (e.g. 120s) during testing is advisable because it is lowering the probability that small crystals of the CSD are overlooked. Depending on the test-frame results the irradiated sample volume needs to be adjusted. For the diffractometer used in our study ~50 spots discernible on a *hkl*-ring are a good number. Once the irradiated sample volume is tuned the exposure time perhaps can be reduced; this should, however, not lower the number of spots on any *hkl*-rings.

2) The rotation step size needs to be set (see Figure 2.1 and Section 2.3.2). This parameter is depending on crystal quality, beam collimation and beam monochromaticity. A good starting value might be 0.025°. To test whether the step size is in a good range a rotation step measurement (see Section 2.3.3) with 30 frames is performed and the resulting frames are visually evaluated. By flipping through the images (e.g. using the software Fiji (Schindelin *et al.*, 2012; Schneider *et al.*, 2012)) the diffraction spots should smoothly appear and disappear; no jumping or flickering should be seen. Spots that appear and disappear should be visible in at least 10, better 15 frames. If they only appear in less than 10 frames the scan step size has to be lowered. In case they appear in more than 20 frames the step size can be increased.

3) Once the above considerations are made, the sample to detector distance is chosen. This has to be done also regarding the *reference* material data collection because *sample* and *reference* have to be measured under the same geometric conditions. The resulting 2Θ-range on the detector has to include at least two, better three *hkl*-rings of the *reference* and at least one, better two *hkl*-rings of the *sample*; more rings of course bear more information and facilitate a better internal consistency check (see Section 2.3.6). Here one should pay attention to the multiplicities and structure factors of the chosen *hkl*-rings because only with different multiplicities and varying structure factors within one measurement one effectively can evaluate the quality auf the measured data; the more varied the multiplicities and the more diverse the structure factors are, the more convincing is the test in case of agreement (see Section 2.3.6).

4) If this is all set, the measurements (*reference* and *sample*) can be started. The total rotation should be at least 2° and can be easily extended to 15°; further extension might not deliver more information because of the appearance of symmetry equivalent reflections (see Section 2.3.3). In some cases, for example if the structure factors of the *sample* are doubtful (see Section 2.5.2), the ring positions are hard to recognize in a single frame or if textures are likely, it is advisable to additionally perform a conventional rotation powder measurement. With this the structure factors can be reviewed (if needed), the *hkl*-ring positions be located, and the presence of textures be checked.

5) Once both data sets are measured (*reference* and *sample*) they can be analyzed with the FXD-CSD software (see Figure App. B-2).

2.5.2 Limiting factors

Despite the generally wide applicability of FXD-CSD some limiting factors need to be discussed here. The following considerations are made for deducing CSDs with a statistical significance, which allow for discrimination between PDFs; this needs good sampling statistics with a sufficient number of bins to describe and discern different mathematical functions. Scenarios where only the mean crystal size or the approximate distribution are requested, the limitations can of course be considerably lower.

Concerning the lower limit of detection (LLOD) and the upper limit of application (ULOA) the limiting factors depend on sample material, X-ray beam quality and beam dimensions. The LLOD is obviously strongly impacted by the X-ray source brilliance and of course depends on the scattering power of the sample under investigation. The latter is nicely shown by comparing the example frames of the LaB_6-Powder sample and the corundum CSF I sample; corundum constitutes a fairly good and LaB_6 an excellent scatterer (Figure 2.7 and Figure 2.8). For the diffractometer and materials used here, 1 µm can be stated as an approximate value for the LLOD. At synchrotron facilities the LLOD is a few hundred nm as recently shown for gas hydrates, a comparatively weak scatterer (Chaouachi *et al.*, 2017). The ULOA is primarily defined by the lateral beam dimensions and the sample thickness. The sample must be penetrable by the X-ray beam to such a degree that the complete CSD is detectable; only if the CSD is completely recorded, the measured intensities can successfully be corrected with the linear absorption coefficient μ (see Section 2.3.5.2 and Appendix B 3.1). The lateral beam dimensions determine the ratio between the ISV and its edges, thus it also controls the potential number of crystals that are only partially illuminated; this is introduced in Section 2.3.3 and called sample edge effect. The number of crystals that are affected by sample edge effect is then related to the beam size as well as to the crystallite size and its distribution. As a rule of thumb the mean crystal size should be at least one order of magnitude smaller than the used collimator radius.

A material-specific limitation for polycrystalline materials is the presence of strong pronounced preferred crystal orientations (texture). They can complicate the data reduction (Section 2.3.4) because crystals with similar orientations will diffract at similar sample orientations and therefore will be detected in similar regions on the detector. In general, texture should be as low as possible and might require special considerations. Even though strong textures can make it impossible to unravel the spots on the detector, special textures like fibre textures can even favour uniform spot distributions on *hkl*-rings inclined to the fibre axis (Neher *et al.*, 2018).

Attenuation effects are, as already mentioned in Section 2.3.5.2 and in the Appendix B 3, not critical for the materials and crystal sizes examined here. Absorption can be corrected if needed and extinction is only taking place to a negligible amount. However, when materials with strong structure factors and with a low mosaicity are under investigations, extinction might become problematic and considerations have to be made. If necessary, extinction can be reduced by using high-indexed *hkl*s and by choosing weaker reflections (Becker & Coppens, 1974*a*,*b*, 1975). Especially for the reference material it is important to keep extinction under control because any bias on the intensity distribution will influence the S1 scaling factor determination and therefore also introduce a systematic error (shifting the distribution) to the determined *sample* CSD. Fortunately, the extinction correction is bounded in case of the *reference* measurement because the expected ID shape is a known quantity; this of course necessitates a *reference* sample beyond doubt (see Section 2.5.3). In case of polycrystalline materials, the radiation is not only attenuated by one crystal, absorption is rather taking place by the whole sample thickness; since the position of the crystals is not known, the exact pathway and therefore its length is not known either. The path length can only be estimated but must be somewhere between the sample thickness s and $\frac{s}{\cos(2\Theta)}$, which is considered not to offer much variation, especially for small 2Θ values, and we are confident that it is not introducing significant errors. As long the material under investigation does not have extremely high linear absorption coefficients and the sample is not considerably thicker than suggested above – the measured samples have to be thin anyway to ensure spotty patterns – the above approximations should be sufficient; previous measurements on polycrystalline alumina ceramics have not shown to be significantly impacted by absorption (Neher *et al.*, 2018). Concerning future measurements of polycrystalline materials in reflection geometry the absorption correction unfortunately is not as straightforward because it is difficult to precisely determine the effective penetration depth of the primary X-ray beam.

As mentioned in Section 2.3.5.2 and described in the Appendix B 3.2 the lateral beam profile can bias FXD-CSD measurements. Ideally the lateral beam profile should be homogenous in its appearance and box-shaped in its cross-section. If this is not the case and the lateral beam profile is known the resulting ID can be de-convoluted. With the presently used diffractometer setups – the one presented here and the one used in an earlier publication (Chaouachi *et al.*, 2017) – the beam profile deconvolution is considered to be unnecessary. Comparing the intensity variations within the beam profile with the width of the volume CSD (see Appendix B 3.2.2) shows such big difference in their extension, the CSD is much broader, that the beam intensity distribution acts almost like a delta-function and therefore has little impact. Furthermore, the deconvolution can introduce additional uncertainties. To improve the procedure of deconvolution a *reference* material beyond doubt (i.e. with a narrow well-defined CSD) is needed because only when the correct distribution shape is known one can be certain that the deconvolution improves the overall result; so far, such a *reference* is not at hand (see Section 2.5.3).

A minor limiting factor on the applicability of FXD-CSD can be the crystal quality itself of the material under investigation. Crystals with high amounts of tension or cracked crystals can lead to odd rocking curve shapes. In conjunction with crowded spotty diffraction rings this impedes the detection of accidental peak overlap and can hamper very seriously the data reduction. If peak overlap can be excluded because of low occupation of spotty diffraction rings, odd shaped rocking curves do, however, not hinder a correct intensity measurement. Of course, this is limited too at some point: if the diffracted intensity of small crystals is spread too much, it might be hard to detect it in the measured single frames.

Many of the points mentioned in this section have shown that the *reference* material quality and its proper characterization is highly crucial to successfully perform CSD measurements with FXD-CSD. For this reason, the following section is solely dedicated to this topic.

2.5.3 *Reference* Material

As stated repeatedly in previous sections the *reference* material quality is of great importance for obtaining precise results with FXD-CSD. The reference material has to be a single crystalline powder with a high scattering power, should have a narrow size distribution in the application range of the used diffractometer, the crystal shapes should be as uniform as possible and show no size-shape dependency; the ideal shape of course is spherical. The key for a reliable calibration is the determination of the crystallites' volume distribution of the *reference*. When deriving the crystal volumes from two-dimensional (SEM) images, incorrect shape assumptions can introduce systematic errors to the deduced CSD of the *reference*. Moreover, two-dimensional crystal shapes could be size dependent, leading – if unnoticed – to a bias in the derived volume CSD and a difference in the mathematical forms of volume and intensity derived CSDs of the *reference*. Ideally the shape of the CSD should be narrow and mathematically well-defined (e.g. log-normally distributed). Then even a circumstantially incompletely measured *reference* ID (as a consequence of LLOD) can be extrapolated with the known shape if only the high intensity tail of the distribution is measured completely; that this is possible was shown in an earlier publication (Chaouachi *et al.*, 2017).

The choices presented here, the LaB_6-Powder and the different corundum crystal size fractions (CSFs), unfortunately do fully satisfy all above-mentioned criteria. The crystals composing the LaB_6-Powder are quite isometric yet have a rather broad CSD (see Figure 2.4 and Figure App. B-10) which reaches down well below the LLOD for common lab X-ray sources (Section 2.4.1) and is close to the LLOD experienced at synchrotron facilities. Thus, for common lab X-ray sources, the LaB_6-Powder is not suitable. The corundum CSFs have quite narrow CSDs, but their individual crystal shapes are much harder to analyse from two-dimensional SEM images; a small size-shape dependency is also likely. One consequence of the size-shape dependence and the resulting CSD bias is that the lateral beam profile deconvolutions could not reliably be checked, by comparing the deconvoluted intensity CSD with the SEM derived volume CSD (see Section 2.3.5.2 and Appendix B 3.2.2.). Interesting materials that could provide a better *reference* are e.g. single crystalline microspheres (Nakamura *et al.*, 2016; Shimogaki *et al.*, 2014; Tasaki *et al.*, 2018; Yang *et al.*, 2008) or idiomorphic single crystals with shapes easily measured with SEM imagery (Pieniążek *et al.*, 2016; Chen *et al.*, 2011).

2.5.4 Outlook

FXD-CSD is the only diffraction method capable of providing reliable and assumption-free CSDs, opening new avenues for fundamental research, for manufacturing and quality management issues in materials research as well as chemical engineering with further ramifications into geosciences or bio-mineralization. Previous efforts to exploit the spottiness of Debye-Scherrer cones have only given access to mean crystallites sizes (He, 2009; 2011; Ida & Licai, 2011; 4) or rudimentary CSD information (Ingham, 2014; Yager & Majewski, 201). The price to pay for the much better resolved, assumption free CSD obtained by FXD-CSD is that the Bragg spots on the ring should not be too densely spaced, in contrast to the other methods listed above, which certainly remain very useful for establishing mean crystallite sizes, in particular for polycrystalline materials. Concerning the size range we know from previous studies at synchrotron facilities that the LLOD can well be lowered to a few hundred nm (Chaouachi *et al.*, 2017), thus close to or even overlapping with the upper limit of the Scherrer method

based on diffraction broadening; with appropriate primary beam dimensions (≥ 1 mm) the ULOA can be increased to at least 100 µm and above.

The EBSD method is now also moving into a 3-dimensional analysis of crystallites by using focused ion beams (FIB) and will in the near future also provide CSD information. However, this technique cannot be applied *in situ*, e.g. to samples under elevated pressures or variable temperature, while FXD-CSD is suitable for studying processes under such non-ambient conditions (Chaouachi et al., 2016).

The work presented here was performed on standard laboratory X-ray equipment. State of the art X-ray optics can widen the range of applicability of FXD-CSD, both in the laboratory and at synchrotron sources. The method solely needs a fast-readout 2D-detector and a rather large (0.3 to 1 mm) well shaped and laterally homogeneous primary beam and of course benefits form high intensities but does not rely on small divergence and high spectral purity. High intensities while having large beam dimensions could be achieved e.g. with crossed-coupled Göbel mirrors or capillary optics in combination with a crossed slit- or pinhole collimator close to the sample.

In the context of studies of time resolved or *in situ* grain growth, the investigation of oriented growth leading to preferred orientations is a certainly interesting topic which could in the future also be addressed by FXD-CSD. Since each individual diffraction spot is measured and saved with its position on the detector, its orientation information is available. With this information it is possible to monitor oriented grain growth and to establish CSDs of special orientations. This has been tried in the past e.g. with an akin synchrotron based procedure (Tommaseo & Klein, 2009) or *via* linear intercept length measurements on micrographs (Takayama *et al.*, 1992). With FXD-CSD it should be more straightforward to obtain datasets and link the results to present theories of texture development (Abbruzzese & Lücke, 1986; Bunge & Dahlem-Klein, 1990; Abbruzzese & Brozzo, 1992; Kazaryan *et al.*, 2001).

2.6 Acknowledgement

We thank Dr. M. Chaouachi and Dr. A. Falenty for fruitful discussions on the FXD-CSD method and its implementation. Special thanks go to Dr. V. Karius and the sedimentology department of the GZG, University of Göttingen for providing the knowledge and tools to prepare the corundum crystal size fraction samples used in this study. We also want to acknowledge the help of Prof. Dr. R. A. Neher on deconvolution issues. Furthermore, we like to thank Kathrin Nützmann for her work on the absorption correction. We also acknowledge the help of our research assistants Stefanie Stracke, Mathias Jansen und Thien An Pham.

2.7 References

Abbruzzese, G. & Brozzo, P. (1992). *Mater. Sci. Forum*. **94–96**, 77–88.

Abbruzzese, G. & Lücke, K. (1986). *Acta Metall.* **34**, 905–914.

Als-Nielsen, J. & McMorrow, D. (2011). Elements of Modern X-ray Physics Hoboken: John Wiley & Sons, Inc.

Andersen, M. S., Dahl, J. & Vanderberghe, L. (2013). CVXOPT: A Python package for convex optimization. cvxopt.org.

Bakar, M. R. A., Nagy, Z. K., Saleemi, A. N. & Rielly, C. D. (2009). *Cryst. Growth Des.* **9**, 1378–1384.

Balzar, D., Audebrand, N., Daymond, M. R., Fitch, A., Hewat, A., Langford, J. I., Le Bail, A., Louër, D., Masson, O., McCowan, C. N., Popa, N. C., Stephens, P. W. & Toby, B. H. (2004). *J. Appl. Crystallogr.* **37**, 911–924.

Becker, P. J. & Coppens, P. (1974*a*). *Acta Crystallogr. Sect. A*. **30**, 129–146.

Becker, P. J. & Coppens, P. (1974*b*). *Acta Crystallogr. Sect. A*. **30**, 148–153.

Becker, P. J. & Coppens, P. (1975). *Acta Crystallogr. Sect. A*. **31**, 417–425.

Berbenni, S., Favier, V. & Berveiller, M. (2007). *Int. J. Plast.* **23**, 114–142.

Bunge, H. J. & Dahlem-Klein, E. (1990). *Textures Microstruct.* **13**, 59–88.

Carniglia, S. C. (1972). *J. Am. Ceram. Soc.* **55**, 243–249.

Chantikul, P., Bennison, S. J. & Lawn, B. R. (1990). *J. Am. Ceram. Soc.* **73**, 2419–2427.

Chaouachi, M., Neher, S. H., Falenty, A. & Kuhs, W. F. (2017). *Cryst. Growth Des.* **17**, 2458–2472.

Chavanne, J., Elleaume, P. & Van Vaerenbergh, P. (1998). *J. Synchrotron Rad.* **5**, 196-201.

Chen, W., Liu, W., Chen, C., Wang, R. & Feng, Q. (2011). *CrystEngComm*. **13**, 3959-3961.

Eberl, D. D., Drits, V. A. & Środoń, J. (1998). *Am. J. Sci.* **298**, 499–533.

Feltham, P. (1969). *Scr. Metall.* **3**, 853–854.

Freedman, D. & Diaconis, P. (1981). *Zeitschrift für Wahrscheinlichkeitstheorie und verwandte Gebiete*. **57**, 453–476.

Fujiwara, M., Nagy, Z. K., Chew, J. W. & Braatz, R. D. (2005). *J. Process Control*. **15**, 493–504.

German, R. M. (2010). *Crit. Rev. Solid State Mater. Sci.* **35**, 263–305.

He, B. B. (2009). Two-Dimensional X-Ray Diffraction Hoboken: J. Wiley & Sons, Inc.

He, B. B. (2011). Method for measuring crystallite size with a two-dimensional X-ray diffractometer US Patent No. 7885383. Washington: US Patent and Trademark Office.

Hillert, M. (1965). *Acta Metall.* **13**, 227–238.

Hiraoka, N., Buslaps, T., Honkimäki, V. & Suortti, P. (2005). *J. Synchrotron Radiat.* **12**, 670–674.

Hirsch, P. B. (1954). *Br. J. Appl. Phys.* **5**, 257–260.

Hirsch, P. B. & Kellar, J. N. (1952). *Acta Crystallogr.* **5**, 162–167.

Ida, T. & Licai, J. (2011). Crystallite Size Analysis Method and Apparatus Using Powder X-Ray Diffraction US Patent No. 2011/0064199. Washington, DC: US Patent and Trademark Office.

Ingham, B. (2014). *J. Appl. Crystallogr.* **47**, 166–172.

Kabsch, W. (1988). *J. Appl. Crystallogr.* **21**, 916–924.

Kazaryan, A., Wang, Y., Dregia, S. A. & Patton, B. R. (2001). *Phys. Rev. B - Condens. Matter Mater. Phys.* **63**, 1–11.

Klapp, S. A., Klein, H. & Kuhs, W. F. (2007). *Geophys. Res. Lett.* **34**, L13608.

Knudsen, E. B., Sørensen, H. O., Wright, J. P., Goret, G. & Kieffer, J. (2013). *J. Appl. Crystallogr.* **46**, 537–539.

Konert, M. & Vandenberghe, J. (1997). *Sedimentology*. **44**, 523–535.

Krill, C. E. & Birringer, R. (1998). *Philos. Mag. A Phys. Condens. Matter, Struct. Defects Mech. Prop.* **77**,

621–640.

Kruzic, J. J., Satet, R. L., Hoffmann, M. J., Cannon, R. M. & Ritchie, R. O. (2008). *J. Am. Ceram. Soc.* **91**, 1986–1994.

Kurzydeowski, K. J. & Bucki, J. J. (1993). *Mater. Sci.* **41**, 3141–3146.

Langford, J. I., Louër, D. & Scardi, P. (2000). *J. Appl. Crystallogr.* **33**, 964–974.

Lasaga, A. C. (1998). Kinetic Theory in the Earth Sciences Princeton: Princeton University Press.

Lipson, H., Langford, J. I. & Hu, H.-C. (2006). *Int. Tables Crystallogr.* **C**, 596-598.

Louat, N. P. & Duesbery, M. S. (1994). *Philos. Mag. A*. **69**, 841–854.

Milch, J. R. & Minor, T. C. (1974). *J. Appl. Crystallogr.* **7**, 502–505.

Müller, G. (1967). Methods in sedimentary petrology E. Schweitzerbart'sche Verlagsbuchhandlung.

Nagy, Z. K. & Braatz, R. D. (2012). *Annu. Rev. Chem. Biomol. Eng.* **3**, 55–75.

Nakamura, D., Tanaka, T., Ikebuchi, T., Ueyama, T., Higashihata, M. & Okada, T. (2016). *Electron. Commun. Japan*. **99**, 58–63.

Neher, S. H., Klein, H. & Kuhs, W. F. (2018). *J. Am. Ceram. Soc.* **101**, 1381–1392.

Nützmann, K. (2013). Crystallite Size Distributions of CH 4 -CO 2 Gas Hydrates from Diffraction Data (Including the Effect of Absorption). MSc. Thesis. University of Göttingen.

Pieniążek, A., Witkowski, B. S., Reszka, A., Godlewski, M. & Kowalski, B. J. (2016). *Opt. Mater. Express*. **6**, 3741 -3750.

Poulsen, H. F., Fu, X., Knudsen, E., Lauridsen, E. M., Margulies, L. & Schmidt, S. (2004). *Mater. Sci. Forum*. **467–470**, 1363–1372.

Raeisinia, B., Sinclair, C. W., Poole, W. J. & Tomé, C. N. (2008). *Model. Simul. Mater. Sci. Eng.* **16**, 025001.

Rodriguez-Navarro, A. B., Alvarez-Lloret, P., Ortega-Huertas, M. & Rodriguez-Gallego, M. (2006). *J. Am. Ceram. Soc.* **89**, 2233–2238.

Rouse, K. D., Cooper, M. J., York, E. J. & Chakera, A. (1970). *Acta Crystallogr. Sect. A*. **26**, 682–691.

Scardi, P., Leoni, M. & Delhez, R. (2004). *J. Appl. Crystallogr.* **37**, 381–390.

Schdanow, H. S. (1935). *Zeitschrift Für Krist.* **90**, 82-91.

Scherrer, P. (1918). *Nachrichten von Der Gesellschaft Der Wissenschaften Zu Göttingen, Math. Klasse*. **1918**, 98–100.

Schindelin, J., Arganda-Carreras, I., Frise, E., Kaynig, V., Longair, M., Pietzsch, T., Preibisch, S., Rueden, C., Saalfeld, S., Schmid, B., Tinevez, J. Y., White, D. J., Hartenstein, V., Eliceiri, K., Tomancak, P. & Cardona, A. (2012). *Nat. Methods*. **9**, 676–682.

Schneider, C. A., Rasband, W. S. & Eliceiri, K. W. (2012). *Nat. Methods*. **9**, 671–675.

Sharma, H., Huizenga, R. M. & Offerman, S. E. (2012*a*). *J. Appl. Crystallogr.* **45**, 693–704.

Sharma, H., Huizenga, R. M. & Offerman, S. E. (2012*b*). *J. Appl. Crystallogr.* **45**, 693–704.

Shi, D., Mhaskar, P., El-Farra, N. H. & Christofides, P. D. (2005). *Nanotechnology*. **16**, S562-S574.

Shimogaki, T., Okazaki, K., Yamasaki, K., Fusazaki, K., Mizokami, Y., Tetsuyama, N., Higashihata, M., Ikenoue, H., Nakamura, D. & Okada, T. (2014). *Appl. Phys. A Mater. Sci. Process.* **117**, 269–273.

Skripnyak, N. V, Skripnyak, E. G., Skripnyak, V. V, Skripnyak, V. A. & Avenue, L. (2017). *Proceedings of the 7th International Conference on Mechanics and Materials in Design*, Vol. edited by J.F. Silva Gomez & M.A. Meguid, pp. 1749–1762. Albufeira, INEGI-FEUP.

Sørensen, H. O., Schmidt, S., Wright, J. P., Vaughan, G. B. M., Techert, S., Garman, E. F., Oddershede, J., Davaasambu, J., Paithankar, K. S., Gundlach, C. & Poulsen, H. F. (2012). *Zeitschrift Fur Krist.* **227**, 63–78.

Stephen, R. A. & Barnes, R. J. (1937). *J. Inst. Met.* **60**, 285–296.

Swanson, P. L., Fairbanks, C. J., Lawn, B. R., Mai, Y.-W. & Hockey, B. J. (1987). *J. Am. Ceram. Soc.* **70**, 279–289.

Takayama, Y., Tozawa, T., Kato, H., Furushiro, N. & Hori, S. (1992). *Mater. Sci. Forum*. **94–96**, 325–330.

Tasaki, R., Higashihata, M., Suwa, A., Ikenoue, H. & Nakamura, D. (2018). *Appl. Phys. A*. **124**, 161.

Tommaseo, C. E. & Klein, H. (2009). *Pract. Metallogr.* **46**, 77–96.

Tschentscher, T. & Suortti, P. (1998). *J. Synchrotron Radiat.* **5**, 286–292.

Ungár, T., Gubicza, J., Ribárik, G. & Borbély, A. (2001). *J. Appl. Crystallogr.* **34**, 298–310.

Vincent, L. & Soille, P. (1991). *IEEE Trans. Pattern Anal. Mach. Intell.* **13**, 583–598.

van der Walt, S., Schönberger, J. L., Nunez-Iglesias, J., Boulogne, F., Warner, J. D., Yager, N., Gouillart, E. & Yu, T. (2014). *PeerJ*. **2**, e453.

Wikipedia contributors (2017). Convolution. https://en.wikipedia.org/wiki/Convolution.

Yager, K. G. & Majewski, P. W. (2014). *J. Appl. Crystallogr.* **47**, 1855–1865.

Yang, W., Wang, H., Cheng, X., Xie, Z. & An, L. (2008). *J. Am. Ceram. Soc.* **91**, 2732–2735.

Chapter 3 Publication - Determination of crystal size distributions in alumina ceramics by a novel X-ray diffraction procedure

Journal

Journal of the American Ceramic Society 2018; 101:1381-1392
https://doi.org/10.1111/jace.15309

Authors

Sigmund H. Neher[1], Helmut Klein[1], Werner F. Kuhs[1]

[1] GZG Abt. Kristallographie, Georg-August-Universität Göttingen, 37077 Göttingen, Germany

Abstract

A novel X-ray diffraction-based method is presented, capable of determining volume-based crystal size distribution (CSD) of polycrystalline materials and crystalline powders with unprecedented sampling statistics; the method is named fast x-ray diffraction crystal size distribution analysis (FXD-CSD). FXD-CSD can be performed with standard laboratory X-ray diffractometers equipped with a position sensitive detector and uses a software package written in Python for the data analysis. FXD-CSD is a destruction-free and generally applicable method to establish CSDs of polycrystalline materials as well as powders for sizes well below 1 µm up to about 100 µm; it even allows for studies of samples enclosed in complex environments e.g. for *in situ* measurements in a furnace or in a pressure cell. To show the capability of the method the microstructural evolution of four alumina substrates with different time-spans of sintering (4h, 8h, 16h, and 24h @ 1600°C) is investigated *via* FXD-CSD and SEM imaging. The corresponding CSDs and average grain sizes are determined, results obtained by FXD-CSD and the line-intersection methods are compared and clear evidence for the presence of abnormal grain growth (AGG) during sintering is shown. From three tested probability density functions (PDF) describing the CSDs a log-normal PDF fits best to the volume based CSDs; the method provides size distributions with unprecedented precision opening the way to a systematic and meaningful comparison between theoretically predicted and observed CSDs.

3.1 Introduction

Alumina ceramics are of great industrial importance and many fundamental scientific findings on sintering of oxide ceramics have been established with alumina (Kingery & Berg, 1955; Coble, 1961; Nichols, 1966; Chantikul *et al.*, 1990; Dillon *et al.*, 2007). In short, alumina is the textbook example for oxide ceramics. The commercial applications of alumina as structural or functional ceramics are diverse. Its high melting point, low thermal und electric conductivity and low thermal expansivity makes alumina very suitable as refractory material and electronic circuit carrier substrate. If alumina is coarse-grained and dense it becomes translucent (Apetz & Bruggen, 2003; Carter & Norton, 2013), thus can be used as watch cover, smartphone screen cover or as bulbs for metal halide lamps; its mechanical and thermal properties are superior compared to glass (Carter & Norton, 2013). All these physical properties are directly influenced by the microstructure of the material (Carter & Norton, 2013). The microstructure is controlled by additives and the applied sintering strategy. Due to the widespread use of alumina, the knowledge and control of its microstructure is of great importance in industry and science (Carter & Norton, 2013).

The sintering behavior of Al_2O_3 is well known and traditionally divided into three stages. During the **first stage**, crystals reduce internal stress, induced by rapid cooling in the manufacturing process (Petzold & Ulbricht, 1991), and undergo recrystallization without grain growth taking place (Petzold & Ulbricht, 1991; Kingery & Berg, 1955) Emerging grain growth is the onset of the **intermediate stage** of solid phase sintering. During this phase voids form connected pore channels which, under ongoing sintering, break up to form discrete pores (Coble, 1961). The **final stage** of sintering starts when only discrete pores exist and occupy four-grain corners and when the relative density has reached 95 % (Coble, 1961; Petzold & Ulbricht, 1991). After Coble (1961) the end of the final stage is either reached when the pore space is consumed completely or when abnormal grain growth occurs (AGG).

In contrast to normal grain growth (NGG), where the shape of the crystal size distribution (CSD) is unchanged and stays while the mean grain size is increasing, AGG is characterized by an increasing deviation from a steady-state distribution. AGG leads to CSD broadening, which can ultimately produce a bimodal distribution. Here and in the following CSDs are defined as the number-occurrence of the grain diameters and the term “grain” is used synonymous to “crystal” or “crystallite”.

The mechanical properties of alumina strongly depend on the porosity and the grain size of the specimen and are commonly estimated by the well-known models from Orowan and Petch (Orowan, 1933; Petch, 1953) which utilize the average grain size to characterize the microstructure. More recent studies however show that from intermediate grain sizes onward (~15 µm) these models are not necessarily valid anymore (Chantikul *et al.*, 1990; Carniglia, 1972) and that rather the CSD should be taken in account (Kruzic *et al.*, 2008; Yousef *et al.*, 2005). Concerning alumina ceramics the most comprehensive study to be mentioned here is the work of Chantikul *et al.* (1990). This study shows that bigger crystals can hinder crack propagation and points out that increased microstructural inhomogeneity (e.g. through controlled abnormal grain growth, or elongated grains) is favorable for producing stronger materials. Concerning the strength of alumina ceramics Yousef *et al.* (2005) and Kruzic *et al.* (2008) also mention the importance of CSD.

Looking at the production-process of high-density ceramics an important objective is the prevention of too fast a grain growth, in particular abnormal grain growth (AGG), because pores can detach from grain boundaries and are trapped within grains prior to reaching the desired density (Brook, 1969); in

case high density is the goal sintering is commonly done in two stages, starting with a lower temperature until a desired density is reached (Ulbricht, 1991; Apetz & Bruggen, 2003; Krell *et al.*, 2003). Besides the already mentioned influence on the mechanical properties of alumina ceramics, residual pores have a counterproductive influence on e.g. the thermal conductivity or the light transmittance (Apetz & Bruggen, 2003). In addition the compressive strength is highly density dependent (Knudsen, 1959; Carter & Norton, 2013). Even if the tendency to AGG is known to be not an intrinsic property of alumina (Bae & Baik, 1993), the amount of impurities needed to trigger AGG is quite small. Bae and Baik (1993) showed that the critical CaO and SiO_2 concentrations to trigger AGG are so low that impurities originating from furnace and crucible can already be enough. MgO is known to hinder AGG; Park and Yoon (2002) examine, in one of the very few studies measuring CSDs (from optical micrographs), the grain growth development in alumina and show how anorthite- and MgO-content is influencing whether NGG or AGG occurs. Interestingly, they also show that the growth mode can affect the grain shape and orientation, which concerns an additional and certainly important aspect of microstructure: Texture (Abbruzzese & Lücke, 1986; Bunge & Dahlem-Klein, 1992). Nettelship *et al.* (2002) also show the appearance of AGG by sintering commercial alumina and point out that the few attempts to model the sintering behavior of alumina considering CSDs always imply NGG by assuming an unchanged relative CSD (Nettleship *et al.*, 2002; Chappell *et al.*, 1986). Additionally Nettelship *et al.* (2002) and German (2010) point out that pretty much all available CSD data (Nettleship *et al.*, 2002) and even average grain size data (German, 2010), obtained from 2D sections is biased because the line intersection data is not unfolded (Saltykov, 1975) or not correctly transformed (German, 2010). Anderson *et al.* verify, by numerical modeling of NGG, the bias of the CSD originating from using 2D-sections and show that depending on whether the data is derived from 2D sections or the sample volume, the distribution shape is changing (Anderson *et al.*, 1989). The knowledge of precisely measured volume-based CSDs may well be the key to link real microstructure development to fundamental theories and to precisely determine occurrence and onset of AGG. CSD data at hand, characterized by a fitted mathematical function enables an objective comparison with model predictions like e.g. a Hillert distribution, occurring when grain growth is grain boundary curvature driven (Introna & Wood, 2004), a Rayleigh distribution when grain boundary sections undergo random motion (Hillert, 1965*b*) or a log-normal distribution when surface tension is controlling grain growth (Feltham, 1969).

Consequently, when material properties need to be precisely understood or tuned, the CSDs have to be considered. While the average grain size is a standard variable, well considered in industry and science, the influence of CSDs is not a common topic. In this work we want to draw attention to CSDs and elaborate the scientific potential of a straightforward method to measure those. In the case of alumina (as well as other polycrystalline materials) the most commonly used methods for determining crystal sizes are based on light- or electron-optical surface observations using 2D sections. In most cases this needs considerable efforts in sample preparation and usually provides only poor counting statistics. As mentioned, it always includes an assumption of how 2D information is converted to volume information (German, 2010; Saltykov, 1975; Novikov, 2000). This becomes quite difficult when the material shows preferred orientations (German, 2010).

X-ray diffraction facilitates a direct and fast way of analyzing and extracting particle size information of polycrystalline materials using the crystal volume to deduce the crystal sizes. The widespread availability of position sensitive X-ray detectors has enabled material scientists and engineers to perform X-ray based microstructural analyses (Rodriguez-Navarro *et al.*, 2006; Ida *et al.*, 2009; He,

2011; Hirsch & Kellar, 1952). Besides being nondestructive, X-Ray diffraction allows the distinction of different phases; thus volume-derived CSDs can individually be determined also for multiphase materials.

In the following we propose a new X-Ray diffraction-based method to determine the volume-based CSDs of polycrystalline materials (which of course also includes the mean and mode crystal size as well as higher moments) within hours and with, compared to conventional stereographic methods e.g. optical microscopy, unprecedented counting statistics. The use of X-ray diffraction to measure crystal sizes enables a destruction-free investigation of representative sample volumes under ambient and also non-ambient conditions.

Here a set of differently sintered alumina substrate ceramics are investigated and analyzed with a Bruker AXS D8 DISCOVER diffractometer with fixed χ-angle equipped with a Bruker AXS SMART Apex II position-sensitive detector operated with a Molybdenum (λ= 0.71073 Å) tube. This laboratory setup allows for the case of alumina to study crystal sizes from a few µm up to about 100 µm.

3.2 Fast X-ray diffraction CSD analysis

3.2.1 Theory:

Our Fast X-Ray Diffraction Crystal Size Distribution (FXD-CSD) analysis method is based on the kinematic diffraction theory of crystals where the intensity diffracted by a crystal is proportional to its irradiated volume (Als-Nielsen & McMorrow, 2011). Consequently, the intensity distribution (ID) of Bragg reflections originating from individual crystals is proportional to the distribution of single crystal volumes *V*. The method requires a calibration with a standard material with known CSD and known crystal structure; likewise, the crystal structure of the material under investigation must be known. Having measured the ID for a specific *hkl* plane (I_{hkl}) of the reference material, it is possible to determine a scaling factor called S_1 (which is specific to the diffractometer setup) between the mean volume of the CSD and the measured mean value of the intensity:

$$V = S_1 \times I_{hkl} \qquad \text{Eq. 3.1}$$

The scaling procedure is shown graphically in Figure 3.1. The reference material should be a powder composed of single-crystalline particles with a known and fairly narrow size distribution (measured with e.g. scanning electron microscopy or laser granulometry).

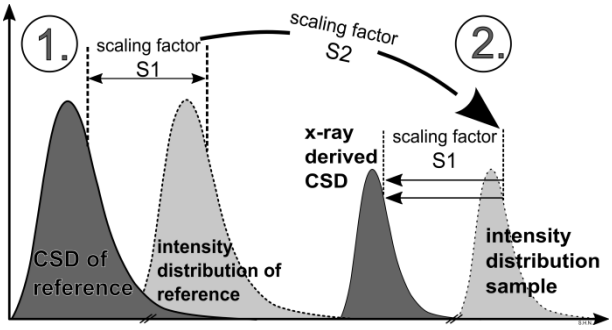

Figure 3.1 Intensity scaling and CSD determination: ① the scaling factor S1 is determined between the mean of the reference material volume distribution (CSD) and the x-ray derived intensity distribution (ID) of the reference material. ② S1 and S2 are applied to the measured sample ID to obtain the x-ray derived CSD of the sample. The S2 scaling factor is introducing the reference/sample structure factor and unit cell volume ratio, taking into account the difference of X-ray diffracting power between reference and sample for the chosen *hkl* reflections.

Preferentially the chosen material should possess a high crystallographic symmetry and good scattering properties (i.e. a large structure factor) to allow for well-separated Debye-Scherrer cones with high count rates (related to the respective structure factors).

As the investigated material and the calibrant usually will have different crystal structures, intensities must be normalized to the structure factor and unit cell volume by establishing the scale factor S_2. The kinematical theory states that the diffracted intensity is proportional to the structure factor squared and inversely proportional to the unit cell volume. Hence:

$$\boldsymbol{I_{hkl}} \propto \frac{\left|\boldsymbol{F^2}\right|_{\boldsymbol{hkl}}}{\boldsymbol{V_c}} \qquad \text{Eq. 3.2}$$

The scale factor S_2 for each *hkl*-family is then calculated as follow:

$$S_2\{hkl\} = \frac{I_{calibrant}}{I_{sample}} = \frac{(|F^2|_{hkl}/V_c)_{calibrant}}{(|F^2|_{hkl}/V_c)_{sample}} \qquad \text{Eq. 3.3}$$

where F^2 is the structure factor and V_c is the unit cell volume.

With the scale factors S_1 and S_2 one can proceed to calculate the CSD of the material of interest using the following formula

$$\boldsymbol{D} = \sqrt[3]{\frac{\boldsymbol{6 \times I \times S_2 \times S_1}}{\boldsymbol{\pi}}} \qquad \text{Eq. 3.4}$$

The second scale factor is of course not necessary if one utilizes a size-calibrated sample of the same material and identical Bragg reflections. It is important to emphasize that our method requires only (but strictly) that the intensity measurements of reference material and of the material of interest are made under identical conditions; it does not need the knowledge of the irradiated volume.

Our method also does not need a special sample preparation and does not depend on the aggregation state (powder or polycrystal) nor the mineralogical composition of the material as the CSDs can be determined from any spotty Debye-Scherrer ring (see Figure 3.2) that is not overlapped with other reflections. However, the selection of Bragg reflections of interest for each phase or material should be done considering their structure factor and multiplicity to get sufficiently strong and well separated observations. Reflections with too small a structure factor coming from crystals on the low side of the CSD may get undetected and lead to CSDs biased towards larger sizes. Bragg reflections with high multiplicities have a higher probability to be affected by peak overlap that cannot be resolved by the image analysis software and hence may also bias the results towards larger crystal sizes. Therefore, preferably *hkl* reflections with low multiplicity and high structure factors should be used.

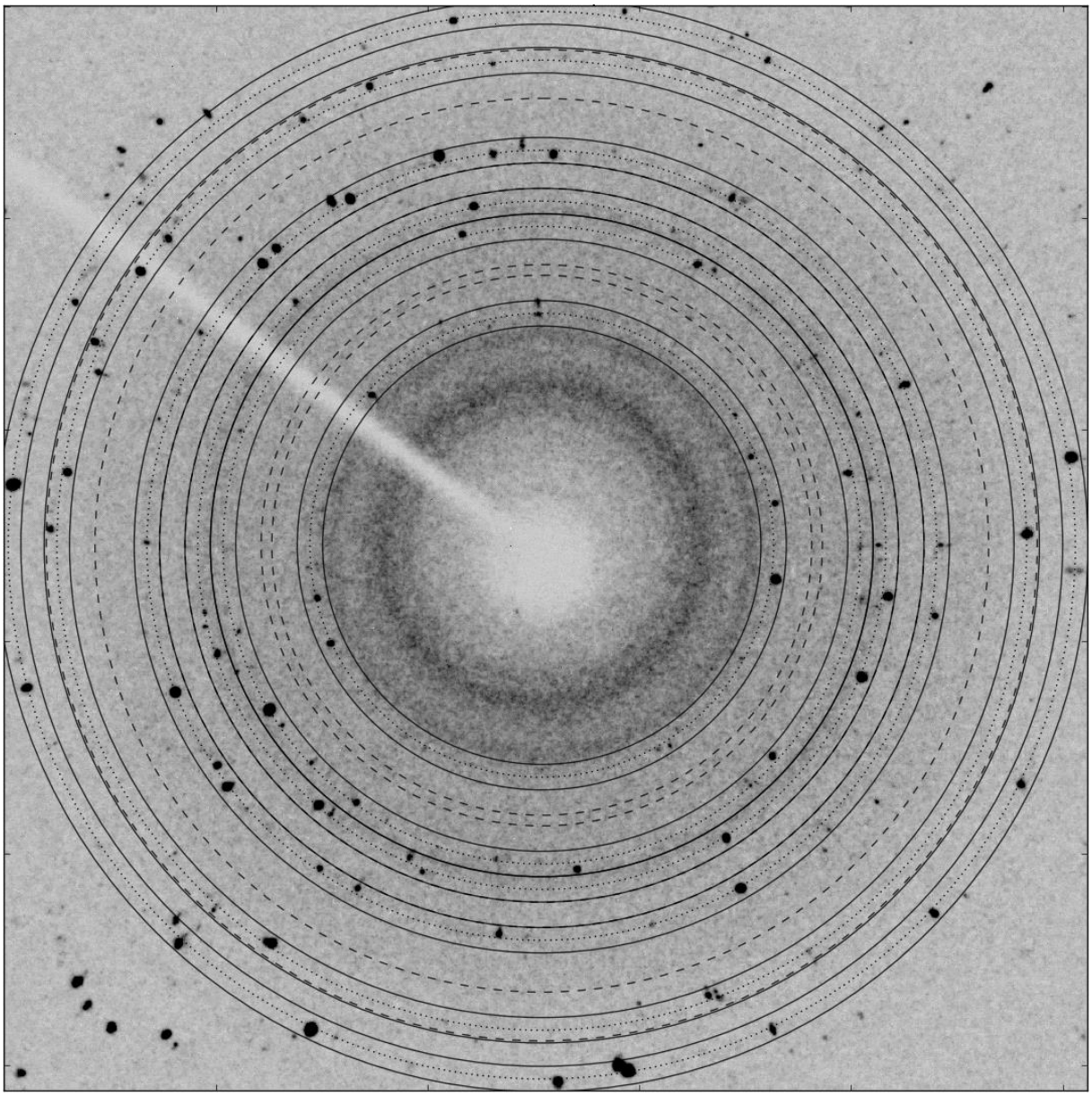

Figure 3.2: Spotty pattern with various “areas of interest” enclosed by solid circles containing Bragg reflections of the same *hkl* family. Dotted lines are the theoretical positions of the considered diffraction rings. Dashed lines delimit the areas used for estimating the background (see Section 3.2.3). The position of the areas used for estimating the background can be either smaller or bigger than the corresponding area of interest.

3.2.2 Requirements and measurement strategy

To analyze CSDs of polycrystalline materials or crystalline powders with the FXD-CSD Method a two-dimensional powder diffraction setup with a flat plate detector is needed. Ideal spotty diffraction patterns (Figure 3.3) are observed when the number of crystals in reflection state is sufficiently small to resolve each reflection and big enough to produce good sampling statistics. Controlling the amount of crystals in reflection state is done by changing the irradiated sample volume, either by changing the primary beam diameter or the sample thickness; a further way to adjust the number of reflections in a diffraction ring is discussed below. In case of powders an additional option is available; the powder can be diluted by adding an amorphous material (like starch). To capture the complete integrated intensity from each spot the sample is turned stepwise around the φ axis. For each sweep step an image is taken. The chosen step size should be at least a tenth of the FWHM of the rocking curve in

orientations perpendicular to the rotation axis. In the present case a step size of 0.025° in φ rotation is used. The total rotation range is normally chosen to be between 2 and 10°. In case of a low number of observations a larger total rotation range can be used to increase crystallite sampling statistics. Performing such a rotation step measurement has two main advantages: 1st the complete, integrated intensity of each refection is available and 2nd the rocking curve can be evaluated (see Figure App. C-1) for its completeness (cut off in the beginning and at the end of a rotation measurement) and for possible peak overlap, either on the single frame (γ and θ direction) or on adjacent images (φ direction).

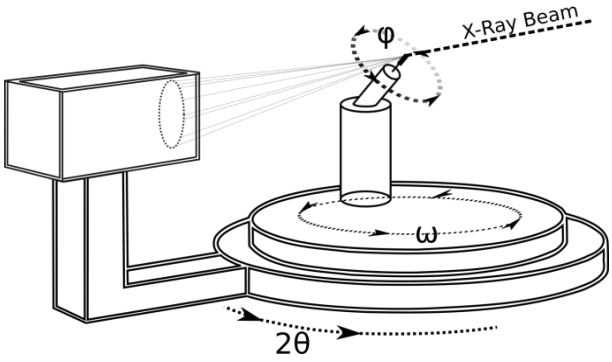

Figure 3.3: Schematic of four-circle Eulerian goniometer.

3.2.3 Data reduction

The data reduction, the intensity scaling and the subsequent CSD calculation is all performed with a newly developed software packager "fxd_csd" written in Python. Since the FXD-CSD analysis is a reference-based method, the data reduction always includes two sets of images which are measured under the same or at least very similar conditions. The following steps are individually performed on both sets and on each chosen *hkl* ring. Up to the S1 intensity scaling, both sample and reference data are treated as similar as possible.

First step

Selection of the area of interest for each chosen *hkl* ring; it is defined by ring radius, ring width and the area where the background intensity is determined (Figure 3.2 and Figure 3.4 left). The background area can be a smaller or bigger adjacent ring on the image or set to a fixed intensity value. The background will be used as threshold and applied on the area of interest to separate signal from background. Multiplied by a threshold-multiplier, the threshold can be adjusted. The threshold operation is therefore γ, θ and φ dependent. This is performed for each ring in each frame.

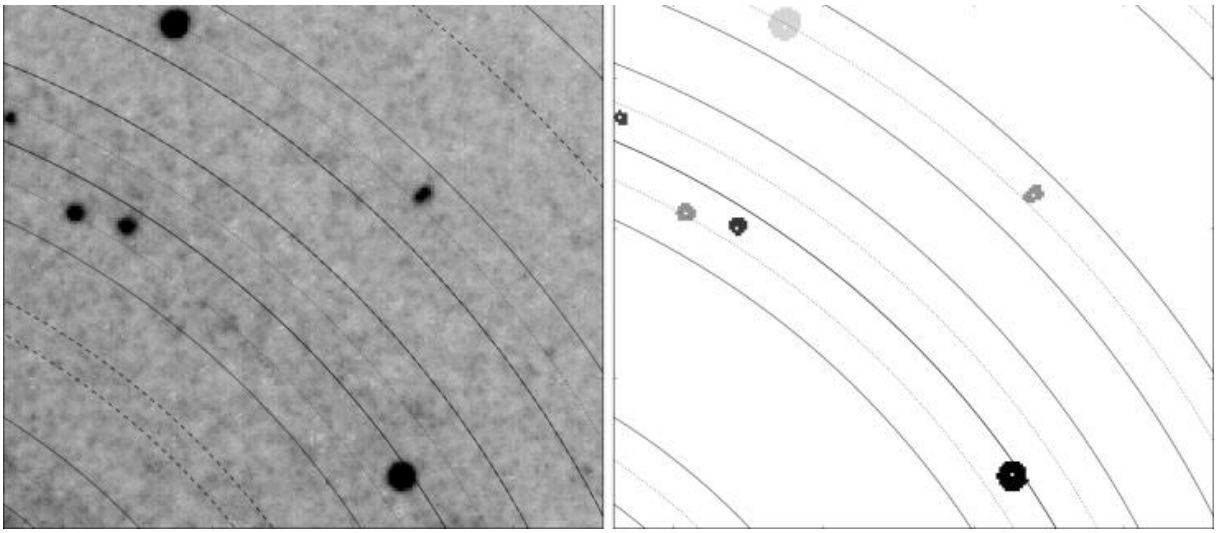

Figure 3.4: Left: Spotty diffraction pattern with "area of interest" enclosed by solid circles. Gray lines are the theoretical positions of the considered diffraction rings. Dashed lines delimit the used area for background-estimates. The inner border of the background is the corresponding area of interest. Right: detected objects with corresponding label to address each spot individually.

Second step

The resulting, cropped data is copied in a three-dimensional array having the frame size in pixel as 1st and 2nd dimension and the image number as 3rd dimension. The image number corresponds to the φ rotation. Subsequently an object detection algorithm is recording each non-zero voxel volume what is separated from others or the array edges as one object and is labelled (Figure 3.4 right). This step is allocating the discrete intensity information of the diffraction spots in each consecutive frame they occur. In case of multiple intensity maxima within one object a three-dimensional watersheding is performed (Vincent & Soille, 1991). Summing up the intensity of each object in the 1st and 2nd array direction reveals the rocking-curve along the 3rd direction; see Figure App. C-1 in the Appendix C.

Third step

The rocking-curve is tested whether it has one maximum and two minima, and the total integrated intensity is obtained by summing the values along the 3rd direction. Now the raw integrated intensities and their detector position information (crystal orientation) of several thousand observations are available.

3.3 Experimental

The analyzed alumina substrate samples are taken from a former study of Böcker (1994; 1994) incorporated in a project funded by the Federal Ministry of Education and Research (BMBF) (Böcker, 1994; Böcker *et al.*, 1994, 1995). Research subject was the texture development in different α-alumina ($R\bar{3}c$) substrate ceramics (circuit carrier ceramics) produced from the manufacturer CeramTech. Böcker examined the influence of different manufacturing steps prior to sintering on texture development: batching, milling and forming. In the forming process different binder substances had been tested. In a subsequent step the influence of the sintering time had been investigated. All samples had been taken out of the running production. The raw material had been ball-milled with water and spray-dried. Afterwards the obtained powder had been dispersed in a mixture of trichlorethylen, ethanol and fish oil and later had been bounded with polyvinylbutyral for the tape casting (Böcker *et al.*, 1995). In the present work one set of these samples with different annealing times was analyzed

with our novel FXD-CSD method. The four samples had been sintered at 1600° C for 4, 8, 16, and 24 hours in a conventional lab furnace. Böcker *et al.* (1994; 1994; 1995) report a rather strong texture development. During sintering a (001) fiber texture is evolving with a preferred orientation perpendicular to the basal plane of the substrate (Böcker *et al.*, 1994; Böcker, 1994; Böcker *et al.*, 1995). In general, strongly textured materials can affect FXD-CSD measurements in a negative way. Crystals with preferred orientations will diffract at similar sample orientations, thus the diffracted x-rays radiation will be more difficult to disentangle on the detector. The present fiber texture on the other hand is favorable for a uniform spot arrangement on the detector because only the (006) reflection is affected. All other *hkl* planes show no preferred orientation because the fiber is axial symmetric (see discussion further below). To support the FXD-CSD results, SEM imaging and EBSD (measured on FEI Quanta 200 FEG) orientation measurements of the sample surface are carried out. On the surfaces the averaged grain size is determined *via* the line intersection method (Underwood, 1970); assuming a spherical grain shape model (German, 2010). For the FXD-CSD measurements the ceramic plates were grinded to a thickness of approximately 500 µm. The grinding is done until the diffraction spot density is in a suitable range (see Section 3.2.2). The sweep-rotation measurements are carried out for all samples and the reference material. A Bruker AXS D8 DISCOVER diffractometer with fixed χ-angle, equipped with a Bruker AXS SMART Apex II detector is used. The used source is a molybdenum X-ray tube (Mo-K_α, λ= 0.71073 Å) with a 0.5 mm collimator. The samples are measured over a rotation angle of 6° in φ with a sweep step size of 0.025°, giving a total number of 240 single frames. The exposure time of each frame is 60 sec. As reference material a carefully prepared single crystalline corundum powder with a narrow and precisely known CSD is used. The grain size fraction was separated *via* sedimentation in water and characterized with SEM imagery. The reference powder is diluted with starch and prepared in a 0.8mm Kapton™ capillary. The reference is measured over a rotation angle of 10° in φ with a sweep step size of 0.025°, resulting in 400 single frames.

3.4 Results

3.4.1 Reference measurement

To determine the S1 scaling factor the reference powder is studied by X-ray diffraction; Figure 3.2 shows an example frame from the sample sweep. For the FXD-CSD measurements the three strongest *hkl* families ({113}, {024}, {116}) were selected and analyzed. The three resulting intensity distributions (ID) are scaled to the structure factor of the {116} *hkl*-family. The histograms are subsequently summed together and treated as one dataset. The S1 determination is shown in Figure 3.5. A Gaussian probability density function (PDF) is fitted to both, the reference ID and the reference volume CSD derived from the SEM imagery. The used scaling factor is 19.111 ln(nm³/counts), calculated from the fitting parameters.

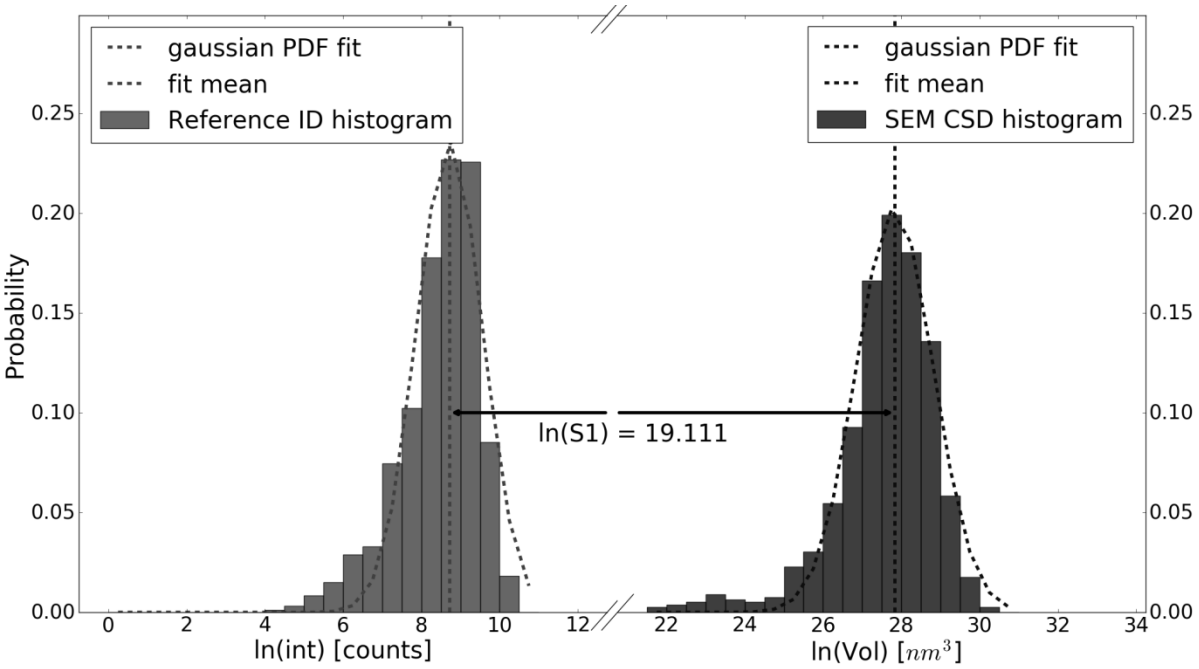

Figure 3.5: S1 scaling factor determination. Probability vs. intensity [counts] in light gray from the diffraction measurement and respectively the probability vs. crystal volume [nm³] from the SEM measurements in dark gray on a log-scale. The mean values from the Gaussian PDF fit are ln(8.79) [counts] and ln(27.83). The χ^2-value of the ID fit is 0.0055 and the one of the volume CSD is 0.0014.

3.4.2 Substrate microstructure

The electron micrographs in Figure 3.6 show in a) a homogenous crystal size distribution and from b) to d) increasing grain size and the appearance of grains bigger than the average crystal size. Numerous single spot EBSD orientation measurements within the connected areas prove them to be single crystals (see also Figure App. C-2 in Appendix C). Unfortunately, the rough sample surface prohibits automated orientation mappings. The observation of significantly bigger crystals than average provides evidence for abnormal grain growth (AGG).

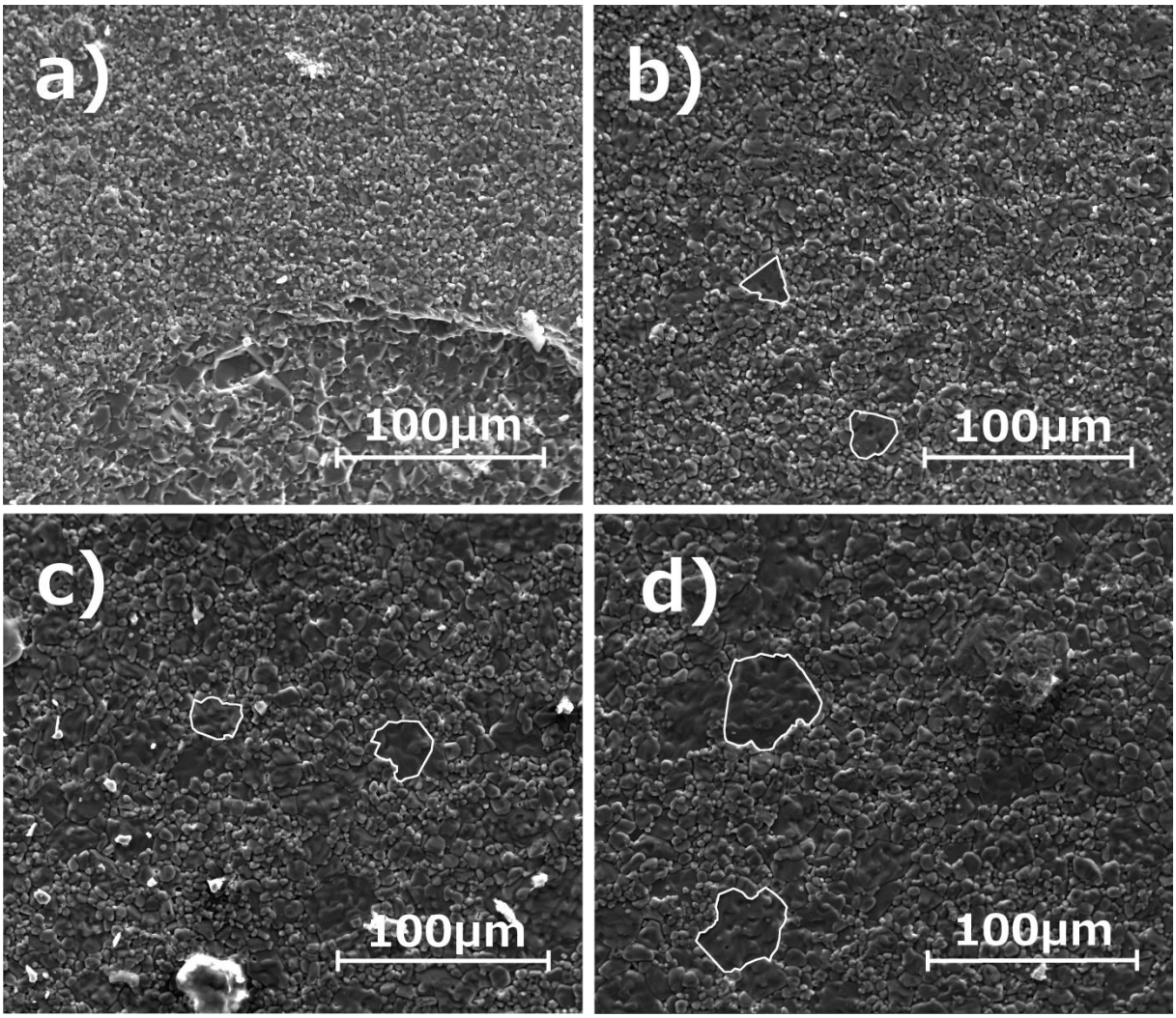

Figure 3.6: SEM images from all four samples. a) 4h, b) 8h, c) 16h, and d) 24h. Shown are the un-grinded surfaces. The 4h sample shows a chipped off area[11] in the lower left part of the image a). In the images b-d) some grains bigger than the average are highlighted by white borders. On areas like this EBSD measurements have been carried out to verify whether these connected areas are single crystalline (see Appendix C 1).

Example frames from the FXD-CSD measurements of each sample are shown in Figure 3.7. All Samples show spotty diffraction patterns with no apparent preferred orientation because of the mentioned (001) fiber texture. It can be observed that the spot intensities are becoming bigger from a) to d). There is a notable change from a) to b) and a clear increase between b) and c). From c) to d) no clear difference can be recognized. For the diffraction analysis the *hkl* families {024} and {116} are used; the {113} is left out to avoid accidental peak overlap because the ring is quite crowded. The resulting IDs are, according to their structure factors, scaled to the {116} *hkl* family and scaled with S1.

[11] LIM on chipped off areas show bigger grain sizes.

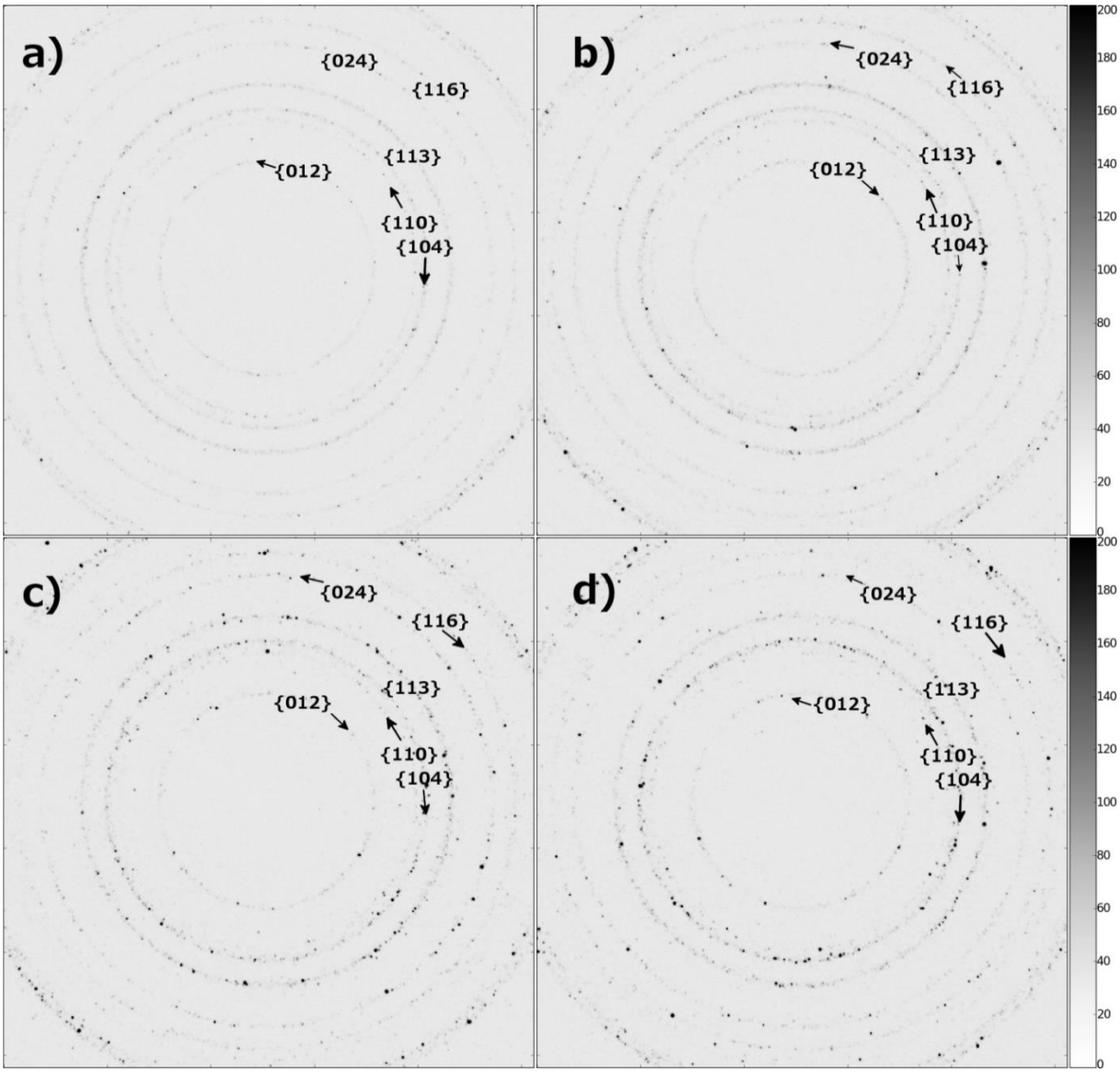

Figure 3.7: Spotty diffraction patterns (single frames) from all four samples. a) 4h, b) 8h, c) 16h, d) 24h. Grayscale represents the intensity.

The CSDs obtained from the FXD-CSD method are shown in Figure 3.8 and Figure 3.9. Log-normal probability density functions (PDFs), Weibull PDFs and Gamma PDFs are fitted to the midpoints of the histogram bars. The fitted parameters and the χ^2-values ($\sum_i^N [Resid_i]^2$), as a measure of the goodness of fit are available in the Appendix C 2. The numerical values and the visual impression show that the log-normal PDF is the best fitting model. Figure 3.10 shows all four log-normal PDF fits in one graph; here coarsening and increasing skewness is most evident. Table 2.1 shows the average crystal size and the distribution skewness obtained from the log-normal PDF fits (fitting done in linear space). The results of the line intersection measurements (LIM) are listed as well. The values obtained with the FXD-CSD measurements are partly in good agreement with the results of the LIMs. Only the values of the two samples with the shorter sintering time differ. In both cases the mean grain size is increasing faster at the beginning of the heat treatment.

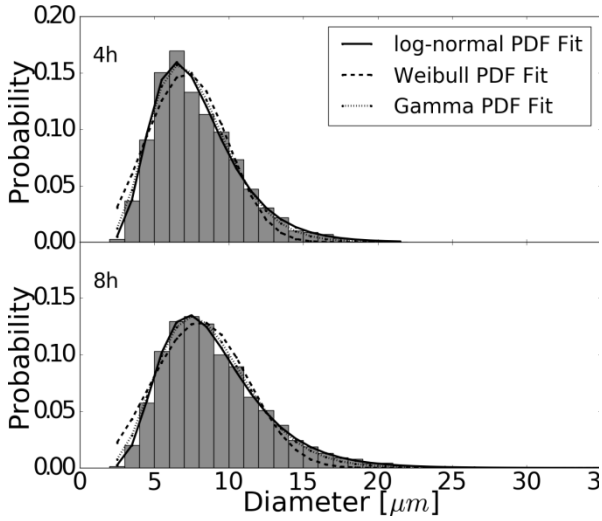

Figure 3.8: Diameter CSDs of the 4h and 8h sample derived from the volume distribution, measured with the FXD-CSD method. With fitted log-normal PDF, Weibull PDF and Gamma PDF.

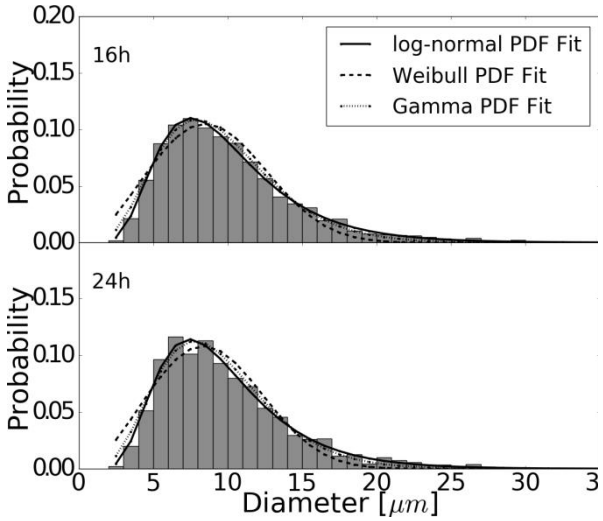

Figure 3.9: Diameter CSDs of the 16h and 24h sample derived from the volume distribution, measured with the FXD-CSD method. With fitted log-normal PDF, Weibull PDF and Gamma PDF.

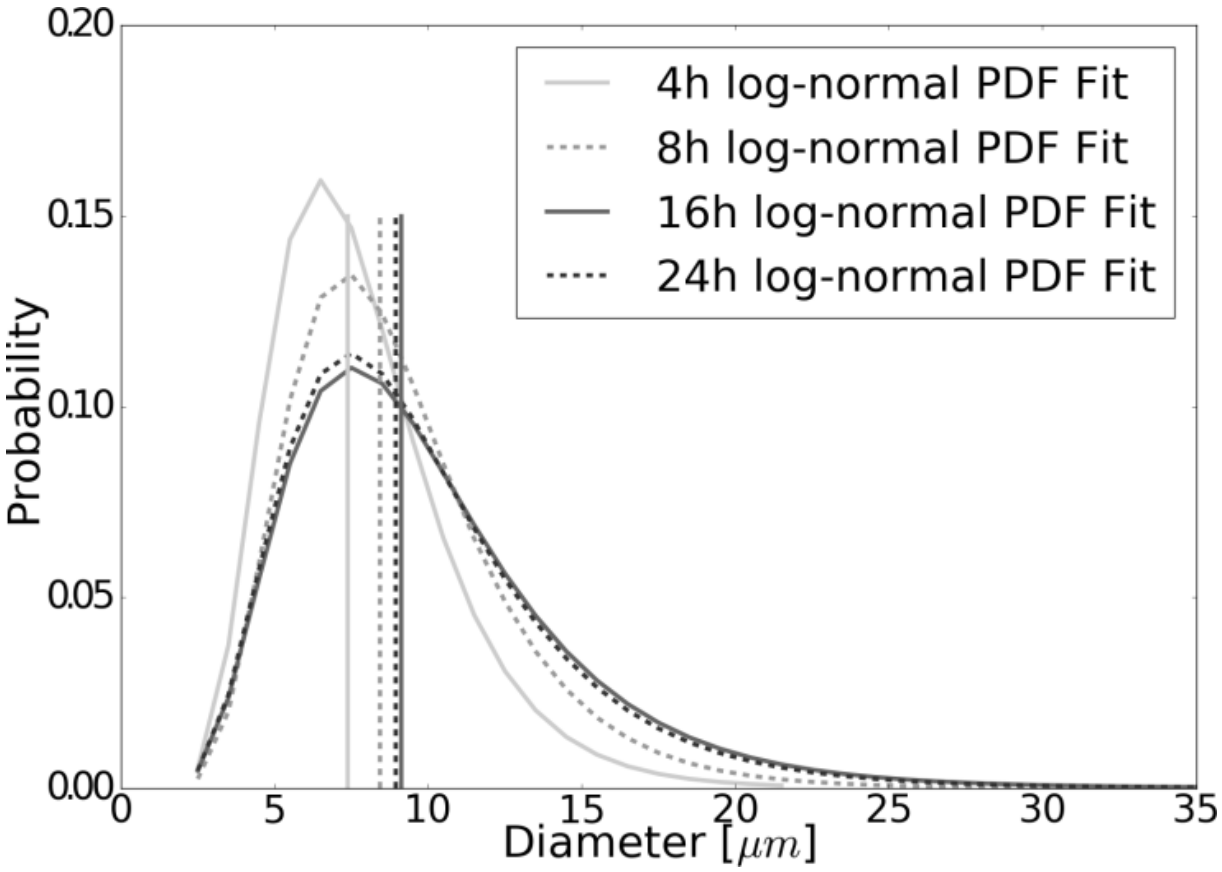

Figure 3.10: Fitted log-normal PDFs of all four samples with location of mean values (vertical lines).

Table 3.1: Evolution of mean grain size and CSD skewness[1]

	Line intersection method[2] (Underwood, 1970; German, 2010)		FXD-CSD		
Sintering Time	**N**	**Mean diameter[2]**	**N**	**Mean[3] diameter from log-normal fit[2]**	**Skewness[1] from log-normal PDF fit**
4h	495	5.0 µm +-0.2[4]	1994	7.89 +-0.13 µm	1.17
8h	531	6.2 µm +-0.3	4001	9.04 +- 0.08 µm	1.23
16h	558	8.8 µm +- 0.4	4182	10.03 +-0.11 µm	1.47
24h	543	9.1 µm +- 0.4	3557	9.80 +-0.14 µm	1.44

[1]Skewness: measure of asymmetry, defined as $\left(e^{\sigma^2}+2\right)\sqrt{e^{\sigma^2}-1}$. [2]Mean grain diameter G, with the assumption of spherical crystals. If G is the true grain size, the measured random intercept size L_R is assumed to be: $L_R = 2/3$ G. [3]Mean diameter (1st arithmetic moment E) calculated from the fitting parameter µ and σ. $E(x) = e^{\mu+0.5\sigma^2}$ [4] $1/\sqrt{N}$

3.5 Discussion

In the context of introducing the new FXD-CSD method we obtained the first X-ray diffraction volume-derived grain size distributions of alumina substrate ceramics and its evolution over time; a number of issues merit some further discussion, based on the observed CSDs.

3.5.1 Abnormal grain growth

The line-intersection method (LIM-) based surface observations and the volume-based FXD-CSD measurements both indicate the presence of AGG; this is apparent from the observation of abnormally large crystallites in the electron microscopic images and from the increasing skewness of the CSDs. This finding is in very good agreement with literature dealing with alumina ceramics of commercial grade purity (Nettleship *et al.*, 2002; Park & Yoon, 2000, 2002; German, 2010), yet provides for the first time means of a quantification of this effect in terms of the skewness of the distribution A reliable determination of the skewness can only be made when the sampling comprises a large number of crystallites; such good sampling statistics are available in the FXD-CSD method.

3.5.2 Average grain size: FXD-CSD vs LIM

The results of the two different measurement techniques are generally in good agreement with each other. Only the data of the 4h and 8h samples in the early phase of the sintering process show deviations in the mean grain-size, with smaller values obtained from the line-intersection method. The most likely reason for this discrepancy is that the sample surface is not representative for the entire sample volume; especially in the beginning of sintering it is likely that material is transported from the surface deeper into the bulk, towards lesser exposed positions like the necks of the pore-network. This leads to a possible shrinking of crystals at the surface or at least to a slower growth compared to the crystals in the volume. Surface effects can aggravate a general sampling issue when using the LIM. Sampling with LIM to the same numbers as easily obtained by FXD-CSD would request considerable additional efforts (see Table 3.1). For average grain size determination, the usual sampling procedures of LIM might well be sufficient; yet if reliable CSDs are needed the FXD-CSD method delivers better results with considerably less effort.

3.5.3 Grain size distribution function

Changing CSDs reflect in a concise manner the evolution of the microstructure during coarsening processes, like NGG and AGG. Details of these processes, their driving forces and rate-limiting steps are likely to be reflected in differences in the observed CSD; indeed, differences emerge from different models suggested for coarsening as discussed in the Introduction. Observed CSDs can be compared to predicted (or approximated) mathematical functions and permit a rigorous, quantitative check of coarsening models; there is a multitude of such functions which are under ongoing debate (e.g. (Nettleship *et al.*, 2002)). Log-normal probability density functions (PDF) CSDs are reported to fit best to commercial grade purity alumina ceramics (Nettleship *et al.*, 2002; Park & Yoon, 2000). In this work three different mathematical forms of CSDs are tested of which indeed the log-normal CSD fits best. Discriminating which model is best, is not always easy. The used χ^2-test helps, but is not independent from the sampling statistic and does not regard the number of function parameters (Stamatis, 2003).

Several attempts to link grain growth mechanisms to the resulting microstructure can be found in literature (Introna & Wood, 2004; Hillert, 1965*b*; Feltham, 1969; Anderson *et al.*, 1989). Most interesting here is the work of Anderson *et al.* (1989) who did three dimensional normal grain growth computer simulations and compared size distributions obtained from linear intersects, from cross-section areas and from the crystal volumes. The most important finding is that the three resulting CSDs are different from each other and that the log-normal distribution fits best when the CSD is volume information base (Anderson *et al.*, 1989). That different methods show different distributions has been demonstrated (Zöllner & Streitenberger, 2004; Takayama *et al.*, 1992). Volume-based CSDs are the least affected by systematic errors (and their attempted corrections) and represent the best choice (Anderson *et al.*, 1989): Comparing the crystal volume with a crystal section area or crystal diameter, only the volume is shape independent. LIM-derived CSD data always includes a general grain shape assumption (German, 2010). When the CSD is not uniform and grains have anisotropic shapes this leads inevitable to uncertainties. Looking at processes during microstructure evolution in polycrystalline materials is closely related to the changing grain boundary network and interfacial energy. Even though FXD-CSD does not provide any grain shape information, a volume base CSD allows a considerably more precise estimate on these two quantities, as long as the grain shapes are not too anisotropic (German, 2010). Finally it should be mentioned that physical properties are depending on the actual CSDs and efforts are presently been made to predict their CSD-dependency; an example is the CSD-dependency of yield strength *via* a generalized Hall-Petch relation (Kurzydeowski & Bucki, 1993; Berbenni *et al.*, 2007*b*).

3.5.4 Advantages and limitations of FXD-CSD

FXD-CSD enables the user to measure volume-based CSDs with unprecedented counting statistics within several hours with standard laboratory X-ray equipment, which exceeds the usually achieved number of data entries easily by 1-2 orders of magnitude. The lower limit of detection (LLOD) with the described equipment is ~ 1 µm. The LLOD is depending mainly on the brilliance (low angular divergence, high wavelength precision) of the X-ray source, the diffraction power of the atoms forming the crystals and the sensitivity of the detector. The LLOD at synchrotron facilities is much smaller because of their superior brilliance. Recent synchrotron measurements of our group on gas hydrates revealed a LLOD of ~ 500 nm for CH_4-hydrate, with a single frame exposure time of 15s (Chaouachi *et al.*, 2017). Compared to corundum, CH_4-hydrate is quite weak scatters (approx. 6 times lower). This means that a strong scattering material like corundum offers opportunism large additional range of

fact. The LLOD on a synchrotron source reaches sizes typical for nanomaterials and thus reach their natural limits due to an increasing particle-size broadening of the reflections. For materials in the µm-size the exposure times can be much reduced on a synchrotron source (less than a second per frame) thus enabling *in situ* measurements of coarsening at elevated temperatures with a time-resolution of several minutes. The upper limit of detection (ULOD) is mainly determined by the dimensions of the primary beam; obviously the crystals have to be significantly smaller than the primary beam diameter, which typically is in the order of 0.5. to 1 mm for laboratory sources.

As mentioned above, the LLOD for synchrotron sources reaches sizes typical for nanomaterials. FXD CSD can therefore be considered as a seamless connection towards larger crystallite sizes (when synchrotron data are available to the well-known line broadening method introduced by Scherrer (1918).

FXD-CSD provides, however, no grain shape information and can reach its LLOD much earlier when preferred crystal orientations are strongly pronounced. Crystals with a similar orientation in strongly textured materials will diffract at similar sample orientations, thus the diffracted x-rays radiation will be more difficult to disentangle on the detector. Concerning the investigated alumina specimens the reported (Böcker *et al.*, 1994; Böcker, 1994; Böcker *et al.*, 1995) axial symmetric preferred (001) fiber orientation perpendicular to the basal plan of the specimen does not affect the FXD CSD measurements. On the contrary, an axial symmetric texture can be favorable for a homogenous spot arrangement on lattice plans inclined to the rotation axis. This type of texture is only evident on a basal lattice plane parallel to the substrate surface. In alumina this is only the (006) reflection which has a very small structure factor (|F|~13) and a low multiplicity (M =2). The (006) reflection is therefore hard to detect.

3.6 Conclusions

The data presented show that our new FXD-CSD method is capable of determining volume-based crystal size distribution (CSD) of polycrystalline materials and crystalline powders. The sampling statistics exceeds the conventionally achieved numbers by an order of magnitude. The microstructural evolution of four alumina substrates with different lengths of sintering (4h, 8h, 16h, and 24h @ 1600°C) is investigated *via* FXD-CSD and SEM imaging. Their CSDs and average grain sizes are determined and clear evidence for the presence of abnormal grain growth (AGG) during sintering is shown. From three tested probability density functions (PDF) the log-normal PDF fits best to the volume based CSDs.

In principle the FXD-CSD method is destruction-free and even allows for studies of samples enclosed in complex environments e.g. for *in situ* measurements in a furnace or in pressure cell. Data sets collected with FXD-CSD usually have exhaustive sampling statistics and, if really needed, the data-sets could easily be extended by additional measurements at different sample positions. Such excellent sampling statistics provides the basis for further detailed studies of the evolution of CSDs during coarsening processes, their modelling and theoretical understanding, which could help eventually to a better control of physical properties of the materials under study.

In summary FXD-CSD is a fast, generally applicable method to investigate the microstructure and its evolution for polycrystalline materials as well as powders; on the basis of the accurate and precise CSDs fundamental research questions concerning their origin and evolution can now be addressed. Furthermore, not only coarsening processes can be studied with our method, it is also well suitable for

a quantitative characterization of crystal growth and re-growth in mass crystallization processes (Chaouachi *et al.*, 2017).

3.7 Literature

Abbruzzese, G. & Lücke, K. (1986). *Acta Metall.* **34**, 905–914.

Als-Nielsen, J. & McMorrow, D. (2011). Elements of Modern X-ray Physics Hoboken: John Wiley & Sons, Inc.

Anderson, M. P., Grest, G. S. & Srolovitz, D. J. (1989). *Philos. Mag. B Phys. Condens. Matter; Stat. Mech. Electron. Opt. Magn. Prop.* **59**, 293–329.

Apetz, R. & Bruggen, M. P. B. (2003). *J. Am. Ceram. Soc.* **86**, 480–486.

Bae, S. I. & Baik, S. (1993). *J. Mater. Sci.* **28**, 4197–4204.

Berbenni, S., Favier, V. & Berveiller, M. (2007). *Comput. Mater. Sci.* **39**, 96–105.

Böcker, A. (1994). Einfluß von Material und Verarbeitung auf die Texturbildung in Al2O3-Substraten. PhD. Thesis. Technische Universität Clausthal.

Böcker, A., Bunge, H. J., Huber, J. & Krahn, W. (1994). *J. Eur. Ceram. Soc.* **14**, 283–293.

Böcker, A., Bunge, H. J., Huber, J., Krahn, W. & Ruska, J. (1995). *Textures Microstruct.* **24**, 167–197.

Brook, R. J. (1969). *J. Am. Ceram. Soc.* **52**, 56–57.

Bunge, H. J. & Dahlem-Klein, E. (1992). *Modeling of Coarsening and Grain Growth*, Vol. edited by S.P. Marsh & C.S. Pande, pp. 133–143. Warrendale, Pennsylvania: TMS.

Carniglia, S. C. (1972). *J. Am. Ceram. Soc.* **55**, 243–249.

Carter, C. B. & Norton, M. G. (2013). Ceramic Materials New York: Springer New York.

Chantikul, P., Bennison, S. J. & Lawn, B. R. (1990). *J. Am. Ceram. Soc.* **73**, 2419–2427.

Chaouachi, M., Neher, S. H., Falenty, A. & Kuhs, W. F. (2017). *Cryst. Growth Des.* **17**, 2458–2472.

Chappell, J. S., Ring, T. A. & Birchall, J. D. (1986). *J. Appl. Phys.* **60**, 383–391.

Coble, R. L. (1961). *J. Appl. Phys.* **32**, 787–792.

Dillon, S. J., Tang, M., Carter, W. C. & Harmer, M. P. (2007). *Acta Mater.* **55**, 6208–6218.

Feltham, P. (1969). *Scr. Metall.* **3**, 853–854.

German, R. M. (2010). *Crit. Rev. Solid State Mater. Sci.* **35**, 263–305.

He, B. B. (2011). Method for measuring crystallite size with a two-dimensional X-ray diffractometer US Patent No. 7885383. Washington, DC: US Patent and Trademark Office.

Hillert, M. (1965). *Acta Metall.* **13**, 227–238.

Hirsch, P. B. & Kellar, J. N. (1952). *Acta Crystallogr.* **5**, 162–167.

Ida, T., Goto, T. & Hibino, H. (2009). *J. Appl. Crystallogr.* **42**, 597–606.

Introna, L. D. & Wood, D. (2004). *Surveill. Soc.* **2**, 177–198.

Kingery, W. D. & Berg, M. (1955). *J. Appl. Phys.* **26**, 1205–1212.

Knudsen, F. P. (1959). *J. Am. Ceram. Soc.* **42**, 376–387.

Krell, A., Blank, P., Ma, H., Hutzler, T., Bruggen, M. P. B. van & Apetz, R. (2003). *J. Am. Ceram. Soc.* **86**, 12–18.

Kruzic, J. J., Satet, R. L., Hoffmann, M. J., Cannon, R. M. & Ritchie, R. O. (2008). *J. Am. Ceram. Soc.* **91**, 1986–1994.

Kurzydeowski, K. J. & Bucki, J. J. (1993). *Mater. Sci.* **41**, 3141–3146.

Nettleship, I., McAfee, R. J. & Slaughter, W. S. (2002). *J. Am. Ceram. Soc.* **85**, 1954–1960.

Nichols, F. A. (1966). *J. Appl. Phys.* **37**, 4599–4602.

Novikov, V. I. U. (2000). Grain Growth and Control of Microstructure and Texture in Polycrystalline Materials Boca Raton: CRC Press.

Orowan, E. (1933). *Zeitschrift für Phys.* **86**, 195–213.

Park, C. W. & Yoon, D. Y. (2000). *J. Am. Ceram. Soc.* **83**, 2605–2609.

Park, C. W. & Yoon, D. Y. (2002). *J. Am. Ceram. Soc.* **85**, 1585–1593.

Petch, N. J. (1953). *J. Iron Steel Inst.* **174**, 25–28.

Petzold, A., Ulbricht, J. (1991). Aluminiumoxid (Aluminium oxide) Leipzig: Deutscher Verlag für Grundstoffindustrie.

Rodriguez-Navarro, A. B., Alvarez-Lloret, P., Ortega-Huertas, M. & Rodriguez-Gallego, M. (2006). *J. Am. Ceram. Soc.* **89**, 2233–2238.

Saltykov, S. A. (1975). Stereometrische Metallographie Leipzig: VEB Deutscher Verlag für Grundstoffindustrie.

Scherrer, P. (1918). *Nachrichten von der Gesellschaft der Wissenschaften du Göttingen, Math.-Phys. Klasse*. **1918**, 98–100.

Stamatis, D. H. (2003). Six Sigma and Beyond, Design for Experiments Boca Raton: CRC Press.

Takayama, Y., Tozawa, T., Kato, H., Furushiro, N. & Hori, S. (1992). *Mater. Sci. Forum*. **94–96**, 325–330.

Underwood, E. E. (1970). Quantitative stereology Reading: Addison-Wesley Publisching Company, Inc.

Vincent, L. & Soille, P. (1991). *IEEE Trans. Pattern Anal. Mach. Intell.* **13**, 583–598.

Yousef, S. G., Rödel, J., Fuller, E. R., Zimmermann, A. & El-Dasher, B. S. (2005). *J. Am. Ceram. Soc.* **88**, 2809–2816.

Zöllner, D. & Streitenberger, P. (2004). *Mater. Sci. Forum*. **467–470**, 1129–1136.

Chapter 4 Publication - Time Resolved Coarsening of Clathrate Crystals: The Case of Gas Hydrates

Journal

Crystal Growth & Design 2017; 17:2458-2472
https://doi.org/10.1021/acs.cgd.6b01875

Authors
Marwen Chaouachi[1], Sigmund H. Neher[1], Andrzej Falenty[1], Werner F. Kuhs*[1]

[1]GZG Abt. Kristallographie, Georg-August-Universität Göttingen, 37077 Göttingen, Germany

Abstract

A new fast diffraction-based method for the determination of crystallite size distributions (CSDs) is presented. The method is destruction-free, applicable to *in situ* and *ex situ* studies and allows for a determination of the crystallites' volumes in powders or polycrystalline aggregates with excellent sampling statistics. The method is applied to the formation and coarsening of gas hydrates (GH) in a sedimentary matrix; both Xe-hydrates and CH_4-hydrates were investigated in a time range from 2 minutes to 6 weeks. The GH crystallites have a size of a few µm when formed, followed by a coarsening process which mainly takes place at the surface of GH aggregates. Important conclusions can be drawn from the time-dependent analysis of CSDs: (1) Coarsening by normal grain growth proceeds several orders of magnitude slower than in normal ice at similar temperatures; this points to very slow grain boundary migration rates seemingly related to the complexity of topological reconstruction of the crystalline network across a disordered grain boundary. (2) The persisting small crystallites together with their known high resistance against deformation by dislocation motion must lead to grain size sensitive creep, most likely governed by grain boundary sliding. (3) The CSDs of GHs formed in the laboratory appear to have distinctly smaller sizes compared to natural GHs. In consequence, laboratory-based studies of GH can only be safely related to the natural situation once the mutual CSDs are characterized.

4.1 Introduction

Crystal size distributions (CSDs) is a fundamental property of crystalline assemblies that provides important insights into the formation mechanisms, driving forces as well as the balance between nucleation and growth rates; CSDs give the number distribution of binned crystal sizes in a sample volume [1]. A time-resolved evolution of crystal sizes taken beyond the initial crystallization also provides a unique opportunity to model the future properties of materials and trace back the initial conditions. This underlying process is generally called coarsening and is commonly realized *via* normal grain growth (NGG) [2, 3] and/or Ostwald ripening (OR) [4, 5]. While these dynamic, time-dependent processes have been frequently studied in simple materials like e.g. metals and ceramics [2, 3, 6] or water ices [7], there is a fundamental interest how the coarsening is realized in more complex, crystalline guest-host compounds where an effective growth of individual crystals [8] is expected to be more difficult. Model examples of guest-host structures are intermetallic clathrates [9], clathrasils [10, 11] or gas hydrates [12] where the expanded host lattice is stabilized by guest atoms. Within this large family of topologically similar guest-host structures the importance of CSDs and their coarsening is certainly well apparent for gas hydrates.

These peculiar crystalline inclusion compounds of hydrogen-bonded water cages enclosing small gas molecules gained much attention due to their role in flow assurance [13], and novel alternative technologies for e.g. heat storage [8] or gas separation [14] ; in all these cases crystal sizes play a pivotal role in physico-chemical properties of multiphase fluids, formation/dissolution kinetics and the ultimate efficiency of technological applications.

Gas hydrates are, nevertheless, most and foremost investigated as an alternative source of hydrocarbons locked in natural occurrences located worldwide in marine sediments and (sub-) permafrost regions [15]. Enclosing predominantly methane, natural gas hydrates (NGHs) are a target of intense geological and geophysical surveys, drillings and well-logging operations aiming at the identification and evaluation of natural deposits of this unconventional source of hydrocarbons [12, 15, 16]. As the quantification of these novel resources with remote sensing methods depends on preconceived petrophysical models [17, 18], a better understanding of CSDs and the coarsening process became also an important factor for the accuracy of these predictions. In the ideal scenario such data could be obtained by core sampling but due to the difficult recovery of unperturbed NGH specimens only a handful of observations could be made to date. Scanning electron microscopy (SEM) [19-21] and *ex situ* tomography [22] on cryo-preserved, presumably quite aged NGH samples have indeed provided the first valuable information on the size and variation of CSDs that spans from a few to a few hundred of µm. Similar results were provided also in later studies of CSDs of NGH from massive accumulations [23-25]. Although certainly very useful, these studies are still insufficient for a general representation of the many possible different environments.

To address this serious limitation numerous attempts were made to recreate the natural environment of GHs in sedimentary matrices in laboratory experiments e.g.[18, 26-39]. It quickly turned out that the preparation method and composition of the fluid phase have a profound impact on obtained size and morphology of crystals [40-44] thus affecting petro-physical properties and the from those deduced GH saturations [17]. Moreover, it has been demonstrated [45] that the local microstructures do not remain static in the course of formation experiments; this dynamic behavior has been related to changes in some petrophysical characteristics of GH-bearing sediments observed in laboratory experiments [46] . Yet, in spite of all various approaches freshly formed clathrate crystals sizes were consistently found

to not exceed a few tens of µm. This clear disagreement with much larger natural hydrates suggests a continuous evolution of CSDs by coarsening during and after the full transformation albeit virtually nothing is known on the p-T dependence, susceptibility to deformations and time constant for these processes.

The initial spread in crystal sizes could be explained by a combination of various nucleation and growth processes, e.g. the site-saturated or constant-nucleation case [47], or various other growth theories [48, 49] that produce characteristic CSDs. The subsequent coarsening could be realized *via* Ostwald ripening [4, 50] and/or normal grain growth [2, 3], both well-established, time dependent processes. In all cases the knowledge of the resulting CSDs alone would help improving predictions of petro-physical and transport properties, in particular the ones connected to the resulting grain-boundary networks [51]. Going one step further, establishing the time constants for the coarsening of hydrate crystals may have two possibly far-reaching consequences: (1) solving a fundamental question whether or not physical properties of freshly laboratory-prepared GH-sediment assemblies do really represent NGHs [45] and (2) paving a road to the long sought dating of formation ages of NGHs [52].

In the following we attempt to address the aforementioned issues with a novel non-destructive approach called fast X-ray Diffraction CSD (FXD-CSD) analysis. The method is used to follow nucleation/ growth processes in sedimentary matrices under *in situ* conditions and also applied to cryo-preserved samples measured *ex situ*. As a result we provide the first quantitative results on the time resolved evolution of CSDs in hydrates and discuss underlying growth mechanisms.

4.2 Fast X-ray diffraction CSD analysis

Investigations with our novel fast X-ray diffraction (FXD) technique give access to CSDs of 3D-accumulations of pure GHs and those dispersed within mineral networks that are sufficiently transparent to an X-ray beam, both for isolated single crystals and polycrystalline aggregates. Our method is a major improvement of a suggestion to determine mean crystal sizes *via* diffraction intensities made by Rodriguez Navarro, et al. [53] allowing now for a flexible and quantitative CSD determination with applications far beyond GHs. Measurements can be performed with any powder diffraction setup in Debye-Scherrer geometry that is equipped with a position sensitive two-dimensional detector (Figure 4.1). When the illuminated sample volume – controlled by the chosen beam size - is sufficiently small, only a limited number of crystals are illuminated and a discontinuous, "spotty" diffraction pattern is formed. Each crystal that fulfils the Bragg condition produces a diffraction spot with an intensity that can be later related to its size. The method does not need any special sample preparation or the knowledge of the irradiated volume and does neither depend on the aggregation state (powder or polycrystal) nor on the mineralogical composition of the material as long as the Debye-Scherrer rings do not overlap. Moreover, a single measurement typically delivers CSDs over populations of several hundred individual crystals. The resolution and measurement time of FXD-CSD will depend on the characteristics of the sample and the hardware used. For instance, weaker and divergent X-ray lab sources are likely to provide less accurate results than brilliant and well defined parallel synchrotron beams. Consequently, the lower detection limit may vary from a few hundred nm to several µm and the measurement time can extend from several minutes to a few hours. To bring more crystals into diffraction condition, the sample is rotated stepwise for few degrees (typically ~ 2 to 5 deg) around the rotation axis ω. The step size is chosen to be ~ 0.001- 0.005 deg; a typical FXD-CSD image stack may contain several hundred 2D frames. Each diffraction spot on the frames is detected and allocated with its occurrence in the neighboring frames. If the individual diffraction peak

is measured in a complete rocking curve, three angular coordinates θ, ω and γ can be assigned to its center. Hence, the analysis of the diffraction frames permits to plot the intensity profile of the fully recorded diffraction spot (i.e. the rocking curve) and to extract the diffracted intensity by integration over this rocking curve. The CSDs in our work are defined simply by the number occurrence of crystals of different sizes (usually binned together for a certain size range) in a given volume which is defined by the part of the sample hit by the X-ray beam. It should be noted that not all crystallites present in the irradiated volume are counted, as not all crystallites are brought into reflection condition due to the limited ω-rotation. However, a statistically representative sub-set is investigated with many hundreds or even thousands of observations.

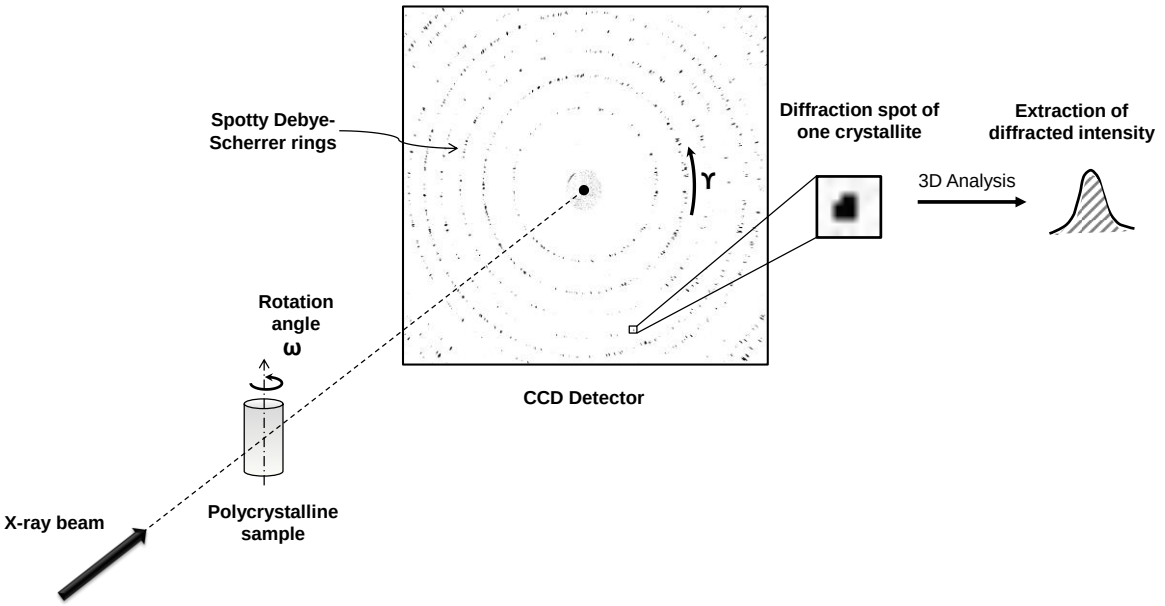

Figure 4.1: Sketch of the X-ray diffraction setup for fast CSD analysis (FXD-CSD). The diffraction of polycrystalline materials produces concentric Debye–Scherrer rings. Using a small beam size, a spotty diffraction pattern is obtained. Each diffraction spot results from the diffraction of one crystallite. Each diffraction peak is defined by the coordinates *Θ*, *ω*, and *γ*, where *γ* is the azimuthal angle along the Debye–Scherrer ring. The collection of the intensity information from all frames permits plotting of the intensity profile of each crystal or spot and to extract the diffracted intensity that corresponds to the area below the rocking curve.

The FXD-CSD method is based on the kinematic diffraction theory of crystals where the intensity diffracted by a crystal is proportional to its irradiated volume [54]; the intensity distribution (ID) of Bragg reflections is assumed to originate from individual crystals and is proportional to the distribution of single crystal volumes *V*. The method requires a calibration with a standard material with known CSD. Having measured the ID for a specific *hkl* plane (I_{hkl}) of the reference material, it is possible to determine a scaling factor called S_1 (which is specific to the diffractometer setup) between the CSD and the measured intensity:

$$V = S_1 \times I_{hkl}$$

An ideal reference material should be a powder composed of single-crystalline isometric/spherical particles with a known and fairly narrow size distribution (measured with e.g. scanning electron microscopy or laser granulometry). Preferentially the chosen calibrant should possess a high crystallographic symmetry and good scattering properties to enable well-separated Debye-Scherrer cones with high count rates (related to the respective structure factors).

As the investigated material and the calibrant usually will have different crystal structures, intensities must be normalized to the structure factor and unit cell volume by establishing the scale factor S_2. The kinematical theory states that the diffracted intensity per unit volume is proportional to the structure factor squared and inversely proportional to the unit cell volume. Hence:

$$I_{hkl} \propto \frac{\left|F^2\right|_{hkl}}{V_c}$$

The scale factor S_2 for each *hkl* is then calculated as follow:

$$S_2\,(hkl) = \frac{I_{calibrant}}{I_{material}} = \frac{\left(\left|F^2\right|_{hkl}/V_c\right)_{calibrant}}{\left(\left|F^2\right|_{hkl}/V_c\right)_{material}}$$

where is the structure factor and V_c is the unit cell volume.

With the scale factors S_1 and S_2 one can proceed to calculate the CSDs of the material of interest from the individually measured reflection intensities I_{hkl} using the following formula for each entry

$$D = \sqrt[3]{\frac{6 \times I \times S_2 \times S_1}{\pi}}$$

The second scale factor is of course not necessary if the user has measured a size-calibrated sample of the material under investigation. It is important to emphasize that our method only requires (but strictly so) that the intensity measurements of reference material and of the material of interest are made under identical conditions. Moreover, the selection of Bragg reflections of interest for each phase or material should be done considering their structure factor and multiplicity to get sufficiently strong and well separated observations. Reflections with too small a structure factor, coming from crystals on the low side of the CSD, may not be detected and lead to CSDs biased towards larger sizes. Bragg reflections with high multiplicities have a higher probability to be affected by peak overlap that cannot be resolved by the image analysis software and hence may also bias the results towards larger crystal sizes. Therefore, preferably *hkl* reflections with low multiplicity and high structure factors should be used.

4.3 Sample preparation and data acquisition

The FXD-CSD method has been applied to a series of *in situ* and *ex situ* experiments exploring the time dependence on crystal growth and coarsening of Xe-clathrate compounds dispersed in a quartz mineral matrix. Results for these experiments are later compared to similar study of CH_4-hydrates. Both gases and resulting clathrates are considered to be close analogs [45] but Xe-hydrates scatter X-rays considerably better than CH_4- filled counterpart, which allows us to push the detection limit to crystals with sub-µm size. Moreover, Xe-hydrates require roughly an order of magnitude lower formation pressures at this temperature and alleviate some of the safety concerns towards experiments with explosive media at large-scale user facilities like synchrotrons.

4.3.1 In-situ CSD (Xe-hydrate)

Samples for the *in situ* experiments were prepared from a mixture of natural quartz sand (200-300 µm) from Lyubertsy (Moscow region, Russia) [55] and fine frost particles that upon melting fill ~55 vol-% of the pore space. A portion of the homogenized starting material was loaded at liq-N_2 temperature in

the custom built environmental cell [45, 56] and warmed up to 276 K and kept stable ± 0.1 °C during the 4 days of experiment. The initial reaction was followed using the "stop-and-go" procedure [45, 57]. The first CSD measurement was taken after the reaction over 2 min and reducing pressure to the stability boundary at 0.22 MPa. It should be noted that at this stage free water is not fully the converted to Xe-hydrate. Once done, the pressure was raised again to allow for the further hydrate formation. The operation was repeated one more time after 30 min, close to a full conversion of water into hydrate. For scans after 2 days and 4 days respectively, the coarsening was slow enough to not affect the data collection and the "stop-and-go" procedure was not necessary. These scans were measured at elevated pressure of 0.4 MPa to avoid any risk of a partial decomposition. These four *in situ* scans have been complemented by additional *ex situ* measurements.

4.3.2 Ex-situ CSD (Xe-and CH_4-hydrate)

Ex situ Xe-hydrate samples were synthesized in-house using a low temperature/high pressure system [58]. The starting mixture of sand and frost was filled into a 2 mm Kapton capillary, inserted into an aluminum pressure cell and molten at 276 K under 0.1 MPa of Xe pressure. The preparation was done under the same p-T conditions as for the *in situ* experiments for a period of 1 week and 4 weeks. Reacted samples were recovered from the pressure cell at liq-N_2 temperature. CH_4 hydrate-bearing sediments samples were prepared with sand similarly to the Xe- counterpart with frost replaced by a fine CH_4 hydrate powder corresponding to a water saturation of 50 vol-% in the pore space [59, 60]. The mixture was also filled into a 2 mm Kapton capillary, loaded into the *in-house* setup and molten under ambient methane pressure at 276 K. After 45 minutes CH_4 hydrates were reformed at 10 MPa, hence using a driving force comparable to what was used for Xe hydrates; the driving force is defined as $\ln(f/f_d)$ where f stands for the fugacity at the experimental conditions and f_d for fugacity at the stability boundary. In total, three CH_4 hydrate samples were synthesized for a period of 3 days, 1 week and 6 weeks. Furthermore, one CH_4 hydrate sample was prepared at a temperature between 268 and 273K starting from ice spheres [58, 59, 60] as such a material is often used in laboratory studies of physical properties of hydrates.

4.3.3 Data collection

The CSDs of *in situ* and *ex situ* grown Xe-ydrates were investigated using synchrotron X-rays at the ID15B beamline located at the ESRF (European Synchrotron Radiation Facility). For the growth of Xe-hydrates in a sedimentary matrix we used the same driving forces and the same basic setup as for synchrotron X-ray tomography [45], but the energy of the beam was set to 87.19 keV (λ = 0.14209 Å); this setting allows for high-penetration depths and fast measurements of the samples inside the complex environmental setup [61]. The *in situ* sample in the pressure cell was mounted with its axis vertical on a rotation stage. Capton capillaries with *ex situ* prepared samples were measured in the horizontal configuration cooled with a cryo-jet set to 100 K. The diffraction data were collected on a Pixium 4700 2D flat-panel detector (Thales Electron Devices, 38430 Moiron, France) with a pixel array of 1910 × 2480 pixels and a pixel size of 154 × 154 µm. In order to obtain “spotty” diffraction patterns suitable for extracting CSDs the beam cross-section was set to 0.3 mm× 0.3 mm. The samples were rotated over a few degrees to record a sufficient number of complete rocking curves of individual crystals; typically the rotation angle was 2 deg with a step-size of 0.005 deg and an exposure time of 5 s giving 400 frames per scan. The collected data were saved as 32 bit TIFF files. The methane hydrate samples were investigated in a separate experiment at the P02 beamline of Petra III at DESY (Deutsches Elektronen-Synchrotron). A beam energy of 59.7 keV (λ = 0.20768 Å) was used. The setup was

equipped with a PerkinElmer XRD 1621 area detector with a pixel array of 2048 × 2048 pixels and a pixel size of 200 × 200 μm^2. The sample inside the Kapton capillary was cooled with a co-axially mounted cryo-jet at 100 K. For each scan, 300 frames with a step-size of 0.005 deg and an exposure time of 15 s were collected.

4.3.4 Data reduction and correction

A good statistical description of a rocking curve for a single reflection crossing the Ewald sphere may require steps as fine as 0.001- 0.005 deg resulting in a series of several hundred of image files for every scan. In order to take advantage of the 2D detector technology and still being able to handle large datasets, the image analysis is done semi-automatically with a software package developed using the interpreter programming language Python. The program is designed to operate on stacks of 2D frames that after processing provide step-scans ("rocking curves") through Bragg reflections of individual single crystals. The data reduction from the single frame processing to extracted integrated peak intensity is performed for each Debye-Scherrer ring, corresponding to a specific Bragg reflection *hkl*, and can be broken down to the following steps:

1. The image is reduced to a ring-shaped area of interest enveloping the chosen Debye-Scherrer ring corresponding to a Bragg reflection *hkl*.
2. A 2θ- and γ-dependent threshold operation is applied to the area of interest to separate peaks (2D-objects) from background.
3. Detected diffraction peaks for single crystals are labelled and correlated between adjacent frames. Objects with multiple maxima are separated from each other with a 3D-watershed algorithm [62].
4. Intensities for correlated reflections are extracted to obtain their corresponding rocking-curves. The area below the rocking-curve gives the diffracted intensity.
5. After extraction of the diffracted intensities a general algebraic Lorentz correction [63] is applied.

The extracted rocking curves undergo an additional selection process evaluating their central moments: second moment, third moment (skewness) and the fourth moment (kurtosis). Data with moments bigger than the average ±2σ (where σ is the standard deviation of the corresponding calculated statistical moment) are discarded; this selection process is important to remove reflections with odd rocking curves resulting from accidentally overlapping Bragg peaks producing too large intensities. The remaining intensities are used for establishing the CSDs. The elimination process was uncritical in the GHs studied here as the rocking curves were generally sharp and well-shaped, thus allowed for a clear distinction between single and overlapping peaks.

4.4 Experimental results

4.4.1 Calibration with LaB_6

The calibration in this study was done with LaB_6 powder (NIST SRM 660a) that meets well the above described criteria. The CSD of this sample was measured on several SEM images of crystals spread on a scotch tape (see Figure App. D-1) and analyzed with "ImageJ" [64]. The area of each non-spherical crystallite seen in the SEM images was transformed into a circle with equivalent projected surface and the volume calculated by assuming an identical particle radius in the direction orthogonal to the observation plane. The LaB_6 calibrant for the FXD-CSD method was additionally diluted with amorphous starch [1:10] (commercial starch Mondamine™) to limit the number of overlapping diffraction spots. Figure 4.2 shows a typical spotty diffraction pattern of LaB_6 measured *in situ*. As the

111 reflection is overlapped with an aluminum reflection of the pressure cell, only the 100 and 110 Bragg reflections remain available for analysis. As can be seen from the comparison of normalized intensities of these two reflections to the structure factor, the most suitable for the calibration is the strongest reflection 110 (Figure App. D-2).

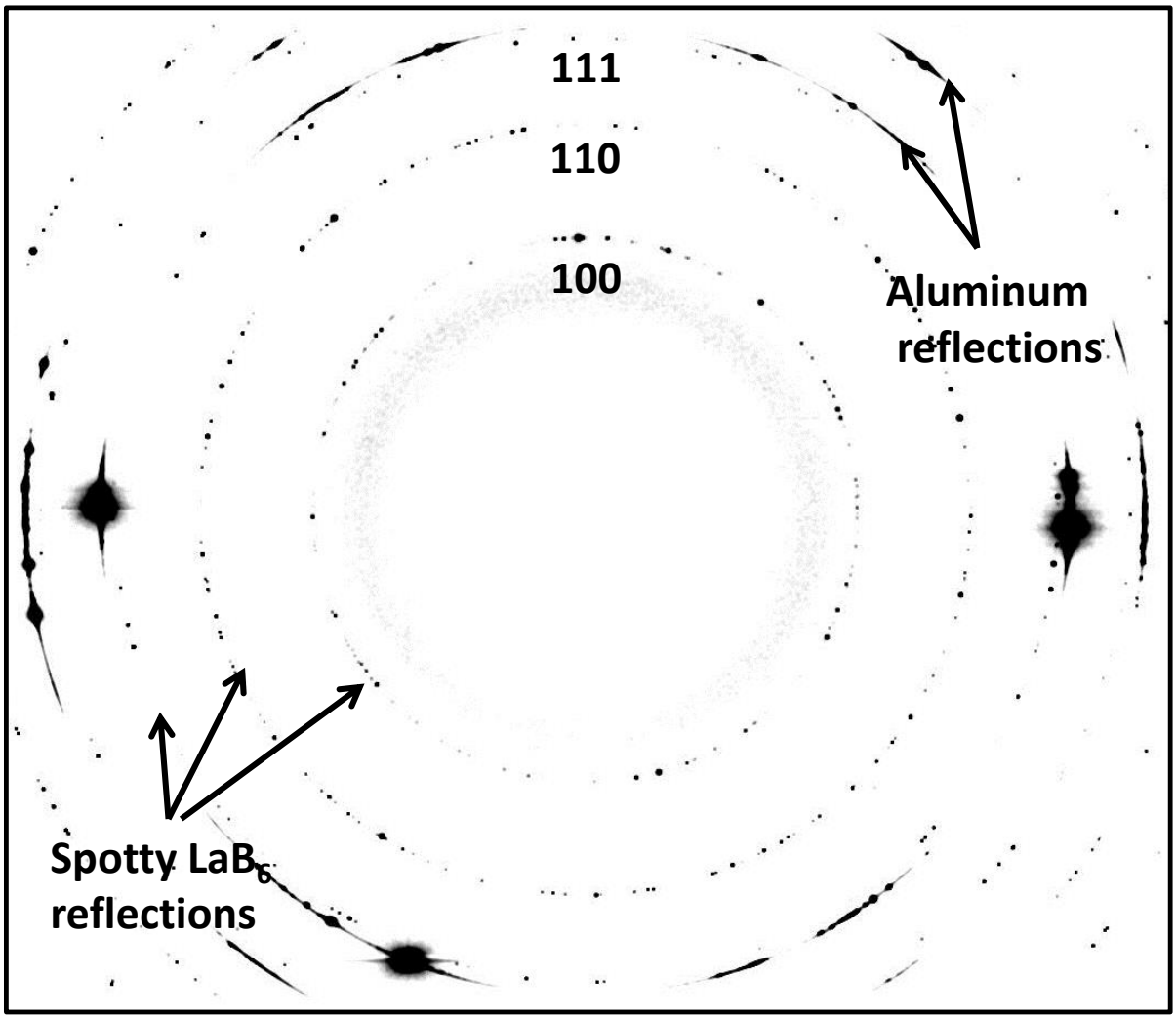

Figure 4.2: Two-dimensional spotty diffraction pattern of LaB_6 measured *in situ* inside an Al sample holder. The 100 and 110 LaB6 reflections are accessible for analysis, while the 111 reflection of LaB_6 is overlapped with one of the Al reflection.

The volume distribution of the 5409 LaB_6 crystallites extracted from SEM images follows closely a log-normal distribution (see Figure 4.3a) with a mean diameter of 2.5 µm. The corresponding ID of the standard is illustrated in Figure 4.3b. By comparing ID and CSD of LaB_6 the first scale factor, S_1, was obtained as $\ln(S_1) = 12.09$. It should be noted that a correction has been applied to take into the account missing low intensity reflections as illustrated in Figure 4.3a. In the same way, scale factors S_1 for the other data sets were established as given in Table App. D-1. Subsequently, the ID of the calibrant is compared to the ID measured for GHs.

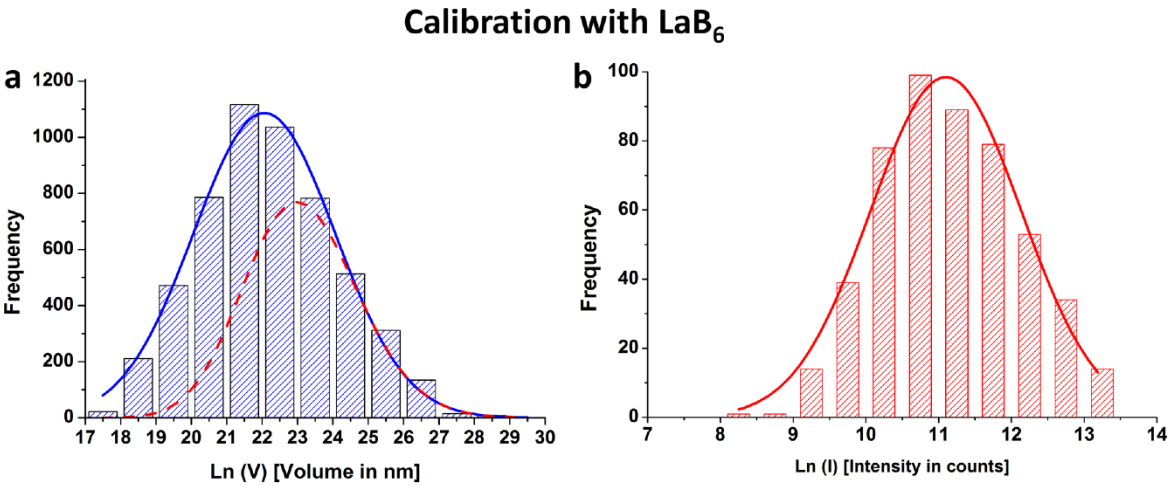

Figure 4.3: (a) Logarithmic volume distribution of 5409 LaB6 crystallites extracted from SEM images. (b) Logarithmic intensity distribution of 110 reflection of LaB6 measured *in situ*. The scale factor $\ln(S_1)$ is calculated from the values of the mean-values of both distribution obtained from the fitting parameters. Since the diffraction data for various X-ray setups may lack sensitivity to detect weak crystallites (low signal/noise ratio and/or high cutoff level of the peak detection), it is sometimes necessary to adjust the intensity distribution using the full width and the leading edge (larger particles side) of the SEM data as reference point; details are given in Table App. D-1. The broken red line in panel **a** show the part of the LaB6 CSD which is detected by the diffraction measurements.

4.4.2 CSDs of Xe- and CH_4 hydrate

The initial analysis of six Bragg reflections (Figure 4.4), i.e. 200, 210, 211, 222, 321 and 400, of Xe hydrate did not produce fully identical results. The obtained mean crystal sizes from each reflection calculated using the S_2 scale factor listed in Table 4.1 were somewhat different and the number of crystals found per reflection did not always match the multiplicity factor (see Table App. D-2). These discrepancies are due to the detection cut-off of weaker reflections (i.e. 200, 210 and 211) for small crystal sizes and the high multiplicity of the 321 reflection leading to frequent accidental overlap. To overcome these inconsistencies, we have discarded those reflections and retrieved CSDs only from the 222 and 400 reflections; both have a large structure factor and a low reflection multiplicity. The crystal sizes collected from these Bragg reflections represent statistically independent subsets of the ensemble of crystals in the sample and can be summed up together into one distribution for each formation step (Figure 4.5). A log-normal distribution has been fitted to each data set which in general gives a reasonable description of the CSDs (Figure App. D-3). The mean sizes and the standard deviations are listed in Table 4.2.

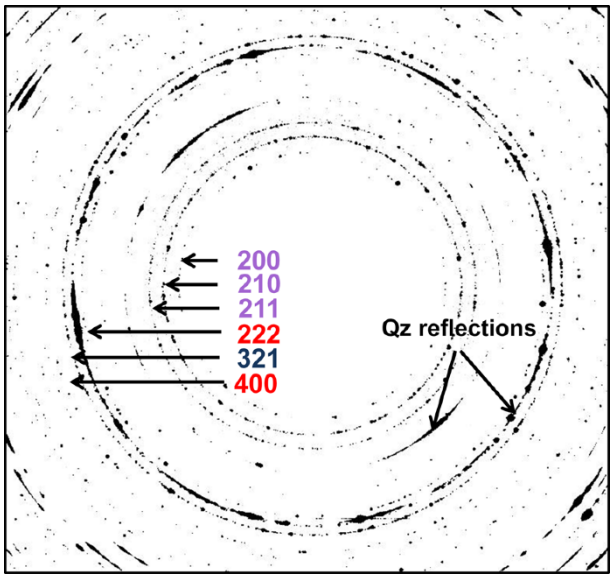

Figure 4.4: Measured spotty diffraction pattern of Xe-hydrate (run 4 days). The Xe-hydrate reflections can be categorized into weak reflections (200, 210, and 211), overcrowded reflection (321), and strong reflections with low multiplicity (222 and 400).

The *ex situ* measurements of cryo-preserved CH_4 hydrates were somewhat hindered by the partial overlap with strong reflections from ice I_h (frozen water), shown in Figure App. D-4, and only the 400 reflection was well suited for a CSD analysis. The calculation of S_2 for this reflection is given in Table 4.1. The CSD results of CH_4 hydrate are shown in Figure 4.6 and their log-normal fits in Figure App. D-5. Table 4.3 summarizes the mean crystal sizes and standard deviations.

Table 4.1 Crystal structure parameters and S_2 calculations.

	hkl	Multiplicity (M)	Structure factor $\|F\|^2$	Unit cell volume (Å^3)	S_2
LaB_6	110	12	2355.16	71.82	n/a
Xe hydrate	200	6	16162.04	1710.80	3.47
	210	24	14986.66		3.74
	211	24	13317.16		4.21
	222	8	61757.22		0.91
	321	48	42530.81		1.32
CH_4 hydrate	400	6	7056	1666.54	7.74

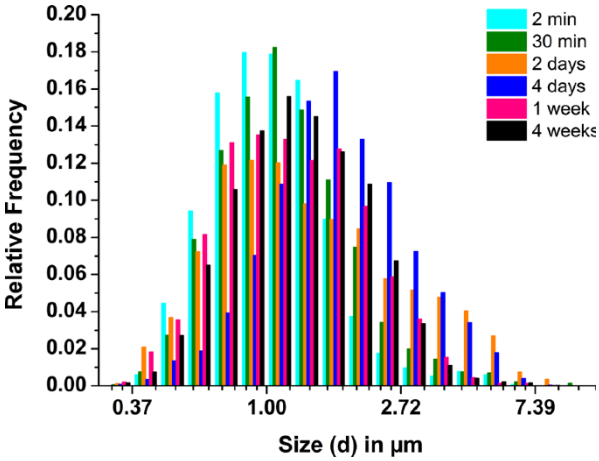

Figure 4.5: Evolution of Xe-hydrate CSDs with time shown in binned histograms on a logarithmic scale with crystallite sizes in micrometer. The different colors correspond to the different durations of the experiments. Please note that the data sets from 2 min to 4 days were obtained in one *in situ* run, while the data sets for 1 week and 6 weeks were obtained in an *ex situ* run for which every sample had to be recovered at low temperature.

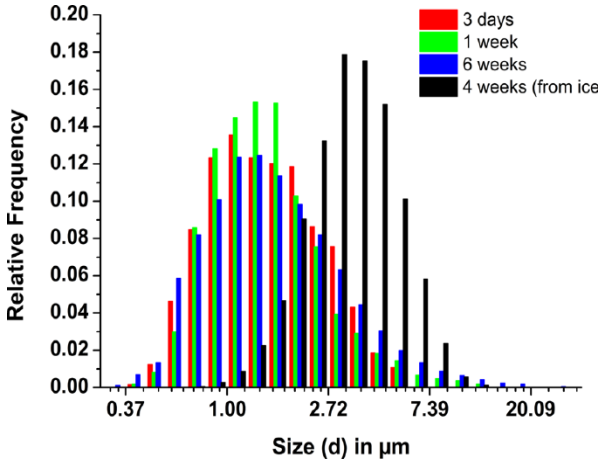

Figure 4.6: Evolution of CH_4-hydrate CSDs with time shown in binned histograms on a logarithmic scale with crystallite sizes in micrometers. The colored entries correspond to time-dependent *ex situ* experiments on CH_4-hydrate formed in a sedimentary matrix, while the black entry represents the results for a formation of CH_4 -hydrate starting from a powder of ice I_h spheres. Please note that all time-dependent data sets were obtained in an *ex situ* run for which every sample had to be recovered at low temperature.

Table 4.2 Counting statistics and fitting results for intensity distributions of individual Bragg peaks and their sums (Standard deviations for the entries are given in brackets). The runs at 1 week and 4 weeks were investigated on *ex situ* samples, all other runs were studied on in situ samples.

	hkl	Threshold	N initial	Ratio	N final	Ratio	Mean	Linear mean	FWHM	Linear FWHM
2 min	222	1.25	5059	1.08	683	1.47	0.101 (0.020)[1]	1.106 (0.022)[2]	0.858 (0.037)[1]	2.358 (0.087)[2]
	400	1.3	4703	1.08	464	1.47	-0.136 (0.033)	0.873 (0.029)	0.940 (0.064)	2.560 (0.164)
	Sum	**n/a**	**9762**	**n/a**	**1147**	**n/a**	**0.018 (0.022)**	**1.018 (0.022)**	**0.917 (0.038)**	**2.502 (0.095)**
30 min	222	1.3	3781	1.32	832	1.33	0.216 (0.016)	1.241 (0.016)	0.904 (0.032)	2.469 (0.079)
	400	1.3	2859	1.32	627	1.33	-0.074 (0.041)	0.929 (0.041)	0.879 (0.070)	2.408 (0.169)
	Sum	**n/a**	**6640**	**n/a**	**1459**	**n/a**	**0.124 (0.025)**	**1.132 (0.028)**	**0.996 (0.040)**	**2.707 (0.108)**
2 days	222	1.3	2045	0.60	443	1.19	0.318 (0.072)	1.374 (0.099)	1.409 (0.154)	4.092 (0.630)
	400	1.3	3387	0.60	372	1.19	0.322 (0.082)	1.380 (0.082)	1.620 (0.155)	5.053 (0.783)
	Sum	**n/a**	**5432**	**n/a**	**815**	**n/a**	**0.285 (0.066)**	**1.330 (0.088)**	**1.366 (0.108)**	**3.920 (0.423)**
4 days	222	1.25	6530	1.20	2266	1.27	0.575 (0.017)	1.777 (0.027)	1.178 (0.030)	3.248 (0.097)
	400	1.3	5441	1.20	1787	1.27	0.454 (0.019)	1.575 (0.030)	1.259 (0.033)	3.522 (0.116)
	Sum	**n/a**	**11971**	**n/a**	**4053**	**n/a**	**0.520 (0.017)**	**1.682 (0.029)**	**1.210 (0.028)**	**3.353 (0.094)**
1 week	222	3.5	8856	1.23	1626	1.18	0.225 (0.029)	1.252 (0.036)	1.13 1(0.043)	3.099 (0.133)
	400	4	7200	1.23	1383	1.18	0.133 (0.031)	1.142 (0.035)	1.226 (0.049)	3.408 (0.167)
	Sum	**n/a**	**16056**	**n/a**	**3009**	**n/a**	**0.180 (0.026)**	**1.197 (0.031)**	**1.199 (0.041)**	**3.317 (0.136)**
4 weeks	222	3.5	8001	1.24	1908	1.27	0.262 (0.015)	1.299 (0.019)	1.105 (0.026)	3.019 (0.078)
	400	4	6467	1.24	1504	1.27	0.156 (0.020)	1.169 (0.023)	1.160 (0.033)	3.190 (0.105)
	Sum	**n/a**	**14468**	**n/a**	**3412**	**n/a**	**0.220 (0.016)**	**1.246 (0.020)**	**1.124 (0.026)**	**3.077 (0.080)**

[a] Standard deviations for the entries are given in brackets. The runs at 1 week and 4 weeks were investigated on *ex situ* samples; all other runs were studied on *in situ* samples. *N* initial: number of diffraction peaks found within each *hkl* before any peak rejections. *N* final: number of diffraction peaks after rejection of defect peaks and application of selection rules. n/a: not applicable. Threshold: factor to the background value to determine the adaptive threshold. Ratio: the ratio of the number of observations *N* for the 222 and 400 Bragg reflections. The expected ratio in all cases is the ratio of the reflection multiplicities, i.e., 8/6 = 1.3333. Mean: mean value on the logarithmic scale obtained from the Gaussian fit. Linear mean: in µm units and obtained by exponentiation of mean. FHWM: full width at half-maximum of the Gaussian fit. Linear FHWM: obtained by exponentiation of FHWM. [b] Standard deviation on the logarithmic scale. [c] Standard deviation on the linear scale (= linear mean × logarithmic error)

Table 4.3 Summary of the crystal sizes of CH_4 hydrate (Standard deviations for the entries are given in brackets)

		N initial	N final	Mean	Linear Mean	FWHM	Linear FWHM
CH_4-hydrate in sediments	3 days	2630	649	0.414 (0.039)	1.513 (0.059)	1.233 (0.064)	3.431 (0.219)
	1 week	9478	2240	0.335 (0.031)	1.398 (0.043)	1.108 (0.053)	3.028 (0.160)
	6 weeks	8232	1709	0.427 (0.038)	1.532 (0.058)	1.381 (0.063)	3.979 (0.250)
CH_4-hydrate from ice	4 weeks	10895	9642	1.211 (0.009)	3.357 (0.030)	1.016 (0.015)	2.762 (0.041)

4.5 Discussion

4.5.1 CSD evolution during nucleation and growth of gas hydrates

The growth of Xe-hydrate in our samples takes place in a complex geometry of pore spaces formed by quartz grains which does not suggest a resulting simple mono-causal CSD. Still, we have no indications from tomography that the quartz surfaces provide preferential nucleation sites [45]; in a way the quartz matrix can be considered as excluded volume of the growth and nucleation process. We should note here that the nucleation stage cannot be observed by diffraction as the critical nuclei are only a few nm large and would give reflections well below the detection limit. Yet the initial growth is very fast and reaches crystal sizes of several 100 nm sizes in less than one minute when they become detectable.

When using juvenile water, the Xe-hydrate formation starts at the gas-water interface [45] forming a thin, continuous film with a thickness of a few µm after 2 minutes of reaction (Figure 4.7). After that the layer continues to thicken preferentially into the water phase. The initial film is composed of quasi-isometric crystals as e.g. straight sections from distinct facets cannot be identified [65], which would point to an extended crystal size in the plane of the film; needle or plate-like crystals more common at higher driving forces [42, 65] were not observed. Nucleation at the gas water interface appears to be a frequent event and must occur more or less concomitantly at many places as also evidenced in earlier micro-optical work [66, 67]. These high nucleation rates at moderate driving forces supports a picture emerging from molecular simulations, which suggest that impurity-free heterogeneous nucleation takes place on hydrate precursors formed at the water-gas interface [68]. The nucleation rates are thus comparable to homogeneous nucleation situations, yet obtainable at lower driving forces. This in turn leads to rather small crystallites. The observed CSDs after 2 minutes of reaction are consistent with a log-normal distribution, which is unexpected for a site-saturated Avrami-type nucleation and growth process, at least not after such a rather short period of growth [47]. Similarly, after 30 min of reaction the CSD is hardly any broader, still looks fairly log-normal and has just a clearly increased mean value (Table 4.2). Such CSD could be expected if slight temperature gradients or gradients in local chemical activity are present in the sample and affect the nucleation rates [65]; a situation which cannot be excluded in our experimental set-up.

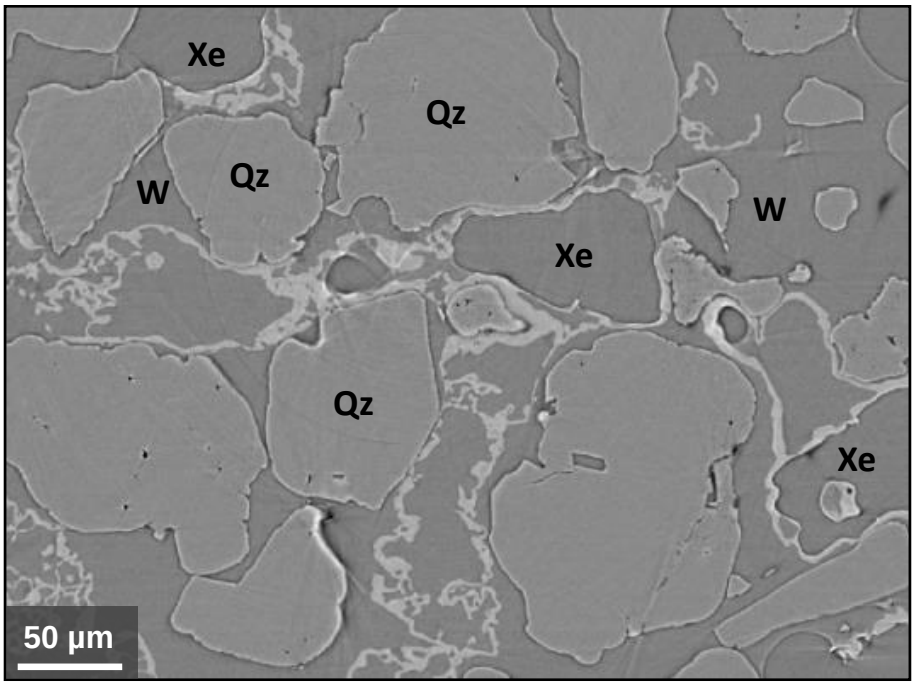

Figure 4.7: Nucleation of GH (white) at the Xe gas (Xe)–water (W) interface; sample formed from juvenile water; water saturation = 67 vol % of pore space between quartz (Qz) grains, reaction time t_R= 1.5 min. Formation of an inhomogeneous micrometer thin GH film which is composed of small isometric crystals below 1 µm as confirmed by the CSD scan after 2 min; individual crystals cannot be discerned.

Our earlier tomographic observations in highly water saturated patches [45] and the new CSD measurements at similar water saturation are in mutual agreement, at least in a sense that crystals detected by inspection of the tomograms fall into the range of CSDs measured by FXD. We should remind the reader that the number-lengths mean values, which are determined by the FXD-CSD method, are different from the volume-mean diameter ("de Brouckere mean"), which will yield distinctly larger crystallite sizes. Tomography tells us also that at this stage some (but definitely not all) crystallites in the initial film have considerably grown up to a size of 10 µm or more as evidenced by their polyhedral appearance now with clearly visible crystal faces (Figure 4.8); number-wise there are not many such large crystals but they dominate volume-wise the distribution and are also more easily discerned. These large crystals extend both into the gas and the water phase with thinner film sections in between. At this stage (about 10 min. after starting the reaction) some GH nucleation and growth also takes place inside the water phase; individual polyhedral crystal shapes can hardly be deduced from tomography at this stage but the sizes appear to be somewhat larger compared to the ones in the initial film. The location inside the water phase is not too far from the GH film and compatible with the nucleation and attachment growth suggested by [65].

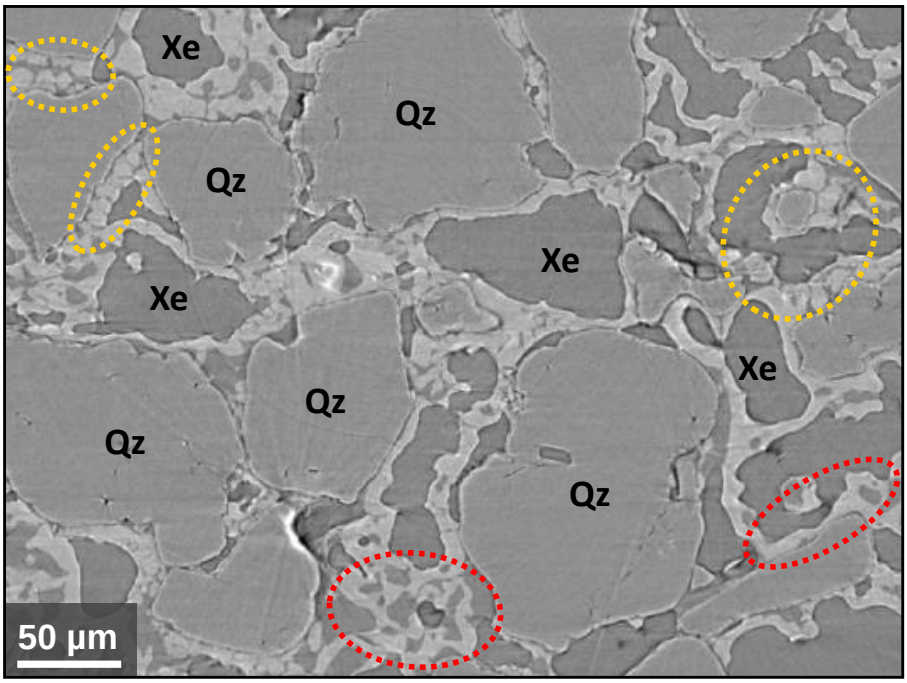

Figure 4.8: Growth and surface coarsening of GH: thickening of the GH film and appearance of coarsened polyhedral crystals up to >10 µm (encircled in yellow); sample formed from juvenile water with initially 67 vol % saturation, reaction time t_R = 7.2 min. In other parts of the sample the GH layers have just thickened (compared to the previous stage shown in Figure 4.7) with no sign of coarsening (encircled in red).

When starting with gas-enriched water, as in the case of CH_4-hydrates investigated here, crystals could be expected to grow preferentially inside the water phase in analogy to the similar experiments with Xe-hydrate [45], in which euhedral crystals of typically 5-10 µm in size were obtained. This may well explain the increase of mean size of CH_4-hydrate (Table 4.3) by a factor of up to 1.3 over the corresponding sizes of Xe-hydrate (Table 4.2). The reason could well be the somewhat lower nucleation rates inside the water phase as compared to the gas-water interface. We can, however, not exclude that the nucleation rates also intrinsically depend on the type of gas; Xe- and CH_4-hydrates may behave somewhat differently as a consequence of the higher activity of Xe in the gas-enriched water and/or as a consequence of modified guest-guest interaction which is important for the formation of the precursor states of nucleation [68].

The obtained CSDs for Xe and CH_4-hydrate can all be described to first approximation by a log-normal distribution (Figure App. D-3 and Figure App. D-5). Yet, the deviations from a log-normal CSD as calculated by a χ^2-test are very significant, even in cases where the fit looks perfectly reasonable. This is related to the well-known behavior of such χ^2-tests which for large sample sizes reject even very reasonable models, while for small sample sizes even bad models will not be rejected (see e.g. Stamatis [69]). Certainly, the FXD-CSD method provides a rather extensive sampling and in some cases the deviations from a model CSD could be assessed by other means, e.g. quantile-quantile (Q-Q) or related plots. Yet, as we do not expect a perfectly log-normal CSD in our case, due to the complexity of growth geometries, we refrain from further action. Site-saturated as well as the constant nucleation case of the Avrami model [47] certainly do not give log-normal CSDs. It is noteworthy, however, that log-normal CSDs were frequently observed in crystallization of minerals [48] and may arise from size-dependent growth [48, 70]. Indeed, various reasons may lead to such a size-dependent growth also in our experimental system as various growth locations with their characteristic nucleation rates (as discussed above) may well experience different growth rates due to different diffusion-limited or even

advection-limited supply rates. It is noteworthy that the CSDs obtained in growth experiments with ice and THF-hydrate slurries also can be described by a log-normal (or the similar Weibull) distribution [8]. These approximately log-normal CSDs formed in the first hours will at longer times undergo a possible coarsening, which should manifest itself by an evolution of the observed CSDs.

4.5.2 Post formation coarsening of gas hydrates

With the exception of the 2 min and 30 min duration runs, all data sets are obtained at the stage where all free water has been transformed into hydrate [45]. Even if the formation of the clathrate phase is nominally completed, the mean size (Table 4.2) and respective CSDs of approximately log-normal shape continue to change as is evidenced by looking at the results after 2 days. At this stage the width of the distribution is 40% larger than after 30 minutes of formation. Indeed, tomography suggests that two different populations seem to be present once the formation inside the bulk water has started: (a) Coarsened GH crystals at the former interface between gas and water and (b) smaller GH crystals inside the former bulk water phase. That such two different populations exist at least at an intermediate stage of the formation process is shown in Figure 4.9, which must lead to a broader CSD. These different populations could persist also at later stages after a full transformation of water into GH. Unfortunately, once the formation is completed it is very difficult to identify individual crystals from tomography (Figure App. D-6) and the only reliable source of information is FXD-CSD measurements. They tell us that in the subsequent coarsening stage the overall crystallite sizes still increase but the net gain is considerably slower in comparison with the earlier, nucleation and growth stage. The fundamental question at this point is the mechanism or a combination of mechanisms that drives the coarsening. The geometric arrangement of the GH crystallites as obtained from the final stage of the tomography experiments is complex (with gas phase separating polycrystalline aggregates of GH) and may well lead to both (1) normal grain growth (NGG) and (2) Ostwald ripening (OR) processes.

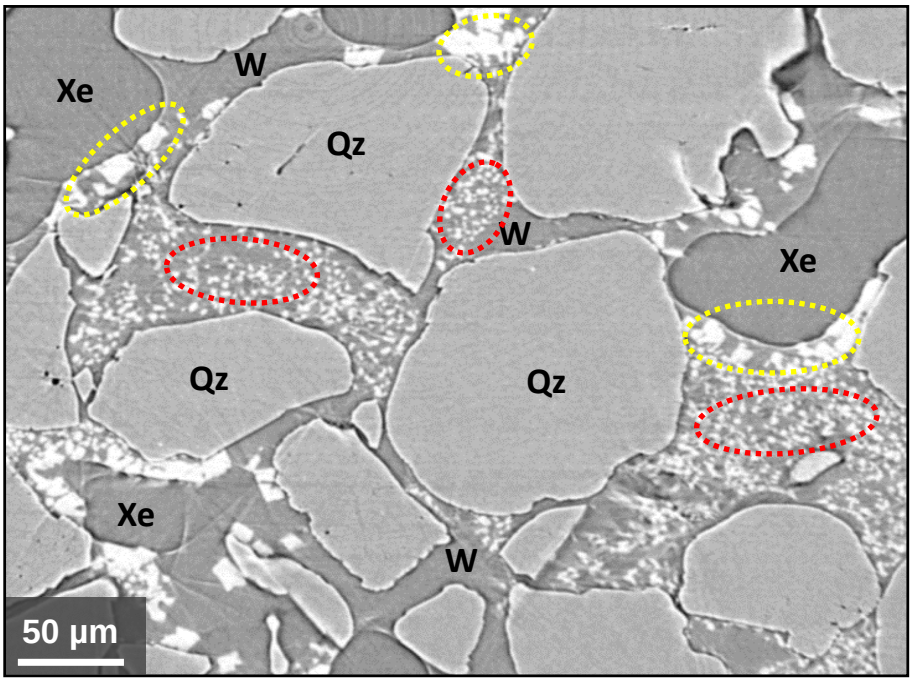

Figure 4.9: Concurrent appearance of GH at the gas–water interface and inside the water phase; sample formed from juvenile water with a water saturation of 81 vol % and a reaction time t_R = 4 min. Two populations of GHs with different crystal sizes are observed: The first consists of larger coarsened crystals initially formed at the gas–water interface (encircled in yellow), the second population is composed of many fine crystals formed inside the water phase (encircled in red). This suggests that the broadened CSD observed after 2 days could well be inherited from such different formation mechanisms.

Coarsening by NGG driven by grain curvature is expected, in a mean-field approach, to follow the "growth law"

$$\langle R\rangle^n - \langle R_0\rangle^n = K_{NGG}\cdot t$$

with n=2 and $\langle R_0\rangle$ the mean grain size at time t=0 and $\langle R\rangle$ the mean grain size at time t [71]. The proportionality factor K_{NGG} depends essentially on the thermodynamic driving forces (grain boundary energy, grain curvature) and the grain boundary mobility. The exponent n=2 is also predicted in a series of alternative scenarios like diffusion-controlled coarsening and were also obtained in numerical simulations [72] the experimentally observed exponents can stretch from below 2 to 4 [73].

The growth law for OR as derived by [4, 50] is given by

$$\langle R\rangle^3 - \langle R_0\rangle^3 = K_{OR}\cdot t$$

with $\langle R_0\rangle$ the mean grain size at time t=0 and $\langle R\rangle$ the mean grain size at time t. The proportionality factor K_{OR} for diffusion-controlled processes contains the thermodynamic driving forces (interfacial energy, particle curvature) and the constituents' mobilities (diffusion constants) as well as their solubilities in the medium - parameters which are usually not constrained sufficiently well to allow for an accurate estimation of expected rates; consequently, K_{OR} is often empirically determined. The theoretical exponent n for OR in Lifshitz-Slyozov-Wagner (LSW) theory [4, 50] (i.e. in the case of infinitely small fractions of the precipitated phase) is 3. This has been experimentally confirmed, both in steady state and certain non-steady state cases. Yet, deviations have also been found, like e.g. for snow metamorphism with n = 4 [74]. This latter case has complex geometries and is certainly non-steady state

and, moreover, suffers from the difficulty of distinguishing clearly crystallites and grains of ice when measuring the change of specific surface area of snow.

Coarsening processes by OR and NGG yield similar CSDs, however with subtle differences. The initially predicted CSD for OR is the so-called LSW function which is skewed towards small sizes (negative skewness) on a linear size-scale. Yet, one has to recall that LSW distributions are only expected once a steady-state has been obtained, thus other distributions may results from transients between nucleation/growth controlled CSDs and an evolving LSW; in actual fact reaching steady-state may often take a long time [75]. A typical such non-steady state situation is encountered during snow metamorphism [74, 76, 77]; likewise, the complexity of GH growth in a porous matrix, with water and gas phase both initially present, can be expected to start in a non-steady state. Certainly none of the CSDs observed in our work are similar to a LSW distribution: Even the longest runs lasting several weeks yield something quite close to a log-normal CSD. We have thus no clear evidence for OR processes from the observed CSDs. Still, NGG may take place by reshuffling material between neighboring crystallites by moving grain boundaries. The predicted size distribution for NGG includes the log-normal case [78] [71] solution which is strongly negatively skewed (like the LSW solution) and a case somewhere in between these two, the Rayleigh distribution [79, 80]. It appears that the growth exponent *n* has no tight relationship to the resulting CSD (Kim et al. 2003). Experimental results for CSDs resulting from NGG do generally not show log-normal CSDs [81] but a distribution with negative skewness. An exception is the grain growth impeded by "impurities" between the coarsening crystals where indeed a log-normal distribution has been suggested [82]. The presence of impurity phases, however, between coarsening GH crystallites finds no support from tomography. Thus again, for our observed CSDs we do not have any evidence for reaching a steady state NGG.

In the light of Frost's [83] remark that CSDs measured with sufficient accuracy can at least be used to exclude certain coarsening models, we can state that there is no sign of an evolution of our CSD towards the LSW, Hillert or Rayleigh distribution; in other words, there is no sign for the pure case of normal OR or NGG. The quasi log-normal CSD developed during the nucleation and growth process still dominates the distribution in the investigated time-frame.. In the light of the above discussion, a correct choice of a growth law and growth exponent *n* to fit obtained CSDs is certainly not trivial and requires additional constraints from other methods.

4.5.3 Coarsening at fluid-GH interface

Some of the missing puzzle blocks to obtain information on the growth exponent can be actually found in earlier [84] and recently obtained [85] cryo-SEM images of polycrystalline gas hydrate aggregates showing an extensive coarsening with larger crystals sticking out of the surface exposed to either GH-forming gas or liquid on a timescale of a few days. Similar phenomena have also been observed in CH_4-hydrate formed in a sandy matrix similar to the ones used for our CSD work (Figure App. D-7). It is quite likely that such interfacial coarsening takes place in experiments presented here and could explain (at least partly) the observed increase of sizes. In fact, increased mobilities of the constituents can be expected in the fluid phase in direct contact with the gas hydrate crystallites' surfaces; in particular smaller grains in the neighborhood of a larger crystallite could easily contribute to the coarsening in a local two-dimensional Ostwald-ripening process, in which no grain boundaries have to migrate (as smaller crystals on the surface shrink on the expense of larger crystals which grow into the fluid phase). Such a local ripening process would lead to a rougher surface of the initial GH film and even a sintering

of individual GH particles that is in agreement both with tomographic [45] and microscopic [86] observations.

If we adopt this explanation one could justify a fit of a growth law with dimensionality *n*=2 to the observations as shown in Figure 4.10. If we extrapolate this fit to the timescale of one year (with all precautions due to the modest goodness-of-fit) we could expect a mean crystallite size about 2 µm for Xe-hydrate and slightly larger values for CH_4-hydrate. This, by all means and whatever happens in detail, is a slow coarsening for a water-based material at +4°C, i.e. only about 10 degrees below its decomposition temperature. Due to this slowness the process is also likely to be far from reaching a steady state.

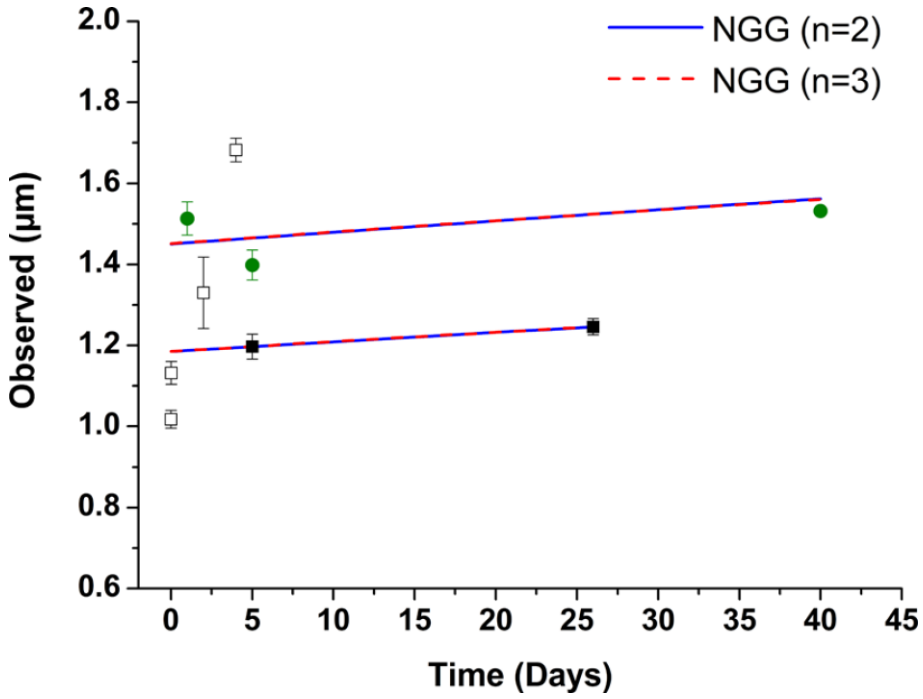

Figure 4.10: Mean values of the CSDs as a function of time after the full formation of Xe- and CH_4-hydrate, which is assumed to be completed after 2 days of reaction. Note that the *in situ* (open squares) and *ex situ* (filled squares) results for Xe-hydrate do not exactly match up; this is easily explained by small differences in the preparation routes (e.g., slightly different nucleation rates, effects of sample recovery). Coarsening laws with *n*= 2 and *n*= 3 are fitted to the Xe-hydrate *ex situ* data result in coarsening constants of 1.65×10^{-20} and 1.51×10^{-26}, respectively. Obviously, there is a rapid coarsening in the first 2 days after formation which ceases at later times; the fits shown relate only to the later slow stage of the coarsening process. The coarsening constants of the CH_4-hydrate data (green filled circles) for n = 2 and n = 3 are 2.43×10^{-20} and 2.69×10^{-26}, respectively.

4.5.4 Mobility at GH-GH grain boundary

Coarsening of a polycrystalline mass of GH will eventually require a three-dimensional process which goes beyond the quasi two-dimensional evolution at the surface described above. This is likely to happen at the grain boundaries where canonically NGG takes place. In simple crystal structures like metals or water ice the boundary movements of this three-dimensional interface is associated with breaking individual bonds in one crystallite and reforming them on a neighboring crystallite. Indeed, the activation energy of NGG, for instance, in ice is very similar to the energy of breaking H-bonds [5b]. In more complex clathrate materials the displacement is considerably more difficult and must include guest and host molecules. From topologic consideration it is clear that neighboring crystals with arbitrarily different crystallographic orientation cannot directly connect up without some form of a transition zone composed of amorphous or metastable non-standard types of cages, perhaps similar

to those recognized in GH precursors [87-89] or in a mediator phase between ice and GH [90] or between sI-sII GH [91]. If this is the case, NGG in gas hydrates would not be just related to breaking and reforming individual H-bonds but require a collective motion and displacement of groups of water molecules and guests in a concerted topological rearrangement of the cage-structures to become part of a neighboring crystal. While water vacancies (i.e. incomplete water cages) may well be present in GHs and allow for gas mobility also within the grain boundary network [85, 92], the synchronized topological rearrangements involving several water molecules will be very difficult to achieve, with resulting much lower rates of grain boundary motion as compared to ice I_h. Indeed, Figure 4.11 shows the coarsening of ice I_h as calculated form established NGG laws (with n=2) for glacier ice [7] in comparison with the best estimate for CH_4-hydrate obtained in the previous chapters. It becomes immediately clear that NGG coarsening in this specific hydrate takes place at much slower timescales, different by about 5 orders-of-magnitude! Grain boundary migration likely depends on the guest-host interactions and should be somewhat different for THF, CO_2 or H_2S with their high affinity towards water compared to CH_4 or Xe [93] with their larger tendency for hydrophobic assembly. It becomes obvious that simple crystalline solids are not good analogues of clathrates in terms of NGG, the resulting CSDs and their related physico-chemical and mechanical properties.

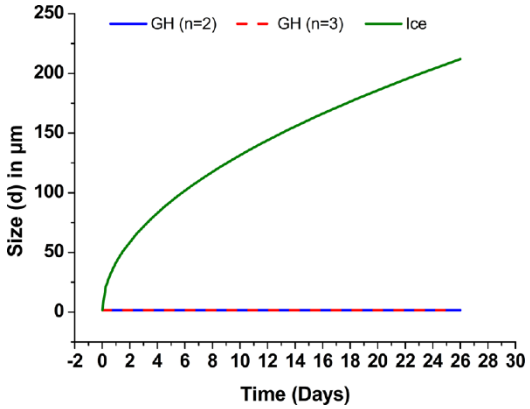

Figure 4.11: Coarsening of Xe-hydrate as a function of time (taken from Figure 4.10) compared to the coarsening of ice I_h at −10 °C with identical initial mean crystal size and a coarsening constant of 5×10^{-15} m^2s^{-1}.[7] The coarsening of ice proceeds about 5 orders of magnitude faster; after 26 days it yields mean crystals sizes which are 170 times larger when starting with identical sizes of ice and GHs.

4.5.5 Coarsening of natural gas hydrates

The coarsening of guest-host crystals is certainly slow and a more precise estimation of GH growth laws will require experiments longer than a few weeks; a scale of months or years seems to be more suitable. As such data are not yet available we turn our attention to natural hydrates that presumably benefit from much longer coarsening periods of time and could give some hints to the possible range of crystal sizes, CSDs and their relation to specific geological environments.

The first distinct class of hydrates is related to disseminate crystals occupying pore spaces in well permeable sandy sediments of marine and permafrost strata. Here GH concentrations can vary from merely a few % of pore volume to nearly full saturation. A handful of fairly well preserved samples from such environments reveal typically polycrystalline NGHs masses with poorly visible grain boundaries [20, 21, 84]. In a few places individual crystals of about 20-50 µm can be recognized but the counting statistics is certainly insufficient to draw any firm conclusion on CSDs. It should be noted that under lithostatic pressure and with narrow pore throats the maximum size of a single crystal is likely to be limited by the intergranular pore volume. For locations like Mallik or Mount Elbert Gas Hydrate

test wells in Alaska [20, 21, 84] the maximum possible size would be roughly 50 to 200 µm. Consequently, NGHs formed in such environments are fairly small but still about one order of magnitude larger than the laboratory formed ensembles; to reach a size of 50 µm starting from µm-sized crystals would take about 1000 years based on an extrapolation of our experimental results.

Other NGHs occurrences are associated with poorly permeable, clay rich sediments in which they are found in nodular or layered form [12]. Such hydrates were often recovered within active and dormant venting systems as knolls and veins grown along discontinuity zones in the sediment. A fair number of well-preserved samples recovered from such locations show a wide range of crystal sizes and CSDs. Cryo-SEM investigations of NGHs from Krishnae-Godavari and Andaman back-arc drill sites revealed crystals of 20 to 80µm size directed towards open voids with well-developed polyhedral faces [19]. Similar sizes were also reported from Gulf of Mexico [84]. On the other hand, the pioneering studies of CSDs in the bulk with X-ray using moving area detector method [24, 52, 94-96] show for other locations a somewhat different picture with crystal sizes of several hundreds of µm. The CSD and mean sizes change between various locations and exhibit some weak dependency on the sampling depth [52]. Interestingly, the maximum size of individual GH crystals found in soft sediments seems to be far less constrained than in the sandy counterparts. In case of samples recovered from Cascadia Margin (ODP 204 1248C 11H-5) some of the single crystals of GH reached even ~1 mm. Given the slow coarsening rates derived in our work recreation of such systems in terms of CSDs is probably beyond the capability of laboratory studies. Yet, at these locations there may well be another and somewhat faster re-growth mechanisms operating, as proposed for the formation of nodular NGHs *via* wetting interactions and compositional diffusion [97] leading to a complete re-growth of NGHs at adjacent sedimentary layers.

When searching for alternative, faster re-growth mechanisms it is worthwhile to look at the coarsening of air hydrates in polar ice cores [98]: Air hydrates initially crystallize from a single air bubble into a polycrystalline aggregate with tens of µm large crystals once the overburden pressure is sufficient to guarantee hydrate stability. These polycrystalline aggregates apparently persist for hundreds of years without any appreciable change of crystallite size, corroborating the slowness of NGG in gas hydrates. Then, likely triggered by stress-induced weakening of the surrounding ice matrix, a large single crystal emerges from the polycrystalline aggregate eventually reaching a final size of more than 100 µm: This process certainly can proceed without movements of grain boundaries of GH and is known as "anomalous grain growth" [2, 3]; it may well also occur in marine GHs under overburden pressure. Indeed, recent MD calculations [99] of a polycrystalline CH_4-hydrate assembly indicated the instability of grain boundaries with the evolution of methane nanobubbles upon applied stress. Nanobubbles are also formed on the surface of GH when they decompose [100]. These findings support a mechanism in which changes to CSDs are accelerated by a decomposition and subsequent anomalous grain growth of GH crystals.

On one side we have experimental evidence for NGHs crystals spanning the range from a few µm to a 1mm, on the other side there is a multitude of possible surface and bulk coarsening and re-growth mechanisms. Unfortunately, a clear link between those two sides is not yet established. In any case, it seems that processes with material transport *via* the fluid phase are quite fast when compared to NGG. Furthermore, there may be constructive and destructive influences on the crystal assembly and resulting CSDs depending on the environment: A) the growth could be supported by a continuous influx of fresh fluids of similar composition leading to the growth of individual, isolated crystals; B) a destructive characteristic is expected upon the change of the fluid composition that triggers a

structural change, i.e. a destruction of existing crystals and the crystallization of new ones [96] thus resetting any coarsening clock. At this stage and without further insight into the prevailing coarsening mechanisms and possible environmental changes it seems impossible to deduce formation ages of NGHs from CSDs; the highly non-linear time- and stress-dependency of anomalous grain growth prevents any firm statements at present. Apparently, a fast general 3-dimensional coarsening mechanism does not exist for GH.

4.5.6 Grain boundaries in gas hydrates and mechanical deformation

One of the often undervalued properties related to CSD of crystalline materials is its response to mechanical deformation. CH_4-hydrate formed from ice I_h is about 20 times stronger than ice I_h just below the ice point[101]; this is likely a consequence of the lower mobility of glide and climb dislocations [102] , linked in part to the larger lattice constants but likely also to the difficulties of topological rearrangements encountered in NGG of GHs. The crystal sizes of methane hydrate formed from 200 µm large ice particles were claimed to be in the range of 20-40 µm [101] as estimated by visual SEM inspection of the compacted hydrate powder sample. However, this visual method will tend to be biased by the more easily discernable larger crystals in the assembly and likely tends to overestimate the averaged particle size. This is supported by the results of our FXD-CSD analysis which gives a one order of magnitude smaller crystallites (see Table 4.3 and Figure 4.6).

It then seems obvious that grain size sensitive creep (GSS creep) will be the dominant way of deforming a polycrystalline mass of GH consisting of small crystallites as formed in laboratory experiments. Indeed grain-boundary sliding (GBS), which is one likely form of GSS creep, appears to be the deformation mechanism encountered in molecular computer simulations (Wu et al. 2014); admittedly this work was performed on even smaller crystallites, but considering the difficulty in moving dislocations in GH creep by GBS is expected to extend to even larger crystallite sizes than in ice I_h. Interestingly, different gas hydrates show somewhat different creep behavior (Durham et al 2010); CO_2-hydrate is more easily deformed than CH_4-hydrate which could well be simply a consequence of the smaller crystallite sizes in CO_2-hydrate (several µm) when formed form ice I_h [103]. The high strength of GH and the likely preponderance of GBS as deformation mechanism will also show its effects in deformation experiments in sandy matrices (Durham et al. 2003) which are of high importance for studies of marine slope stability [104]. Clearly, the CSDs of GH in laboratory experiments need to be established as they will influence creep tests in the GSS regime. Moreover, as not much is known about the CSDs of marine GH dispersed in a sedimentary matrix, it is not obvious how to relate these laboratory tests to the situation in submarine sediments. Should the crystallites be considerably bigger than what is usually obtained in laboratory experiments, e.g. be comparable to the pore size of the sandy matrix as discussed above or even hundreds of µm in layers or nodules [95], one would expect brittle failures to occur frequently (in contrast to laboratory experiments).

4.6 Conclusion

The coarsening rates presented here leave no doubt that the related intrinsic processes affecting polycrystalline clathrate assemblies are indeed extremely slow. Starting from crystallites of a few µm in size, obtained under common laboratory conditions from liquid water and gas, it would take hundreds to thousands of years to reach crystal sizes encountered in some NGHs, at least when assuming a normal grain growth mechanism. Anomalous grain growth may intervene and increase crystal sizes, in particular under overburden load and local stresses; too little is known to cast this process into a model with predictive power, thus impeding the determination of formation ages of

NGHs this stage. The large discrepancies in CSDs are nevertheless an alarming perspective for studies attempting to recreate natural conditions in laboratories.

The FXD-CSD method applied to gas hydrates further supports the predominance of log-normal CSDs in nucleation and growth processes, established in mineralogy [48, 49], yet probably also valid in other fields. Very good sampling statistics can be achieved in determining the CSDs, permitting for critical tests and subtle distinctions of models for nucleation and growth as well as coarsening processes. Moreover, it allows in the future for testing the influence of CSDs on grain-size sensitive processes, e.g. the CSD-dependence of yield strength *via* a generalized the Hall-Petch relation [105, 106].

The new fast CSD determination certainly shows its potential not only for GHs but also in other fields of applications beyond mineralogy, petrology, metals and ceramics. CSDs are of major importance in the product engineering of pharmaceuticals [107] or the chemical engineering of batch crystallization [108]; FXD-CSD can provide a destruction free access to quantitative distributions, also for samples enclosed in complex environments and it could, if necessary, be even automated. The direct access to the crystallites volume avoids complex and error-bound extrapolations from one-dimensional or two-dimensional observations (as obtained by optical microscopy or electron backscattering), which cannot be made without assumptions [109-112]. Compared to imaging methods like tomography it allows for a quantification of crystal sizes without going through a very often problematic rendering process [56] and is also applicable were optical resolution reaches its limits in the µm-range. It appears that FXD-CSD is the only method available to get reliable, quantitative information on crystal size distributions centred in the few to some tens of µm range, a range which turned out to be of central interest in gas hydrate research.

4.7 Acknowledgements

We acknowledge the European Synchrotron Radiation Facility (ESRF) in Grenoble, France for providing synchrotron radiation beamtime at the ID15 beamline; we are very grateful to Simon Kimber and Jessica Hudspeth for their competent help during the experiment. Likewise, we acknowledge the DESY/ PETRA in Hamburg, Germany for providing synchrotron radiation beamtime at the P02-1 beamline; we are very grateful to Hanns-Peter Liermann for his competent help during the experiment. We also thank Helmut Klein, Kathrin Nützmann, Patrick Lafond, Matthias Leck, Mathias Jansen and Stefanie Stracke (all Göttingen) for their valuable help during the experiments or data analysis. We acknowledge useful discussions with Helmut Klein (Göttingen) concerning the link between CSDs and mechanical properties of materials. SHN thanks Richard Neher for useful discussions. We also thank Laura Stern (Menlo Park) for comments on the SEM images shown in reference 101. The pressure cell was designed and constructed by Ulf Kahmann and Heiner Bartels (both Göttingen). The financial support from the Deutsche Forschungsgemeinschaft (DFG Grant Ku 920/18 and Ke 508/20) as well as the BMBF in the framework of the SUGAR-III program (grant 03G0856B) is gratefully acknowledged.

4.8 References

1. Lasaga, A. C., *Kinetic Theory in the Earth Sciences*. Princeton University Press: Princeton, New Jersey, USA, 1998.
2. Humphreys, F.; Hatherly, M., *Recrystallization and Related Annealing Phenomena*. 2nd ed.; Elsevier Ltd: Oxford, UK, 2004.
3. Novikov, V. I., *Grain Growth and Control of Microstructure and Texture in Polycrystalline Materials*. CRC Press: 1997.
4. Lifshitz, I. M.; Slyozov, V. V. The Kinetics of Precipitation from Supersaturated Solid Solutions. *Journal of Physics and Chemistry of Solids* **1961,** *19*, 35-50.
5. Wagner, C. Theorie Der Alterung Von Niederschlägen Durch Umlösen (Ostwald-Reifung). *Zeitschrift für Elektrochemie, Berichte der Bunsengesellschaft für physikalische Chemie* **1961,** *65*, 581-591.
6. Chiang, Y. M.; Birnie, D.; Kingery, W. D., *Physical Ceramics: Principles for Ceramic Science and Engineering*. Wiley: 1997.
7. Schulson, E. M.; Duval, P., *Creep and Fracture of Ice*. Cambridge University Press: 2009.
8. Delahaye, A.; Fournaison, L.; Guilpart, J. Characterisation of Ice and THF Hydrate Slurry Crystal Size Distribution by Microscopic Observation Method. *Int J Refrig* **2010,** *33*, 1639-1647.
9. Cros, C.; Pouchard, M. Clathrate-Type Phases of Silicon and Related Elements (C, Ge, Sn). *Comptes Rendus Chimie* **2009,** *12*, 1014-1056.
10. Momma, K.; Ikeda, T.; Nishikubo, K.; Takahashi, N.; Honma, C.; Takada, M.; Furukawa, Y.; Nagase, T.; Kudoh, Y. New Silica Clathrate Minerals That Are Isostructural with Natural Gas Hydrates. *Nat. Commun.* **2011,** *2*, 196.
11. Gies, H. Studies on Clathrasils .3. Crystal-Structure of Melanophlogite, a Natural Clathrate Compound of Silica. *Z Kristallogr* **1983,** *164*, 247-257.
12. Sloan, E. D.; Koh, C. A., *Clathrate Hydrates of Natural Gases*. 3rd ed.; CRC Press, Taylor & Francis Group: Boca Raton, FL, 2008.
13. Zerpa, L. E.; Salager, J.-L.; Koh, C. A.; Sloan, E. D.; Sum, A. K. Surface Chemistry and Gas Hydrates in Flow Assurance. *Ind. Eng. Chem. Res.* **2011,** *50*, 188-197.
14. Eslamimanesh, A.; Mohammadi, A. H.; Richon, D.; Naidoo, P.; Ramjugernath, D. Application of Gas Hydrate Formation in Separation Processes: A Review of Experimental Studies. *J.Chem.Thermodyn.* **2012,** *46*, 62-71.
15. Collett, T.; Bahk, J. J.; Baker, R.; Boswell, R.; Divins, D.; Frye, M.; Goldberg, D.; Husebo, J.; Koh, C.; Malone, M., et al. Methane Hydrates in Nature-Current Knowledge and Challenges. *J. Chem. Eng. Data* **2015,** *60*, 319-329.
16. Moridis, G. J.; Collett, T. S.; Pooladi-Darvish, M.; Hancock, S.; Santamarina, C.; Boswell, R.; Kneafsey, T.; Rutqvist, J.; Kowalsky, M. B.; Reagan, M. T., et al. Challenges, Uncertainties, and Issues Facing Gas Production from Gas-Hydrate Deposits. *SPE Reserv. Eval. Eng.* **2011,** *14*, 76-112.
17. Waite, W. F.; Santamarina, J. C.; Cortes, D. D.; Dugan, B.; Espinoza, D. N.; Germaine, J.; Jang, J.; Jung, J. W.; Kneafsey, T. J.; Shin, H., et al. Physical Properties of Hydrate-Bearing Sediments. *Rev. Geophys.* **2009,** *47*, Rg4003.
18. Dai, S.; Santamarina, J. C.; Waite, W. F.; Kneafsey, T. J. Hydrate Morphology: Physical Properties of Sands with Patchy Hydrate Saturation. *J. Geophys. Res.-Solid Earth* **2012,** *117*, B11205.
19. Stern, L. A.; Lorenson, T. D. Grain-Scale Imaging and Compositional Characterization of Cryo-Preserved India Nghp 01 Gas-Hydrate-Bearing Cores. *Marine and Petroleum Geology* **2014,** *58, Part A*, 206-222.

20. Techmer, K. S.; Heinrichs, T.; Kuhs, W. F. *Cryo-Electron Microscopic Studies of Structures and Compositions of Mallik Gas-Hydrate-Bearing Samples*; Bulletin 585; Geological Survey of Canada: 2005; pp 1-12.

21. Stern, L. A.; Lorenson, T. D.; Pinkston, J. C. Gas Hydrate Characterization and Grain-Scale Imaging of Recovered Cores from the Mount Elbert Gas Hydrate Stratigraphic Test Well, Alaska North Slope. *Mar. Pet. Geol.* **2011,** *28*, 394-403.

22. Murshed, M. M.; Klapp, S. A.; Enzmann, F.; Szeder, T.; Huthwelker, T.; Stampanoni, M.; Marone, F.; Hintermuller, C.; Bohrmann, G.; Kuhs, W. F., et al. Natural Gas Hydrate Investigations by Synchrotron Radiation X-Ray Cryo-Tomographic Microscopy (SRXCTM). *Geophys. Res. Lett.* **2008,** *35*, L23612.

23. Klapp, S. A.; Klein, H.; Kuhs, W. F. First Determination of Gas Hydrate Crystallite Size Distributions Using High-Energy Synchrotron Radiation. *Geophys. Res. Lett.* **2007,** *34*, 5 pp, L13608.

24. Klapp, S. A.; Klein, H.; Kuhs, W. F. Gas Hydrate Crystallite Size Investigations with High-Energy Synchrotron Radiation. *Geological Society, London, Special Publications* **2009,** *319*, 161-170.

25. Klapp, S. A.; Hemes, S.; Klein, H.; Bohrmann, G.; MacDonald, I.; Kuhs, W. F. Grain Size Measurements of Natural Gas Hydrates. *Mar. Geo.* **2010,** *274*, 85-94.

26. Berge, L. I.; Jacobsen, K. A.; Solstad, A. Measured Acoustic Wave Velocities of R11 (CCl_3F) Hydrate Samples with and without Sand as a Function of Hydrate Concentration. *J. Geophys. Res.-Solid Earth* **1999,** *104*, 15415-15424.

27. Best, A.; Priest, J.; Clayton, C., A Resonant Column Study of the Seismic Properties of Methane-Hydrate-Bearing Sand. In *Geophysical Characterization of Gas Hydrates*, Riedel, M.; Willoughby, E. C.; Chopra, S. Eds.; Society of Exploration Geophysicists: 2010; pp 337-347.

28. Best, A. I.; Priest, J. A.; Clayton, C. R. I.; Rees, E. V. L. The Effect of Methane Hydrate Morphology and Water Saturation on Seismic Wave Attenuation in Sand under Shallow Sub-Seafloor Conditions. *Earth Planet. Sci. Lett.* **2013,** *368*, 78-87.

29. Dvorkin, J.; Nur, A.; Uden, R.; Taner, T. Rock Physics of a Gas Hydrate Reservoir. *The Leading Edge* **2003,** *22*, 842-847.

30. Ecker, C.; Dvorkin, J.; Nur, A. M. Estimating the Amount of Gas Hydrate and Free Gas from Marine Seismic Data. *Geophysics* **2000,** *65*, 565-573.

31. Hu, G. W.; Ye, Y. G.; Zhang, J.; Liu, C. L.; Diao, S. B.; Wang, J. S. Acoustic Properties of Gas Hydrate-Bearing Consolidated Sediments and Experimental Testing of Elastic Velocity Models. *J. Geophys. Res.-Solid Earth* **2010,** *115*, B02102.

32. Li, F. G.; Sun, C. Y.; Zhang, Q.; Liu, X. X.; Guo, X. Q.; Chen, G. J. Laboratory Measurements of the Effects of Methane/Tetrahydrofuran Concentration and Grain Size on the P-Wave Velocity of Hydrate-Bearing Sand. *Energy Fuels* **2011,** *25*, 2076-2082.

33. Priest, J. A.; Best, A. I.; Clayton, C. R. I. Attenuation of Seismic Waves in Methane Gas Hydrate-Bearing Sand. *Geophys. J. Int.* **2006,** *164*, 149-159.

34. Priest, J. A.; Rees, E. V. L.; Clayton, C. R. I. Influence of Gas Hydrate Morphology on the Seismic Velocities of Sands. *J. Geophys. Res.-Solid Earth* **2009,** *114*, B11205.

35. Spangenberg, E.; Kulenkampff, J. Influence of Methane Hydrate Content on Electrical Sediment Properties. *Geophys. Res. Lett.* **2006,** *33*, L24315.

36. Yun, T. S.; Francisca, F. M.; Santamarina, J. C.; Ruppel, C. Compressional and Shear Wave Velocities in Uncemented Sediment Containing Gas Hydrate. *Geophys. Res. Lett.* **2005,** *32*, L10609.

37. Zhang, Q.; Li, F. G.; Sun, C. Y.; Li, Q. P.; Wu, X. Y.; Liu, B.; Chen, G. J. Compressional Wave Velocity Measurements through Sandy Sediments Containing Methane Hydrate. *Am. Miner.* **2011,** *96*, 1425-1432.

38. Wang, Y.; Feng, J.-C.; Li, X.-S.; Zhang, Y.; Li, G. Large Scale Experimental Evaluation to Methane Hydrate Dissociation Below Quadruple Point in Sandy Sediment. *Applied Energy* **2016,** *162*, 372-381.

39. Wang, Y.; Li, X. S.; Xu, W. Y.; Li, Q. P.; Zhang, Y.; Li, G.; Huang, N. S.; Feng, J. C. Experimental Investigation into Factors Influencing Methane Hydrate Formation and a Novel Method for Hydrate Formation in Porous Media. *Energy Fuels* **2013,** *27*, 3751-3757.

40. Tohidi, B.; Anderson, R.; Clennell, M. B.; Burgass, R. W.; Biderkab, A. B. Visual Observation of Gas-Hydrate Formation and Dissociation in Synthetic Porous Media by Means of Glass Micromodels. *Geology* **2001,** *29*, 867-870.

41. Hauge, L. P.; Gauteplass, J.; Høyland, M. D.; Ersland, G.; Kovscek, A.; Fernø, M. A. Pore-Level Hydrate Formation Mechanisms Using Realistic Rock Structures in High-Pressure Silicon Micromodels. *Int J Greenh Gas Con* **2016,** *53*, 178-186.

42. Watanabe, S.; Saito, K.; Ohmura, R. Crystal Growth of Clathrate Hydrate in Liquid Water Saturated with a Simulated Natural Gas. *Crystal Growth & Design* **2011,** *11*, 3235-3242.

43. Aifaa, M.; Kodama, T.; Ohmura, R. Crystal Growth of Clathrate Hydrate in a Flowing Liquid Water System with Methane Gas. *Crystal Growth & Design* **2015,** *15*, 559-563.

44. Saito, K.; Kishimoto, M.; Tanaka, R.; Ohmura, R. Crystal Growth of Clathrate Hydrate at the Interface between Hydrocarbon Gas Mixture and Liquid Water. *Crystal Growth & Design* **2011,** *11*, 295-301.

45. Chaouachi, M.; Falenty, A.; Sell, K.; Enzmann, F.; Kersten, M.; Haberthür, D.; Kuhs, W. F. Microstructural Evolution of Gas Hydrates in Sedimentary Matrices Observed with Synchrotron X-Ray Computed Tomographic Microscopy. *Geochemistry, Geophysics, Geosystems* **2015,** *16*, 1711-1722.

NB: *Note that in Figure S2 of Ref. 45 the horizontal scale was labelled erroneously in hours while in fact it should have been minutes.*

46. Spangenberg, E.; Priegnitz, M.; Heeschen, K.; Schicks, J. M. Are Laboratory-Formed Hydrate-Bearing Systems Analogous to Those in Nature? *Journal of Chemical & Engineering Data* **2015,** *60*, 258-268.

47. Lasaga, A. C., *Kinetic Heory in the Earth Sciences*. Princeton University Press: Princeton, New Jersey, U.S.A, 1998.

48. Eberl, D. D.; Drits, V. A.; Srodon, J. Deducing Growth Mechanisms for Minerals from the Shapes of Crystal Size Distributions. *Am. J. Sci.* **1998,** *298*, 499-533.

49. Eberl, D. D.; Kile, D. E.; Drits, V. A. On Geological Interpretations of Crystal Size Distributions: Constant Vs. Proportionate Growth. *Am. Miner.* **2002,** *87*, 1235-1241.

50. Wagner, C. Theorie Der Alterung Von Niederschlägen Durch Umlösen (Ostwald-Reifung). *Zeitschrift für Elektrochemie, Berichte der Bunsengesellschaft für physikalische Chemie* **1961,** *65*, 581-591.

51. Priester, L., *Grain Boundaries*. Springer Dordrecht 2013.

52. Klapp, S. A.; Klein, H.; Kuhs, W. F. First Determination of Gas Hydrate Crystallite Size Distributions Using High-Energy Synchrotron Radiation. *Geophys. Res. Lett.* **2007,** *34*, L13608.

53. Rodriguez Navarro, A. B.; Alvarez-Lloret, P. O.-H., M.; Rodriguez-Gallego, M. Automatic Crystal Size Determination in the Micrometer Range from Spotty X-Ray Diffraction Rings of Powder Samples. *Journal of American Ceramic Society* **2006,** *89*, 2232-2238.

54. Als-Nielsen, J.; McMorrow, D., *Elements of Modern X-Ray Physics*. 2nd Edition ed.; Wiley: 2011.

55. Chuvilin, E. M.; Istomin, V. A.; Safonov, S. S. Residual Nonclathrated Water in Sediments in Equilibrium with Gas Hydrate Comparison with Unfrozen Water. *Cold Reg. Sci. Technol.* **2011,** *68*, 68-73.
56. Sell, K.; Saenger, E. H.; Falenty, A.; Chaouachi, M.; Haberthur, D.; Enzmann, F.; Kuhs, W. F.; Kersten, M. On the Path to the Digital Rock Physics of Gas Hydrate-Bearing Sediments - Processing of in Situ Synchrotron-Tomography Data. *Solid Earth* **2016,** *7*, 1243-1258.
57. Falenty, A.; Chaouachi, M.; Neher, S. H.; Sell, K.; Schwarz, J.-O.; Wolf, M.; Enzmann, F.; Kersten, M.; Haberthur, D.; Kuhs, W. F. Stop-and-Go in Situ Tomography of Dynamic Processes - Gas Hydrate Formation in Sedimentary Matrices. *Acta Crystallographica Section A* **2015,** *71*, s154.
58. Genov, G.; Kuhs, W. F.; Staykova, D. K.; Goreshnik, E.; Salamatin, A. N. Experimental Studies on the Formation of Porous Gas Hydrates. *Am. Miner.* **2004,** *89*, 1228-1239.
59. Kuhs, W. F.; Staykova, D. K.; Salamatin, A. N. Formation of Methane Hydrate from Polydisperse Ice Powders. *J. Phys. Chem. B* **2006,** *110*, 13283-13295.
60. Staykova, D. K.; Kuhs, W. F.; Salamatin, A. N.; Hansen, T. Formation of Porous Gas Hydrates from Ice Powders: Diffraction Experiments and Multistage Model. *J. Phys. Chem. B* **2003,** *107*, 10299-10311.
61. Daniels, J. E.; Drakopoulos, M. High-Energy X-Ray Diffraction Using the Pixium 4700 Flat-Panel Detector. *J. Synchrot. Radiat.* **2009,** *16*, 463-468.
62. Soille, P. J.; Ansoult, M. M. Automated Basin Delineation from Digital Elevation Models Using Mathematical Morphology. *Signal Process* **1990,** *20*, 171-182.
63. Milch, J. R.; Minor, T. C. The Indexing of Single-Crystal X-Ray Rotation Photographs. *Journal of Applied Crystallography* **1974,** *7*, 171-182.
64. Schneider, C. A.; Rasband, W. S.; Eliceiri, K. W. Nih Image to ImageJ: 25 Years of Image Analysis. *Natural Methods* **2012,** *9*, 671-675.
65. DuQuesnay, J. R.; Posada, M. C. D.; Beltran, J. G. Novel Gas Hydrate Reactor Design: 3-in-1 Assessment of Phase Equilibria, Morphology and Kinetics. *Fluid Phase Equilib.* **2016,** *413*, 148-157.
66. Taylor, C. J.; Miller, K. T.; Koh, C. A.; Sloan, E. D. Macroscopic Investigation of Hydrate Film Growth at the Hydrocarbon/Water Interface. *Chem. Eng. Sci.* **2007,** *62*, 6524-6533.
67. Davies, S. R.; Sloan, E. D.; Sum, A. K.; Koh, C. A. In Situ Studies of the Mass Transfer Mechanism across a Methane Hydrate Film Using High-Resolution Confocal Raman Spectroscopy. *J. Phys. Chem. C* **2010,** *114*, 1173-1180.
68. English, N. J.; Lauricella, M.; Meloni, S. Massively Parallel Molecular Dynamics Simulation of Formation of Clathrate-Hydrate Precursors at Planar Water-Methane Interfaces: Insights into Heterogeneous Nucleation. *J. Chem. Phys.* **2014,** *140*, 204714.
69. Stamatis, D. H., *Six Sigma and Beyond: Statistics and Probability, Volume Iii*. CRC Press Taylor & Francis Group: 2002; Vol. III.
70. Kile, D. E.; Eberl, D. D. On the Origin of Size-Dependent and Size-Independent Crystal Growth: Influence of Advection and Diffusion. *Am. Miner.* **2003,** *88*, 1514-1521.
71. Hillert, M. On the Theory of Normal and Abnormal Grain Growth. *Acta Metallurgica* **1965,** *13*, 227-238.
72. Kim, B.-N.; Suzuki, T. S.; Morita, K.; Yoshida, H.; Sakka, Y.; Matsubara, H. Densification Kinetics During Isothermal Sintering of 8ysz. *Journal of the European Ceramic Society* **2016,** *36*, 1269-1275.
73. Humphreys, F. J.; Hatherley, M., *Recrystallization and Related Annealing Phenomena*. 1st ed.; Pergamon Press: Oxford, UK, 2002.

74. Legagneux, L.; Taillandier, A.-S.; Domine, F. Grain Growth Theories and the Isothermal Evolution of the Specific Surface Area of Snow. *J. Appl. Phys.* **2004,** *95*, 6175-6184.

75. Fischmeister, H. G., G., Ostwald Ripening – a Survey. In: Materials Science Research. In *Sintering and Related Phenomena* Kuczynski, G. C. Ed.; Plenum Press: New York. London; 1973; Vol. 6, pp 119-149.

76. Legagneux, L.; Domine, F. A Mean Field Model of the Decrease of the Specific Surface Area of Dry Snow During Isothermal Metamorphism. *Journal of Geophysical Research: Earth Surface* **2005,** *110*.

77. Taillandier, A.-S.; Domine, F.; Simpson, W. R.; Sturm, M.; Douglas, T. A. Rate of Decrease of the Specific Surface Area of Dry Snow: Isothermal and Temperature Gradient Conditions. *Journal of Geophysical Research: Earth Surface* **2007,** *112*, n/a-n/a.

78. Feltham, P. Grain Growth in Metals. *Acta Metallurgica* **1957,** *5*, 97-105.

79. Louat, N. P. On the Theory of Normal Grain Growth. *Acta Metallurgica* **1974,** *22*, 721-724.

80. Anderson, M. P.; Srolovitz, D. J.; Grest, G. S.; Sahni, P. S. Computer Simulation of Grain Growth—I. Kinetics. *Acta Metallurgica* **1984,** *32*, 783-791.

81. Srolovitz, D. J.; Anderson, M. P.; Sahni, P. S.; Grest, G. S. Computer Simulation of Grain Growth—Ii. Grain Size Distribution, Topology, and Local Dynamics. *Acta Metallurgica* **1984,** *32*, 793-802.

82. Berger, A.; Herwegh, M. Grain Coarsening in Contact Metamorphic Carbonates: Effects of Second-Phase Particles, Fluid Flow and Thermal Perturbations. *Journal of Metamorphic Geology* **2004,** *22*, 459-474.

83. Frost, H. J. Stochastic Models of Grain Growth *Mat. Sci. Forum* **1992,** *94-96*, 903-908.

84. Stern, L. A.; Kirby, S. H.; Circone, S.; Durham, W. B. Scanning Electron Microscopy Investigations of Laboratory-Grown Gas Clathrate Hydrates Formed from Melting Ice, and Comparison to Natural Hydrates. *Am. Miner.* **2004,** *89*, 1162-1175.

85. Falenty, A.; Qin, J.; Salamatin, A. N.; Yang, L.; Kuhs, W. F. Fluid Composition and Kinetics of the in-Situ Replacement in Ch4-Co2 Hydrate System. *The Journal of Physical Chemistry C* **2016,** *120*, 27159-27172.

86. Uchida, T.; Kishi, D.; Shiga, T.; Nagayama, M.; Gohara, K. Sintering Process Observations on Gas Hydrates under Hydrate-Stable and Self-Preservation Conditions. *J. Chem. Eng. Data* **2015,** *60*, 284-292.

87. Jacobson, L. C.; Hujo, W.; Molinero, V. Amorphous Precursors in the Nucleation of Clathrate Hydrates. *American Chemical Society* **2010,** *132*, 11806-11811.

88. Vatamanu, J.; Kusalik, P. G. Observation of Two-Step Nucleation in Methane Hydrates. *Phys. Chem. Chem. Phys.* **2010,** *12*, 15065-15072.

89. Zhang, Z.; Walsh, M. R.; Guo, G.-J. Microcanonical Molecular Simulations of Methane Hydrate Nucleation and Growth: Evidence That Direct Nucleation to Si Hydrate Is among the Multiple Nucleation Pathways. *Phys. Chem. Chem. Phys.* **2015,** *17*, 8870-8876.

90. Pirzadeh, P.; Kusalik, P. G. Molecular Insights into Clathrate Hydrate Nucleation at an Ice-Solution Interface. *J. Am. Chem. Soc.* **2013,** *135*, 7278-7287.

91. Dec, S. F. Surface Transformation of Methane-Ethane Si and Sii Clathrate Hydrates. *J. Phys. Chem. C* **2012,** *116*, 9660-9665.

92. Salamatin, A. N.; Falenty, A.; Hansen, T. C.; Kuhs, W. F. Guest Migration Revealed in Co_2 Clathrate Hydrates. *Energy Fuels* **2015,** *29*, 5681-5691.

93. Hansen, T. C.; Falenty, A.; Kuhs, W. F. Lattice Constants and Expansivities of Gas Hydrates from 10 K up to the Stability Limit. *J. Chem. Phys.* **2016,** *144*, 054301.

94. Klapp, S. A.; Enzmann, F.; Walz, P.; Huthwelker, T.; Tuckermann, J.; Schwarz, J. O.; Pape, T.; Peltzer, E. T.; Mokso, R.; Wangner, D., et al. Microstructure Characteristics During Hydrate Formation and Dissociation Revealed by X-Ray Tomographic Microscopy. *Geo-Mar. Lett.* **2012,** *32*, 555-562.

95. Klapp, S. A.; Hemes, S.; Klein, H.; Bohrmann, G.; MacDonald, I.; Kuhs, W. F. Grain Size Measurements of Natural Gas Hydrates. *Mar. Geol.* **2010,** *274*, 85-94.

96. Klapp, S. A.; Murshed, M. M.; Pape, T.; Klein, H.; Bohrmann, G.; Brewer, P. G.; Kuhs, W. F. Mixed Gas Hydrate Structures at the Chapopote Knoll, Southern Gulf of Mexico. *Earth Planet. Sci. Lett.* **2010,** *299*, 207-217.

97. Rempel, A. W. A Model for the Diffusive Growth of Hydrate Saturation Anomalies in Layered Sediments. *Journal of Geophysical Research: Solid Earth* **2011,** *116*, B10105.

98. Kipfstuhl, S.; Pauer, F.; Kuhs, W. F.; Shoji, H. Air Bubbles and Clathrate Hydrates in the Transition Zone of the Ngrip Deep Ice Core. *Geophys. Res. Lett.* **2001,** *28*, 591-594.

99. Wu, J. Y.; Ning, F. L.; Trinh, T. T.; Kjelstrup, S.; Vlugt, T. J. H.; He, J. Y.; Skallerud, B. H.; Zhang, Z. L. Mechanical Instability of Monocrystalline and Polycrystalline Methane Hydrates. *Nat. Commun.* **2015,** *6*.

100. Bagherzadeh, S. A.; Alavi, S.; Ripmeester, J.; Englezos, P. Formation of Methane Nano-Bubbles During Hydrate Decomposition and Their Effect on Hydrate Growth. *The Journal of Chemical Physics* **2015,** *142*, 214701.

101. Durham, W. B.; Kirby, S. H.; Stern, L. A.; Zhang, W. The Strength and Rheology of Methane Clathrate Hydrate. *J. Geophys. Res.-Solid Earth* **2003,** *108*, 11, 2182.

102. Durham, W. B.; Prieto-Ballesteros, O.; Goldsby, D. L.; Kargel, J. S. Rheological and Thermal Properties of Icy Materials. *Space Science Reviews* **2010,** *153*, 273-298, ^Durham2010^.

103. Kuhs, W. F.; Klapproth, A.; Gotthardt, F.; Techmer, K.; Heinrichs, T. The Formation of Meso- and Macroporous Gas Hydrates. *Geophys. Res. Lett.* **2000,** *27*, 2929-2932.

104. Ning, F.; Yu, Y.; Kjelstrup, S.; Vlugt, T. J. H.; Glavatskiy, K. Mechanical Properties of Clathrate Hydrates: Status and Perspectives. *Energy Environ. Sci.* **2012,** *5*, 6779-6795.

105. Kurzydłowski, K. J.; Bucki, J. J. Flow Stress Dependence on the Distribution of Grain Size in Polycrystals. *Acta Metallurgica et Materialia* **1993,** *41*, 3141-3146.

106. Berbenni, S.; Favier, V.; Berveiller, M. Micro–Macro Modelling of the Effects of the Grain Size Distribution on the Plastic Flow Stress of Heterogeneous Materials. *Computational Materials Science* **2007,** *39*, 96-105.

107. Abu Bakar, M. R.; Nagy, Z. K.; Saleemi, A. N.; Rielly, C. D. The Impact of Direct Nucleation Control on Crystal Size Distribution in Pharmaceutical Crystallization Processes. *Crystal Growth & Design* **2009,** *9*, 1378-1384.

108. Hounslow, M. J.; Reynolds, G. K. Product Engineering for Crystal Size Distribution. *Aiche J.* **2006,** *52*, 2507-2517.

109. Higgins Michael, D., Measurement of Crystal Size Distributions. In *Am. Miner.*, 2000; Vol. 85, p 1105.

110. Higgins Michael, D., Closure in Crystal Size Distributions (, Verification of CSD Calculations, and the Significance of CSD Fans. In *Am. Miner.*, 2002; Vol. 87, p 171.

111. Higgins, M. D. Comment on Berger A., Herwegh M., Schwarz J.-O., Putlitz B., (2011). Quantitative Analysis of Crystal/Grain Sizes and Their Distributions in 2d and 3d. J. Struct. Geol. 33(12):1751–1763. *Journal of Structural Geology* **2012,** *40*, 54-55.

112. MOCK, A.; JERRAM, D. A. Crystal Size Distributions (CSD) in Three Dimensions: Insights from the 3d Reconstruction of a Highly Porphyritic Rhyolite. *Journal of Petrology* **2005,** *46*, 1525-1541.

Chapter 5 Conclusions and outlook

In this thesis, the novel method 'fast X-ray diffraction crystal size distribution analysis' (FXD-CSD) and its development has been presented. It is shown, that FXD-CSD enables the user to measure CSDs with unprecedented sampling statistics and accuracy. CSDs are obtained from polycrystalline materials and crystalline powders, measured in transmission geometry. To accomplish this, a minimal amount of sample preparation is needed. Utilizing integrated X-ray diffraction intensities of individual crystals to deduce size information, gives the unique possibility to directly deduce volume derived CSDs. This is considered to be more accurate and robust, than deriving size information from two-dimensional arbitrarily cut surfaces, like they are recorded with electron microscopy or light microscopy. Two-dimensional techniques need assumptions on the crystal shapes to deduce volume information, or the volume has to be constructed from many, tediously obtained sections, *e.g. via* focused ion beam ablation. Not in need of this, FXD-CSD constitutes a destruction-free method with such fast sampling rates (few hours) that enable the unique possibility to perform CSD-based *in situ* measurements of coarsening phenomena with good sampling statistics. Of course, it is always possible to calculate the average crystal size from a measured CSD.

In Chapter 2, comprising the 1st manuscript presented, the method has been described in all its details and an extensive discussion of the limiting factors and range of application is given. The latter is based on the results obtained by measuring crystalline powders with known CSDs. Comparing the known CSDs with the FXD-CSD derived CSDs has shown good agreement.

With these comparisons the conclusion could be drawn, that the lower limit of detection mainly depends on the incident beam brilliance and the scattering power of the material under investigation. With the used lab equipment (molybdenum X-ray tube with pinhole collimator) this is found to be 1 µm; in Chapter 4, the 3rd publication presented, it is shown that this can be brought down easily to 500 nm when using synchrotron radiation.

Furthermore, it has been possible to formulate a more general statement about the upper limit of application regarding the average crystal size. It is essentially determined by the incident beam dimensions. The illuminated sample area, the area hit by the incident beam, should be large to ensure that only a small portion (ideally less than 5 %) of the crystals are affected by sample edge effect (Appendix B 2).

A further conclusion drawn, is that the reference quality is crucial to obtain accurate results. The reference has to be single crystalline, should have a narrow size distribution, and the crystals should be isometric and uniform. Associated errors arise mainly from difficulties when deducing the crystal volume distribution of the potential reference materials *via* two-dimensional imaging techniques. Since two-dimensional images lack precise information about the third dimension, universal crystal shape assumptions have to be made. These assumptions can only be correct when the crystals are uniform in shape. The crystal quality of the reference plays a subordinated role but can broaden the rocking curve to such an extent that they become difficult to be analyzed properly. Crystals with high internal tension or cracked crystals can produce broad and odd-shaped rocking curves. These rocking curves increase potential peak overlap (Appendix B 2.3) and are hard to discern from rocking curves evolving from overlapping diffraction spots.

The results presented in Chapter 3, the 2nd publication presented, show that with FXD-CSD it is possible to determine CSDs of technical ceramics with a minimum of preparation efforts. This publication constitutes an application example analyzing a technical ceramic and using a common lab diffractometer. By this means, we were able to qualify CSDs with such a statistical significance that alike probability density functions (PDF) could safely be discriminated *via* least square fitting. This enables one to make statements about the underlying growth mechanism. Concerning the alumina ceramics, a log-normal PDF fits best. Furthermore, we were able to identify upcoming abnormal grain growth in the measured CSDs.

In Chapter 4, the 3rd publication, the results of a coarsening study on gas hydrate are presented. The data were obtained using synchrotron radiation (Synchrotron Research Facility, ESRF). The presented results are mainly aiming to answer fundamental research questions. Among other findings, it was shown that grain growth proceeds several orders of magnitude more slowly than in normal water ice at similar PT conditions. Besides that, the results show that FXD-CSD is quite flexible regarding its application range and equipment used.

Regarding the aspect of the methodology including the computational implementation of FXD-CSD two major improvements can be addressed in the future: 1) The evaluation of individual rocking curves can be improved. 2) New and more suitable reference materials should be tested or manufactured. These two points are presented in the following.

1) Besides the manual examination, so far, the individual rocking curves are routinely only tested by simple measures: the rocking curves need to have a certain minimum length – their extension in sample rotation direction, equivalent to the number of images they appear – and the existence of one single maximum between the tails of the rocking curves. This of course leaves space for all sorts of odd shaped rocking curves, e.g. through close overlapping peaks not showing two maxima. So far controlling the amount of peak overlap and manually verifying the shape of the rocking curves was sufficient to prevent bias.

   To automate the recognition of odd shaped rocking curves, the variance within their individual central moments (*i.e.* standard deviation, variance, skewness, and peakedness) constitute a promising tool to be used as rejection criteria (Appendix B 6). One would for example reject a rocking curve which turned out to be extraordinary broad (too high a variance). This approach was tested and partially implemented in the software but is not routinely applied.

   Applying this automated data treatment necessitates the correction of the rocking curve for the angular velocity factor (see Figure App. B-4). Up to now this has not been done. At present, only the integrated intensity is corrected and not the extension they appear in reflection state.

   Properly implemented, the central moment rejection criteria should constitute a robust rejection argument and is likely to further improve data quality.

   A different and more sophisticated approach to further improve data quality is to fit mathematical functions (e.g. a Voigt function (Young & Wiles, 1982) or a learned-function (Hepp & Baerlocher, 1988)) to each rocking curve. Analogue to the approach described above, the fit parameters can be used as rejection criteria. Of course, this also requires the correction for the angular velocity factor prior to the fitting.

Besides the option of rejecting odd rocking curves, this approach offers the possibility to fit multiple peak functions to the rocking curve, which could be used to separate overlapping peaks more accurate and minimize the number of rejected peaks.

This ideally is done in three-dimensions, meaning that three-dimensional peak functions are fitted to the voxel volume (recall Section 2.3.4) of the diffracted intensity. Peak fitting in three-dimensions would replace the water-shedding (recall Section 2.3.4). This would improve data quality and increase the resolution but would also increase computational time.

2) Finding a more suitable reference sample should certainly be one goal in the future. The materials tested so far, namely the LaB_6-Powder and the corundum crystal size fractions did either show too broad distributions (see Section 2.4.1) which lead to difficulties defining the left tail of the distribution because they are partially below the detection limit or showed complicated crystal shapes which needed to be tediously measured (see Section 2.4.1 and Appendix A 2). The task of finding other materials can be addressed in two ways: i) By following the same manner as it was done for the corundum crystal size fractions but using a different staring material. For their production, a single crystalline starting material was grinded and subsequently separated in to several narrow crystal size fraction *via* sedimentation in water (see Appendix B 4). A different material e.g. with a strong pronounced cleavage, might shatter in more isometric shapes and produce better results. ii) A different approach is to use perfect micro-meter sized single crystals, which unfortunately are not easily available. However, recent developments in the field of nanomaterials did produce promising results. These are achieved *via* subsequent crystallization of micro spheres (Nakamura *et al.*, 2016; Shimogaki *et al.*, 2014; Tasaki *et al.*, 2018; Yang *et al.*, 2008) or *via* mass-crystallization (Pieniążek *et al.*, 2016; Chen *et al.*, 2011).

In the following section the technical components of diffractometers used for FXD-CSD measurements, will be discussed regarding possible improvements to enhance data quality and speed up data collection. FXD-CSD works best with a homogenous and bright beam with a large cross-section and low divergence. At first possible improvements concerning the X-ray source and the used X-ray optics are presented. Later on, advances in detector technique are presented.

Concerning the technical aspects of the used X-ray diffraction equipment and the possible improvements which could be applied, one has to differentiate between lab sources and synchrotron sources. Synchrotron radiation, from a 3rd generation source, simply has such superior characteristics in terms of brilliance[12], that there is not much room for improvements. Conversely, the lab source used in our work, a molybdenum tube with monochromator crystal and pinhole collimator, provides several entry points to enhance the quality of the measured data by improving the incident beam quality. The sealed tube used, operating with a line-focused electron beam, is producing a rectangular shaped diverging X-ray beam which is hitting the graphite monochromator crystal right after leaving the tube. The diffracted, monochromatic beam is collimated by a pinhole collimator, which means that most parts of the beam are blocked and only a small portion of the intensity is used.

To improve the performance of X-ray sources the most important point is, increasing the intensity emerging the X-ray source because once the radiation is emitted, brightness can only be increase on

[12] Brilliance: number of photons passing a surface with a unit solid angle [photons/second per mm^2 per milliradian^2]

the expense of divergence. Thus, there are two options: 1) using a more efficient source and 2) using more suitable X-ray optics.

1) In a conventional X-ray tube, the anode is stationary while it is hit by the electron beam. The accelerated electrons are causing the anode to emit X-rays. The amount of emitted X-rays depends on the electron flux hitting the target. While it is relatively easy to increase the electron-flux hitting the anode to increase the X-ray output, dissipating the occurring heat is challenging and a possible target melt down is the limiting factor. The limit is usually given as power load (kW) or as specific power load (kW mm^{-2}). A conventional copper X-ray tube has recommended power loads well below 1 kW mm^{-2} (Arndt, 2006). To increase the possible power load, several solutions are available: I) microfocus sources work with a highly focused electron beam hitting the anode. Such a small focal point can produce high brilliance X-rays while having a relatively small heat production. Here the power load is relatively low, but the specific power load is high. II) rotating anodes tubes constitute another solution delivering high brilliance and beams with large cross-sections. By constructing the anode as rotating disk, hit off-center by the electron beam, the produced heat energy is distributed over much bigger area and thus can be exhausted more easily. (Arndt, 2006; Arndt *et al.*, 2006) III) a different approach are liquid-metal anodes. Here the electron beam hits a vertical metal-jet. The liquid metal, usually gallium or indium alloys, is pumped around in a closed cycle which easily can be cooled and obviously does not run into danger of melting.

   With such improvements the possible power load and therefore the emitted X-ray radiation can be increased by about an order of magnitude.

2) Using suitable X-ray optics can improve the utilization rate of the produced radiation. The key to achieve an improved utilization is to capture a large solid angel of the radiation exiting the tube window. Since the exiting X-rays are radial spreading from the focal area, the distance between cathode and optics has to be as small as possible. One way to achieve an improvement is to use cross-coupled Göbel mirrors which at once monochromatize and collimate the X-rays but do not block most of the intensity like a pinhole does. A Göbel mirror is a bent multilayered artificial crystal. Its parabola shaped surface is parallelizing the beam. With this setup, beams with large cross sections can be produced. A different solution are capillary fiber optics in combinations with a monochromator crystal. Such fiber optics are arrays of hollow glass tubes that guide the X-rays by total reflections along the surfaces of the fibers. Fiber optics have the advantage that they can be placed near the source. This way the fiber optic captures large amount s of the emitted intensity.(He, 2009)

   No matter how the beam is monochromatized and brought into shape, all setups are ideally combined with two variable crossed slit systems near the sample. Being able to freely manipulate the incident beam dimensions gives the opportunity to change the irradiated sample volume easily to control the number or observations on the detector (see Appendix B 2.1). A pair of crossed slits is needed to block the radiation scattered at the first (in beam direction) slit system.

Another technical aspect which can be improved are the detectors used. As mentioned in the introduction of this thesis, the availability of two-dimensional detectors, such as image plates, enabled the FXD-CSD method in the first place. CCD (charged-couple device) detectors and the advances made

with them in terms of higher frame rates, facilitated the three-dimensional measurement procedure. It is thus no surprise that the now upcoming improved CMOS (complementary metal-oxide-semiconductors) detectors will bring further improvements. Compared to CCD detectors CMOS detectors are able to read out each pixel individually, what reduces the frame rate to 20 Hz and allows for continuous data collection. Recent developments have improved the performance of CMOS detectors regarding their X-ray hardness, their dynamic range and it was possible to reduce thermal and readout noise (Hasegawa *et al.*, 2009; Thompson *et al.*, 2013, 2014).

By now the performance of CMOS detectors is comparable with common CCD detectors but they are much faster, have lower power consumption and are more flexible in the way how the data is read out. It should, for example, be possible to only read out certain areas of the detector to reduce the amount of unnecessary data; regarding FXD-CSD and other diffraction experiments performed with known structures this should be possible because the region where the diffracted intensity is hitting the detector is known. This way one could lower the amount of data that needs to be process drastically.

Regarding the computational implementation of FXD-CSD the needed processing time is a further point what can be improved. So far, the software *fxd-csd* is written in Phyton which is, regarding the computation time, for sure not the best choice. But still, besides than switching to a faster language (e.g. C++), there are other ways to improve performance. These are for example a multithreading approach, meaning that e.g. the intensity extraction (see Section 2.3.4) does not have to be done one by one in strict procedural manner. Switching at least partially to GPU (graphical processing unit) processing instead of only using the CPU (central processing unit) would also improve the performance.

In the following, possible applications or rather application environments of FXD-CSD are presented. So far it was shown that with FXD-CSD one is able to measure real volume based CSDs of polycrystalline materials with a minimum of sample preparation. The low amount of preparation effort needed is due to the highly penetrative nature of X-rays and is delivering further opportunities. Working with X-rays means that one does not have to have direct sight or contact to the sample under investigation. This means, as we already have shown with our high-pressure gas hydrate studies (see Chapter 4), that one is able to measure under non-ambient conditions. In general, one can state, whenever one is able to perform two-dimensional powder diffraction measurements of decent quality one should be able to also apply FXD-CSD. The demand that powder diffraction measurements are possible ensures that a sufficient angular range of the diffraction cones are detectable, which ensures good sampling statistics and might become important if the needed structure factors are not known for the present P/T conditions. If they are not available the (radially integrated) powder patterns can be used to calculate the structure factors *via* a Rietveld analysis (Rietveld, 1969) e.g. using *EXPGUI* (Toby, 2001) which is a graphical user interface for *GSAS*(Larson & Von Dreele, 2000)

Such a non-ambient environment may for example be a halogen lamp furnace with a protective atmosphere, equipped with windows for X-rays diffraction measurements (e.g. Klinkenberg & Klein, 2016). In case of measurements in any sort of container, one of course always has to measure a reference sample in the same environment (yet usually at ambient conditions) to account for the likely attenuation effects e.g. caused by the windows in use. The gas hydrate studies presented in Chapter 4 provide a good example for a high-pressure application and an example for a situation where the

reference sample had to be measured inside the sample container to have the same attenuation effects for both, reference and sample measurements.

A further possible environment are high pressure measurements e.g. in Paris-Edinburgh cells. These high-pressure cells are built for diffraction or tomography experiments measuring rather large sample volumes (several mm³). The new RoToPEc module for example is capable of reaching pressures up to 15 GPa an 2500K. (Philippe *et al.*, 2016)

The gas hydrate studies presented in Chapter 4 show that *in situ* studies can be carried out with FXD-CSD. Whether it is possible to resolve the CSD evolution over time with FXD-CSD depends on the time period the processes take place one wants to study. So far, we were able to resolve changes on an hour scale (down to 0.5h) using synchrotron radiation working with a rather weak scatterer. With faster detectors and strong scatterers like metals or ceramic it should be straightforward to bring this down to the minute or even second scale (fast detectors needed). Working with lab sources, with a set-up designed for FXD-CSD, one should be able to resolve time dependent processes down to the hour or upper minute scale. In combination with the possibility to measure under non-ambient environmental conditions this opens unique opportunities to study coarsening processes combined with texture development. With simple modifications to the software it should also be possible to investigate directed growth in combination with texture development (Tommaseo & Klein, 2009), which certainly could open up new perspectives to FXD-CSD. Since the Bragg spot positions of each crystal is stored, it is possible to calculate their orientation. With the crystal size, the orientation and its change over time it will be possible to make statements about the interplay of texture, CSD and its development.

5.1 References

Arndt, U. W. (2006). *International Tables for Crystallography*, Vol. *F*, pp. 159–167. Chester, England: Published for the International Union of Crystallography by Kluwer Academic Publishers.

Arndt, U. W., Creagh, D. C., Deslattess, R. D., Hubbell, J. H., Indelicato, P., Kessler JR, E. G. & Lindroth, E. (2006). International Tables for Crystallography Chester, England: Published for the International Union of Crystallography by Kluwer Academic Publishers.

Chen, W., Liu, W., Chen, C., Wang, R. & Feng, Q. (2011). *CrystEngComm*. **13**, 3959–3961.

Hasegawa, K., Hirata, K., Shimizu, T., Shimizu, N., Hikima, T., Baba, S., Kumasaka, T. & Yamamoto, M. (2009). *J. Appl. Crystallogr.* **42**, 1165–1175.

He, B. B. (2009). Two-Dimensional X-Ray Diffraction Hoboken: J. Wiley & Sons, Inc.

Hepp, A. & Baerlocher, C. (1988). *Aust. J. Phys.* **41**, 229–236.

Klinkenberg, C. & Klein, H. (2016). *Mater. Sci. Forum*. **879**, 948–953.

Larson, A. C. & Von Dreele, R. B. (2000). General Structure Analysis System (GSAS) Los Alamos: National Laboratory Report LAUR.

Nakamura, D., Tanaka, T., Ikebuchi, T., Ueyama, T., Higashihata, M. & Okada, T. (2016). *Electron. Commun. Japan*. **99**, 58–63.

Philippe, J., Le Godec, Y., Mezouar, M., Berg, M., Bromiley, G., Bergame, F., Perrillat, J. P., Alvarez-Murga, M., Morand, M., Atwood, R., King, A. & Régnier, S. (2016). *High Press. Res.* **36**, 512–532.

Pieniążek, A., Witkowski, B. S., Reszka, A., Godlewski, M. & Kowalski, B. J. (2016). *Opt. Mater. Express*. **6**, 3741–3750.

Rietveld, H. M. (1969). *J. Appl. Crystallogr.* **2**, 65–71.

Shimogaki, T., Okazaki, K., Yamasaki, K., Fusazaki, K., Mizokami, Y., Tetsuyama, N., Higashihata, M., Ikenoue, H., Nakamura, D. & Okada, T. (2014). *Appl. Phys. A Mater. Sci. Process.* **117**, 269–273.

Tasaki, R., Higashihata, M., Suwa, A., Ikenoue, H. & Nakamura, D. (2018). *Appl. Phys. A*. **124:161**, 6.

Thompson, A. C., Nix, J. C., Achterkirchen, T. G. & Westbrook, E. M. (2013). *Journal of Physics:*

Conference Series, Vol. *425*, p. 012018. Bristol: IOP Publishing.
Thompson, A. C., Westbrook, E. M., Lavender, W. M. & Nix, J. C. (2014). *Journal of Physics: Conference Series*, Vol. *493*, p. 012019. Bristol: IOP Publishing.
Toby, B. H. (2001). *J. Appl. Crystallogr.* **34**, 210–213.
Tommaseo, C. E. & Klein, H. (2009). *Pract. Metallogr.* **46**, 77–96.
Yang, W., Wang, H., Cheng, X., Xie, Z. & An, L. (2008). *J. Am. Ceram. Soc.* **91**, 2732–2735.
Young, R. A. & Wiles, D. B. (1982). *J. Appl. Crystallogr.* **15**, 430–438.

Appendix A Appendix of 1st publication

A 1 Intensity corrections

Complementary to the main part of the article the additional or optimal intensity corrections are described here.

A 1.1 Polarization

Depending on the source and the X-ray optics in use, the polarization of the indecent beam can affect the performed intensity measurements. The decisive factors are the primary degree of polarization coming from the source and the angle between the primary beam and the diffracted beam by the monochromator. The monochromatic beam is polarized a second time by the crystals in the sample. From this a crystal orientation dependent polarization factor is calculated. Analogue to the Lorentz correction, describe in the main article, a position sensitive detector necessitates a general expression for the polarization correction *P*. This is derived from (Kabsch, 1988).

$$P = (1 - 2\mathrm{p})\left[1 - \left(\frac{\mathbf{n}\cdot\mathbf{h_r}}{|\mathbf{h_r}|}\right)^2\right] + \mathrm{p}(1 + \left[\frac{\mathbf{h_r}\cdot\mathbf{S_0}}{|\mathbf{h_r}| * |\mathbf{S_0}|}\right]^2) \qquad \text{Eq. App. A 1}$$

With *p* being the degree of polarization; expressed by the ratio of the two perpendicular electromagnetic field vectors, both being perpendicular to the propagation direction, $\mathbf{n}$ the polarization plane normal, $\mathbf{S_0}$ the incident beam vector, and $\mathbf{h_r}$ the reciprocal lattice vector in diffraction state. Concerning the data presented in the main body of the article and previously published data (Chaouachi *et al.*, 2017), the measurements are either performed with radiation form a X-ray tube (Molybdenum λ ~ 0.71Å) or with three-pole wiggler injection divides at the ESRF (Synchrotron λ < 0.2 Å). Both sources are circularly polarized (Chavanne *et al.*, 1996; Tschentscher & Suortti, 1998; Hiraoka *et al.*, 2005) and of short wavelength, what makes the polarization negligibly small. Figure App. B-15 in the supporting information shows the theoretical function graph for both sources.

A 2 Crystal volume calculation from SEM data

To estimate the volume based CSD of the samples, the individual crystal dimensions are extracted from the SEM images (Figure 2.4 and Figure 2.5 and Figure App. B-7 - Figure App. B-9). For the SEM measurements a small sample portion is placed on a glass plate and spread with a droplet of ethanol. After the ethanol is completely evaporated the SEM sample holder, equipped with double-sided adhesive carbon tape is pressed on the sample. If done with care, size fractionation has to be avoided, this ensures a well spread and separated subsampling of the bulk sample powder. The taken SEM images are investigated manually with a small Python script by dragging a rectangular enclosing box around each crystal. The half axis (d_x, d_y) of these boxes are automatically stored and used for the volume calculation. Since the crystals are not ideally shaped and the SEM images are only two-dimensional, at best can be called semi three-dimensional, they do not provide reliable information of the 3rd dimension and assumptions have to be made. In case of the LaB_6-Powder sample the third dimension is assumed to be similar to the d_x and d_y direction because the crystal shape is approximately spherical (see Figure 2.4). Therefore, the mean of the box dimensions d_m is taken as crystal diameter and used for a spherical volume calculation.

Concerning the corundum CSFs samples, the crystal shapes differ significantly from a spherical habitus. To estimate the crystal volume as accurate as possible the following approach is chosen: the measured crystal dimensions are used to estimate the crystal area in the images and modified by a factor of 0.75 because the enclosing boxes are always bigger than the crystal (which are not rectangular but rather more ellipsoidal. The third dimension is estimated by taking half of the smaller box dimension d_{small} because it is very likely that the crystals are lying on their adhesively or mechanically most stable largest side. This assumption is supported by the sample preparation method (spreading the powder with an ethanol droplet) and was visually verified by stereo microscopy. With this information the crystal volume V_c is calculated.

$$V_c = \left(\frac{d_x * d_y}{2}\right)^2 * 0.75 * \ d_{small} * 0.5 \qquad \text{Eq. App. A 2}$$

A 3 Error estimation

A 3.1 S1 Error estimation.

The *S1* scaling factor is determined between the fitted mean values ($\mu_{ref\ CSD}$ and $\mu_{ref\ ID}$) of the SEM derived *reference* volume distribution and the diffraction derived *reference* intensity distribution (see Section 2.3.1); the distributions are fitted in log-space. The uncertainties of both fitted mean values contribute to the total uncertainty:

$$\Delta S1_{\ln(Vol)} = \sqrt{\Delta\mu^2_{ref\ ID} + \Delta\mu^2_{ref\ CSD}} \qquad \text{Eq. App. A 3}$$

Since S1 is not only used in log-space its uncertainty is also given in linear space where the error is asymmetric; here the positive error is given:

$$\Delta S1_{Vol^+} = e^{(\mu+\Delta S1_{\ln(Vol)})} - e^{(\mu)} \qquad \text{Eq. App. A 3}$$

The error contributed by the *S1* determination to the final result, the *sample* diameter distribution, is given by the following expression; again, the positive error is used.

$$\Delta S1_{Dia^+} = \sqrt[3]{\frac{6}{\pi}}\, e^{\frac{\mu}{3}}\left(e^{\frac{\Delta S1_{\ln(Vol)^+}}{3}} - 1\right) \qquad \text{Eq. App. A 4}$$

A 3.2 Error introduce by log-normal PDF fitting to the final CSD

The resulting *sample* distribution is represented in linear-space and fitted by a log-normal PDF function. Its mean value is calculated as follows:

$$e^{\mu+\sigma^2/2} \qquad \text{Eq. App. A 5}$$

With μ and σ, the fitting parameters of the log-normal PDF, being the mean and the standard deviation of the variables natural logarithm; both having the uncertainties $\Delta\mu$ and $\Delta\sigma$ respectively. To estimate the error introduced by the fitting the partial derivatives are needed.

$$\frac{\partial f(\sigma,\mu)}{\partial \sigma} = \sigma\, e^{\mu+\sigma^2/2}$$

$$\frac{\partial f(\sigma,\mu)}{\partial \mu} = e^{\mu+\sigma^2/2}$$

The total error of the mean value arises from:

$$\Delta_{Mean^+} = \sqrt{\left(\frac{\partial f(\sigma,\mu)}{\partial \sigma}\Delta\sigma\right)^2 + \left(\frac{\partial f(\sigma,\mu)}{\partial \mu}\Delta\mu\right)^2 + (\Delta S1_{Dia^+})^2} \qquad \text{Eq. App. A 6}$$

Analogue, this is done for the mode of the log-normal PDF:

$$e^{\mu-\sigma^2} \qquad \text{Eq. App. A 7}$$

With its partial derivatives:

$$\frac{\partial f(\sigma,\mu)}{\partial \sigma} = -2\sigma\, e^{\mu-\sigma^2}$$

$$\frac{\partial f(\sigma,\mu)}{\partial \mu} = e^{\mu-\sigma^2}$$

Hence, total error of the mode arises from:

$$\Delta_{Mode^+} = \sqrt{\left(\frac{\partial f(\sigma,\mu)}{\partial \sigma}\Delta\sigma\right)^2 + \left(\frac{\partial f(\sigma,\mu)}{\partial \mu}\Delta\mu\right)^2 + (\Delta S1_{Dia^+})^2} \qquad \text{Eq. App. A 9}$$

The Median of the log-normal PDF is:

$$e^{\mu} \qquad \text{Eq. App. A 10}$$

The total error of the median is calculated as follows:

$$\Delta_{Median^+} = \sqrt{(e^{\mu}\,\Delta\mu)^2 + (\Delta S1_{Dia^+})^2} \qquad \text{Eq. App. A 11}$$

Appendix B Supporting information - A fast X-ray diffraction-based method for the determination of crystal size distributions (FXD-CSD).

AUTHORS

Sigmund H. Neher[a]*, Helmut Klein[a] and Werner F. Kuhs[a]*

[a]GZG Crystallography, University of Göttingen, Goldschmidtstr.1, Göttingen, 37077, Germany

B 1 Supporting figures

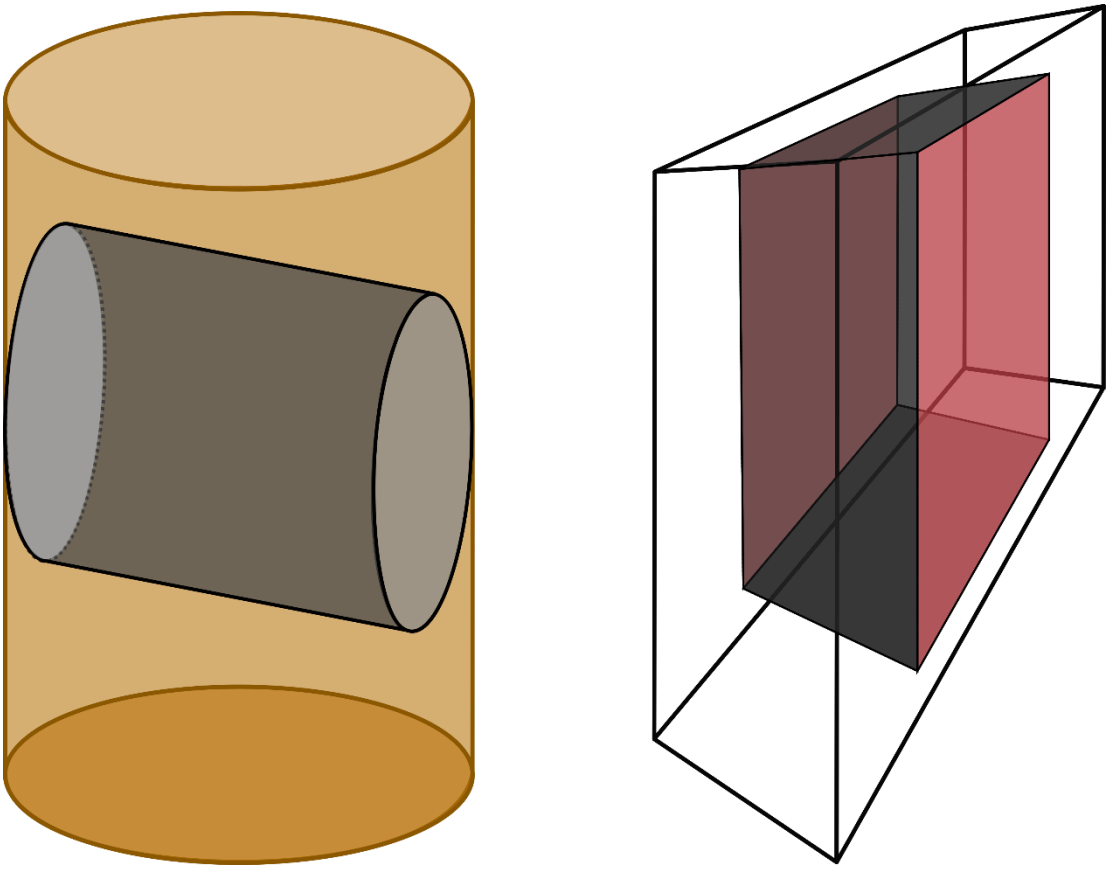

Figure App. B-1: Irradiated sample volume (ISV) examples for different specimen types and incident beam geometries. Left: Kapton capillary filled with powder hit by a circular incident beam (pinhole collimator). Only the dark gray area contributes to the sample edge effect. Right: Polycrystalline specimen hit by a rectangular collimated incident beam. The gray areas contribute to the sample edge effect. The red areas can contribute as well if they are effected by sample preparation (e.g. by cutting).

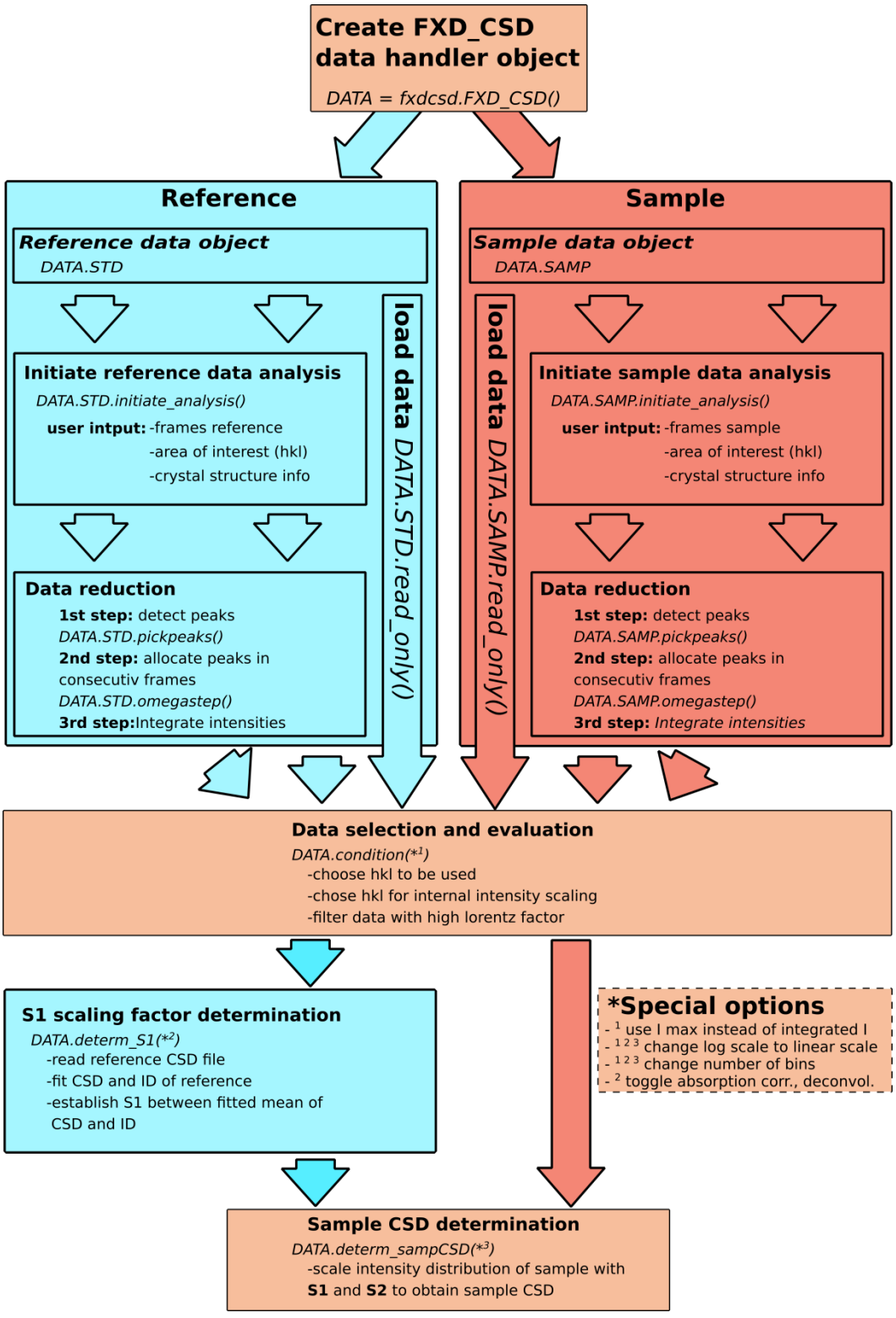

Figure App. B-2: FXD-CSD data flow. To allow a fast and convenient data analysis the software package / module *fxdcsd* has been developed. The program, written in Python, can be run directly from the command line/terminal or executed as script. After importing the module it is executed by importing the data handler object.

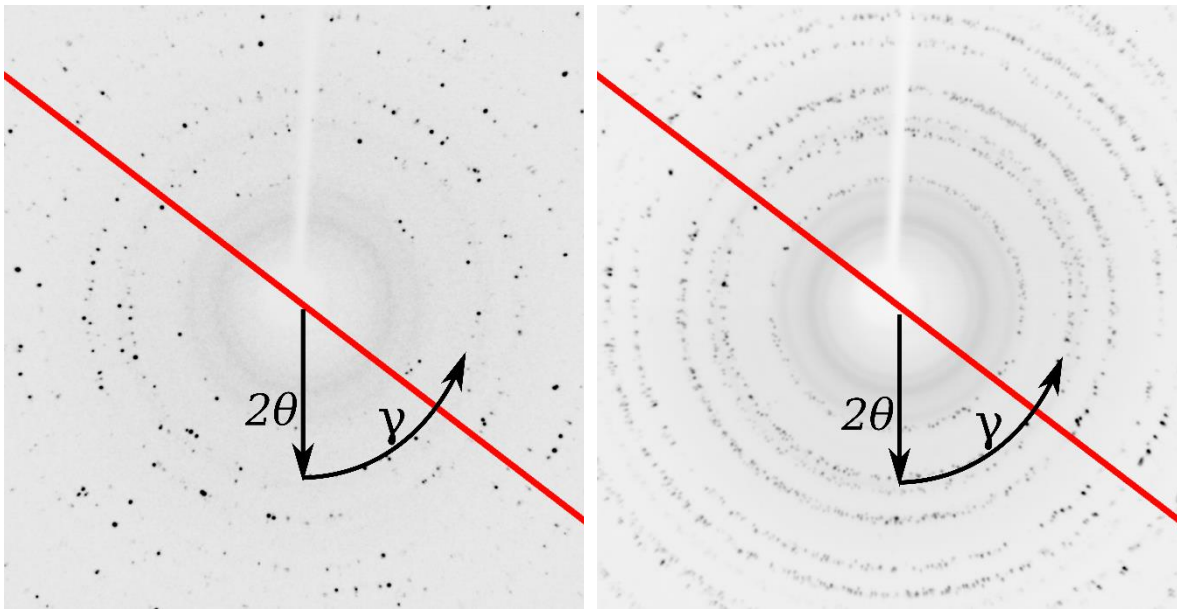

Figure App. B-3: Effect of sample rotation during image acquisition using a 54.74° (the half octahedral dihedral angle) inclined φ-rotation axis. The red line represents the trace of the sample rotation axis on the detector. The 2θ and γ direction are indicated. Left: single frame; no apparent influence. Right: summation of several frames; reflections near the trace of the rotation axis show much higher intensities because they stay longer in diffraction state.

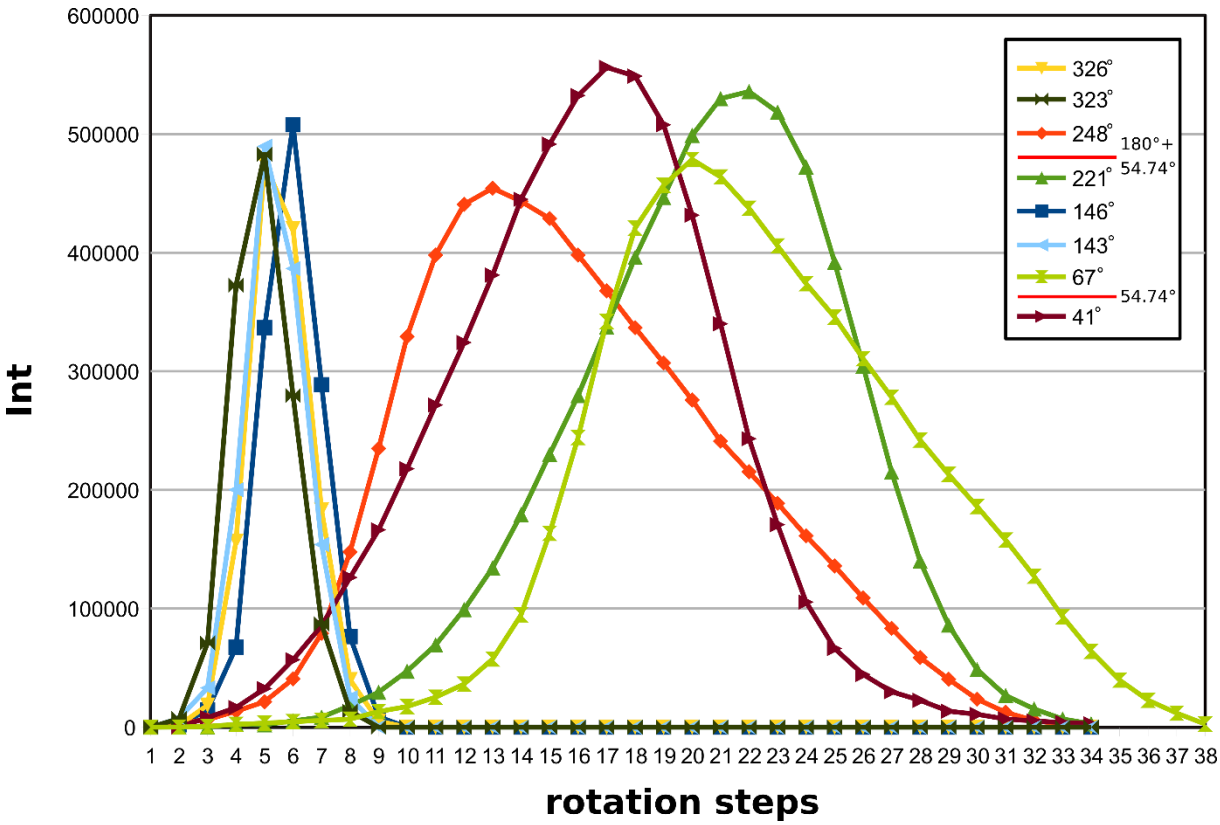

Figure App. B-4: Rocking curves of diffraction spots intersecting the Ewald spear with different speed due to different orientation in respect to the rotation axis γ. The data originates from test measurements of a spherical Ylid single crystal usually used for intensity calibration. The measurement is performed in the same manner as described in Section 2.3.3 (recall Figure 2.2). The numbering of the coloured lines corresponds to their position on the ring, given in degree γ. The φ-rotation axis is again inclined about 54.74° in χ. Please note that the exceptional widths of some of the reflections is the sole consequence of an angular position in γ close to the nodes of the Lorentz factor correction function.

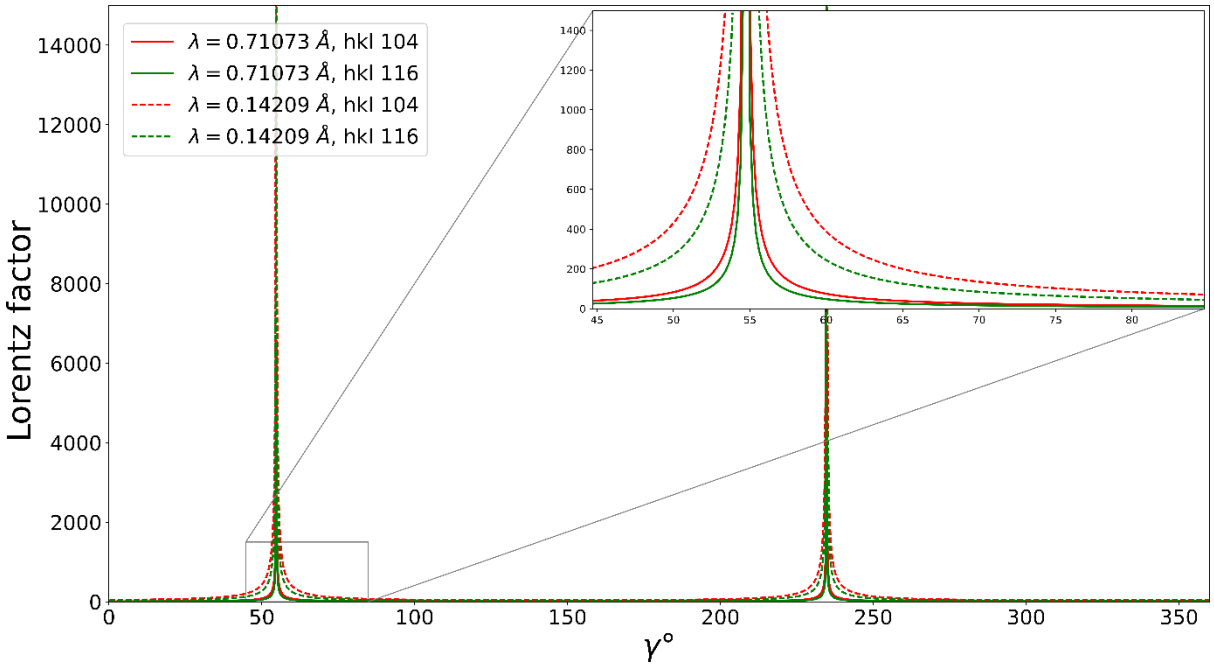

Figure App. B-5: Lorentz factor function graph plot for two different wavelengths from simulated data. The plotted lines result from Eq. 2.7 in Section 2.3.5.1, fed with simulated reciprocal lattice vectors in diffraction state (hr), calculated from the pixel positions of 1800 evenly distributed spots on a circle. All other parameters are also inspired by a real measurement including the 54.74° inclined rotation axis. This results in the function peak at 54.74° γ. The correction factor is applied to the integrated crystal intensity. To test the correction a stepwise rotation measurement, in the FXD-CSD manner, of a spherical intensity reference ylid single crystal was performed and verified the correctness of the applied correction (see Figure App. B-4).

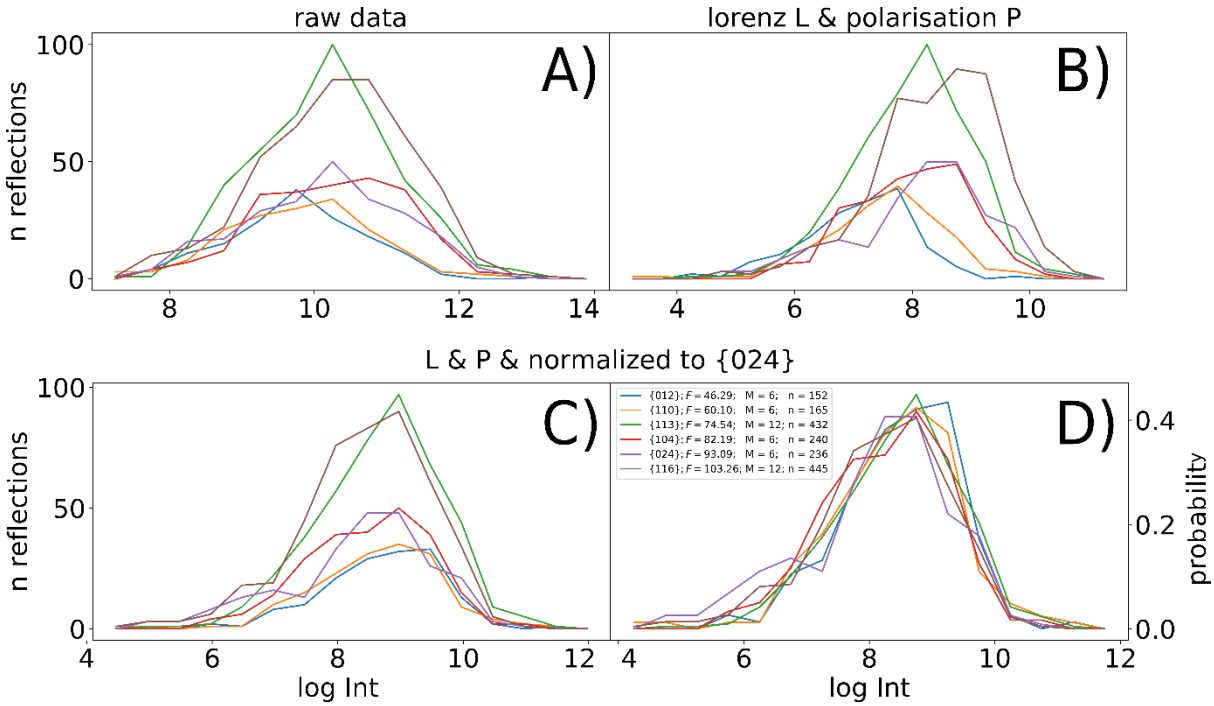

Figure App. B-6: Subplots A-D from CSFIII, automatically produced by the *condition()* function. They show the intensity histograms from all chosen *hkl*-rings in different stages of data treatment. These are: A) the uncorrected data, B) the impact of the Lorentz and polarisation factor and the influence of the internal intensity scaling, according to the chosen structure factor. The latter is plotted as C) number of occurrence histogram and D) as probability histogram. In C) one can nicely observe the effect of varying multiplicities on counting statistics. D) shows how well the measured and scaled IDs match.

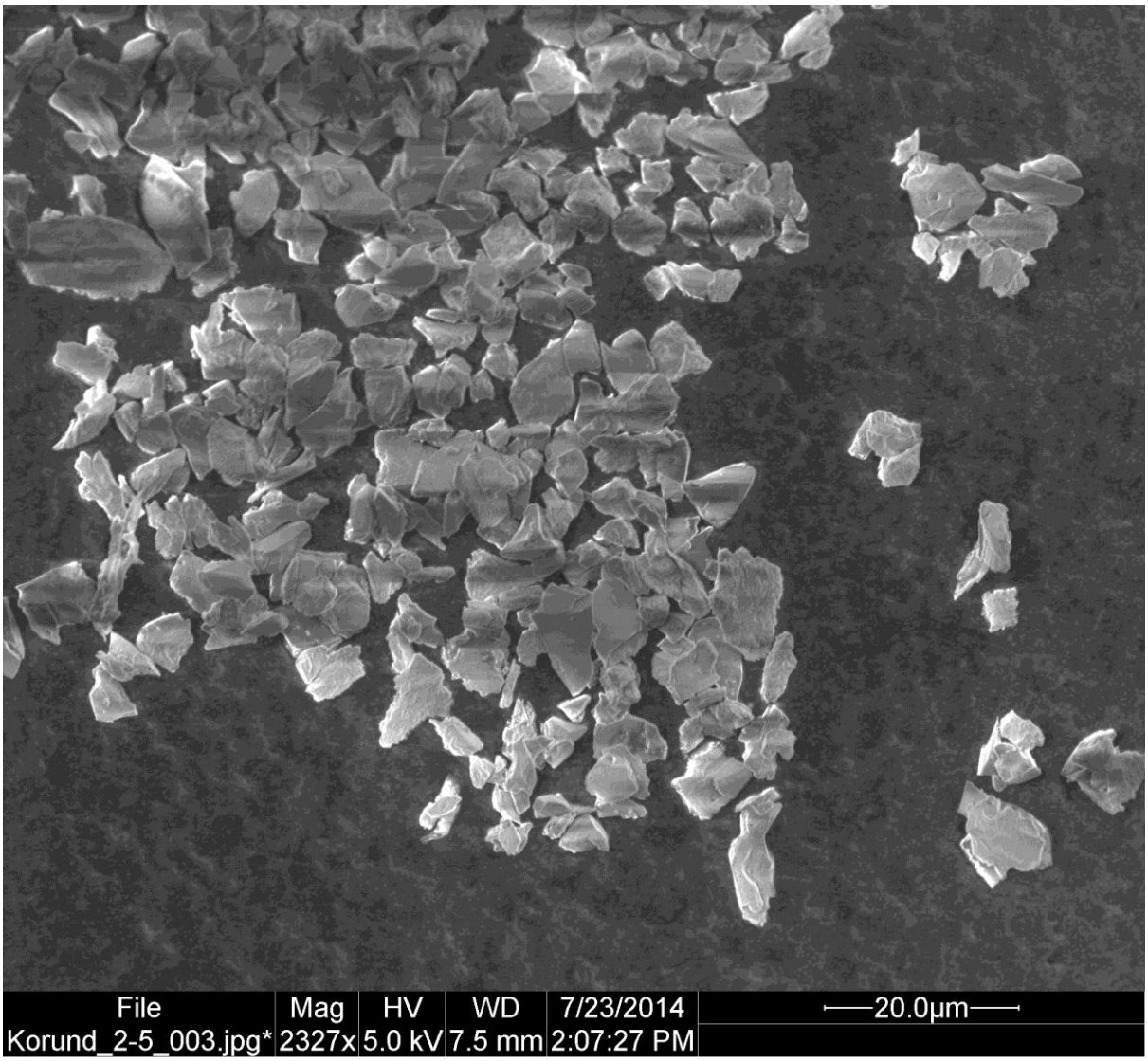

Figure App. B-7: Example SEM image of the CSF I sample powder.

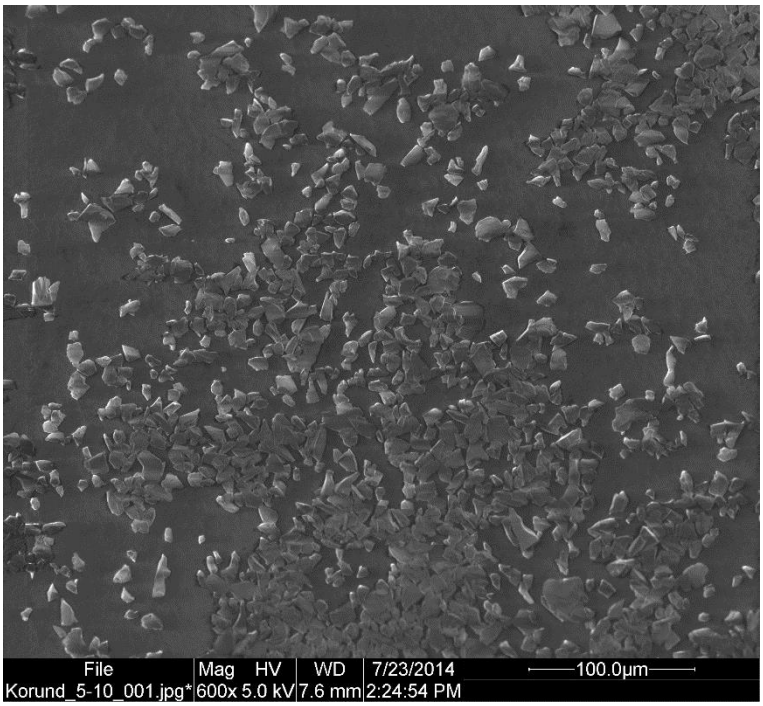

Figure App. B-8: Example SEM image of the corundum CSF II sample powder.

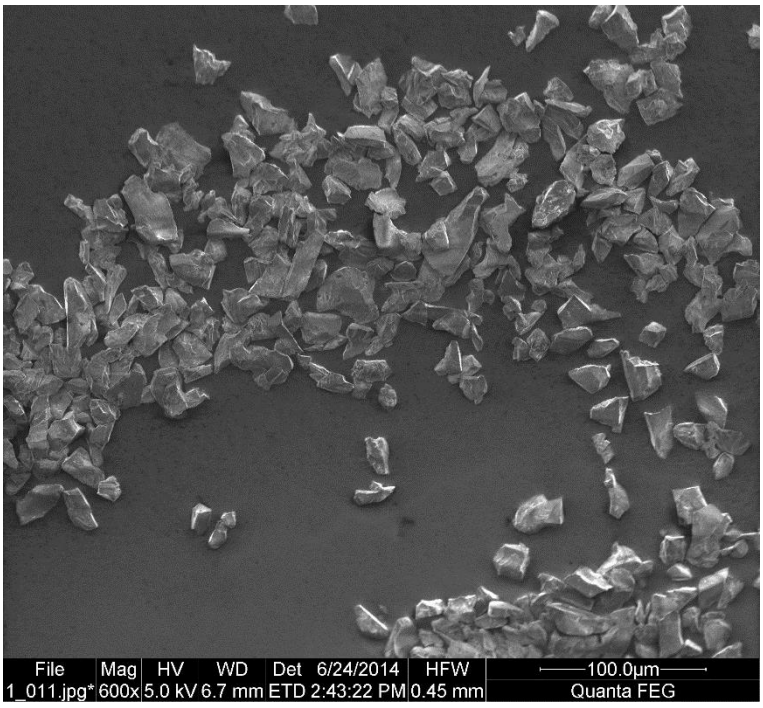

Figure App. B-9: Example SEM image of the corundum CSF IV sample powder.

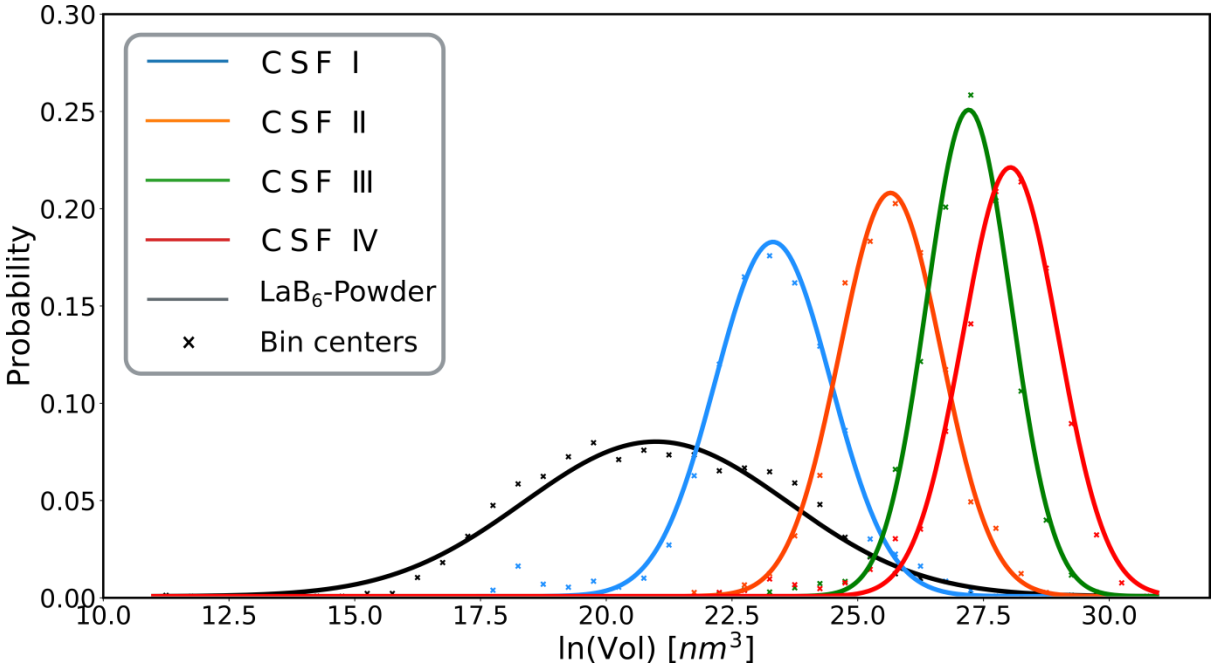

Figure App. B-10: SEM derived volume CSDs of all measured samples with Gaussian PDF fits. The fitting parameter are presented in Table 2.5.

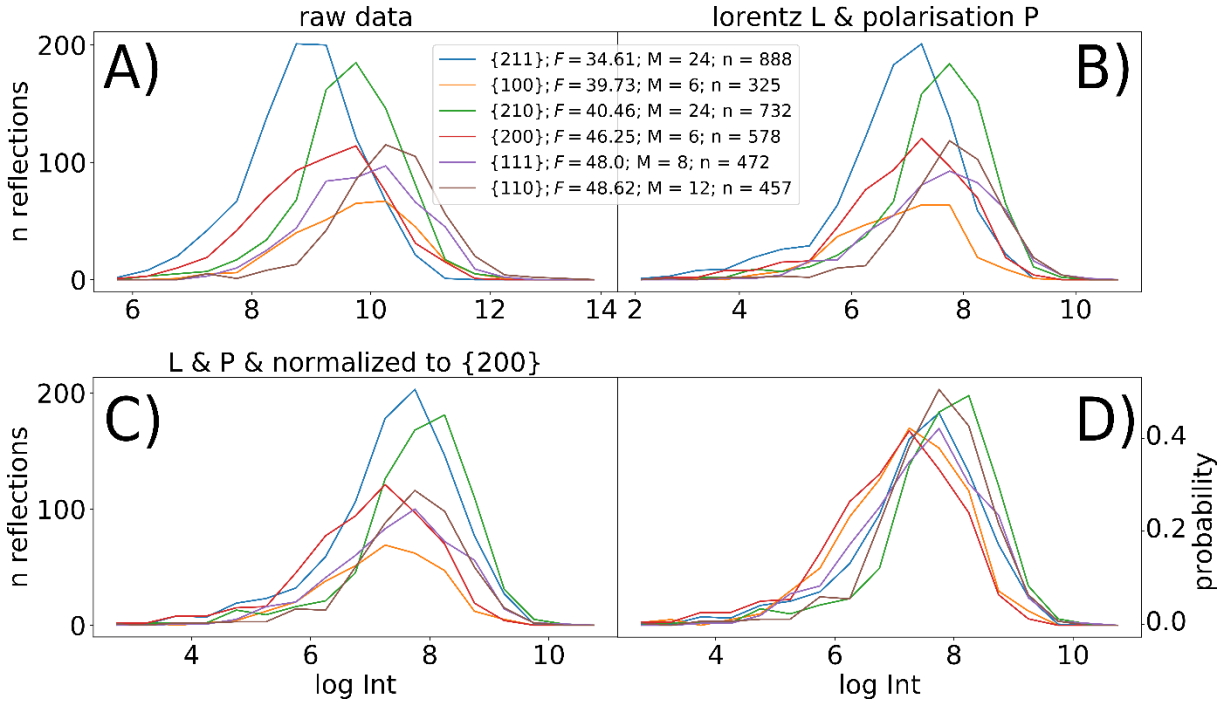

Figure App. B-11: Subplots A-D of the LaB6-Powder sample, automatically produced by the *condition()* function. A) shows the uncorrected data, B) the impact of the Lorentz and polarisation factor. C) and D) show the intensity distribution histograms after the intensity correction and internal structure factor normalization: C) shows the number of occurrence representation; D) shows the probability density representation where the number of occurrence in each bin is divided by the total number of occurrence of each IDH. Apparent is that neither sides of the histograms match in position, which on the left side is due to $ID_{cut\text{-}off}$ and on the right side is due to $ID_{exaggeration}$. Although the internal agreement between the different hkl is respectable, the results are not trustworthy, as the sizes (obtained with CSFIII as reference material) are distinctly higher than the size distribution from SEM observations – see Table 2.4 of main text).

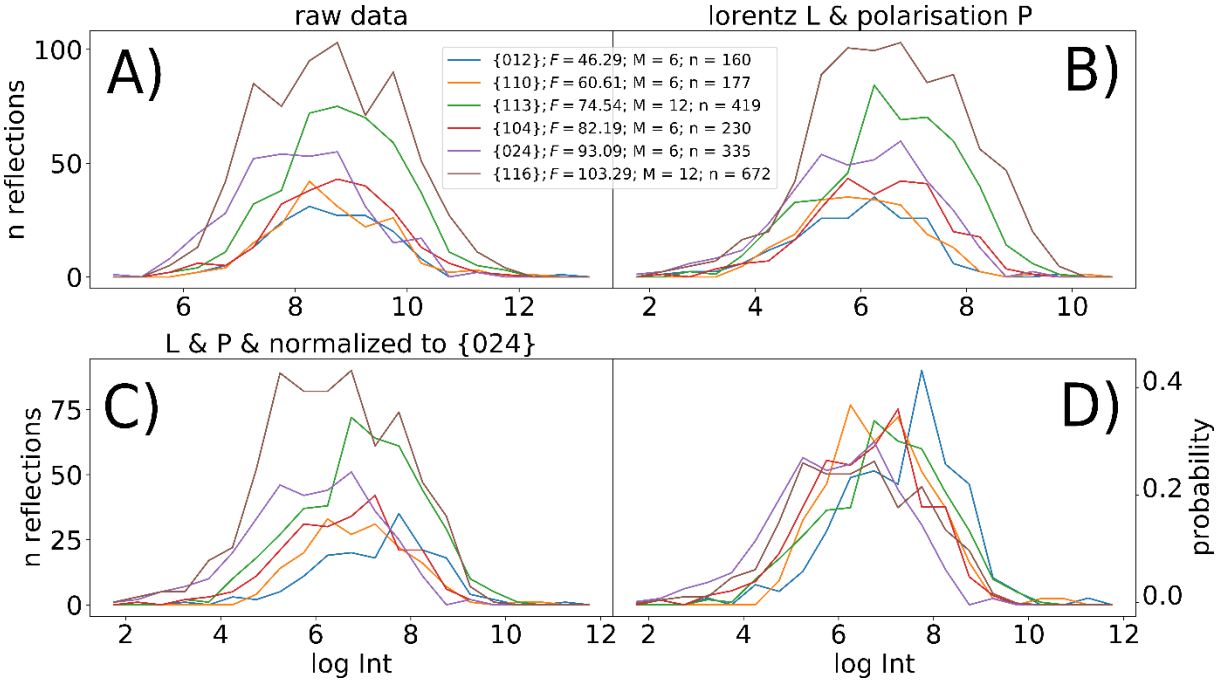

Figure App. B-12: Subplots A-D from CSFI, automatically produced by the *condition()* function. A) shows the uncorrected data, B) the impact of the Lorentz and polarisation factor. C) and D) show the intensity distribution histograms after the intensity correction and internal structure factor normalization: C) shows the number of occurrence representation; D) shows the probability density representation. For the latter the number of occurrence in each bin is divided by the total number of occurrence of each IDH. Apparent is that neither side of the histograms match in position, which on the left side is due to $ID_{cut\text{-}off}$ and on the right side is due to $ID_{exaggeration}$. The number of observations in the legend also reveal $ID_{cut\text{-}off}$. The number of observations should reflect their multiplicities but obviously rather follow their structure factor.

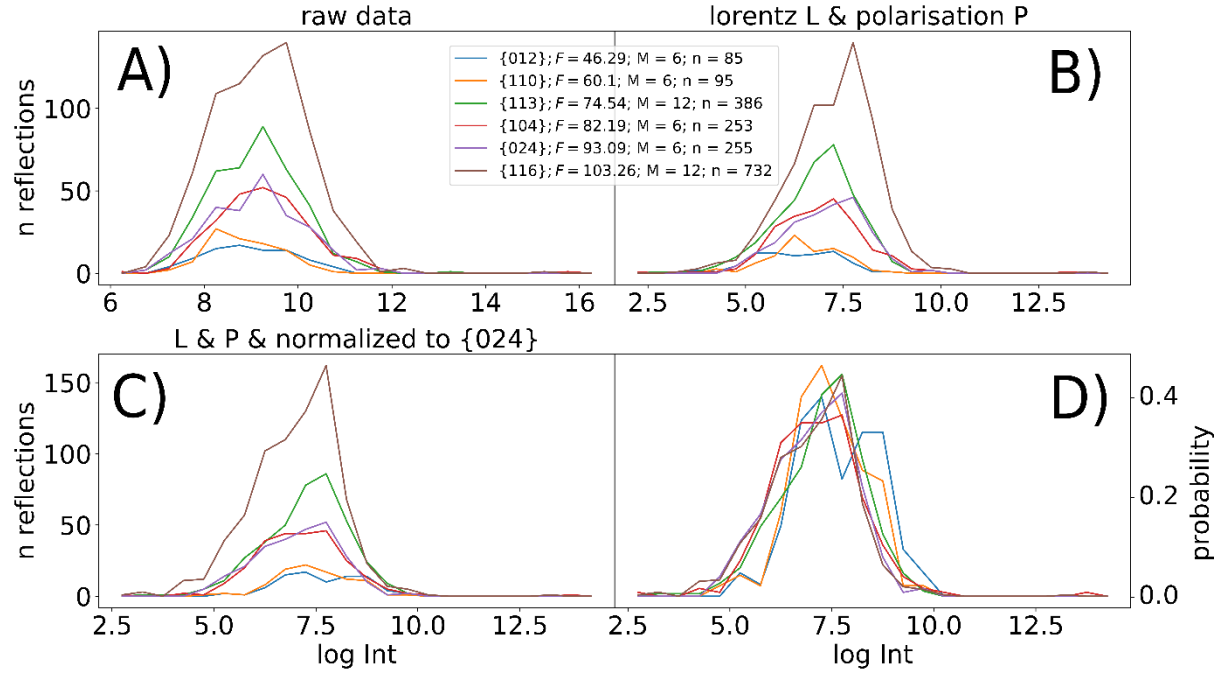

Figure App. B-13: Subplots A-D from CSFII, automatically produced by the *condition()* function. A) shows the uncorrected data, B) the impact of the Lorentz and polarisation factor. Plot C) and D) show the intensity distribution histograms after the intensity correction and internal structure factor normalization: Apparent is that only the stronger reflections match in position. The number of occurrence histogram C) shows the impact of the multiplicity on the number of observations and is partially in agreement with the expectation (see also Table 3). Plot D) shows the probability representation. In both plots, C and D) it is particular evident that the IDHs of the 012 and 110 *hkl*-rings do not match with the other IDHs. In conjunction with the small structure factors of the 012 and 110 *hkl*-rings this is strong evidence for $ID_{cut\text{-}off}$.

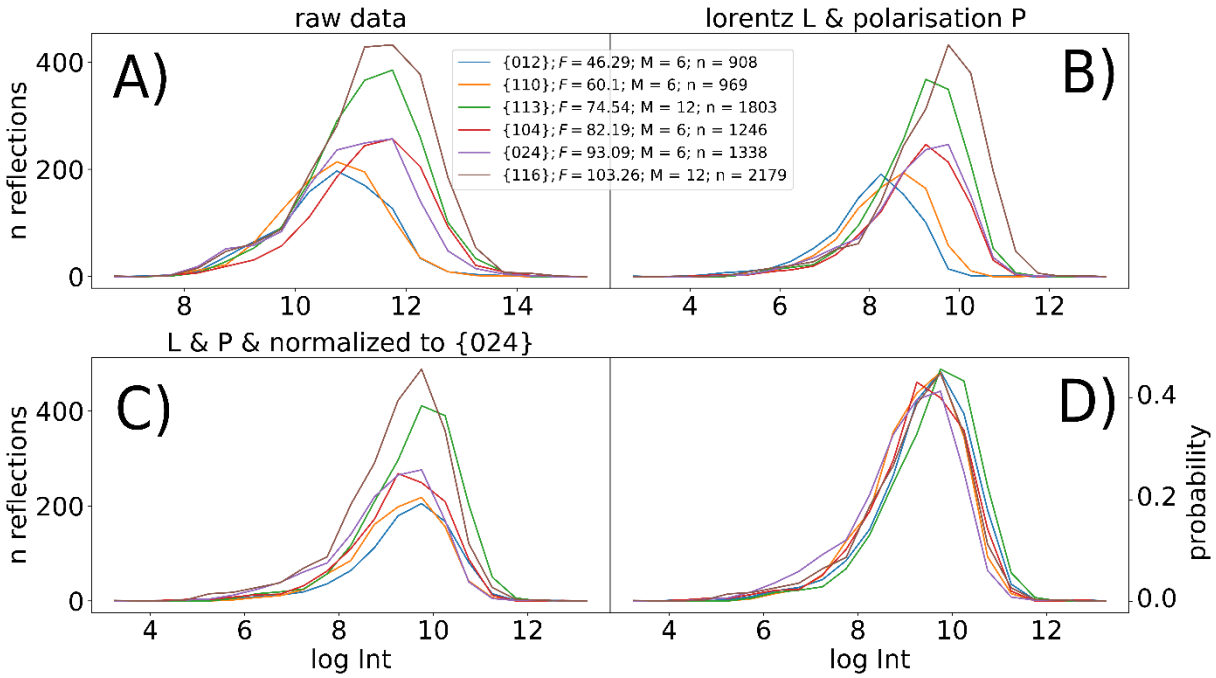

Figure App. B-14: Subplots A-D from CSFIV, automatically produced by the *condition()* function. A) shows the uncorrected data, B) the impact of the Lorentz and polarisation factor. The plots C) and D) show the intensity distribution histograms after the intensity correction and internal structure factor normalization. Apparent is that both sides of the histograms match in position. The number of occurrence histogram, C) shows the impact of the multiplicity on the number of observations and is in good agreement with the expectation (see also Table 3). The plot D) shows the probability representation; here the number of occurrence in each bin is divided by the total number of occurrence of each IDH.

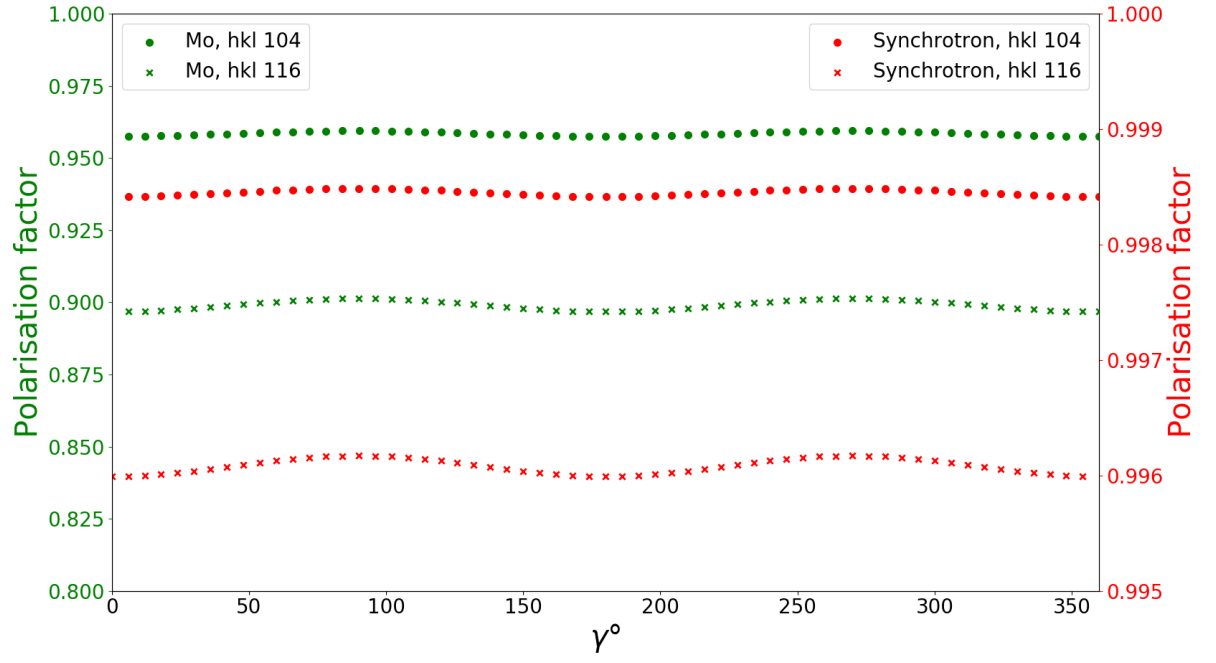

Figure App. B-15: Example calculation of the polarisation factor function graph for two corundum *hkl*-rings and two different X-ray sources. Mo: Molybdenum tube, K_α, λ= 0.71073 Å with graphite monochromator crystal and synchrotron radiation at the ESRF ID 15B with λ= 0.14 Å (Chavanne *et al.*, 1996; Tschentscher & Suortti, 1998).

B 2 General conditions on sample edge effect, sampling, and peak overlap

Obtaining spotty diffraction patterns is the key demand of FXD-CSD. In this section we provide a theoretical approach to estimate and test whether the general conditions of FXD-CSD can be met with the used diffractometer setup.

B 2.1 Irradiated sample volume and sample edge effect

One requirement of FXD-CSD is to keep the sample edge effect *SEF* low, as the diffracted intensity of crystals only partially irradiated by the incident beam, cannot reflect their true volume. The *SEF* can be estimated with the mean crystal diameter d_{cryst} and its projected area A_{cryst}, and with the incident beam dimensions, expressed as its area A_{beam} and its perimeter P_{beam}. Therefore, *SEF* may be expressed by:

$$SEF = \frac{n_P}{n_A} \qquad \text{Eq. App. B 1}$$

With n_A defined as:

$$n_A = \frac{A_{beam}}{A_{cryst}} \qquad \text{Eq. App. B 2}$$

And n_P defined as:

$$n_P = \frac{P_{beam}}{d_{cryst}} \qquad \text{Eq. App. B 3}$$

In case of polycrystalline materials, crystals on the sample surface are likely to be affected by sample preparation, e.g. being cut by grinding. If this is the case, the sample surfaces perpendicular to the incident beam direction affected by preparation have to be taken in to account. Generally, we advise the user, that the sample edge effect should not exceed 5% for CSD measurements (10 % to 20% if only the mean crystal size is aimed for).

B 2.2 Relationship of sample statistics, Irradiated sample volume and mean crystal size

CSDs represented as histograms need a large number of observations, to install sufficiently small histogram bins to faithfully represent the distribution. As stated in the main article (see Section 2.3.6) the number of bins needed, can be assured by applying the Freedman-Diaconis rule (Freedman & Diaconis, 1981). To estimate the approximate number of observations n_{obs} , expected within a certain total φ-rotation range φ_{tot} , the approximate irradiated sample volume ISV and the approximate mean crystal size serve as input; randomly orientated crystals are assumed. The total number of crystals n_{tot} in the ISV is simply determined by dividing the ISV with the mean crystal volume; the crystal volume (and the packing factor of powder samples) should be estimated as accurately as possible.

$$n_{obs} = \frac{n_{tot} \sum 2M_{hkl}\, \varphi_{tot} rad}{4\pi} \qquad \text{Eq. App. B 4}$$

Whether these numbers produce a critical amount of peak overlap on the individual *hkl*-rings is considered in the following section.

B 2.3 Ring occupation and overlap

The ring occupation and the expected peak overlap depend on the angular resolution of the diffractometer res_{hkl}, the number of crystals n_{tot} in the ISV and the *hkl*-multiplicity M_{hkl}. $res_{hkl,}$ is depending on the spatial resolution of the detector and the ring radius and is estimated concerning the resolution in the φ-rotation direction and along the used *hkl*-ring:

$$res_{hkl} = n_{\varphi-steps}\ \varphi_{\text{step}}\text{rad}\ \ n_{pix}\ (\frac{1}{r_{ring}}) \qquad \text{Eq. App. B 5}$$

with r_{ring} in pixels and the distance between the reflection maxima in both directions, $n_{\varphi-steps}$ and n_{pix}. Values for $n_{\varphi-steps}$ and n_{pix} depend on the peak spread on the detector (depending on the resolution function of the diffractometer, the crystal size and quality); with the setup described in the main article, using twice the peak spread has turned out to give reasonable results. With that the probability *P* of having overlap can be calculated. Using the number of possible orientations n_{pos} and the given number of crystals n_{tot} in the ISV, one obtains

$$P = \frac{1}{n_{pos}}\ n_{tot} = 1/(\frac{4\,\pi}{M_{hkl}\ res_{diff}})\ n_{tot} \qquad \text{Eq. App. B 6}$$

B 2.3.1 Accidental overlap

Accidental full overlap arising from crystals with the same orientation cannot be resolved or detected by the software and therefore cannot be discarded. To estimate its portability of occurrence the equations Eq. App. B5 and Eq. App. B6 can be used. To do this one only needs to set $n_{\varphi-steps}$ and n_{pix} to 4, the minimum distance what can be resolved by the software. For example, using the setup described in Section 2.3.3 of the main article with an ISV of ~ 0.125 mm³ and having about 20.000 crystals in it, gives a chance of 0.37 that accidental full overlap is happening once on a *hkl*-ring with the multiplicity of 10, hence is neglectable small.

B 3 Intensity corrections

B 3.1 Absorption

Attenuation affects depend on the linear absorption coefficient (μ) and the path length the X-ray radiation travels through the crystal; together they define the transmission factor A_{hkl}. μ is known because it is material and wavelength specific. The path length has to be estimated because in the case of FXD-CSD neither the shape nor the exact individual crystal size is a known property. Therefore A_{hkl} can only be estimated for the average crystal size in each bin of the CSD histogram by assuming a spherical crystal shape and can be calculate by an analytical expression (Rouse *et al.*, 1970).

$$A_{hkl} = e^{-(a_1+b_1\,sin^2\,\theta)\mu r-(a_2+b_2\,sin^2\,\theta\,)(\mu r)^2} \qquad \text{Eq. App. B 7}$$

With *r* the crystal radius and the coefficients a_1 = 1.5108, b_1=-0.03145, a_2=-0.0951 and b_2=-0.2898 (Rouse *et al.*, 1970).

For the *reference* measurement the correction can only be applied in an iterative procedure because the intensity derived *reference* CSD, needed to estimate the crystal path length 2*r*, is obtained by the S1 scaling, which changes when the correction is applied to the *reference* ID. For this reason, the

correction is considered to be self-correlated and must be bounded to be self-consistent. The used bound is a distribution shape match between the intensity derived CSD and the *reference* volume CSD, derived *via* SEM imagery. In the first iteration cycle S1 is determined and used to calculate the CSD derived from the ID. Calculating the transmission factors with the size information obtained (*r*) and applying it to the ID, changes the shape of the ID what again changes the S1 scaling factor. The altered scaling factor is used for the second iteration. Ideally the iterations are carried out until the ID shape matches the shape of the SEM derived volume CSD. To perform the correction in this manner the CSD of the *reference* must be beyond doubt which is up to now not necessarily the case (see Section 2.5.3). In practice it turned out that for the used reference materials (LaB_6 (Nützmann, 2013) and corundum) the change in crystal size is well below 2% in the first iteration cycle. Thus, without a better reference material, the correction is not considered to improve the results and therefore not applied.

The correction of the sample material ID is straightforward. A_{hkl} could be calculated for the obtained crystal sizes and used for a correction.

B 3.2 Beam profile deconvolution

B 3.2.1 Theory

In the theoretical consideration of measuring the grain size with X-ray diffraction a lateral homogenous, boxed shaped beam is assumed. In practice, especially in the case of lab equipment and collimators with big diameters, this is not necessarily the case (Figure App. B-16). Inhomogeneities broaden the measured intensity distributions and blur the relationship between crystal size and measured intensity. Mathematically this corresponds to a convolution. In a dataset convoluted like this, one cannot tell the difference between a small crystal diffracting in a high intensity region, from a bigger crystal diffracting in a low intensity region. This effect is influencing the distribution shape and its mean value. Since both, crystal size and local beam intensity are uncorrelated, and the beam profile can be measured, a deconvolution is possible.

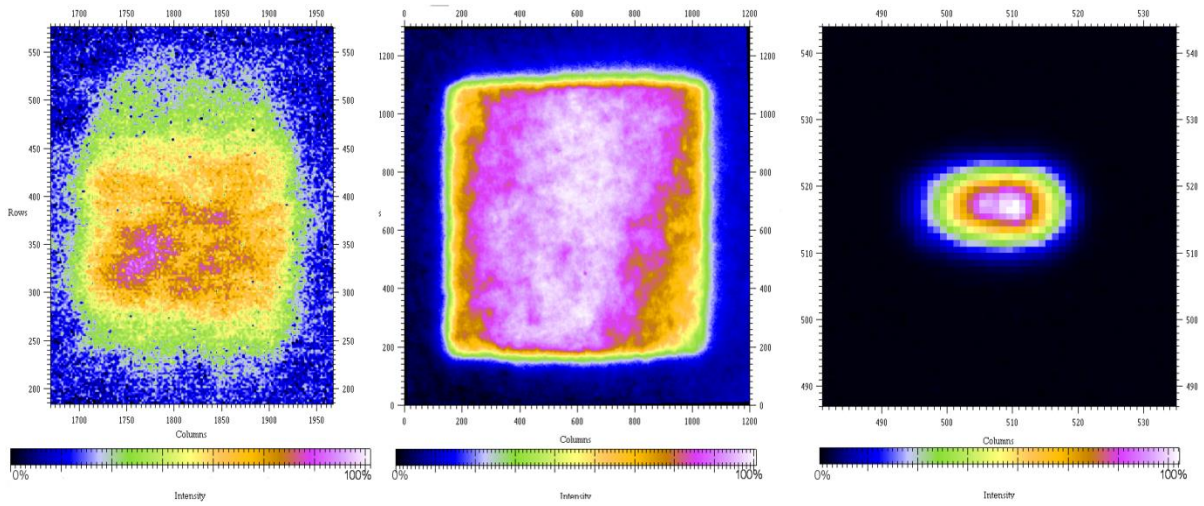

Figure App. B-16: Examples for lateral profiles of primary X-ray beams. Left: ESRF ID15. Middle: DESY Petra III P08. Right: Bruker Apex II 0.5 Collimator.

The position of each crystal in the initial beam is not known therefore the spatial information of the beam profile is redundant and the correction can be done in a probabilistic manner *via* a mathematical deconvolution. For this a discrete intensity histogram over log-intensity of the primary beam is created.

In the following the nomenclature of signal processing is used. The intensity histogram $f(x)$ of the initial beam is the representation of the filter and the measured diffracted intensity distribution histogram (IDH) $s(x)$ the representation of the signal. The sought information is the true IDH $g(x)$. The Convolution $f(x) * g(x)$ – occurring while measuring – is written as follows (Wikipedia contributors, 2017):

$$(f * g)(i) \int_{-\infty}^{\infty} g(i)\, f(i-j)\, dj \qquad \text{Eq. App. B 8}$$

The variable j is inverting the order of f. Since the data available in this case is not continuous the convolution is sufficiently described by a discrete form (Wikipedia contributors, 2017) :

$$(f * g)[i] := \sum_{j=-k}^{k} g[j] f[i-j] \qquad \text{Eq. App. B 9}$$

To perform the deconvolution the beam profile $f(x)$ and the measured ID $s(x)$ need to be known and converted to a usable from. The beam profile can be measured either with a high-resolution X-ray photo film and scanned afterward or measured directly with a 2D detector. The direct measurement can only be done with lab sources because it is easily possible to lower its intensity by using minimal current (5 mA); otherwise it is likely to damage the detector. Since FXD-CSD uses a statistical approach to determine the CSD and the measured ID $s(x)$ is just a representation of it, the beam profile is only needed as relative measure and hence can be represented by an intensity histogram. The number and the size of the histogram bins need to have the same size as the measured ID. Once the filter $f(x)$ is converted in to a histogram and written as matrix $F_{ij} = f[i-j]$, the convolution can be - in conformity with Eq. App. B4 - written as matrix multiplication:

$$S_i = \sum_{j=-k}^{k} F_{ij} g_j \qquad \text{Eq. App. B10}$$

The least square solution for g_j minimizes $\sum_i (S_i - \sum_j F_{ij} g_j)^2$, which corresponds to a vanishing derivative with respect to g_r:

$$\sum_i F_{ir} (S_i - \sum_j F_{ij} g_j) = F^T s - F^T F g = 0 \qquad \text{Eq. App. B11}$$

What can be solved for g:

$$g = (F^T F)^{-1} F^T s \qquad \text{Eq. App. B12}$$

The problem when solving for g_j by least squares is that the result can be wiggly and needs to be regulated. We are looking for a smooth solution, hence we penalize curvature. To achieve this we minimizes both, least square deviation and to some measure (λ multiplier) the ruggedness of the curve. This could be for example the curvature term $c_i = g_{i-1} + g_{i+1} - 2g_i$. Hence a suitable function is

$$\sum_i (S_i - \sum_j F_{ij} g_j)^2 + \lambda \sum c_i^2 = \sum_i (S_i - \sum_j F_{ij} g_j)^2 + \lambda \sum_i (g_{i-1} + g_{i+1} - 2g_i)^2$$

The curvature term can be expressed as a matrix multiplication $c_i = \sum_j D_{ij} g_j$ with $D_{ii} = -2$, $D_{i,i-1} = 1$, $D_{i,i+1} = 1$, but the boundaries $i = -k$ and $i = k$ need to be modified. The curvature term is then $\sum_i c_i^2 = \sum_{ijl} g_l D_{il} D_{ij} g_j$. Again, to minimize we differentiate with respect to g_r and set the derivative to zero:

$$0 = \sum_i F_{ir} \left(s - \sum_j F_{ij} g_j \right) + \lambda \sum_{ij} D_{ik} D_{ij} g_j$$
$$= F^T s - F^T F g + \lambda D^T D g = F^T s - (F^T F - \lambda D^T D) g$$

Now this can be solved for g by inverting the matrix $(F^T F - \lambda D^T D)$.

$$g = (F^T F - \lambda D^T D)^{-1} F^T s$$

This is done by the *solver.qp* function of the *cvxopt* (Andersen *et al.*, 2013) python package.

B 3.2.2 Example deconvolution

Before the deconvolution can be performed the primary beam profile (the filter) is converted into log space, normalized to the maximum bin value of the ID and, converted into a histogram with bins the same size like the ID (Figure App. B-17). While the high-end value of the beam profile is clearly defined by the highest pixel value, the lower end of the primary beam profile intensity distribution is not clearly defined. The low end is somewhere between the background of the measured beam profile and some fraction of the lowest measured crystal intensity. To determine where the cut-off threshold – the low intensity end of the filter – is to be placed (a multiple of the step size in log space) two measures are used: 1) The deviation between the volume distribution of the reference material and the deconvoluted measured ID, which should be as small as possible (Figure App. B-18) and 2) the deviation between the measured ID and the re-convolved signal. For the latter the deconvolution is reversed (re-convoluted) to check whether the former signal is reproduced. The deviation should be as small as possible. Both measures are used for optimizing the cut-off threshold. If the automated threshold determination is not working a value can be set manually.

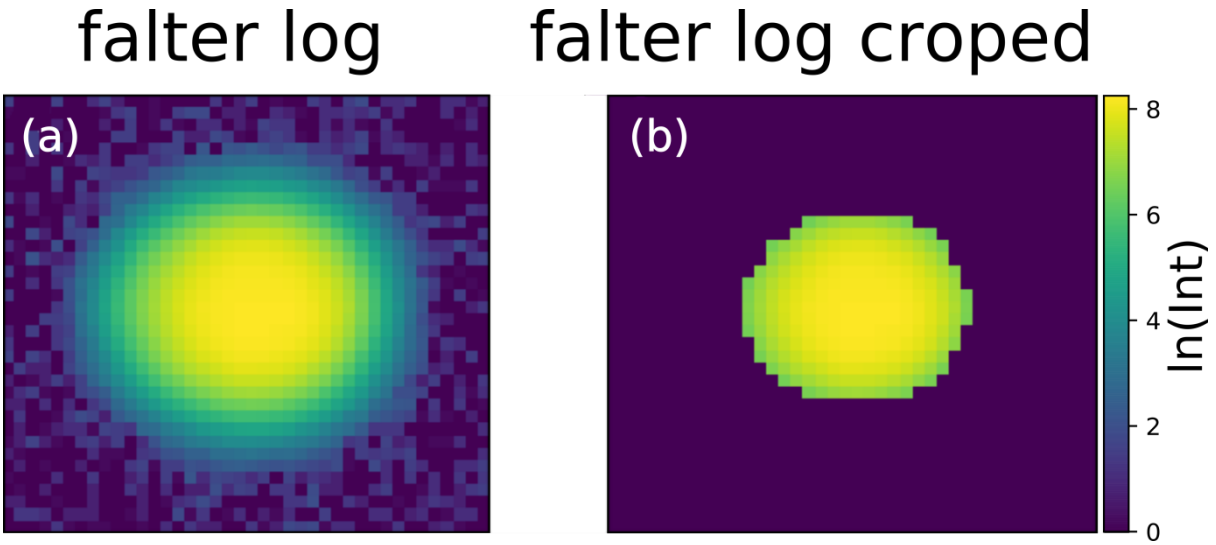

Figure App. B-17: Lateral beam profile

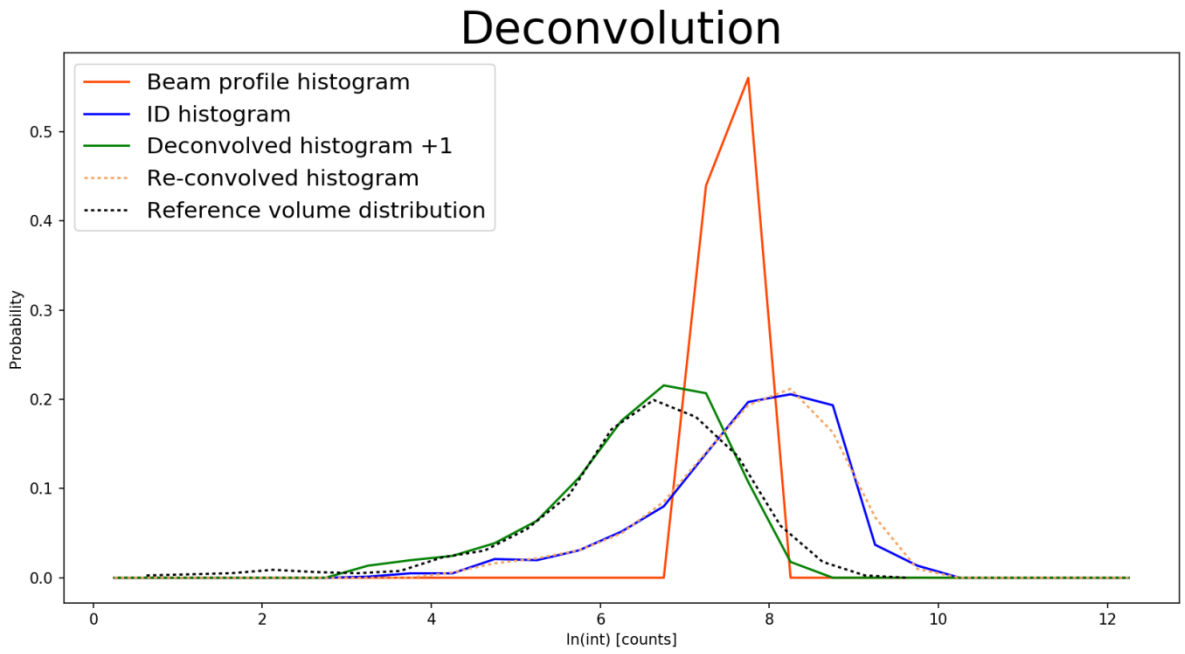

Figure App. B-18: Deconvolution

In practice it turned out, that the ID convolution has not a strong influence on the resulting CSDs, which is generally smaller than the uncertainties originating from uncertainties of the reference volume distribution. In case of the smaller grain size fractions presented in Section 2.4 of the main article, the fitted half width at half maxima (HWHM) of the IDs are smaller than the HWHM of the reference volume CSDs. This is not true for the bigger grain size fraction – which was one reason for implementing the deconvolution – but turned out to originate from evolving satellite peaks (see Section 2.4 in the main article) not from beam inhomogeneities.

B 4 Crystal size fraction separation *via* sedimentation

To obtain a consecutive series of crystal size fractions (CSF) to verify the FXD-CSD method a corundum blasting abrasive powder (Edelkorund F 120, Kuhmichel Abrasiv GmbH) is used as starting material. The material is grinded in a mortar and separated into several CSFs *via* sedimentation in water. A so called Atterberg cylinder, a glass cylinder with a faucet a few cm above the bottom and a filling mark at the top, is used to separate the following nominal CSFs: <2 µm, 2 - 5 µm, 5 – 10 µm, 10 - 15 µm, 15 – 20 µm, 20 – 25 µm, 25 – 35 µm, 35 - 40 µm, 40 – 45 µm. The 2 – 5 µm, 5 - 10 µm, 10 - 15 µm and 15 - 20 µm CSFs, called CSD I-IV, are presented here. The cylinder is filled with water to a certain level and the bulk powder is given in the cylinder and closed with a lid. After rocking the cylinder until the whole sample is floating the cylinder is put aside upright. After a certain time, calculated *via* Stokes law fed with the crystal size to be separated and the water column height, the faucet is opened and the water is collected (for further information see Müller, 1967). The collected water contains only crystals smaller than the size used for the calculation of the sedimentation duration. The sediment on the bottom and the suspension below the faucet level contain the bigger crystals and parts of the smaller CSF; at the beginning of each separation step the crystals are evenly distributed in the water column, therefore the fall distance is not the same for all particles and parts of the small fraction will sediment during the calculated time period. To separate the majority of the small CSF the procedure is carried out several times (up to ten times for the smallest fractions).

B 5 Satellite peaks

Besides the samples presented (CSF I-IV) in the main article several other samples with bigger mean crystal sizes have been produced (see Appendix A 2) and characterized with SEM imagery. The subsequent FXD-CSD data analysis revealed that with increasing crystal size, artificial satellite peaks evolve on the detector which wander through their main peaks (see Figure App. B-19). This problem did occur several times in the past when using our diffractometer (Bruker AXS Apex II CCD diffractometer (D8 Base) with a molybdenum tube and graphite monochromator) to measure large single crystals; it was also observed while performing calibration measurements carried out with a spherical ylid crystal used as intensity standard provided by the diffractometer manufacturer. The most likely explanation for this artefact is a deficient monochromator crystal which produces small amounts of crossfire radiation. Even though a mending work around is implemented in our software – suppressing peaks close together by increasing the minimum distance parameter (min_distance of the pickpeaks() function) of the software – we decided to only present data sets which are not or only slightly affected in the main article.

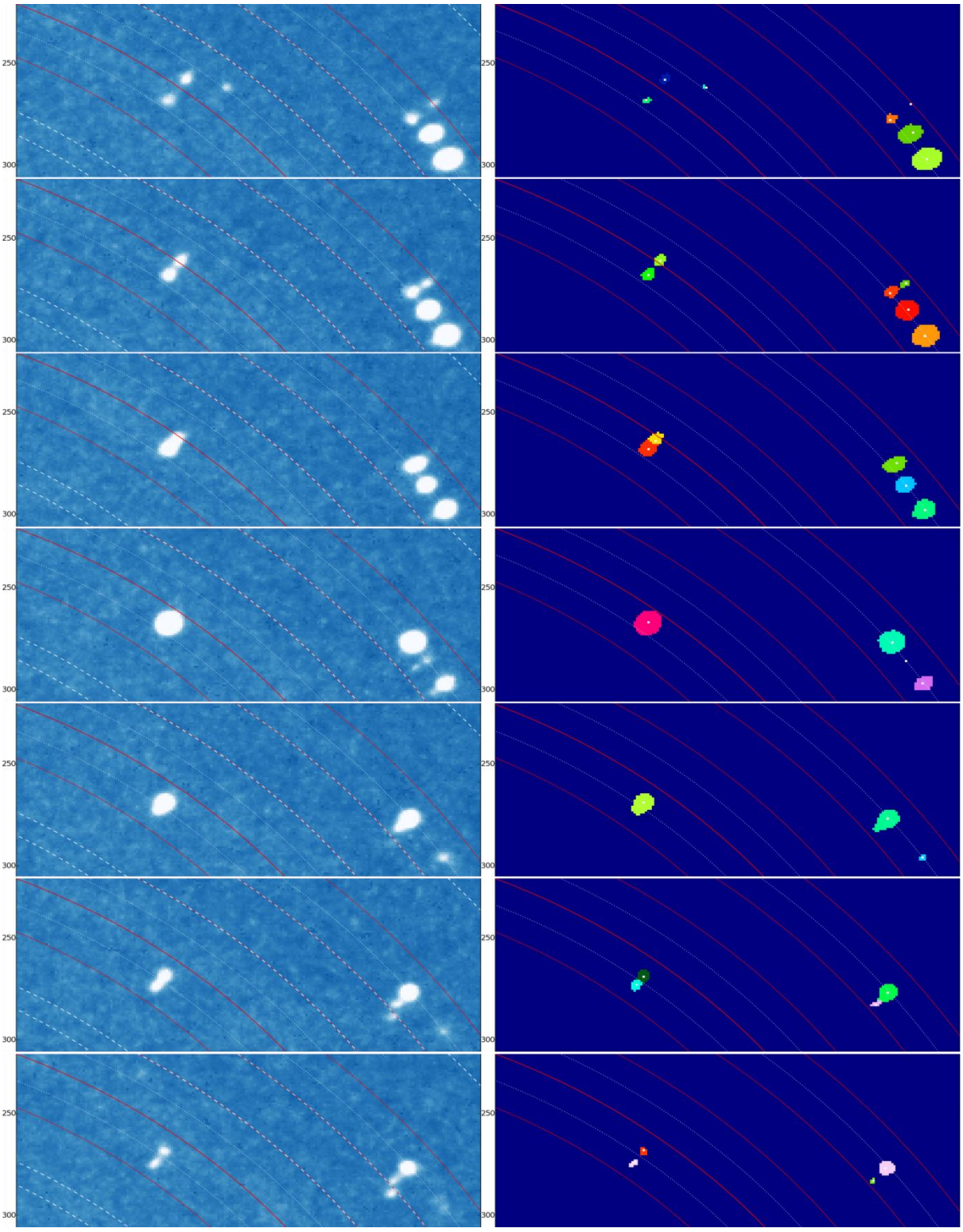

Figure App. B-19: Satellite Peaks

B 6 Data evaluation

The rocking curves of each reflection can be evaluated using their central moments, which than can be used as rejection criteria. These are: Weighted-mean $\acute{x}$, -variance Var, -skewness γ, and -kurtosis γ_2, describing the mean position, peak spread, the asymmetry of the curve and the flatness or peakedness, respectively (see Section 2.3.4 3rd Step).

$$\acute{x} = \frac{1}{w}\sum_{n}^{i=1} x_i w_i \qquad \text{Eq. App. B 13}$$

$$Var = \frac{1}{n-1}\sum_{n}^{i=1} w_i (x_i - \acute{x}) \qquad \text{Eq. App. B 14}$$

$$\gamma = \frac{n(n+1)}{(n-1)(n-2)}\sum_{n}^{i=1} w^{\frac{3}{2}} \left(\frac{x_i - \acute{x}}{s}\right)^3 \qquad \text{Eq. App. B 15}$$

$$\gamma_2 = \frac{n(n+1)}{(n-1)(n-2)(n-3)}\sum_{n}^{i=1} w_i^2 \left(\frac{x_i - \acute{x}}{s}\right)^4 - \frac{3(n-1)^3}{(n-2)(n-3)} \qquad \text{Eq. App. B 16}$$

B 7 References

Andersen, M. S., Dahl, J. & Vanderberghe, L. (2013). CVXOPT: A Python package for convex optimization. cvxopt.org.

Chavanne, J., Elleaume, P. & Van Vaerenbergh, P. (1996). *Rev. Sci. Instrum.* **67**, 3346.

Freedman, D. & Diaconis, P. (1981). *Zeitschrift Für Wahrscheinlichkeitstheorie und Verwandte Gebiete*. **57**, 453–476.

Müller, G. (1967). Methods in sedimentary petrology E. Schweitzerbart'sche Verlagsbuchhandlung.

Nützmann, K. (2013). Crystallite Size Distributions of CH 4 -CO 2 Gas Hydrates from Diffraction Data (Including the Effect of Absorption). MSc. Thesis. University of Göttingen.

Rouse, K. D., Cooper, M. J., York, E. J. & Chakera, A. (1970). *Acta Crystallogr. Sect. A*. **26**, 682–691.

Tschentscher, T. & Suortti, P. (1998). *J. Synchrotron Radiat.* **5**, 286–292.

Wikipedia contributors (2017). Convolution. https://en.wikipedia.org/wiki/Convolution.

Appendix C Supplementary material – Coarsening in alumina ceramics - Introducing an X-ray diffraction method for determining crystallite size distributions

AUTHORS

Sigmund H. Neher[1], Helmut Klein[1], Werner F. Kuhs[1]

[1] GZG Abt. Kristallographie, Georg-August-Universität Göttingen, 37077 Göttingen, Germany

C 1 Supplementary figures

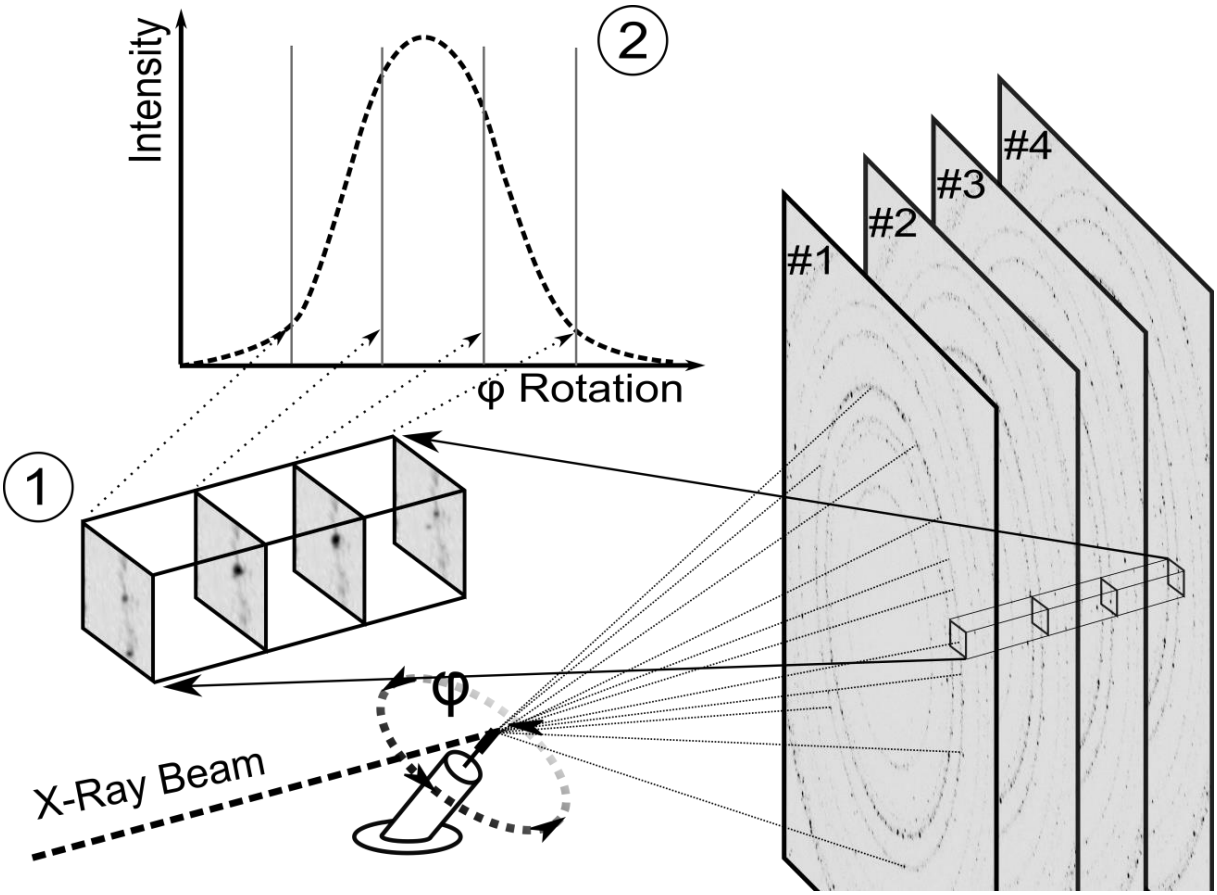

Figure App. C-1: Rocking-curve obtained from spotty diffraction patterns, schematically. A stepwise rotation is moving individual crystals in a polycrystalline material or powder through the diffraction condition. Insert ① shows how the intensity is evolving on the detector (Bragg peak located in the center of the area-of-interest) when the sample is rotated; each frame corresponds to one step in φ. Insert ② shows the integrated intensity of the selected Bragg reflection in each frame is plotted vs. the sample rotation φ.

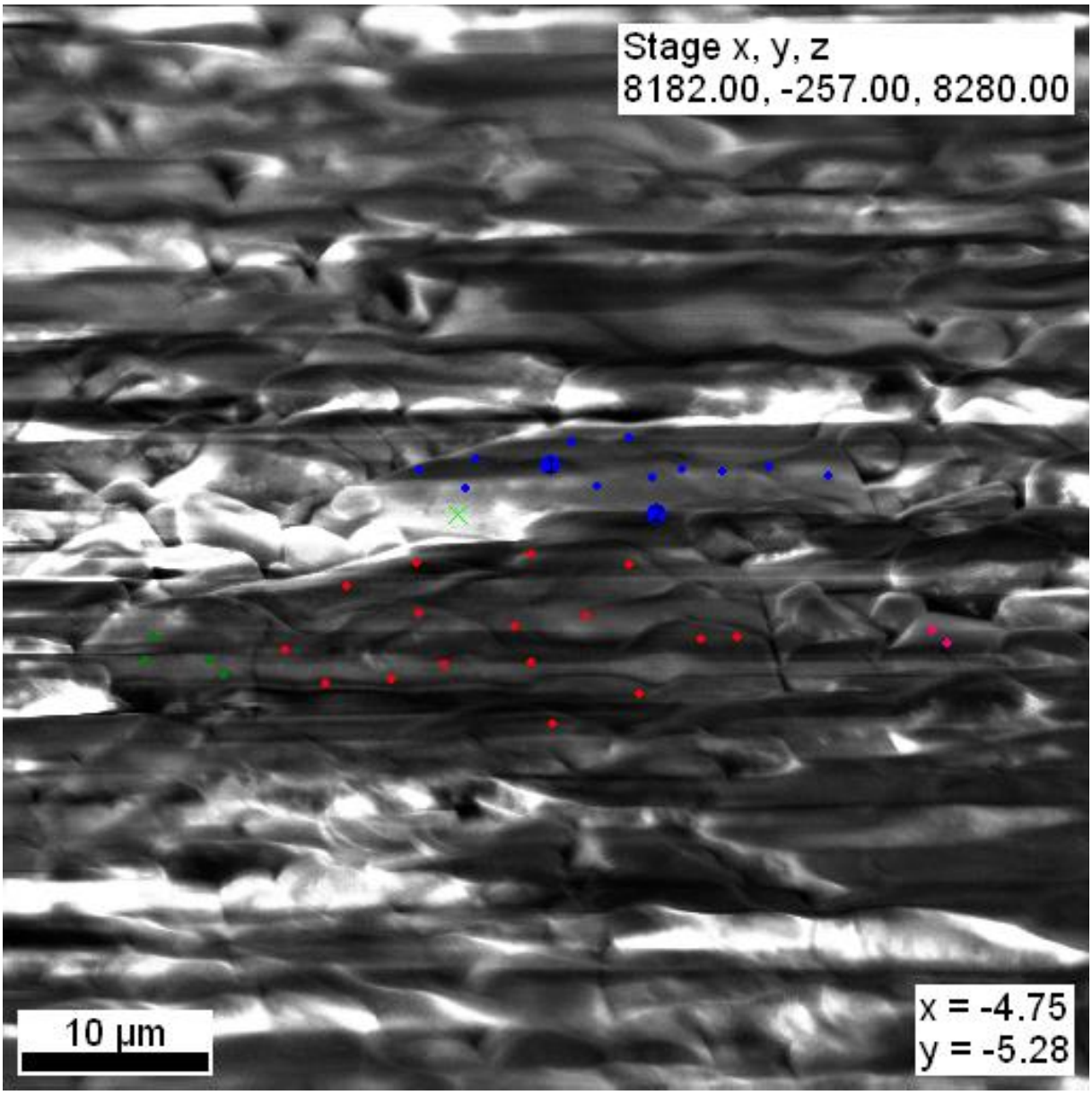

Figure App. C-2: SEM micrograph taken during EBSD measurements. The colored dots show the EBSD measurement positions. Each color represents measurements with the same crystal orientation. They show that the connected areas, also visible in Figure 3.6, are single crystals.

C 2 Supplementary tables

Table App. C-1 Log-Normal PDF[S1] fit parameters

Sintering Time	Amplitude	σ	μ	X^2
4h	1 (fixed)	0.3786824+/- 0.00215	1.7871351+/- 0.00742	0.0006
6h	1 (fixed)	0.3786824+/- 0.00215	1.9169233+/- 0.00260	0.0001
16h	1 (fixed)	0.4385498+/- 0.00416	1.9947868+/- 0.00502	0.0002
24h	1 (fixed)	0.4304394+/- 0.006249	1.9740847+/- 0.00756	0.0005

[S1]: log-normal pdf $f(x) = \frac{1}{x\sigma\sqrt{2\pi}} e^{-\frac{(lnx-\mu)^2}{2\sigma^2}}$

Table App. C-2 Weibull PDF[S2] fitting parameters

Sintering Time	Scale α	Shape κ	X^2
4h	6.5571356	3.1190272	0.004
6h	7.4560984	3.0364047	0.003
16h	8.1609488	2.6271661	0.002
24h	2.6271661	2.6271661	0.004

[S2]:Weibull PDF for x≥0, $f(x;\ \lambda, k) = \frac{k}{\lambda}(\frac{x}{\lambda})^{k-1}\ e^{(z/\lambda)^k}$

Table App. C-3 Gamma PDF[S3] fitting parameters

Sintering Time	α	β	X^2
4h	8.0220810+/- 0.39074	1.2993022+/- 0.06702	0.001
6h	7.50077445+/- 0.18708	1.0656867+/- 0.02827	0.000
16h	5.74036037+/- 0.19113	0.7460345+/- 0.02689	0.001
24h	5.95274680+/- 0.24856	0.7902281+/- 0.03570	0.001

[S3] $f(x;\alpha,\beta) = \frac{\beta^\alpha}{\Gamma(\alpha)} x^{\alpha-1} e^{-\beta x}$ for x>0 and α, β> 0, with the Gamma function Γ

Appendix D Supporting Information - Time resolved coarsening of clathrate crystals: Case of gas hydrates

Marwen Chaouachi[1], Sigmund H. Neher[1], Andrzej Falenty[1], Werner F. Kuhs*[1]

[1]GZG Abt. Kristallographie, Georg-August-Universität Göttingen, 37077 Göttingen, Germany

D 1 Supporting figures

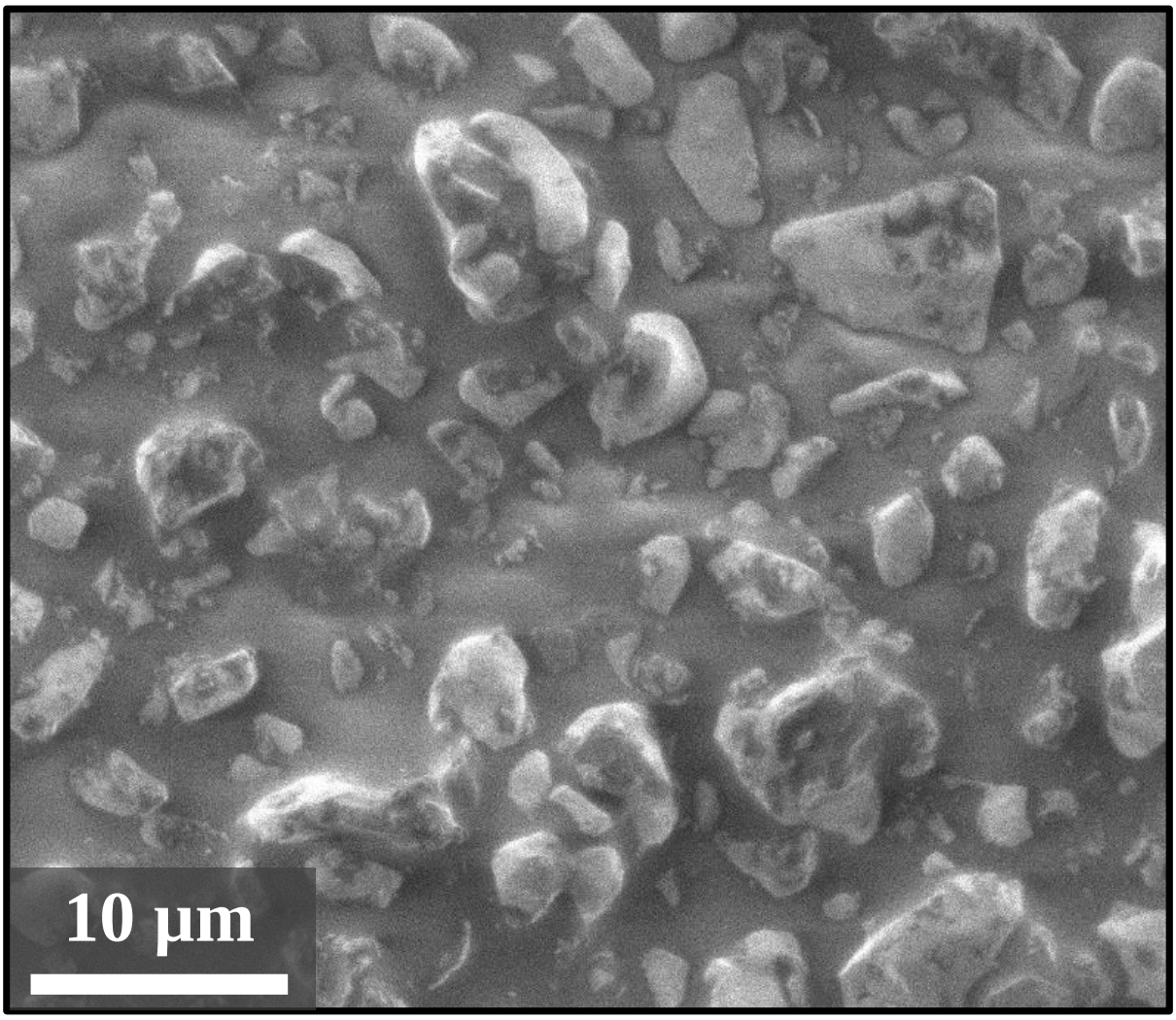

Figure App. D-1: Typical SEM image of LaB_6 NIST 660 a powder. Each particle represents a monocrystal.

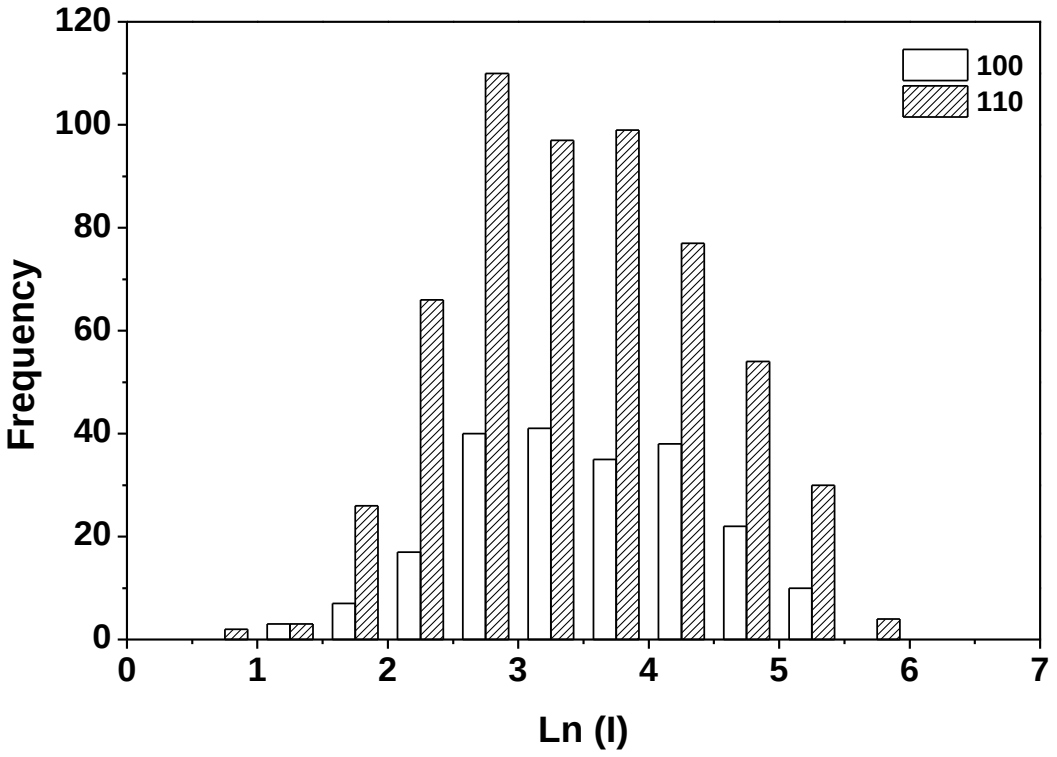

Figure App. D-2: Comparison of 100 and 110 intensities after normalization with the structure factor. The 110 Bragg reflection has a lower size detection limit (<1) than the 100 reflection. The different number occurrences for the 100 and 110 reflections are due to the different reflection multiplicities (6 for the 100 reflection and 12 for the 110 reflection).

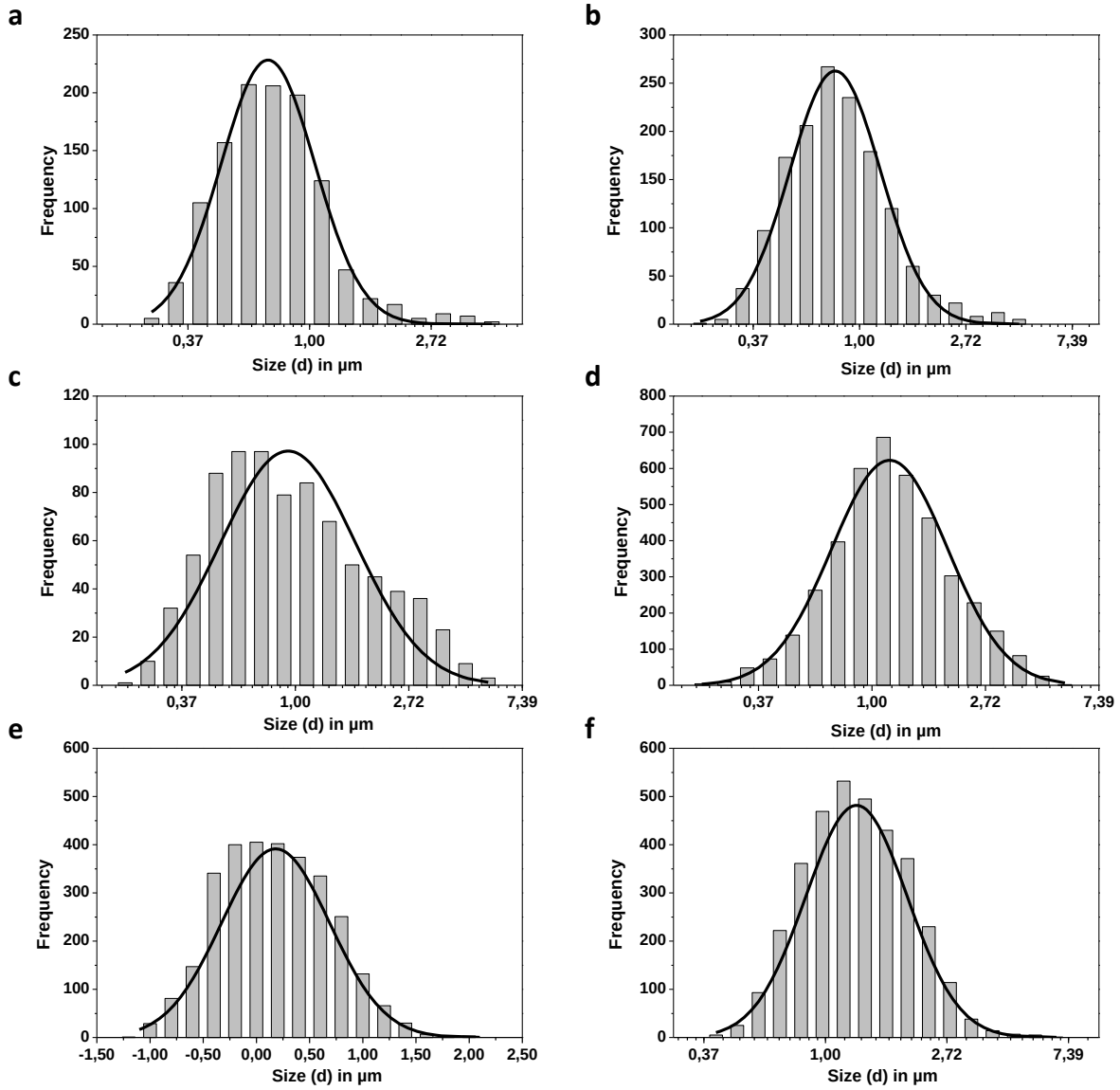

Figure App. D-3: Log-normal distributions of Xe hydrate with Gaussian fit (black curve) for each scan. **a**: 2 min (χ^2= 3.76), **b**: 30 min (χ^2= 4.31), **c**: 2 days (χ^2= 6.42), **d**: 4 days (χ^2= 4.63), **e**: 1 week (χ^2= 7.39), **f**: 4 weeks (χ^2= 3.94) where χ^2 is the reduced chi square value. The 2 days shown in Figure App. D-3c show a broad non-Gaussian distribution, which is very likely the consequence of the coexistence of two types of hydrate crystals – one related to the ripened initial interfacial film and a second type of smaller size crystals grown inside liquid water (see Figure 4.9).

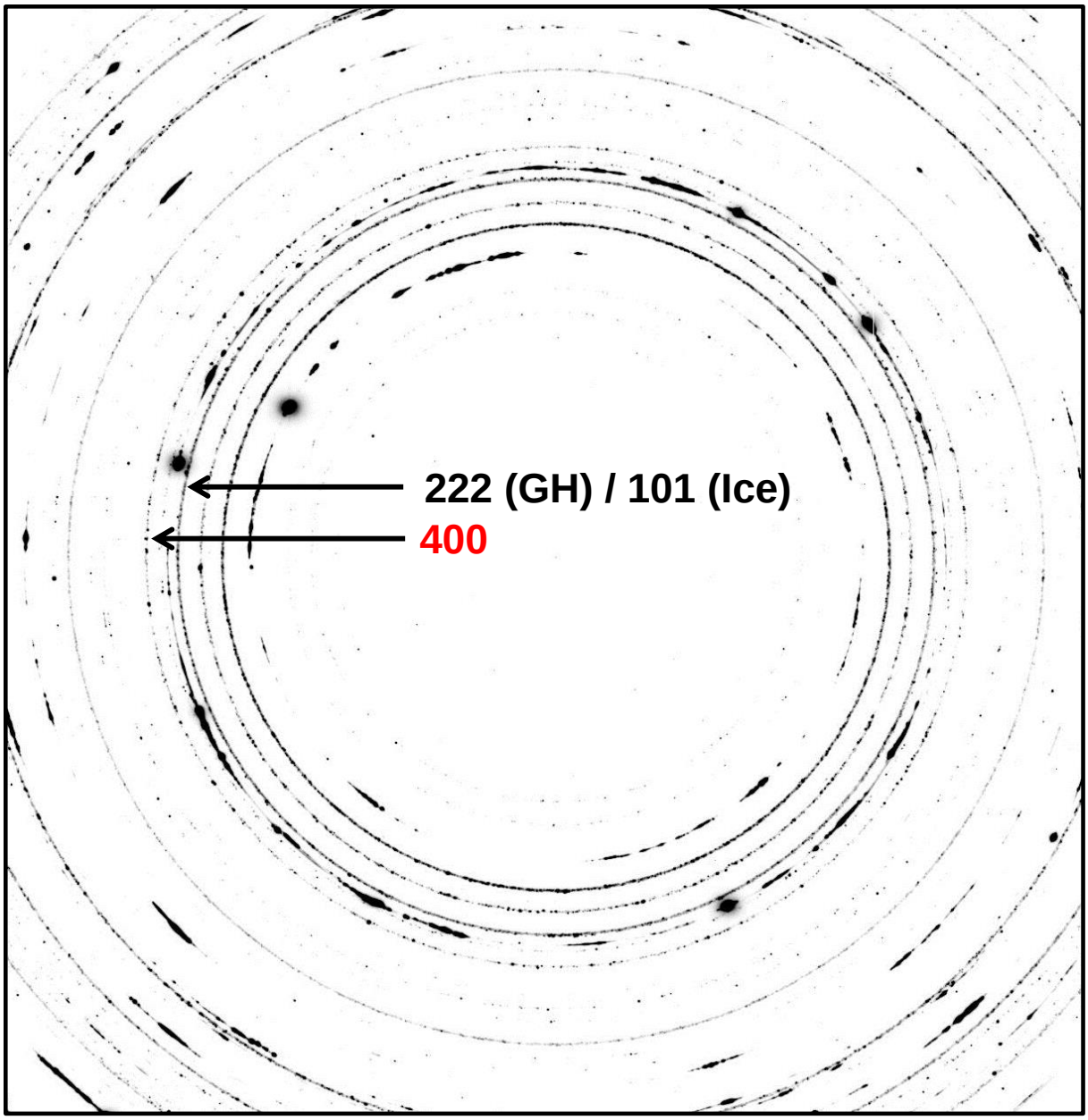

Figure App. D-4: Two-dimensional diffraction pattern of CH_4 hydrate in quartz sand. Only the 400 GH Bragg reflection was accessible for analysis. The 222 *hkl* reflection is overlapped with the 101 ice reflection.

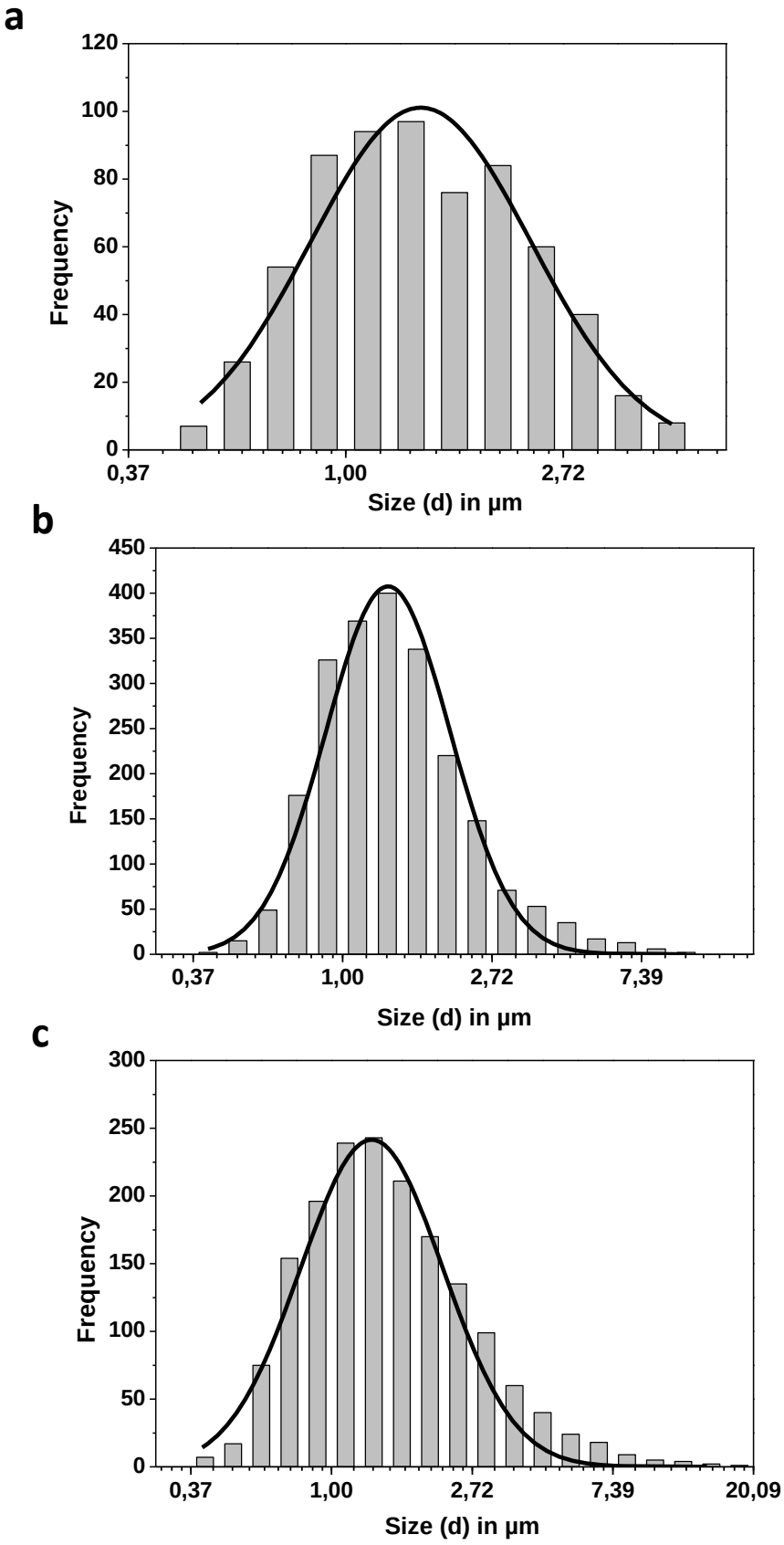

Figure App. D-5: Log-normal distributions of CH_4 hydrate with Gaussian fit (black curve) for each scan. **a**: 3 days (χ^2= 1.85), **b**: 1 week (χ^2= 8.76) , **c**: 6 weeks (χ^2= 5.54), where χ^2 is the reduced chi square value.

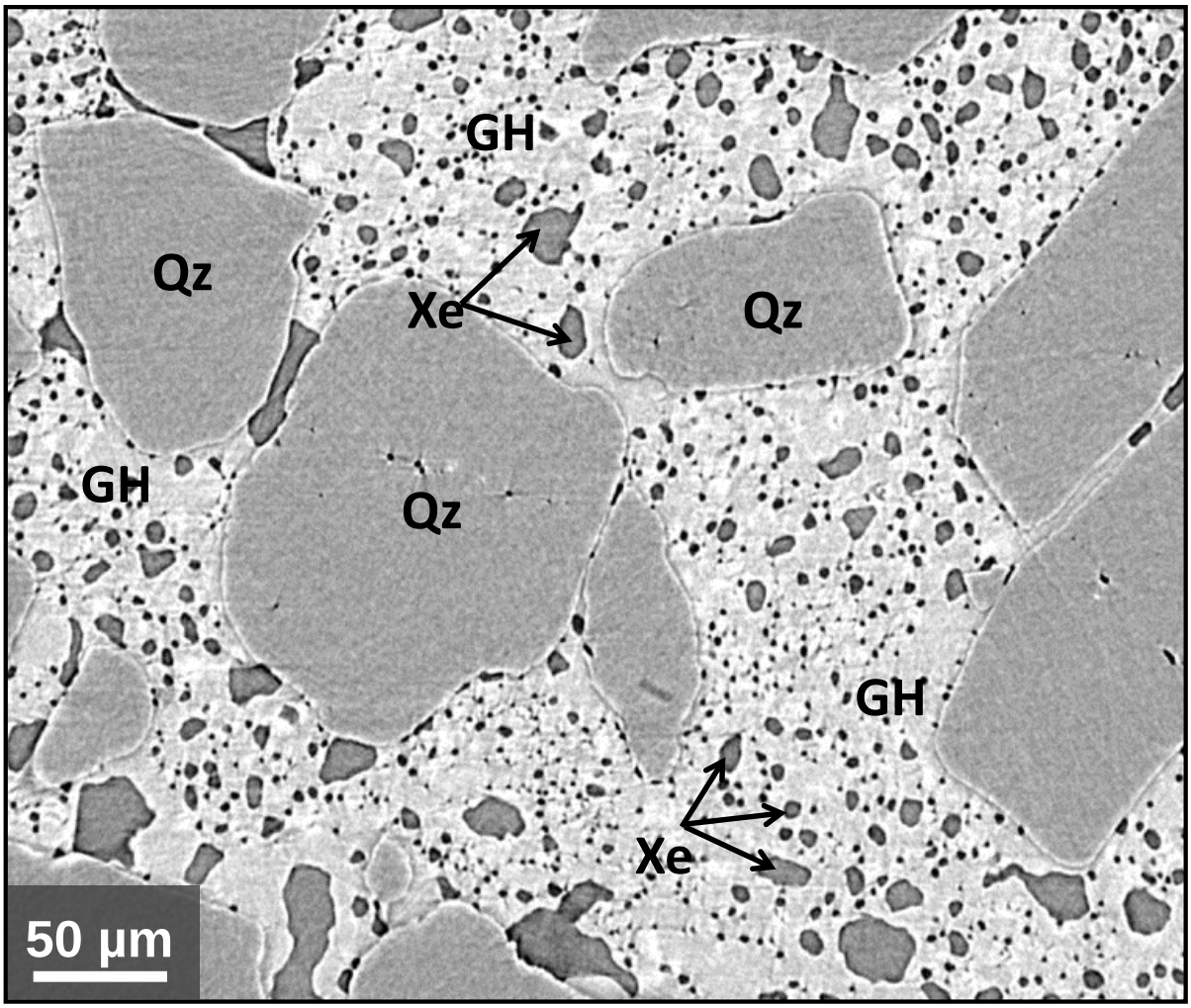

Figure App. D-6: Completed GH formation in the pore space between quartz grains (Qz); sample formed from juvenile water with initial saturation of 88 vol.% and t_R = 35 min. At this final stage of formation, individual crystals are difficult to discern and can no longer be reliably identified.

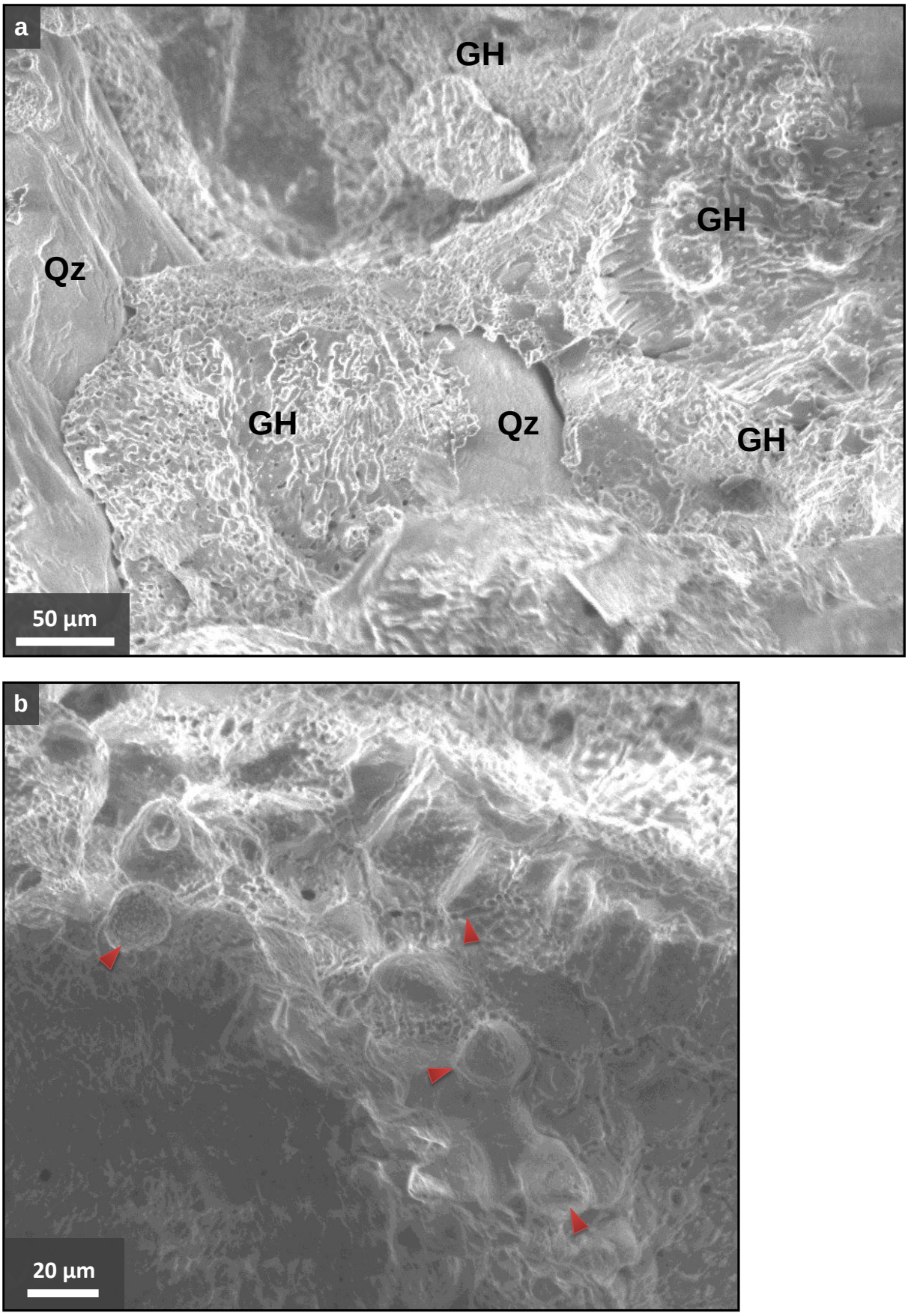

Figure App. D-7: SEM images of synthetic CH_4 hydrate in quartz sand. **a**: Overview image of GH distributed in pore spaces. **b**: Magnified image showing a surface with some coarsened 15 - 20 µm GH crystals (some examples marked by red arrows).

D 2 Supporting tables

Table App. D-1: Calculation of scale factors S_1 with correction for missing low-intensity reflections

Data sets	Mean of ln(I) of LaB_6 intensity data[1]	FWHM of ln(I) of intensity data[1]	Correction for missing reflections	Ln(S_1)[2]
Xe-hydrate *in situ* in sand	11.10(5)	2.45(11)	(4.70 – 2.45)/2	12.09
Xe-hydrate *ex situ* in sand	9.05(17)	5.28(43)	0.0	13.01
CH_4-hydrate *ex situ* in sand	8.48(5)	3.98(12)	(4.70 – 3.98)/2	13.94
CH_4-hydrate from ice I_h	9.73(6)	3.55(10)	(4.70 – 3.55)/2	12.91

[1] Estimated standard deviations obtained from log-normal fitting are given in brackets.
[2] Calculated by taking into account the canonical value for the SEM data of LaB6, i.e. 22.06(7) for the mean ln(V) in nm 3 and 4.70(14) for the FWHM(V) and using the expression ln(S1) = 22.06 – Mean ln(I) + (4.70 – FWHM ln(I)). The Xe-hydrate *ex situ* data sets gave the full expected width, thus did not need a correction for missing low-intensity reflections.

Table App. D-2: Mean crystal sizes and standard deviations of rejected Xe hydrate Bragg reflections.

		hkl	N total	N final	Mean	SE of Mean	Linear mean (µm)	Std. Dev (µm)
2 min		321	110	59	0.797	0.054	2.219	0.120
		211	152	16	0.885	0.084	2.423	0.204
		210	25	14	1.105	0.110	3.019	0.332
30 min		321	354	135	0.230	0.033	1.259	0.042
		211	97	35	0.516	0.046	1.675	0.077
		210	107	65	0.485	0.039	1.624	0.063
		200	32	14	0.498	0.073	1.645	0.120
2 days		321	807	493	0.832	0.021	2.298	0.048
		211	331	184	0.794	0.029	2.212	0.064
		210	377	226	0.911	0.029	2.487	0.072
		200	90	50	0.776	0.063	2.173	0.137
4 days		321	2281	978	0.959	0.011	2.609	0.029
		211	1008	353	1.04	0.018	2.829	0.051
		210	1174	562	0.995	0.013	2.705	0.035
		200	384	169	0.863	0.025	2.370	0.059
1 week		321	2172	1023	0.999	0.011	2.716	0.030
		211	888	422	1.052	0.016	2.863	0.046
		210	828	399	1.122	0.014	3.071	0.043
		200	253	85	0.838	0.035	2.312	0.081
4 weeks		321	1593	868	0.950	0.012	2.586	0.031
		211	640	329	1.050	0.019	2.858	0.054
		210	589	321	1.140	0.016	3.127	0.050
		200	183	111	0.789	0.025	2.201	0.055

Mean: mean value on logarithmic scale
SE of mean: Standard deviation of the mean on logarithmic scale
Linear mean: Exp (Mean)
Std. Dev: Standard deviation on linear scale (= linear mean x SE of mean)

Curriculum vitae:

- Since 2005 student at the Georg-August-University of Göttingen, Geoscience
- April 2009 Bachelor of Science (Geoscience) at the Georg-August-University of Göttingen
- February 2012 Diploma in Geoscience
- 2012 Employment as research assistant at the crystallography department of the Georg-August-University of Göttingen. Field of activity: Preparation of the DFG grant proposal KU920/20-1 to fund my doctoral student position.
- since 2013 doctoral student an der Georg-August-University of Göttingen

Lebenslauf:

- Seit 2005 Student der Geowissenschaften an der Georg-August-Universität Göttingen
- April 2009 Bachelor of Science (Geowissenschaften) an der Georg-August-Universität Göttingen
- Februar 2012 Diplom in Geowissenschaften an der Georg-August-Universität Göttingen
- 2012 Anstellung als wissenschaftliche Hilfskraft in der Abteilung Kristallographie, Georg-August-Universität Göttingen. Tätigkeit: Ausarbeitung des DFG-Antrags KU920/20-1 zur Finanzierung meiner Promotion
- Seit 2013 Promotionsstudent an der Georg-August-Universität Göttingen